



TECHNISCHE
UNIVERSITÄT
WIEN



CoQuS
ComplexQuantumSystems

DISSERTATION

Relaxation to a Phase-locked Equilibrium State in a One-dimensional Bosonic Josephson Junction

von

MSc. Marine Pigneur

Matrikelnummer 1329604

Neustiftgasse 96/2/5

1070 Wien, Österreich

ausgeführt zum Zwecke der Erlangung des akademischen Grades eines
Doktors der Naturwissenschaften

eingereicht an der
Technischen Universität Wien
Fakultät für Physik

unter der Leitung von
Univ.-Prof. Dipl.-Ing. Dr. techn. Hannes-Jörg Schmiedmayer
Atominstitut (E141)

Wien, Oktober 2019

Marine Pigneur

Diese Dissertation haben begutachtet:

H.-J. Schmiedmayer

M. Oberthaler

A. Smerzi



Die approbierte gedruckte Originalversion dieser Dissertation ist an der TU Wien Bibliothek verfügbar.
The approved original version of this doctoral thesis is available in print at TU Wien Bibliothek.

Abstract (English)

Relaxation to a Phase-locked Equilibrium State in a One-dimensional Bosonic Josephson Junction

The relaxation of isolated quantum many-body systems is a major unsolved problem of modern physics. It connects to many fundamental questions, ranging from the state of the early universe and heavy-ion collisions to the electron dynamics in condensed matter physics.

However, realizations of quantum many-body systems which are both well isolated from their environment and accessible to experimental study are scarce. In recent years, the field has experienced rapid progress, partly attributed to the unprecedented insights provided by ultra-cold atoms.

In this thesis, we present the experimental study of a relaxation phenomenon occurring between two elongated coupled superfluids. This system, known as one-dimensional Bosonic Josephson junction (1D-BJJ), benefits from numerous advantages. From an experimental point of view, the 1D-BJJ presents the versatility, high controllability and isolability characteristic to ultra-cold atom systems. This allows a rigorous and wide-ranging study of the relaxation. From a theoretical point of view, the 1D-BJJ benefits from extensive theoretical works provided in particular by the sine-Gordon model. This model has proven successful in describing the equilibrium dynamics of two coupled 1D atomic superfluids up to very high order correlations. However, it fails to describe the relaxation we observe and it is therefore strongly challenged by this work.

In a first set of experiments, a well-defined non-equilibrium state is created by coherent splitting of a single one-dimensional Bose gas into two halves. A precise phase difference between the two halves is introduced while preserving a high phase coherence. The subsequent dynamics exhibit a relaxation to a phase-locked equilibrium state, the timescale of which exceeds theoretical expectations. We support the experimental results with an empirical model that allows quantitative discussions. Various experimental parameters, among which the atom number and the tunnel coupling strength, are varied to investigate their impact on the relaxation mechanism and to help determining its origin.

The second experiment investigates the dynamics of a pair of 1D Bose gases differing by their atomic density. In this case, the system presents a more complex distribution of excitations and its dynamics exhibits a threshold above which the relaxation is dominated by a dephasing. It provides additional insights into the relaxation mechanism as some experimental parameters such as the trap geometry, become more relevant in this case compared to the first set of experiments.

These observations attest to the existence of a relaxation phenomenon in a 1D-BJJ and illustrate how strongly the non-equilibrium dynamics differ from the equilibrium one, which is well described by thermodynamics and statistical physics.

Zusammenfassung (Deutsch)

Relaxation zu einem Phasen-Stabilen Gleichgewichtszustand in einem Eindimensionalen Josephson Kontakt

Es ist eine der größten Fragen der modernen Physik, ob und auf welche Weise ein Quanten-Vielteilchensystem nach einer Störung einen thermodynamischen Gleichgewichtszustand erreicht. Verbunden mit dieser "Quanten Relaxation" sind viele weitere fundamentale Fragen, vom Zustand des frühen Universums über Schwerionen-Kollisionen bis hin zur Dynamik von Elektronen in Festkörpersystemen.

Zur ihrer Untersuchung benötigt man Quanten-Vielteilchensystemen die einerseits von ihrer Umwelt isoliert, als auch experimentell zugänglich sind. In diesem Feld sind in den letzten Jahren große Fortschritte erzielt worden, verbunden mit der einzigartigen Kontrolle, welche ultrakalte atomare Quantengase bereitstellen.

In dieser Arbeit, präsentieren wir eine experimentelle Studie von Relaxationsphänomenen, welche zwischen zwei ausgedehnten, tunnel-gekoppelten Superflüssigkeiten auftreten. Das System, welches auch als eindimensionaler Josephson Kontakt bekannt ist (1D-BJJ), hat viele Vorteile gegenüber anderen Systemen. Vom experimentellen Standpunkt zeigt der 1D-BJJ große Flexibilität, leichte Kontrollierbarkeit und Isolierbarkeit, Eigenschaften die generell charakteristisch für kalte Atome sind. Dies erlaubt eine umfangreiche quantitative Studie der auftretenden Relaxation sowie des Endzustandes durchzuführen. Von einem theoretischem Standpunkt betrachtet existieren für den 1D-BJJ bereits umfassende theoretische Modelle, speziell das sogenannte sine-Gordon Modell. Dieses Modell beschreibt sehr erfolgreich den Gleichgewichtsdynamik von zwei gekoppelten 1D Atomwolken, bis zu hohen Ordnungen der Korrelationsfunktion. Bemerkenswerterweise scheitert das Modell, die beobachtete Relaxationsdynamik zu erklären, und wird durch diese Arbeit in Frage gestellt.

In einem ersten Experiment präparieren wir einen sehr wohldefinierten Nicht-Gleichgewichts-Zustand durch kohärentes Auftrennen von einem eindimensionalen Bose-Gas in zwei Hälften. Ein präziser Phasenunterschied zwischen den beiden Hälften wird kontrolliert aufgeprägt, wobei die Phasenkohärenz erhalten bleibt. Die darauffolgende Tunneldynamik zeigt eine Entwicklung zu einem phasenstabilen Gleichgewichtszustand. Dabei weicht die Zeitskala der Dynamik wesentlich von den Vorhersagen der theoretischen Modelle ab. Wir entwickeln ein empirisches Modell um diese Dynamik quantitativ zu beschreiben, in sehr guter Übereinstimmung mit den experimentellen Daten. Verschiedene experimentelle Parameter, wie die Atomzahl oder die Stärke der Tunnelkopplung werden variiert, um den Effekt auf die Dynamik zu untersuchen und Einblicke in den Ursprung der Relaxation zu gewinnen.

Ein zweites Experiment untersucht die Dynamik eines tunnel-gekoppelten Paares von 1D Bose Gasen mit unterschiedlichen Atomdichten. In diesem Fall zeigt das System eine kompliziertere Verteilung von Anregungen und die Dynamik zeigt einen Schwellwert, über dem die Relaxation von Dephasierung dominiert wird. Dieses Experiment liefert zusätzliche Einblicke in die Relaxationsmechanismen insbesondere da Parameter wie die Fallengeometrie einen größeren Einfluss haben.

Beide Experimentreihen zeigen zweifelsfrei eine Relaxation in einem 1D-BJJ und illustrieren, wie stark sich Nicht-Gleichgewichtssysteme von Gleichgewichtssystemen unterscheiden, für welche es exzellente Beschreibungen durch statistische Physik und Thermodynamik gibt.

Contents

Introduction	1
1 Theoretical framework	3
1.1 The ideal Bose gas	3
1.1.1 Bose statistics and density of states	3
1.1.2 Bose-Einstein condensation in 3D	4
1.1.3 Quasi-condensation in 1D	6
1.2 Weakly interacting Bose gas	7
1.2.1 Many-body Hamiltonian in second quantization	7
1.2.2 Mean-field model: the Gross-Pitaevskii equation	8
1.2.3 The Thomas-Fermi limit	9
1.2.4 Crossover 3D/1D	12
1.3 Bose Gases in a double-well potential	14
1.3.1 Two-mode approximation	15
1.3.2 Ideal dynamics in the mean-field formalism	17
1.3.2.1 Standard and improved two-mode models	17
1.3.2.2 Tunneling dynamics in a symmetric trap	18
1.3.2.3 Generalization to an asymmetric BJJ	28
1.3.2.4 Link between the TMBH and the pendulum parameters	29
1.3.2.5 Limitation of the analytical solutions	31
1.3.3 Quantum fluctuations	31
1.3.3.1 Quantum model	31
1.3.3.2 Ground state properties	33
1.3.4 Dynamics with fluctuations in the semi-classical picture	34
1.3.4.1 Principle of the Monte-Carlo like model	35
1.3.4.2 Ground state and static states	36
1.3.4.3 Squeezing oscillations	38
1.3.4.4 Dephasing	40
1.3.4.5 Interaction-induced phase diffusion	42
1.3.4.6 Adiabatic squeezing generation by linear ramp	47
1.3.4.7 Improved squeezing generation protocols	53
1.4 Conclusion of the theoretical chapter	56
2 Experimental setup and measurement of the observables	57
2.1 Overview of the experimental sequence	57
2.2 Experimental apparatus	59
2.2.1 Vacuum chamber and Rubidium dispensers	59
2.2.2 Copper structure and atom chip	59

2.2.3	External coils	62
2.2.4	Lasers system and optics	62
2.2.5	Radio-frequency generators	63
2.2.6	Computer control and acquisition	64
2.3	Magnetic trapping of atoms with an atom chip	65
2.3.1	Magnetic trapping with static fields	65
2.3.1.1	Magnetic interaction	65
2.3.1.2	Transverse confinement in a wire-guide	66
2.3.1.3	Longitudinal confinement in an H trap	69
2.3.1.4	Trap simulation with realistic wires	70
2.3.1.5	Trap characterization	70
2.3.2	Magnetic trapping with radio frequency fields	72
2.3.2.1	Magnetic resonance and coupling to a classical rf field	72
2.3.2.2	Adiabatic potential for rf dressed atoms	74
2.3.2.3	The dressed Ioffe-Pritchard trap	76
2.3.2.4	Implementation of a double-well with an atom chip	81
2.3.2.5	Calibration and double-well characterization	83
2.3.2.6	Estimation of the tunnel coupling	86
2.4	Imaging and data analysis	86
2.4.1	Imaging systems	86
2.4.1.1	Absorption imaging	86
2.4.1.2	Light sheet fluorescence imaging	92
2.4.2	Estimation of the relative phase	97
2.4.2.1	Experimental implementation	97
2.4.2.2	Determination of the phase	97
2.4.2.3	Global phase statistics: averaging and fluctuations	102
2.4.2.4	Post selection and noise correction	102
2.4.3	Estimation of the atom number difference	105
2.4.3.1	Experimental implementation	105
2.4.3.2	Noise correction and number squeezing factor	106
3	Relaxation of the Josephson oscillations in a 1D-BJJ	109
3.1	Preparation of the initial state	109
3.1.1	Experimental requirements	109
3.1.2	Coherent splitting of the wave function by linear ramp	111
3.1.3	Phase accumulation	114
3.1.4	Recoupling	117
3.2	Relaxation of the oscillating tunneling dynamics	120
3.2.1	Relaxation versus dephasing and dissipation	120
3.2.2	Empirical model for the relaxation	126
3.2.2.1	Dissipative BJJ in the TMBH model	126
3.2.2.2	Analytical pendulum model of the dissipative BJJ	126
3.2.2.3	Application to experimental data	129
3.2.3	Experimental dependence of the relaxation timescale	135
3.2.3.1	Initial phase and initial energy	135

3.2.3.2	Tunnel coupling strength	138
3.2.3.3	Atom number	142
3.2.3.4	Initial temperature	143
3.2.3.5	Transverse and longitudinal cloud extensions	145
3.2.3.6	Effective relaxation-free dynamics	145
3.3	Conclusion	148
4	Transition to a relaxation-free regime	149
4.1	Initial state preparation by asymmetric splitting	149
4.2	Decay and relaxation	153
4.2.1	Experimental evolution of the mean values	153
4.2.2	Dissipative BJJ in the MQST	153
4.2.2.1	Numerical models	153
4.2.2.2	Analytical pendulum solution in the MQST	155
4.2.3	Relaxation through local dynamics	157
4.2.3.1	Experimental evidences of a local relaxation channel	157
4.2.3.2	Model using an array of independent BJJ	158
4.3	Transition to a relaxation-free regime	162
4.4	Conclusion	164
5	Outlook: Consequence of a relaxation on the splitting of a 1D Bose gas	167
5.1	Adiabatic splitting	167
5.1.1	Estimation of the effective duration of the relaxation	167
5.1.2	Simulation of a linear splitting with relaxation	169
5.2	Two-step splitting	171
5.2.1	Two-step splitting with relaxation	171
5.2.2	Preliminary results on the implementation of the first ramp	172
	Bibliography	177
	Acknowledgements	189
	List of Publications	193
	Curriculum Vitae	194



Die approbierte gedruckte Originalversion dieser Dissertation ist an der TU Wien Bibliothek verfügbar.
The approved original version of this doctoral thesis is available in print at TU Wien Bibliothek.

Introduction

How and to which extent does an isolated quantum many-body system relax? The question is as relevant as it is puzzling.

Relevant first, because it is an open problem covering vastly different scales of energy, length and time. It ranges from the expansion dynamics of the early universe [1–3] and the physics of quark-gluon plasmas [4–6], to the coherence properties of solid-state materials [7–10] and future quantum information devices [11]. Therefore, a thorough understanding could both clarify the origins of our universe and lead to important technological advances.

Puzzling also, because it appears as a contradiction. A phenomenon of relaxation generally implies a dissipation of energy from the system through its interaction with an environment. However, in an isolated quantum many-body system, such an environment is by definition absent, such that a relaxation seems in contradiction with a unitary evolution. In recent years, both theoretical and experimental work proved that non-integrable systems can reach a thermal equilibrium state resembling a Gibbs ensemble [12–21].

A more precise formulation of the question is: how can the unitary non-equilibrium evolution of an isolated quantum many-body system lead to observables which relax to steady, thermal expectation values?

To address this question, the experimentalist must face several challenges such as the realization of truly isolated systems and the highly controlled preparation and accurate measurement of non-equilibrium dynamics. Over the last years, ultra-cold gases have been established as ideal model systems in this context [22]. The large set of methods to isolate, manipulate and probe these gases [23] resulted in unprecedented advances. The most remarkable example illustrating the versatility of ultra-cold gases might be their tunable interactions [24, 25] and their application as quantum simulators [26]. To extract information, these systems can be probed with single-atom sensitivity [27–29].

In particular, the experimental realization of one-dimensional (1D) quantum gases enables a detailed study of numerous theoretical models [30, 31], among which the Luttinger liquids [32, 33] and the sine-Gordon model [34–38]. The 1D Bose gas is an example of integrable systems [39], for which the existence of many conserved quantities has a strong influence on the dynamics. In the experiment, these conserved quantities are realized only approximately, which opens up the possibility of studying relaxation close to an integrable point [40, 41].

We investigate in this thesis the dynamics between two 1D Bose gases coupled by tunneling which realize a 1D Bosonic Josephson junction (1D-BJJ) [42]. The experiment relies on an atom chip device [43–46], on which micro-fabricated wires allow the precise manipulation of ultra-cold gases using static and radio-frequency (rf) magnetic fields [47–49]. For example, we can realize a coherent splitting of a single 1D quantum gas into two parallel 1D halves by introducing a double-well potential. A subsequent energy

difference between the two sites of the double-well results in a global phase difference and initializes a well-controlled and reproducible non-equilibrium evolution. The resulting dynamics can be investigated in great detail through matter-wave interference between the two halves [50–52].

While we expect from the equilibrium dynamics that the sine-Gordon model provides an accurate description of the system [41], the observed relaxation goes beyond theoretical predictions [38, 53–55] and exhibits a microscopic mechanism of energy transfer which remains to be described [56]. The coherent manipulation of the 1D superfluids enables several experiments demonstrating that the non-equilibrium dynamics of a 1D-BJJ.

This thesis is structured as follow.

- In chapter 1, we establish the theoretical framework describing Bose-Einstein condensates in an elongated double-well potential. The elongated dimension is treated by the Gross-Pitaevskii equation (GPE) while the description of the transverse dynamics relies on the two-mode Bose Hubbard model (TMBH). We establish in this chapter the analytical solution of the BJJ based on the mechanical analogy with a pendulum published in [57]. The last section presents a semi-classical description of the fluctuations of the system and describes phenomena expected in the TMBH model such as squeezing oscillations and interaction-induced phase diffusion.
- Chapter 2 is dedicated to the experimental apparatus. After a review of the hardware of the experiment, we detail the magnetic trapping with the atom chip, which provides a versatile tool to manipulate coherently the Bose gases. Thereafter, we detail the techniques to measure and analyze the observables experimentally accessible: phase difference and atomic imbalance.
- We present in chapter 3 the central experimental results of this thesis published in [56]. We detail the preparation of the non-equilibrium initial state and the experimental relaxation of the oscillating dynamics. A quantitative discussion is made possible by an empirical model [57]. We establish a timescale of the relaxation and investigate its dependence on well-controlled experimental parameters.
- Finally, chapter 4 treats the more complex situation of a pair of one-dimensional Bose gases initially differing by their atom number and atomic density. In this case, the relaxation is observed below a threshold, above which the phase-locking is dominated by a dephasing. We attribute this effect to the trap geometry and the complex energy spectrum of the initial state.

1 Theoretical framework

1.1 The ideal Bose gas

The term boson refers to a particle of integer spin, such as an atom composed of an even number of elementary particles. The neutral atoms of ^{87}Rb studied in this thesis fall into this category, as it contains 37 protons, as many electrons and 50 neutrons.

The statistical properties of a collection of identical bosons at low temperature differ strongly from their classical counterpart. This was first pointed out by Bose in his derivation of the Planck's law for photons [58]. It revealed that the wave function of identical bosons was symmetric under exchange of two particles and that the particles were indistinguishable. As a consequence, there is no limit to the atomic population of a given quantum state. Soon afterwards [59], Einstein realized that, as a direct consequence of the Bose statistics, bosons can accumulate in the ground state and form a single coherent object named Bose-Einstein condensate. The ideal Bose gas has been extensively described in the literature, among which [60–62] were used for this section.

1.1.1 Bose statistics and density of states

An ideal quantum gas at thermal equilibrium is well described by statistical mechanics. Rather than a tedious description of the individual particles, statistical mechanics links the macroscopic properties of a system to their underlying microscopic properties using statistical tools. It derives the thermodynamics macroscopic variables such as temperature and entropy from the average over an ensemble that represents all possible microscopic states. A suitable ensemble for quantum statistics is the grand canonical ensemble, which allows an exchange of both heat and particles with a bath.

We consider a generic distribution of N ideal bosons occupying a volume \mathcal{V} , in contact with a bath imposing the temperature T . Assuming that a thermal equilibrium is reached, one can show that the occupation number N_k of a non-degenerate quantum state k of energy ε_k obeys the Bose-Einstein distribution:

$$N_k = \frac{1}{\zeta^{-1} \exp(\varepsilon_k/k_B T) - 1}, \quad (1.1)$$

where $\zeta = \exp(\mu/k_B T)$ is the fugacity, μ is the chemical potential and k_B is the Boltzmann constant. To ensure that the occupation N_k is positive, the chemical potential μ is constrained to remain negative. Therefore, the fugacity must fulfill $0 < \zeta < 1$, where the limit $\zeta \rightarrow 0$ corresponds to the classical Boltzmann statistics and $\zeta \rightarrow 1$ corresponds to the quantum regime.

In the semi-classical approximation ($N \rightarrow \infty$, N/\mathcal{V} constant), the discrete level structure ε_k is approximated by a continuous spectrum called density of states $\mathcal{D}(\varepsilon)$. After

normalization of the Bose-Einstein distribution to the total atom number $N = \sum_k N_k$, the total density of the atoms n obeys the equation of state:

$$n = n_0 + n_{\text{th}}(T, \mu), \quad (1.2)$$

where n_0 is the atomic density in the ground state defined by:

$$n_0 = \frac{1}{\zeta^{-1} \exp(\varepsilon_0/k_{\text{B}}T) - 1}, \quad (1.3)$$

and n_{th} is the atomic density in the thermal states defined by:

$$n_{\text{th}}(T, \mu) = \int_0^{\infty} d\varepsilon \mathcal{D}(\varepsilon) n(\varepsilon). \quad (1.4)$$

1.1.2 Bose-Einstein condensation in 3D

While the thermal density given by Eq. (1.4) is general, its value depends on the density of states $\mathcal{D}(\varepsilon)$, therefore on the geometry and dimensionality of the system. In the following, we consider two geometries where ideal Bose-Einstein condensation occurs, namely the uniform gas in a 3D box and the inhomogeneous gas in a 3D harmonic potential.

Uniform ideal gas The density of states in a box of dimension d is given by:

$$\mathcal{D}(\varepsilon) = \Omega_d \frac{\mathcal{V}}{(2\pi)^d} \frac{1}{2} \left(\frac{2m}{\hbar^2} \right)^{d/2} \varepsilon^{d/2-1}, \quad (1.5)$$

with m the atomic mass, $\hbar = h/2\pi$ the reduced Planck constant and Ω_d defined by:

$$\Omega_d = \begin{cases} 4\pi, & \text{for } d = 3, \\ 2\pi, & \text{for } d = 2, \\ 1, & \text{for } d = 1. \end{cases} \quad (1.6)$$

In this case, one can show that the thermal density $n_{\text{th}}(T, \mu)$ reads:

$$n_{\text{th}}(T, \mu) = \frac{1}{\lambda_{\text{dB}}^3} g_{3/2}(\zeta), \quad (1.7)$$

with $g_{3/2}(\zeta)$ the Bose function defined by:

$$g_k(\zeta) = \sum_{j=1}^{\infty} \frac{\zeta^j}{j^k} \quad (1.8)$$

and λ_{dB} the thermal de Broglie wavelength defined by:

$$\lambda_{\text{dB}} = \sqrt{\frac{2\pi\hbar^2}{mk_{\text{B}}T}}. \quad (1.9)$$

The constraint on the fugacity $0 < \zeta < 1$ and the variations of the Bose function impose the upper bound $g_{3/2}(1) \approx 2.612$ on the density of thermal states. Therefore, a transition occurs when the phase space density, defined by the product of the atomic density and the de Broglie wavelength, reaches:

$$n\lambda_{\text{dB}}^3 = 2.612, \quad (1.10)$$

i.e. when the thermal de Broglie wavelength λ_{dB} is of the order of the mean inter-particle distance $n^{-1/3}$. It defines a critical temperature T_c :

$$T_c = \frac{2\pi\hbar^2}{k_B m} \left(\frac{n}{2.612} \right)^{2/3}, \quad (1.11)$$

which is, for ^{87}Rb , in the sub μK range. For a fixed number of particles N and for $T < T_c$, the thermal states of the system are saturated and all other atoms are forced to accumulate collectively in the ground state. The atomic density reads:

$$n = n_0 + 2.612 \left(\frac{mk_B T}{2\pi\hbar^2} \right)^{3/2}, \quad (1.12)$$

divided between a condensate density n_0 and a saturated thermal density decreasing with the temperature. In terms of critical temperature, the condensed fraction reads:

$$n_0 = 1 - \left(\frac{T}{T_c} \right)^{3/2}. \quad (1.13)$$

Ideal gas in a 3D harmonic trap The case of a harmonic trap is close to the experimental configuration of this thesis. The density of state reads [60]:

$$\mathcal{D}(\varepsilon) = \frac{\varepsilon^{d-1}}{(d-1)! \prod_{i=1}^d \hbar\omega_i}, \quad (1.14)$$

with ω_i the trap frequencies in the different spatial directions. In 3D, the Bose-Einstein condensation occurs at the critical temperature:

$$T_c = \frac{\hbar\bar{\omega}}{k_B} \left(\frac{n}{g_3(1)} \right)^{1/3}, \quad (1.15)$$

where $\bar{\omega} = (\omega_x\omega_y\omega_z)^{1/3}$ is the geometric mean trap frequency. The dependence of the condensed fraction with the temperature reads:

$$n_0 = 1 - \left(\frac{T}{T_c} \right)^3. \quad (1.16)$$

The harmonic trap $V(\vec{r})$ introduces an inhomogeneity in the system, which translates into a position-dependent chemical potential $\mu(\vec{r})$. As a result, the atoms located at different positions reach the condensation threshold at different critical temperatures. This situation can be described by considering Eq. (1.2) in the local density approximation

(LDA), which consists in assuming local equilibrium and defines the chemical potential locally as $\mu(\vec{r}) = \mu - V(\vec{r})$. The highest atomic density \tilde{n} is located at the trap minimum. When decreasing the temperature, it is the first area of the cloud to reach the condensation threshold when

$$\tilde{n}\lambda_{\text{dB}}^3 = 2.612. \quad (1.17)$$

In the $T = 0$ limit, all atoms condense in the ground state and each atom is described by the single-particle Gaussian ground state wave function of the harmonic trapping potential:

$$\psi_0(i) = \frac{1}{a_{\text{ho},i}\sqrt{\pi}} \exp(-i^2/2a_{\text{ho},i}^2) \quad (1.18)$$

with $i = x, y, z$. The harmonic length $a_{\text{ho},i} = \sqrt{\hbar/m\omega_i}$ characterizes the length of the ideal condensate in the direction i . The total wave function is the product of the single-particle wave functions and the density profile reads:

$$n(\vec{r}) = N|\psi_0(\vec{r})|^2. \quad (1.19)$$

1.1.3 Quasi-condensation in 1D

The dimensionality of the system is crucial as it alters the description of Bose-Einstein condensation previously introduced. In a 1D uniform box, the density of state given by Eq. (1.5) results in the Bose function $g_{1/2}(\zeta)$ which diverges when $\zeta \rightarrow 1$. Therefore, there is no clear phase transition in 1D. In such case, it was demonstrated in [60, 63] that condensation can still occur for finite N but at lower temperatures than the one at which the inter-particle spacing is comparable to the thermal de Broglie wavelength.

The case of a very anisotropic trap with $\omega_z \ll \omega_x, \omega_y$ is treated in [63]. We consider a temperature such that the thermal energy $k_B T$ is small compared to $\hbar\omega_x$ and $\hbar\omega_y$. The particles are therefore in the lowest energy state for the motion along the x and y directions and the number of particles in the excited states along z is given by

$$n_{\text{th}} = \sum_{k=1}^{\infty} \frac{1}{\exp(k\hbar\omega_z/k_B T) - 1}. \quad (1.20)$$

This quantity diverges in the continuous limit. However, the lowest excitation energy is $\hbar\omega_z$ such that a better estimate is obtained by a cut off of the integral off at $k = 1$. The number of thermal atoms is given by:

$$N \approx \frac{k_B T}{\hbar\omega_z} \ln \left(\frac{k_B T}{\hbar\omega_z} \right) \quad (1.21)$$

and leads to a critical temperature T_c :

$$T_c \approx \frac{\hbar\omega_z}{k_B} \frac{N}{\ln N}. \quad (1.22)$$

Equation (1.20) illustrates that, contrary to the 3D case, trapped atoms in 1D populate many momentum modes (Fig. 1.1), which results in strong density and phase fluctuations

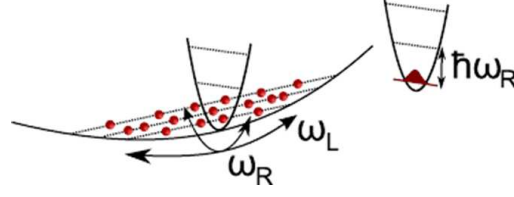


Figure 1.1: Schematic of 1D quasi-condensation. The condition $k_B T \ll \hbar \omega_R$ leads to a condensation into the transverse ground state. In the direction of weaker confinement, the small energy spacing between the energy levels leads to the population of many energy states.

in 1D Bose gases. It has been demonstrated by Mermin, Wagner and Hohenberg [64, 65] that the fluctuations prevent Bose-Einstein condensation of 1D Bose gases, even at $T = 0$.

Therefore, the critical temperature given by Eq. (1.22) merely defines a temperature scale for the quantum regime. Depending on the temperature and strength of the interactions, the trapped 1D Bose gases present three regimes of quantum degeneracy separated by smooth crossovers [66]. For weakly-interacting atoms, such as treated in this thesis, the 1D Bose gas is in the quasi-BEC regime, characterized by suppressed density fluctuations and accordingly increased phase fluctuations.

1.2 Weakly interacting Bose gas

1.2.1 Many-body Hamiltonian in second quantization

The Bose distribution given by Eq. (1.1) requires a system at thermal equilibrium which can only be reached by interaction. Therefore, a realistic microscopic theory of Bose gas involves the many-body Hamiltonian in the second quantization formalism [60, 61]. It consists of a single-particle Hamiltonian \hat{H}_0 and an interaction Hamiltonian \hat{H}_{int} :

$$\hat{H} = \hat{H}_0 + \hat{H}_{\text{int}}, \quad (1.23)$$

with

$$\hat{H}_0 = \int d^3 r \hat{\Psi}^\dagger(\vec{r}, t) \left(-\frac{\hbar^2 \nabla^2}{2m} + V(\vec{r}) \right) \hat{\Psi}(\vec{r}, t) \quad (1.24)$$

and

$$\hat{H}_{\text{int}} = \frac{1}{2} \int d^3 r d^3 r' \hat{\Psi}^\dagger(\vec{r}, t) \hat{\Psi}^\dagger(\vec{r}', t) U(\vec{r} - \vec{r}') \hat{\Psi}(\vec{r}, t) \hat{\Psi}(\vec{r}', t). \quad (1.25)$$

$V(\vec{r})$ is the external trapping potential and $U(\vec{r} - \vec{r}')$ describes the effective scalar two-body interactions. At the low temperature required to reach quantum degeneracy, the low energy and low momenta tend to limit the collisional processes to simple s -wave scattering [67]. It is characterized by a single parameter, namely the s -wave scattering length a_s . As long as the interparticle distance is large compared to a_s , i.e. for:

$$n |a_s|^3 \ll 1, \quad (1.26)$$

the system is in the weakly interacting regime and the exact interaction potential is well approximated by the effective contact potential:

$$U(\vec{r} - \vec{r}') = g_{3D}\delta(\vec{r} - \vec{r}'), \quad (1.27)$$

with g_{3D} the 3D interaction constant defined by

$$g_{3D} = \frac{4\pi\hbar^2}{m}a_s. \quad (1.28)$$

The sign of g_{3D} reflects the attractive ($a_s < 0$) or repulsive ($a_s > 0$) character of the interactions. Since we consider a degenerate gas of ^{87}Rb , for which $a_s \approx 5.24 \text{ nm} \approx 100a_{\text{Bohr}}$ [68], we consider only the case of repulsive interactions in this thesis.

In Eqs. (1.24, ??), $\Psi(\vec{r}, t)$ are the time-dependent field operators in the Heisenberg picture obeying bosonic equal time commutation relations $[\hat{\Psi}(\vec{r}), \hat{\Psi}(\vec{r}')^\dagger] = \delta(\vec{r} - \vec{r}')$. The field operators can be written as the sum:

$$\hat{\Psi}(\vec{r}, t) = \sum_{\alpha} \psi_{\alpha}(\vec{r}, t)\hat{a}_{\alpha} \text{ and } \hat{\Psi}^\dagger(\vec{r}, t) = \sum_{\alpha} \psi_{\alpha}^*(\vec{r}, t)\hat{a}_{\alpha}^\dagger. \quad (1.29)$$

$\psi_{\alpha}(\vec{r}, t)$ are the single-particle wave functions and $\hat{a}_{\alpha}^\dagger, \hat{a}_{\alpha}$ are the corresponding creation/annihilation operators. They also obey the usual bosonic commutation relations and are defined by:

$$\hat{a}_{\alpha}^\dagger|n_0, n_1 \dots n_{\alpha}, \dots\rangle = \sqrt{n_{\alpha} + 1}|n_0, n_1 \dots n_{\alpha} + 1, \dots\rangle, \quad (1.30)$$

$$\hat{a}_{\alpha}|n_0, n_1 \dots n_{\alpha}, \dots\rangle = \sqrt{n_{\alpha}}|n_0, n_1 \dots n_{\alpha} - 1, \dots\rangle. \quad (1.31)$$

Here n_{α} is the eigenvalue of the operator $\hat{n}_{\alpha} = \hat{a}_{\alpha}^\dagger\hat{a}_{\alpha}$ and corresponds to the the number of atoms in the single-particle α state.

The dynamics of the field operators can be determined from the Heisenberg equation such that:

$$\begin{aligned} i\hbar\frac{\partial}{\partial t}\hat{\Psi}(\vec{r}, t) &= -\left[\hat{H}, \hat{\Psi}\right] \\ &= \left(-\frac{\hbar^2\nabla^2}{2m} + V(\vec{r})\right)\hat{\Psi}(\vec{r}, t) + g_{3D}\hat{\Psi}(\vec{r}, t)^\dagger\hat{\Psi}(\vec{r}, t)\hat{\Psi}(\vec{r}, t). \end{aligned} \quad (1.32)$$

In principle, Eq. (1.32) allows to compute the full dynamics of the many-body system. In practice, this is extremely demanding and for large atom number, one usually resorts to approximations such as the mean-field formalism presented in the next section.

1.2.2 Mean-field model: the Gross-Pitaevskii equation

The mean-field description of a dilute Bose gas was first formulated by [69]. Its key point consists in isolating the contribution of the condensate in the definition of the field operator given by Eq. (1.29). As Bose-Einstein condensation is a macroscopic occupation of the ground state, the corresponding operators \hat{a}_0 and \hat{a}_0^\dagger can be treated like complex numbers. The field operators read:

$$\hat{\Psi}(\vec{r}, t) = \sqrt{n_0}\psi(\vec{r}, t) + \hat{\Psi}'(\vec{r}, t), \quad (1.33)$$

with $\psi(\vec{r}, t)$ the contribution of the ground state and $\hat{\Psi}'(\vec{r}, t)$ the sum over $\alpha > 0$.

For an almost pure condensate, $\hat{\Psi}'(\vec{r}, t)$ is negligible (Bogoliubov approximation). Therefore, $\psi(\vec{r}, t)$ is the expectation value of the field operator $\psi(\vec{r}, t) = \langle \hat{\Psi}(\vec{r}, t) \rangle$ and is called the wave function of the condensate. Using the normalization condition $\int d\vec{r} \psi^2 = N$, we derive a classical field theory by replacing the fields operators $\hat{\Psi}, \hat{\Psi}^\dagger$ by the complex function ψ and its complex conjugate:

$$\hat{\Psi}(\vec{r}, t) \rightarrow \psi(\vec{r}, t) \text{ and } \hat{\Psi}^\dagger(\vec{r}, t) \rightarrow \psi^*(\vec{r}, t). \quad (1.34)$$

Combining Eqs. (1.32, 1.34), we obtain the non-linear Schrödinger equation known as time-dependent Gross-Pitaevskii equation (GPE) [70, 71]:

$$i\hbar \frac{\partial}{\partial t} \psi(\vec{r}, t) = \left(-\frac{\hbar^2 \nabla^2}{2m} + V(\vec{r}) + g_{3D} |\psi(\vec{r}, t)|^2 \right) \psi(\vec{r}, t). \quad (1.35)$$

The non-linearity comes from the mean-field term $g_{3D} |\psi(\vec{r}, t)|^2$ proportional to the atomic density. It is equivalent to an effective potential experienced by each particle as a result of its interaction with all the others.

The mean-field ground state is easily obtained by writing the condensate wave function as $\psi(\vec{r}, t) = \psi(\vec{r}) \exp(-i\mu t/\hbar)$. Here, μ is the chemical potential and ψ is real. It leads to the stationary GPE:

$$\left(-\frac{\hbar^2 \nabla^2}{2m} + V(\vec{r}) + g_{3D} |\psi(\vec{r})|^2 \right) \psi(\vec{r}) = \mu \psi(\vec{r}), \quad (1.36)$$

which is in general not analytically solvable.

1.2.3 The Thomas-Fermi limit

A very good approximation of Eq. (1.36) for a large number of atoms is found in the limit where the interaction and potential energy dominate over the kinetic energy. In this case, known as the Thomas-Fermi limit, Eq. (1.36) reads:

$$V(\vec{r}) \psi(\vec{r}) + g_{3D} n(\vec{r}) \psi(\vec{r}) = \mu \psi(\vec{r}), \quad (1.37)$$

and admits the algebraic solution:

$$n(\vec{r}) = |\psi(\vec{r})|^2 = \frac{\max(\mu - V(\vec{r}), 0)}{g_{3D}}. \quad (1.38)$$

The chemical potential defines both the peak density by $\mu = g_{3D} n_0$ and the cloud extension, characterized by the lengths \vec{R} satisfying $\mu = V(\vec{R})$.

Isotropic harmonic trap In the case of an isotropic harmonic trap defined by

$$V(\vec{r}) = \frac{1}{2} m \omega (x^2 + y^2 + z^2), \quad (1.39)$$

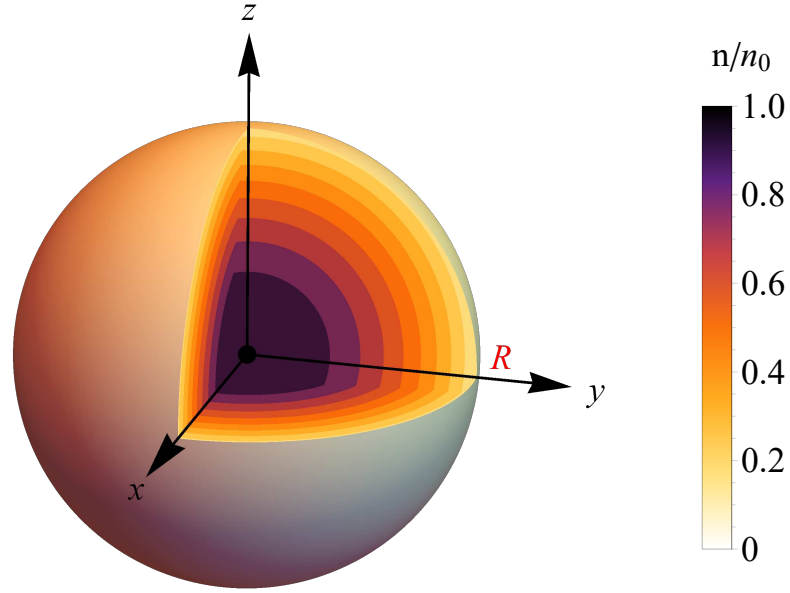


Figure 1.2: Atomic cloud in an isotropic harmonic trap within the Thomas-Fermi limit. The atomic cloud has a spherical shape characterized by the Thomas-Fermi radius R . The density at the center is n_0 and presents a quadratic decrease in the three directions of space. Once at the distance R , the density reaches zero and the energy reaches the chemical potential energy $\mu = \frac{1}{2}m\omega R^2$.

the cloud has a spherical shape represented in Fig. 1.2 characterized by the Thomas-Fermi radius R :

$$\mu = \frac{1}{2}m\omega^2 R^2. \quad (1.40)$$

The density profile is a paraboloid defined by:

$$n(\vec{r}) = n_0 \left(1 - \frac{x^2 + y^2 + z^2}{R^2} \right). \quad (1.41)$$

Up to the chemical potential, i.e. for $r < R$, the atomic density decreases and the associated energy increases as $E(r) = \frac{1}{2}m\omega^2 r^2$. The integration in space of Eq. (1.41) added to the normalization condition leads to:

$$\mu = \frac{\hbar\omega}{2} \left(15N \frac{a_s}{a_{\text{ho}}} \right)^{2/5}, \quad (1.42)$$

with $a_{\text{ho}} = \sqrt{\hbar/m\omega}$ the harmonic oscillator length. It follows that the Thomas-Fermi radius as a function of the atom number reads:

$$R = a_{\text{ho}} \left(\frac{15N a_s}{a_{\text{ho}}} \right)^{1/5}. \quad (1.43)$$

While the size of an ideal cloud is a_{ho} , Eq. (1.43) shows that, in an isotropic harmonic trap, the repulsive interactions increase the size of the cloud by a factor proportional to $N^{1/5}$.

3D harmonic trap with anisotropy In the case where one trap frequency is smaller than the others, $\omega_z < \omega_{x,y}$, the frequency and harmonic length appearing in the chemical potential given by Eq. (1.42) are replaced by their geometric means: $\bar{\omega} = (\omega_z \omega_x \omega_y)^{1/3}$ and $\bar{a}_{\text{ho}} = \sqrt{\hbar/m\bar{\omega}}$. We distinguish between the longitudinal and transverse TF radii R_z and R_{\perp} defined by:

$$R_{z,\perp} = \sqrt{\frac{2\mu}{m\omega_{z,\perp}^2}} \quad (1.44)$$

with $\omega_{\perp} = \sqrt{\omega_x \omega_y}$. In this case, the density profile reads:

$$n(\vec{r}) = n_0 \left(1 - \frac{x^2 + y^2}{R_{\perp}^2} - \frac{z^2}{R_z^2} \right), \quad (1.45)$$

with $n_0 = \mu/g_{3\text{D}}$.

1D Thomas Fermi regime In the 1D case, where $\omega_z \ll \omega_{\perp}$, the 3D GPE can be solved assuming a separable wave function $\psi(\vec{r}) = \phi(x, y)\varphi(z)$ as detailed in [72, 73]. The transverse ground state is a Gaussian and its influence on the longitudinal wave function is taken into account through a redefinition of the interaction pseudo-potential

$$g_{1\text{D}} = 2\hbar\omega_{\perp}a_s \quad (1.46)$$

and of the chemical potential:

$$\mu_{1\text{D}} = \frac{\hbar\omega_{\perp}}{2} [2 + (3\chi)^{2/3}]. \quad (1.47)$$

The parameter χ is defined as:

$$\chi = Na_s \frac{a_{\perp}}{a_z^2}, \quad (1.48)$$

with $a_{\perp} = \sqrt{\hbar/m\omega_{\perp}}$ and $a_z = \sqrt{\hbar/m\omega_z}$ the harmonic oscillator lengths.

The longitudinal wave function obeys an effective GPE resembling Eq. (1.36) where $g_{3\text{D}}$ and μ are replaced by $g_{1\text{D}}$ and $\mu_{1\text{D}}$. In the Thomas-Fermi limit, the density profile reads:

$$n_{1\text{D}}(z) = n_0 \left(1 - \frac{z^2}{R_z^2} \right), \quad (1.49)$$

with $n_0 = \mu_{1\text{D}}/g_{1\text{D}}$ and $R_z = \sqrt{2\mu_{1\text{D}}/m\omega_z^2}$.

The Thomas-Fermi in the 3D case does not simply connect to the 1D case when reducing the longitudinal frequency (increasing χ). This is expressed by the dependence of the chemical potential (normalized to the transverse ground state energy) with the parameter χ displayed in the left panel of Fig. 1.3. Therefore, in the crossover regime, which corresponds to our experimental regime, one must take into account the coupling between the transverse and longitudinal direction more carefully than by assuming a separable wave function.

1.2.4 Crossover 3D/1D

The crossover between 3D elongated to truly 1D is presented in several studies [72–76]. We follow [76] and consider a separable trapping potential of general form:

$$V(\vec{r}) = V_{\perp}(\rho) + V_z(z), \quad (1.50)$$

with $\rho = x, y$. When decreasing the confinement along z , the dynamics of the condensate is governed by two different timescales. The characteristic evolution time of the transverse motion (ω_{\perp}^{-1}) is small compared to the one governing the longitudinal motion (ω_z^{-1}). One can therefore assume that, at every instant, the transverse degrees of freedom adjust instantaneously to the lowest-energy configuration compatible with the instantaneous longitudinal configuration. This realizes the adiabatic approximation. The wave function can therefore be factorized as:

$$\psi(\rho, z, t) = f_{\perp}(\rho; n_1(z, t))\phi(z, t). \quad (1.51)$$

Here $n_1(z, t)$ the local density per unit length of the longitudinal configuration

$$n_1(z, t) = N \int d^2\rho |\psi(\rho, z, t)|^2. \quad (1.52)$$

With the normalization condition $\int d^2\rho |f_{\perp}(\rho; n_1)|^2 = 1$, we obtain:

$$n_1(z, t) = N |\phi(z, t)|^2. \quad (1.53)$$

In the following, we omit the notation related to the spatial and temporal dependence for clarity. Using the 3D GPE, one establishes

$$\left(i\hbar\partial_t\phi + \frac{\hbar^2}{2m}\partial_z^2\phi - V_z(z)\phi \right) f_{\perp} = \left(-\frac{\hbar^2}{2m}\nabla_{\rho}^2 f_{\perp} + V_{\perp}(\rho)f_{\perp} + gn_1|f_{\perp}|^2 f_{\perp} \right) \phi. \quad (1.54)$$

We assume that $n_1(z)$ presents slow variations along z and therefore neglect the spatial variation of f_{\perp} due to $n_1(z)$. The time derivative of f_{\perp} is neglected as a result of the adiabatic approximation. By multiplying the above equation by f_{\perp}^* and integrating over ρ we reach:

$$i\hbar\partial_t\phi = -\frac{\hbar^2}{2m}\partial_z^2\phi + V_z\phi + \mu_{\perp}(n_1)\phi, \quad (1.55)$$

with

$$\mu_{\perp}(n_1) = \int d^2\rho f_{\perp}^* \left(-\frac{\hbar^2}{2m}\nabla_{\rho}^2 + V_{\perp}(\rho) + gn_1|f_{\perp}|^2 \right) f_{\perp}. \quad (1.56)$$

Equation (1.55) is an effective 1D mean-field equation that governs the longitudinal dynamics taking into account the transverse degrees of freedom through $\mu_{\perp}(n_1)$. By substitution of Eq. (1.55) in Eq. (1.54), we reach a more familiar expression:

$$\left(-\frac{\hbar^2}{2m}\nabla_{\rho}^2 f_{\perp} + V_{\perp}(\rho)f_{\perp} + gn_1|f_{\perp}|^2 f_{\perp} \right) \phi = \mu_{\perp}(n_1)\phi. \quad (1.57)$$

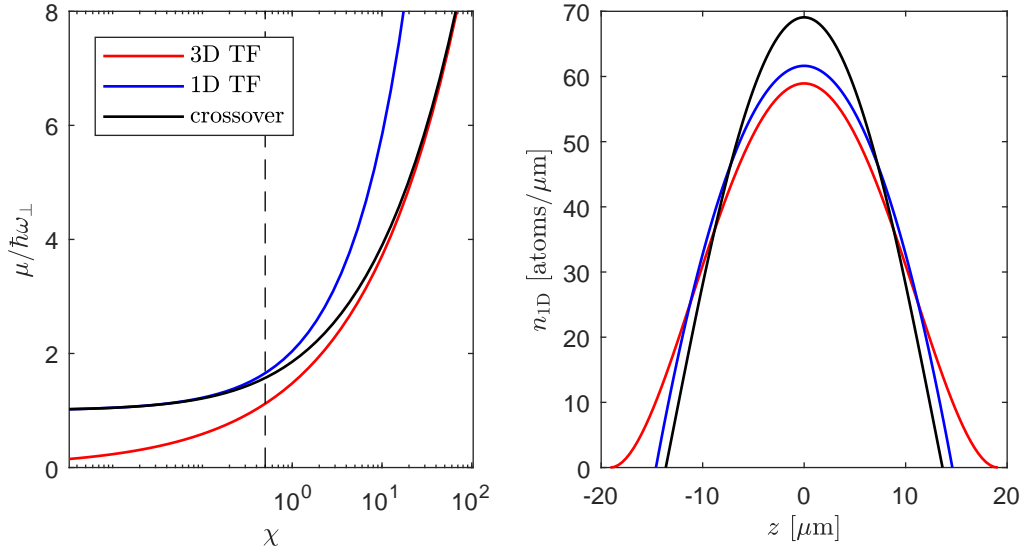


Figure 1.3: Mean field predictions for the 1D, 3D Thomas Fermi regimes and crossover. **Left:** Chemical potential for $N = 1200$ atoms as a function of χ . χ is varied through ω_z for a constant $\omega_{\perp} = 1.3$ kHz (experimental value). The crossover description (black line) smoothly connects the 1D and 3D TF predictions. **Right:** Density profile along the elongated axis for $\chi = 0.5$. In the 3D case, the integration along the transverse directions leads to a Gaussian shaped density while the 1D TF density profile is a parabola of higher peak density. The density obtained in the crossover description matches the integrated 1D density for $\chi \ll 3.73$ and the 3D one for $\chi \gg 3.73$.

Knowing the transverse potential $\mu_{\perp}(n_1)$ is the key feature to derive a useful 1D effective equation of motion. For example, in the local density approximation (LDA), the knowledge of the transverse $\mu_{\perp}(n_1)$ allows an analytical determination of the longitudinal ground state and of $n_1(z)$. To establish the LDA condition, we start by considering the stationary situation, where the condensate states must satisfy

$$\phi(z, t) = \phi_0(z) \exp(-i\mu t/\hbar). \quad (1.58)$$

After substitution in Eq. (1.55), we obtain:

$$-\frac{\hbar^2}{2m} \partial_z^2 \phi_0 + V_z(z) \phi_0 + \mu_{\perp}(n_1) \phi_0 = \mu \phi_0, \quad (1.59)$$

where the chemical potential μ is the Lagrange multiplier that guarantees the normalization condition. In the case where ϕ_0 presents slow variation along z , we neglect the first term of Eq. (1.59). This leads to the LDA:

$$\mu = \mu_{\perp}(n_1) + V_z(z). \quad (1.60)$$

In the following, we restrict ourselves to the LDA and consider a potential of the form:

$$V(\vec{r}) = \frac{1}{2} m \omega_{\perp}^2 \rho^2 + V_z(z). \quad (1.61)$$

The solution of Eq. (1.57) in this case is obtained either by numerical integration [73] or locally, i.e for each z as done in [74]. In the local approach, f_{\perp} is a Gaussian trial wave

function, the width of which is a variational parameter depending on n_1 . The minimization of the chemical potential μ_\perp leads to the expression of the chemical potential

$$\mu_\perp(n_1) = \hbar\omega_\perp\sqrt{1 + 4a_s n_1}. \quad (1.62)$$

For a harmonic longitudinal potential:

$$V_z(z) = \frac{1}{2}m\omega_z^2 z^2, \quad (1.63)$$

the density profile reads [74]:

$$n_1(z) = \frac{\alpha}{16a_s} \left(1 - \frac{z^2}{R^2}\right) \left[\alpha \left(1 - \frac{z^2}{R^2}\right) + 4\right]. \quad (1.64)$$

R is the radius of the cloud defined by

$$R = \frac{\sqrt{\alpha}a_z^2}{a_\perp}, \quad (1.65)$$

with α a parameter link to the chemical potential by:

$$\mu = \hbar\omega_\perp(1 + \alpha/2). \quad (1.66)$$

α is determined by solving

$$\alpha^3(\alpha + 5)^2 = \chi^2. \quad (1.67)$$

When changing χ , μ smoothly interpolates between the predictions of the 3D and 1D Thomas-Fermi regimes, as displayed in the left panel of Fig. 1.3.

For $\alpha \gg 5$, Eq. (1.67) simplifies to $\alpha \approx (15\chi)^{2/5}$ i.e. to $\chi \gg 3.73$. In this case, μ reads:

$$\mu \approx \frac{\hbar\omega_\perp}{2}(15\chi)^{2/5}. \quad (1.68)$$

This is the result of the 3D Thomas Fermi given by Eq. (1.42), where $a_\perp = a_z$.

For $\alpha \ll 5$, $\alpha \approx (3\chi)^{2/3}$ and the chemical potential reads:

$$\mu \approx \hbar\omega_\perp \left(1 + \frac{(3\chi)^{2/3}}{2}\right) \quad (1.69)$$

and we recover Eq. (1.47) of the 1D case.

1.3 Bose Gases in a double-well potential

In this section, we consider two pure 1D Bose gases coupled by tunneling and realizing a 1D-Bosonic Josephson Junction (1D-BJJ). For the two coupled condensates, one can define the phase $\phi_{L,R}(z, t)$ and the local atom number $n_{L,R}(z, t)$. When the two Bose gases are transversally coupled by tunneling, the phase and atom number difference are susceptible to evolve under the effect of tunneling.

We restrict the description to negligible longitudinal fluctuations of the phase and imbalance such that these quantities are defined globally. While this is not generally true, the description of the dynamics restricted to the transverse dimension is to a large extent suitable to describe the experiments carried out in the thesis. We therefore limit ourselves to an effective 0D description of two coupled Bose gases.

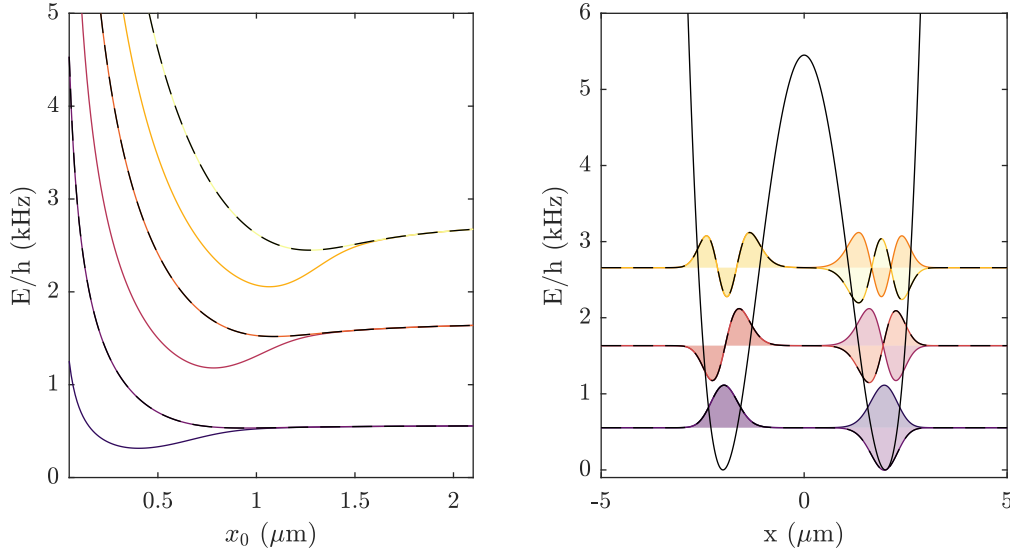


Figure 1.4: Eigenstates and eigenenergies in the single-particle picture. **Left:** Eigenenergy of the six eigenmodes of lowest energy for a harmonic double-well of $\omega = 2\pi \times 0.3 \text{ kHz}$ as a function of the half inter-well spacing x_0 . The eigenenergy of the antisymmetric modes are represented with a color and black dashed line for clarity. When increasing the distance between the two sites, the energy levels become degenerate two by two. **Right:** Six eigenmodes of lowest energy for $x_0 = 2 \mu\text{m}$ and $\omega = 2\pi \times 0.3 \text{ kHz}$. The eigenmodes form doublets of symmetric and antisymmetric states. The ground state and first excited state realize the two mode approximation.

1.3.1 Two-mode approximation

An ensemble of indistinguishable bosons in a double-well potential is well described by a wave function restricted to a superposition of the two lowest energy states of the potential [77–80]. This two-mode approximation reduces the dimension of the Hilbert space to $N + 1$ and allows exact calculations for the experimental parameters.

To establish the validity of the two-mode approximation, we consider a generic symmetric double-well $V(x)$ defined by:

$$V(x) = \frac{E_b}{x_0^4} (x^2 - x_0^2)^2, \quad (1.70)$$

where x_0 refers to the half inter-well spacing and E_b to the potential barrier. The inter-well spacing is large enough to approximate the trap minima by the harmonic potential $V_{\text{ho}} = \frac{1}{2}m\omega^2(x - x_0)^2$ characterized by the harmonic length $a_{\text{ho}} = \sqrt{\hbar/m\omega}$. Experimentally, the atom chip does not allow an independent control of the inter-well spacing and barrier height as demonstrated by Eq. (2.40). However the harmonic approximation is well realized such that for a trap of constant ω , the barrier height and the inter-well spacing are linked by:

$$E_b = \frac{\hbar\omega}{4} \frac{x_0^2}{a_{\text{ho}}^2}. \quad (1.71)$$

In the mean-field formalism presented in Sec. 1.2.2, the wave function ψ of an ensemble

of bosons in such a trap obeys the GPE equation:

$$i\hbar \frac{\partial \psi}{\partial t} = -\frac{\hbar^2}{2m} \frac{\partial^2 \psi}{\partial x^2} + V(x)\psi + Ng|\psi|^2\psi. \quad (1.72)$$

In the non-interacting limit ($g \rightarrow 0$), the exact stationary solutions of Eq. (1.72) read:

$$\psi(x, t) = \varphi_n(x) \exp(-i\beta_n t), \quad (1.73)$$

with $\psi_n(x)$ the n -th stationary modes of eigenenergy β_n . The eigenenergy of the six lowest modes, obtained by numerical diagonalization of the non-interacting Hamiltonian is displayed in Fig. 1.4 as a function of the inter-well spacing for the frequency $\omega = 2\pi \times 0.3$ kHz. When increasing x_0 the energy spectrum is formed of doublets of quasi-degenerate symmetric and antisymmetric states. Therefore, while the level spacing between the ground state and first excited states decreases for larger barrier, the energy separating them from the higher levels increases, realizing the two-mode approximation.

For repulsive interactions ($g > 0$), we can define non-linear eigenmodes obeying:

$$\beta_n \varphi_n + \frac{\hbar^2}{2m} \frac{\partial^2 \varphi_n}{\partial x^2} - V(x)\varphi_n - Ng|\psi|^2\varphi_n = 0. \quad (1.74)$$

As presented in [79], the dependence of $\beta_{0,1}$ with x_0 (equivalently E_b) resembles the one of the ideal case but the doublets have a higher energy. Therefore, the two-mode approximation is valid in the ideal and interacting case.

We construct the two modes as a combination of the ground state and first excited state:

$$\varphi_{L,R}(x) = \frac{1}{\sqrt{2}} [\varphi_0(x) \pm \varphi_1(x)]. \quad (1.75)$$

These modes are by construction primarily localized on the left and right well respectively. Since $\varphi_{L,R}$ are not eigenstate of the system, an atom prepared in one of these states will exhibit oscillations. In the ideal case, the atom oscillates at the Rabi frequency defined by $\Omega_R = (\beta_1 - \beta_0)/\hbar$. When increasing the barrier height, the levels spacing $\beta_1 - \beta_0$ decreases and the dynamics gets slower. In the limit of high barrier, the levels are degenerated and the tunneling dynamics is so slow as to be considered suppressed.

Limitation of the two-mode approximation The two-mode approximation breaks down when higher energy states are accessible to the atoms.

This occurs for example when the temperature of the system is of the order of the energy spacing between the first and second excited state. Typically, as in Fig. 1.4, the energy spacing to the second excited state ΔE_{2-0} is above 1 kHz, which corresponds to a temperature above 50 nK. Experimentally, we consider typical temperatures of 20 nK and exclude excitations to higher transverse modes.

Excitations to higher modes can also arise when introducing an energy difference ϵ between the two sites of the double-well as it modifies the energy spacing between the levels. We assume that this detuning ϵ is much smaller than the barrier height, such that we can always define two sites. Additionally, we consider only the levels of energy much below the barrier height. Qualitatively, the detuning affects both the wave function shape

and its energy. It adds an energy offset ϵ between the levels of the left and right site, which prevents the formation of doublets of symmetric and antisymmetric states. For a large level spacing, where the symmetric double-well fulfill the two-mode approximation, a detuning ϵ with the value equal to half the level spacing on the left (equivalently right) well, all energy levels considered are equally separated by ϵ , breaking down the two-mode approximation. Experimentally, this means that the detuning has to be kept small with respect to $\Delta E_{2-0}/2$.

Even for small detuning values, the general definitions of the two modes in an asymmetric trap is more difficult as the ground state and first excited state themselves gets localized on one well preferentially. Therefore, Eq. (1.75) does not define two modes localized on the left and right site. However, the localized modes can still be built as a linear combination of ground and first excited state. In the following, we consider generic left and right modes, assuming that they can be built.

1.3.2 Ideal dynamics in the mean-field formalism

1.3.2.1 Standard and improved two-mode models

We consider a symmetric double-well in the two-mode approximation. The wave function Ψ of a condensate containing N atoms is defined as a superposition of the left and right modes of Eq. (1.75):

$$\Psi(x, t) = \psi_L(t)\varphi_L(x) + \psi_R(t)\varphi_R(x). \quad (1.76)$$

$\psi_{L,R}(t)$ are two complex-valued functions defining the superposition between the two modes at the instant t . They are defined by:

$$\psi_{L,R}(t) = |\psi_{L,R}(t)|^2 \exp[i\phi_{L,R}(t)], \quad (1.77)$$

where $\phi_{L,R}$ describes the phase argument and $|\psi_L(t)|^2 + |\psi_R(t)|^2 = N$.

The dynamics of the wave function is obtained by the substitution of the ansatz (1.76) in the time-dependent GPE (1.72), in addition to the stationary condition given by the GPE (1.74). The derivation is detailed in [80] and leads to the improved two-mode (I2M) model:

$$i\frac{d\psi_L}{dt} = \left(F + A|\psi_L|^2 - \frac{\Delta\gamma}{4}\psi_L\psi_R^* \right) \psi_L - \left(\frac{\Delta\beta}{2} - \frac{\Delta\gamma}{4}|\psi_R|^2 - C^2\psi_L^*\psi_R \right) \psi_R \quad (1.78)$$

$$= \mathcal{M}_L\psi_L - \mathcal{J}_L\psi_R, \quad (1.79)$$

$$i\frac{d\psi_R}{dt} = \left(F + A|\psi_R|^2 - \frac{\Delta\gamma}{4}\psi_R\psi_L^* \right) \psi_R - \left(\frac{\Delta\beta}{2} - \frac{\Delta\gamma}{4}|\psi_L|^2 - C^2\psi_R^*\psi_L \right) \psi_L \quad (1.80)$$

$$= \mathcal{M}_R\psi_R - \mathcal{J}_R\psi_L. \quad (1.81)$$

The various terms of the above equations adopt the notations of [80] and read:

$$\Delta\beta = \beta_1 - \beta_0, \quad \Delta\gamma = \gamma_{11} - \gamma_{00}, \quad (1.82)$$

$$A = \frac{10\gamma_{01} - \gamma_{00} - \gamma_{11}}{4}, \quad B = \Delta\beta - \frac{\Delta\gamma}{2}, \quad (1.83)$$

$$C = \frac{\gamma_{00} + \gamma_{11} - 2\gamma_{01}}{4}, \quad F = \frac{\beta_0 + \beta_1}{2} - \gamma_{01}. \quad (1.84)$$

For $i, j = 0, 1$, $\beta_{i,j}$ is the eigenenergy of the level i, j given by Eq. (1.74) and $\gamma_{i,j}$ defines the wave function overlaps:

$$\gamma_{i,j} = Ng \int \varphi_i^2(x) \varphi_j^2(x). \quad (1.85)$$

In the I2M model, the tunnel coupling $\mathcal{J}_{L,R}$ of Eqs. (1.79, 1.81) includes a non-linear interaction term $\propto C^2$ such that if the atom number differs between the left and right side of the double-well, it leads to $\mathcal{J}_L \neq \mathcal{J}_R$. When more atoms are located on the left side, the wave function on the left side expands due to repulsive interaction, leading to an increase of the tunneling rate toward the right side. Simultaneously, less atoms are located on the right side which decreases the tunneling to the left. It translates into $\mathcal{J}_L > \mathcal{J}_R$. Therefore, in the I2M model, the tunneling directly depends on the atom-atom interaction and includes the contribution of the interaction tunneling. The I2M model has been verified experimentally by [81].

When the interaction-induced transfers of particles between the two modes is negligible, $C \approx 0$ and Eqs. (1.78, 1.80) simplify to the standard two-mode (S2M) model:

$$i\hbar \frac{d\psi_L}{dt} = (E_L^0 + U_L |\psi_L|^2) \psi_L - J \psi_R, \quad (1.86)$$

$$i\hbar \frac{d\psi_R}{dt} = (E_R^0 + U_R |\psi_R|^2) \psi_R - J \psi_L. \quad (1.87)$$

Here,

$$E_{L,R}^0 = \int dx \left(\frac{\hbar^2}{2m} |\nabla \varphi_{L,R}|^2 + |\varphi_{L,R}|^2 V \right) = \frac{\beta_0 + \beta_1 - \gamma_{00} - \gamma_{11}}{2}, \quad (1.88)$$

$$U_{L,R} = g \int dx |\varphi_{L,R}|^4 = A + 2C, \quad (1.89)$$

$$J = - \int dx \left(\frac{\hbar^2}{2m} |\nabla \varphi_L \nabla \varphi_R|^2 + \varphi_L V \varphi_R \right) = \frac{\Delta\beta - \Delta\gamma}{2}. \quad (1.90)$$

1.3.2.2 Tunneling dynamics in a symmetric trap

Equation (1.77) allows to define the normalized atomic imbalance:

$$n(t) = \frac{|\psi_L(t)|^2 - |\psi_R(t)|^2}{N} \quad (1.91)$$

and the relative phase

$$\phi(t) = \phi_L(t) - \phi_R(t). \quad (1.92)$$

In the I2M model, [80] demonstrates that the atomic imbalance and the relative phase obey the equations of motions given by:

$$\dot{\phi} = An + \frac{Bn}{\sqrt{1-n^2}} \cos \phi - Cn \cos 2\phi, \quad (1.93)$$

$$\dot{n} = -B\sqrt{1-n^2} \sin \phi + C(1-n^2) \sin 2\phi. \quad (1.94)$$

These equations can be written in Hamiltonian form

$$\dot{\phi} = \frac{\partial H_{\text{I2M}}}{\partial n}, \dot{n} = -\frac{\partial H_{\text{I2M}}}{\partial \phi}, \quad (1.95)$$

such that ϕ and n are conjugate variables for the I2M Hamiltonian:

$$H_{\text{I2M}} = A \frac{n^2}{2} - B \sqrt{1 - n^2} \cos \phi + \frac{1}{2} C (1 - n^2) \cos 2\phi. \quad (1.96)$$

It follows that the relative phase and the atomic imbalance are two conjugate variables.

In the S2M model, $C \approx 0$ and the equations of motion are reduced to [77, 78, 82]:

$$\dot{\phi}(t) = \frac{2J}{\hbar} \left[\Lambda n(t) + \frac{n(t)}{\sqrt{1 - n^2(t)}} \cos \phi(t) \right], \quad (1.97)$$

$$\dot{n}(t) = \frac{2J}{\hbar} \sqrt{1 - n(t)^2} \sin \phi(t). \quad (1.98)$$

Λ is a dimensionless parameter defined by $\Lambda = NU/2J$ which characterizes the interplay between the atom-atom interactions and the tunneling, with $U = U_L = U_R$. Relative phase and atomic imbalance are conjugate variables for the S2M Hamiltonian:

$$H_{\text{S2M}} = \frac{2J}{\hbar} \left[\frac{\Lambda}{2} n^2(t) - \sqrt{1 - n^2(t)} \cos \phi(t) \right], \quad (1.99)$$

which we recognize as the two-mode Bose-Hubbard Hamiltonian in the mean field formalism.

The dynamical modes are fully determined by Λ and by the initial conditions (n_0, ϕ_0) . They define the initial energy of the system, that we rescale by $2J/\hbar$ to define the parameter α as:

$$\alpha = \frac{\Lambda}{2} n_0^2 - \sqrt{1 - n_0^2} \cos(\phi_0). \quad (1.100)$$

For repulsive interactions, U and therefore Λ are positive. In this case, α varies between -1 and $\alpha_M = \text{Max}[1, (\Lambda^2 + 1)/2\Lambda]$. We distinguish between the Rabi regime where $\alpha_M < 1$ and the Josephson regime where $\alpha_M \geq 1$.

Each regime contains different dynamical modes conveniently represented in the (ϕ, n) space [83]. The horizontal axis of this space represents the phase and is 2π periodic. The vertical axis corresponds to the imbalance. It is bounded by $n = \pm 1$, which corresponds to the case where all the atoms are located in one site and where the phase difference is not defined. Therefore, the (ϕ, n) space can be seen as a sphere of radius 1 where the elevation gives the imbalance and the azimuth gives the phase. For convenience, we however represent it in a two dimensional plane. For each time t of the evolution, the couple $(\phi(t), n(t))$ defines the coordinates of a point. The time evolution is depicted as a trajectory characterized by a constant value of α . The (ϕ, n) space is a compact representations of all dynamical modes (all possible values of α) for a fixed Λ .

We illustrate this in Table 1.1 for four distinct values of Λ .

In all regimes, the minimum value of α is -1 and corresponds to the stable equilibrium point where the phase and imbalance remain zero at all time (black cross in Table 1.1).

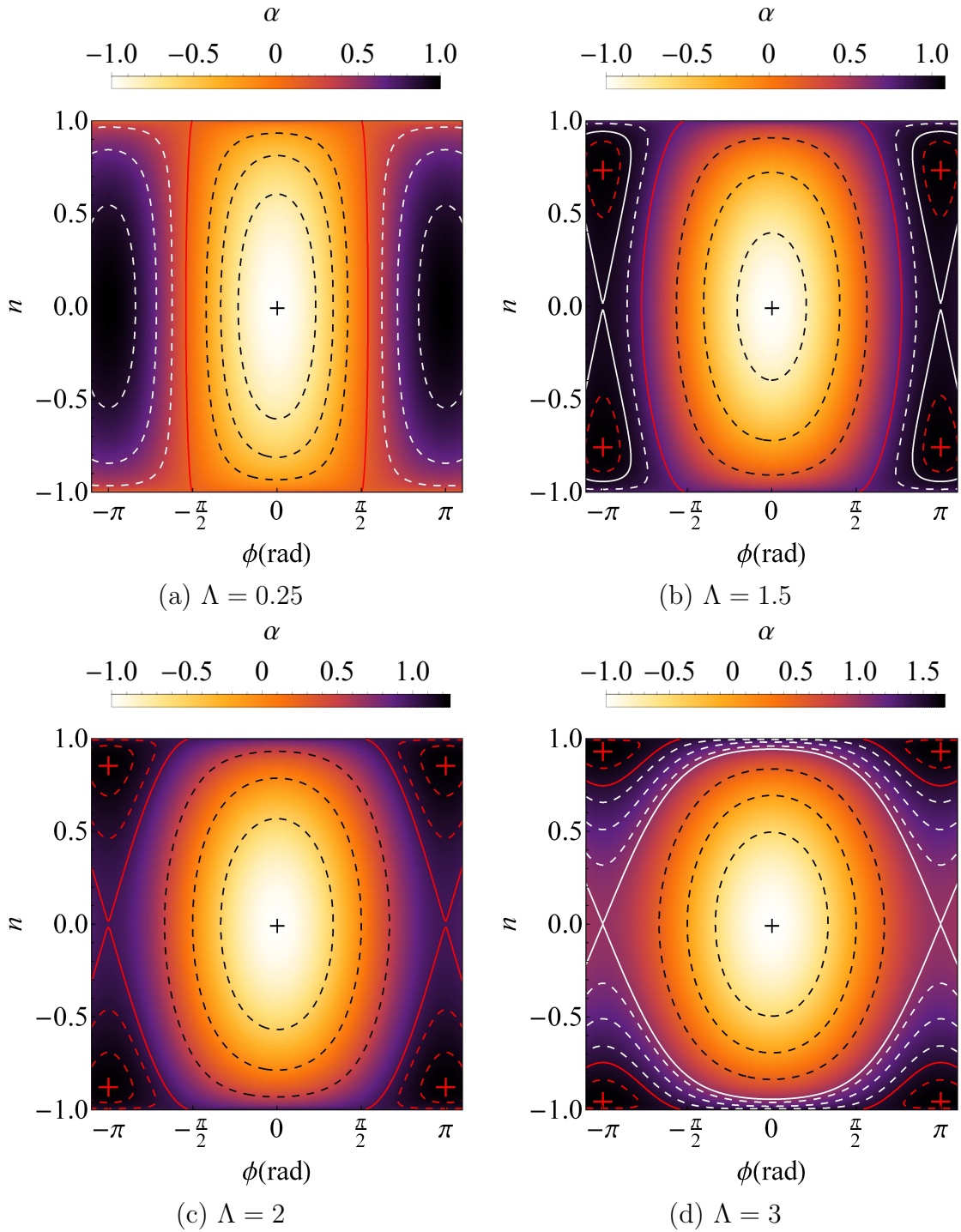


Table 1.1: Phase portrait representation for 4 values of Λ . The black crosses correspond to the equilibrium points and the red crosses to the unstable equilibrium points (saddle points). The red and white full lines correspond to the sets of separatrices delimiting the dynamical regimes. The dashed white lines represent either the Rabi/Josephson regime oscillations in the regime of same name. The white dashed lines are the π_0 -oscillating trajectories for $\Lambda < 2$ and the self-trapped trajectories for $\Lambda > 2$. The red dashed lines are the π_{\pm} -oscillating trajectories, strongly suppressed for large Λ .

Rabi Regime The values of Λ obeying $\Lambda < 1$ corresponds to the Rabi regime. The typical features of the dynamics are illustrated in Table 1.1(a) for $\Lambda = 0.25$. In this case, $-1 < \alpha < 1$ and the dynamics consists of π out-of-phase oscillations of the phase and imbalance. In the (ϕ, n) space, the dynamics appears as closed trajectories.

For $-1 < \alpha < \Lambda/2$, the oscillations are centered on $(\phi = 0, n = 0)$. The amplitude and anharmonicity of the oscillations increase with α while their frequency decreases slightly. In the (ϕ, n) space, a point on these trajectories evolves clock-wise.

$\alpha = \Lambda/2$ is a threshold value defining a pair of separatrices (red lines in Table 1.1). The equation of the separatrix linking n_{\pm} and ϕ reads [82]:

$$n_{\pm}(\phi) = \pm \begin{cases} \sqrt{1 - (2 \cos \phi / \Lambda)^2} & \text{for } |\phi| > \pi/2, \\ 1 & \text{for } |\phi| < \pi/2. \end{cases} \quad (1.101)$$

For $\Lambda/2 < \alpha < 1$, the oscillations are centered on $(\phi = \pi, n = 0)$ and are referred to as π_0 oscillations (white dashed lines of Table 1.1(a)). In the (ϕ, n) space, a point on these trajectories evolves counter clock-wise. The frequency of the oscillations is slightly lower than for the ones centered on $(0, 0)$.

Josephson regime When $\Lambda \geq 1$, the system is in the Josephson regime. Contrary to the Rabi regime, the highest value of α exceeds 1 and this introduces additional dynamical modes. Even though any $\Lambda \geq 1$ refers to the Josephson regime, we can distinguish between three sub-regimes according to the value of Λ .

- The dynamics for $1 \leq \Lambda < 2$ is illustrated in Table 1.1(b) for $\Lambda = 1.5$.

As in the Rabi regime, the dynamics for $-1 < \alpha < \Lambda/2$ consists of oscillations around the stable equilibrium point $\alpha = -1$ (black cross) and are referred to as Josephson oscillations (dashed black lines) [84–86]. At small amplitudes ($-1 \lesssim \alpha$), the oscillations are harmonic and characterized by the plasma frequency ω_0 . Oscillations of larger amplitude become anharmonic, which affects the shape of the oscillations and decrease their frequency compared to ω_0 .

$\alpha = \Lambda/2$ defines the first set of separatrices obeying Eq. (1.101).

$\Lambda/2 < \alpha < 1$ corresponds to π -oscillations. However, they are deformed due to two saddle points which emerge in $(\phi_s = \pm\pi, n_s = \pm\sqrt{1 - \Lambda^{-2}})$ (red crosses in Table 1.1).

The equation $\alpha = 1$ defines a new set of separatrices, which form an eight encircling both saddle points displayed by the whites lines in Table 1.1. The separatrix equation is given by the four combinations:

$$n_{\pm}(\phi) = \pm \sqrt{(\Lambda/2)} \left(1 - \cos^2 \phi/2 \pm \cos \phi \sqrt{(\cos \phi / \Lambda)^2 + 1 - 2/\Lambda} \right)^2, \quad (1.102)$$

for $\pi/2 < |\phi| < \pi$.

For $1 < \alpha < \alpha_M$, the π oscillations are closed trajectories around one of the saddle point. We refer to them as π_{\pm} oscillations to distinguish them from the π_0 oscillations centered on $n = 0$.

- $\Lambda = 2$ is a limiting case represented in Table 1.1(c) for which the separatrices merge and the dynamical regimes are restricted to Josephson oscillations and π_{\pm} oscillations.
- The dynamics for $\Lambda > 2$ is illustrated in Table 1.1(d) for $\Lambda = 3$. As $1 < \Lambda/2$, the role of the two separatrices lines is now interchanged. The Josephson oscillations, previously bounded by $-1 < \alpha < \Lambda/2$ are now limited to $-1 < \alpha < 1$. One consequence is the reduction of the largest amplitude of the imbalance oscillations n_c defined by:

$$n_c = 2 \frac{\sqrt{\Lambda - 1}}{\Lambda} < 1. \quad (1.103)$$

The time evolution is displayed in Fig. 1.5 for $\Lambda = 40$. The π_{\pm} oscillations are obtained for $\Lambda/2 < \alpha < \alpha_M$. The exchange of the separatrices opens a new regime for the values of α obeying $1 < \alpha < \Lambda/2$. It corresponds to the macroscopic quantum self-trapping (MQST) regime. The time evolution in the MQST is displayed in Fig. 1.5 for $\Lambda = 40$ and positive $n(0)$. The imbalance presents oscillations around $n \neq 0$. The mean imbalance and the frequency of the oscillations increases with α while the amplitude decreases. The phase accumulates with a slope increasing with α .

The experiments carried out in this thesis are deep in the Josephson regime ($\Lambda \approx 100$). In this case, the π_{\pm} oscillations are strongly suppressed and the dynamics is limited to Josephson oscillations and MQST. The critical imbalance is about $n_c \approx 0.1$ and the oscillating features appearing in the evolution of the phase and imbalance are strongly suppressed.

Dynamical modes in the pendulum analogy The symmetric BJJ is analogous to a classical pendulum of momentum-dependent length [78,87,88]. The relative phase is analogous to the pendulum angle while the imbalance is analogous to its momentum $n \propto \dot{\phi}$. The length of the pendulum is defined by $l(t) = \sqrt{1 - n^2(t)}$. For a better understanding of the analogy, we describe the pendulum behavior in the (x, y) plane with $x(t) = l(t) \sin \phi(t)$ and $y(t) = -l(t) \cos \phi(t)$. The various modes in the pendulum picture are displayed in Table 1.2 for four values of Λ . The red cross indicates the attachment point of the pendulum and the colored lines represent the pendulum trajectories in the (x, y) plane for various initial energies α . The color scale goes from white (stable equilibrium) to black corresponding to the maximal value of α .

The Rabi regime ($\Lambda < 1$) is represented for $\Lambda = 0.25$ in Table 1.2(a). For small energy, the oscillations resembles those of a rigid pendulum with too little energy to swing over. These oscillations are entirely contain in the $y < 0$ plane. However, for larger energy, the momentum-shortening leads to π oscillations where a rigid pendulum would undergo full swing. While the pendulum is still attached to $(0,0)$, these oscillations resemble oscillations of a momentum-dependent pendulum with an effective attachment point located in $(0, 1)$. All these oscillations are entirely in the $y > 0$ sector, i.e. above the point where the pendulum is physically attached.

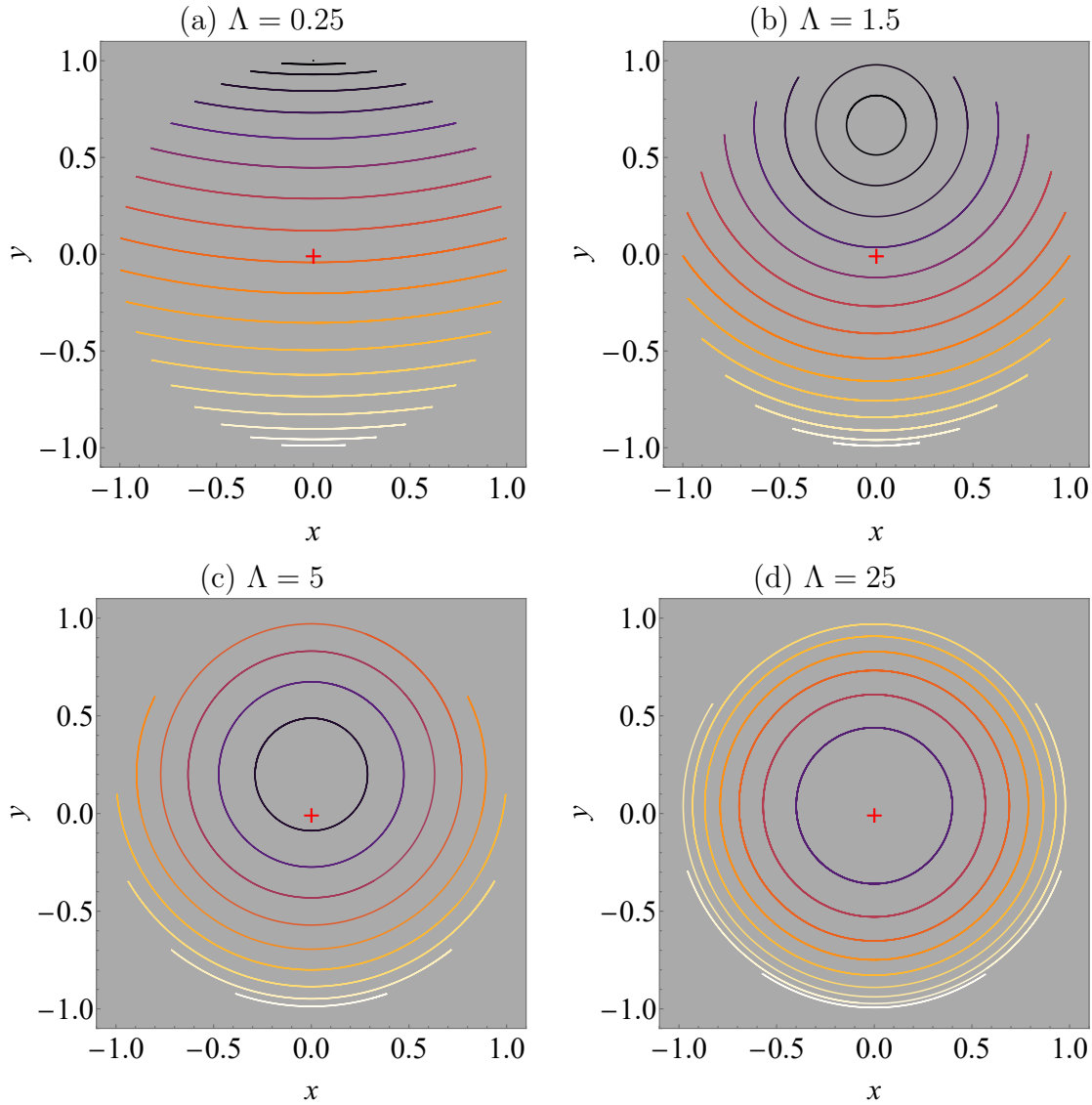


Table 1.2: Dynamical modes in the momentum-shortened pendulum analogy. (a) $\Lambda = 0.25$. The trajectories are limited to oscillating behaviors, either as for a pendulum attached in $(0, 0)$ or as an effective pendulum attached in $(1, 0)$ (π_0 oscillations). (b) $\Lambda = 1.5$ The new trajectories corresponding to π_0 oscillations appear as full swings around the effective attachment point $(0, \sqrt{1-n_s^2})$, with $n_s = \sqrt{1-\Lambda^{-2}}$ the imbalance coordinate of the saddle point. (c) $\Lambda = 5$. The saddle points migrates toward 1 such that the effective attachment point migrates toward $(0, 0)$. Consequently, some closed trajectories now encircle the physical point of attachment. These trajectories corresponds to the MQST. (d) $\Lambda = 25$. The difference between the effective and physical points of attachment is negligible. The dynamics is reduced to Josephson oscillations resembling the oscillations of a pendulum, and to the MQST analogous to the full swing. In this case, the effect of the momentum shortening is negligible.

In the Josephson regime ($\Lambda > 1$), the oscillations at low energy are still present as illustrated in Table 1.2(b,c,d). Therefore, the Josephson oscillations are analogous to the oscillating motion of a classical pendulum. The π_0 oscillations are still visible for $\Lambda \gtrsim 1$. The effective attachment point is displaced to $(0, \sqrt{1-n_s^2})$ with $n_s = \sqrt{1-\Lambda^{-2}}$ the

imbalance coordinate of the saddle point. This position determines the averaged velocity and therefore the averaged length of the pendulum $\bar{l} = \sqrt{1 - n_s^2}$. Additionally, the π_{\pm} oscillations appear as full swings around the effective attachment point.

For $\Lambda > 2$, the π oscillations are restricted to π_{\pm} oscillations, i.e. to full swing evolutions around a saddle point which gets closer to the equilibrium point (Table 1.2(c,d)). In this representation, the MQST trajectories are indistinguishable from the π_{\pm} oscillations and consist in full swings around an attachment point which migrates toward $(0, 0)$ for increasing Λ . When it merges with the physical attachment point $(0, 0)$, the rigid pendulum approximation is valid.

Quantitative analogy in the rigid pendulum approximation The derivation of the pendulum equation establishes a quantitative correspondence between the two systems. In particular, we seek to establish the definition of the harmonic oscillation frequency and the correspondence between n and $\dot{\phi}$. We do so in the rigid pendulum limit, which translates to the approximation $n(t) \ll 1$.

The main consequence of this approximation is that the π -oscillations and the position of the saddle points are not described. However, as soon as Λ exceeds ≈ 5 , the domain of existence of the π -oscillations is negligible. We will see that the analytical solutions of the pendulum allow to establish a criterion to define precisely the range of validity of the rigid pendulum approximation.

The pendulum-like differential equation for the phase evolution is obtained by combining Eq. (1.98) and the time derivative of Eq. (1.97):

$$\ddot{\phi}(t) + \omega_0^2 \sin(\phi(t)) = 0. \quad (1.104)$$

ω_0 is the plasma frequency defined by:

$$\omega_0 = \frac{2J}{\hbar} \sqrt{\Lambda + \lambda}, \quad (1.105)$$

with $\lambda = \cos(\phi_0)$ often approximated to 1. To solve Eq. (1.104) numerically, one must know Λ, J and the initial conditions ϕ_0 and $\dot{\phi}_0$ given by Eq. (1.97).

The time evolution of the imbalance is deduced from Eq. (1.98) by:

$$n(t) \approx \frac{\hbar}{2J} \frac{1}{\Lambda + \lambda} \dot{\phi}(t). \quad (1.106)$$

Despite the approximations of Eq. (1.104), the numerical solutions of Eqs. (1.104, 1.106) and of Eqs. (1.97, 1.98) give very similar results. This is displayed in Fig. 1.5. For oscillations of very large amplitude, the frequency of the oscillations differs slightly. However, Fig. 1.6 illustrates that the discrepancy does not appear on the (ϕ, n) space representation, which shows that the amplitudes are well estimated. A small discrepancy also arises deep in the MQST regime on the amplitude, frequency and mean value of the imbalance oscillations (and the equivalent effect on ϕ due to the link between n and $\dot{\phi}$).

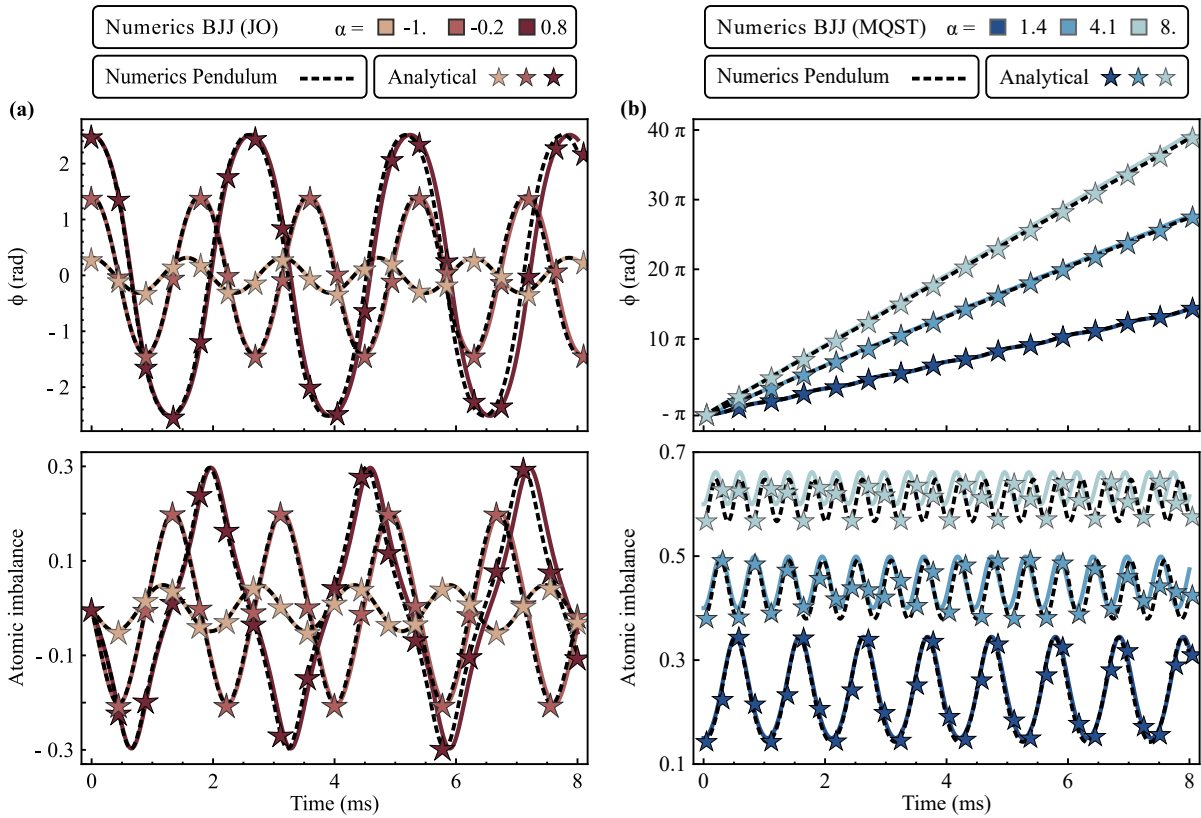


Figure 1.5: Regimes of the BJJ for large Λ and pendulum solutions. Taken from [57]. Dynamics of six initial states for $N = 5000$ atoms, $J/\hbar = 50$ Hz, $U/\hbar = 0.8$ Hz resulting in $\Lambda = 40$. The numerical solutions of the TMBH model are displayed in color lines, the numerical solutions of the equivalent pendulum are the dashed line and the corresponding analytical pendulum solutions are the stars of matching color. **(a) Josephson oscillations.** The three initial state have the imbalance $n_0 = 0$ and the phase $\phi = [0.1, 0.45, 0.8]\pi$. The pendulum solutions match the TMBH numerical solutions up to high initial phase. It reproduces the increasing anharmonicity, which affects the shape of the oscillations and slows down their frequency. For very large initial phase, the frequency is slightly under evaluated by the pendulum model. **(b) Macroscopic quantum self trapping.** The initial phase is $\phi_0 = -\pi$ and the initial imbalance takes three values: $n_0 = [0.15, 0.45, 0.8]$. The swing over of the pendulum reproduces the features of the MQST. The phase accumulates linearly and the imbalance presents oscillations of limited amplitude around a finite averaged value. A small discrepancy of frequency and amplitude appears for very large imbalance values.

Analytical solutions in the rigid pendulum approximation The rigid pendulum has analytical solutions both in the oscillating regime and in the full-swing regime which can be adapted to the BJJ in the Josephson regime [78, 82, 89]. We follow a similar approach to derive these solutions adapted to the BJJ. We published this work in [57].

The energy function E of a mechanical pendulum is the sum of a kinetic and potential energy. In the language of the BJJ, the energy function E of the symmetric BJJ is a conserved quantity given by

$$E = \dot{\phi}^2(t) + 4\omega_0^2 \sin^2\left(\frac{\phi(t)}{2}\right), \quad (1.107)$$

with $\phi(t)$ the phase and ω_0 the plasma frequency [90]. At $t = 0$, the energy function reads:

$$E_0 = \dot{\phi}_0^2 + 4\omega_0^2 \sin^2\left(\frac{\phi_0}{2}\right), \quad (1.108)$$

with $\dot{\phi}_0$ given by Eq. (1.97) as

$$\dot{\phi}_0 = \frac{2J}{\hbar} [\Lambda + \lambda] n_0. \quad (1.109)$$

We express $\dot{\phi}(t)$ using Eqs. (1.107, 1.108) to obtain the differential equation for the phase:

$$\dot{\phi}(t)^2 = E_0 - 4\omega_0^2 \sin^2\left(\frac{\phi(t)}{2}\right). \quad (1.110)$$

We perform the change of variable $y(t) = \phi(t)/2$ and $\tilde{t} = k\omega_0 t$ where k^2 is the ratio of the total energy to the maximal potential energy:

$$k^2 = \frac{E_0}{4\omega_0^2}. \quad (1.111)$$

Eq. (1.110) becomes:

$$\frac{dy}{d\tilde{t}} = \sqrt{1 - k^{-2} \sin^2(y)}, \quad (1.112)$$

and is solved for $\phi_0 = 0$ by the Jacobi amplitude function $\text{am}(y|k^{-2})$ [91]. This definition of the Jacobi amplitude adopts the convention of [91] and of Wolfram MathematicaTM. We deduce that the evolution of the relative phase in a BJJ reads:

$$\phi(t) = 2\sigma_0 \text{am}(k\omega_0 t + \delta\phi|k^{-2}). \quad (1.113)$$

In Eq. (1.113), σ_0 refers to the sign of $\phi(0)$ and is given by $\dot{\phi}_0$ (equivalently n_0):

$$\sigma_0 = \begin{cases} \text{sign}(n_0) & \text{if } n_0 \neq 0, \\ 1 & \text{if } n_0 = 0. \end{cases} \quad (1.114)$$

The term $\delta\phi$ accounts for the value of the initial phase ϕ_0 . By convention, the initial value of the Jacobi amplitude is zero which we compensate using:

$$\delta\phi = \text{sn}^{-1}\left(\sin\left(\frac{\phi_0}{2}\right) \middle| k^{-2}\right), \quad (1.115)$$

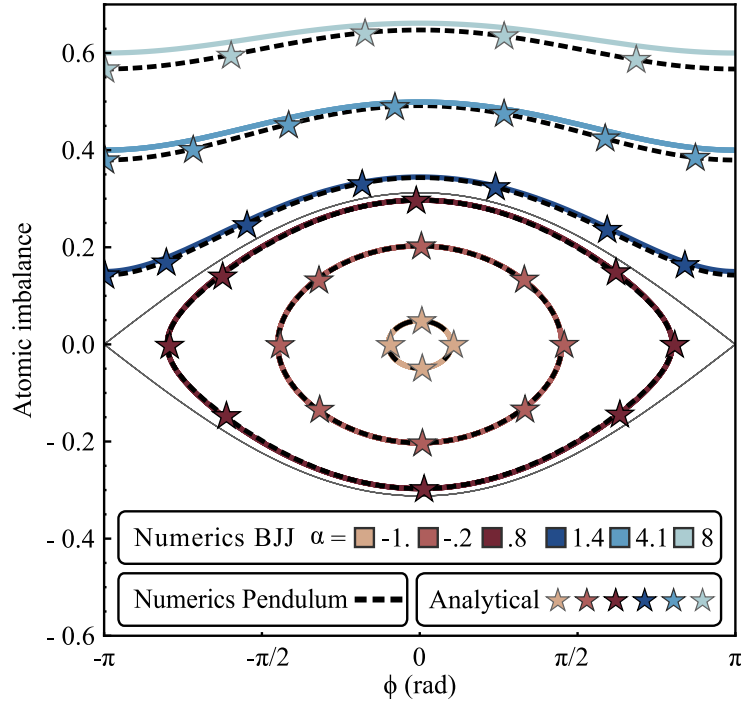


Figure 1.6: Taken from [57]. Dynamics of $N = 5000$ atoms in the (ϕ, n) space for $J/\hbar = 50$ Hz, $U/\hbar = 0.8$ Hz resulting in $\Lambda = 40$. It represents the six initial states of Fig. 1.5 where the full lines are the TMBH solutions, the dashed lines are the numerical pendulum solutions and the color stars are the analytical solutions. It shows that the amplitudes of the Josephson oscillations is well reproduced by the pendulum model and that only a slight discrepancy occurs deep in the MQST.

with sn^{-1} the inverse Jacobi-SN elliptic function [91].

The imbalance is deduced from its relation to the phase derivative. The derivative of the Jacobi amplitude is the Jacobi-DN elliptic function [91]:

$$\frac{d}{dt} \text{am}(k\omega_0 t | k^{-2}) = k\omega_0 \text{dn}(k\omega_0 t | k^{-2}). \quad (1.116)$$

Therefore, the imbalance evolution $n(t)$ is:

$$n(t) = \sigma_0 N_0 \text{dn}(k\omega_0 t + \delta\phi | k^{-2}), \quad (1.117)$$

with N_0 the extremal value reached by the imbalance defined by:

$$N_0 = \frac{2k}{\sqrt{\Lambda + \lambda}}. \quad (1.118)$$

Eqs. (1.113, 1.117) describe all dynamical modes of the BJJ, which differ by the value of k . This is illustrated in Figs. (1.5, 1.6). For $k = 0$, the system is at equilibrium. For $0 < k < 1$, the dynamics present Josephson oscillations. For $k = 1$, the dynamics follow the separatrix. Finally, $1 < k \leq (\sqrt{\Lambda + \lambda})/2$ corresponds to the MQST. The upper boundary on k comes from the limitation that the largest possible imbalance is $N_0 = 1$.

1.3.2.3 Generalization to an asymmetric BJJ

We consider an asymmetric trap for which we assume that the asymmetry maintains the trap frequencies and that consequently J and U are not modified. Additionally, we assume that the detuning is small enough for the two-mode approximation to hold true. In the TMBH model, an energy difference ϵ between the two sites of the double-well introduces a detuning term in the Hamiltonian:

$$H_{\text{BH}} = \frac{2J}{\hbar} \left[\frac{\Lambda}{2} n^2(t) - \sqrt{1 - n^2(t)} \cos \phi(t) \right] + \frac{\epsilon}{\hbar} n, \quad (1.119)$$

such that the equations of motions read [77, 78]:

$$\dot{\phi}(t) = \frac{\epsilon}{\hbar} + \frac{2J}{\hbar} \left(\Lambda n(t) + \frac{n(t)}{\sqrt{1 - n^2(t)}} \cos \phi \right), \quad (1.120)$$

$$\dot{n}(t) = -\frac{2J}{\hbar} \sqrt{1 - n^2(t)} \sin \phi(t). \quad (1.121)$$

The description of the detuning goes beyond the pendulum analogy. However, we can adapt the solutions defined previously to include an arbitrary detuning. For this we evaluate Eq. (1.120) at the initial time for $\epsilon \neq 0$:

$$\dot{\phi}_0(\epsilon) = \frac{\epsilon}{\hbar} + \frac{2J}{\hbar} (\Lambda + \lambda) n_0, \quad (1.122)$$

and interpret the detuning as an additional contribution to the kinetic energy. Consequently, the anharmonicity parameter k now depends on ϵ :

$$k(\epsilon) = \frac{1}{2\omega_0} \sqrt{\dot{\phi}_0(\epsilon)^2 + 4\omega_0^2 \sin^2\left(\frac{\phi_0}{2}\right)}. \quad (1.123)$$

The effect of the detuning on the dynamics can be partly described by its effect on the anharmonicity k . We illustrate this in Fig. 1.7 for multiple initial conditions involving the different combinations of $n_0 = [-0.2, 0, 0.2]$ and $\phi_0 = [-\pi, -\pi/2, 0, \pi/2, \pi]$. From Eq. (1.123), we deduce that k reaches a minimum at $\epsilon_L = -2J(\Lambda + \lambda)n_0$. In the specific case of $\phi_0 = 0$, the system is at equilibrium as $k(\epsilon_L) = 0$. It follows that the detuning shifts the equilibrium point in imbalance similarly as in [92] which describes the integrable sub-regime of the three-mode BH model.

We observe that the behavior of k presents several symmetries with respect to ϵ , as illustrated in Fig. 1.7. We first notice that $k(n_0, \pm\phi_0)$ and $k(-n_0, \pm\phi_0)$ are symmetric with respect to $\epsilon = 0$. This is explained by the geometry of the double-well. Indeed, the imbalance n_0 in an ϵ -detuned trap is indistinguishable from the imbalance $-n_0$ in a $-\epsilon$ -detuned trap.

Additionally, k presents a symmetry with respect to $\epsilon = \epsilon_L$ such that $k(\epsilon_L \pm \epsilon)$ has an identical value. This can be understood geometrically in the phase portrait representation: the initial state (n_0, ϕ_0) is at equal distance to the two equilibrium points of the traps of detuning $\epsilon_L + \epsilon$ and $\epsilon_L - \epsilon$. However, the initial state in these two traps does not have the

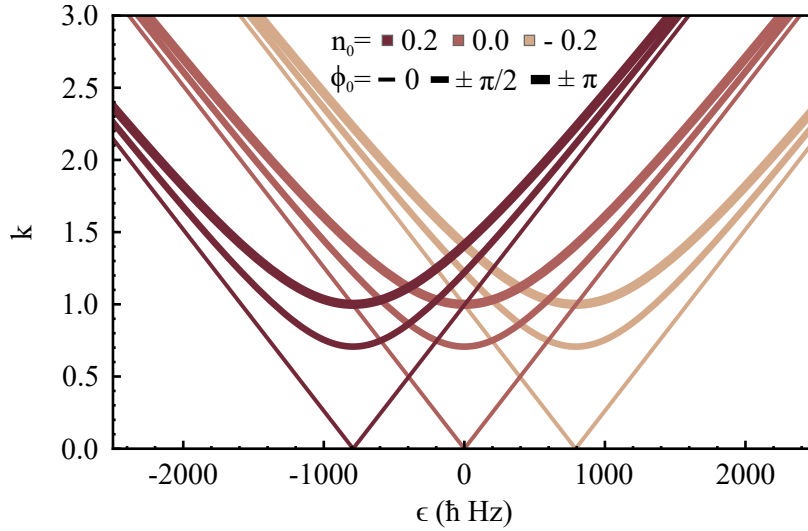


Figure 1.7: Taken from [57]. Effect of the detuning ϵ on k for 15 initial states. The trap is characterized by $J/\hbar = 20$ Hz and $\Lambda = 100$. The detuning shifts the position of the equilibrium state along the imbalance axis and changes the energy of the system characterized by k .

same dynamics as it evolves with respect to different equilibrium points. It shows that k is not sufficient to describe the detuning.

We mentioned that ϵ shifts the imbalance value of the equilibrium position. Using Eq. (1.97), we define the imbalance offset δn as:

$$\delta n = -\frac{\epsilon}{2J(\Lambda + \lambda)}. \quad (1.124)$$

As a result, the imbalance obeys:

$$n(t) = \sigma_0 N_0 \text{dn}(k(\epsilon)\omega_0 t + \delta\phi|k^{-2}) + \delta n - \bar{n}, \quad (1.125)$$

with σ_0 the sign function of $n_0 - \delta n$ and \bar{n} the mean value of the imbalance defined by:

$$\bar{n} = \begin{cases} 0 & k \leq 1, \\ \frac{N_0(\sqrt{1 - k^{-2}} + 1)}{2} & k > 1. \end{cases} \quad (1.126)$$

In the MQST ($k > 1$), the averaged value of $n(t)$ is deduced from the variations of the Jacobi DN function written in Eqs. (1.112, 1.116). The term \bar{n} is introduced to center the oscillations around zero. Indeed, the modification of k by ϵ can lead to a transition between Josephson oscillations and MQST which introduces an offset \bar{n} that we want to distinguish from δn .

The phase evolution is described by Eq. (1.113) given that we take into account the new definitions of $k(\epsilon)$ and $\sigma_0(\delta n)$.

1.3.2.4 Link between the TMBH and the pendulum parameters

In this section, we express the parameters of the TMBH model as a function of the pendulum parameters. We can combine the definitions of ω_0 , N_0 and k given by

Eqs (1.105,1.118,1.123) to express J as:

$$J = \frac{\hbar\omega_0}{4|\sin(\phi_0/2)|} \sqrt{|N_0^2 - 4(n_0 - \delta n)^2|}. \quad (1.127)$$

Using the definition of ω_0 , it immediately follows that:

$$\Lambda = \frac{4 \sin(\phi_0/2)^2}{|N_0^2 - 4(n_0 - \delta n)^2|} - \lambda, \quad (1.128)$$

from which we deduce U using $\Lambda = NU/2J$. From Eq. (1.124) we establish:

$$\epsilon = -\frac{2\hbar|\sin(\phi_0/2)|\delta n}{\sqrt{|N_0^2 - 4(n_0 - \delta n)^2|}}. \quad (1.129)$$

For a small asymmetry, the dependence of k with ϵ is negligible and the definitions simplifies to:

$$J = \frac{\hbar\omega_0}{2} \frac{N_0}{2k}, \quad (1.130)$$

$$\Lambda = \frac{4k^2}{N_0^2} - \lambda, \quad (1.131)$$

$$\epsilon = -\frac{2\hbar\omega_0 k}{N_0} \delta n. \quad (1.132)$$

One advantage of the pendulum model is that its parameters $N_0, \delta n, k, \omega_0$ are directly readable on the experimental data as explained in the following paragraphs.

Imbalance maximum and offset: N_0 is the highest imbalance reached by the system (in absolute value) and is directly seen on the imbalance dynamics, both in the oscillating and in the MQST regime. $\delta n - \bar{n}$ is a shift of the imbalance that can be easily obtained from the data as the averaged imbalance over time.

Energy ratio k : k is readable on the data but appears differently depending on the regime considered. In the oscillating regime and for small ϵ , we evaluate Eq. (1.111) at a maximum of the phase oscillations $\phi = \Phi_0, \dot{\phi} = 0$. Therefore $k = \sin(\Phi_0/2)$ where Φ_0 is the amplitude of the oscillations in phase, easily accessible experimentally. In the MQST, k affects the amplitude of the imbalance oscillations. Following Eqs. (1.112, 1.116), the imbalance varies (in absolute value) between N_0 and $N_0\sqrt{1 - k^{-2}}$. The value of k is then deduced from the amplitude of the imbalance oscillations.

Plasma frequency ω_0 : Due to the anharmonicity, the frequency of the oscillations is not directly the plasma frequency. However, a first-order correction relates the two frequencies by:

$$\omega \approx \omega_0 \left(1 - \frac{\Phi_0^2}{16}\right). \quad (1.133)$$

As Φ_0 is well determined by the oscillation amplitude, ω_0 is reliably derived from ω . The fit parameter is directly ω_0 but Eq. (1.133) allows a visual check of the fit result.

In the MQST, the plasma frequency ω_0 appears in the slope of the phase accumulation which reads $2\omega_0 k$.

1.3.2.5 Limitation of the analytical solutions

The description of the BJJ with the analytical solutions of a rigid pendulum holds true as long as the maximal variation of the pendulum length $l(t)$ defined by $l(t) = \sqrt{1 - n^2(t)}$ is negligible.

In the oscillating regime, the variations of the imbalance are given by:

$$\delta n \leq |n(t)| \leq N_0 + \delta n. \quad (1.134)$$

Consequently, the maximal variation of the pendulum length in the oscillating regime reads

$$\delta_{JO} = \sqrt{1 - (N_0 + \delta n)^2} - \sqrt{1 - (\delta n)^2}. \quad (1.135)$$

In the MQST regime, the amplitude of the imbalance oscillation is given by the variations of the Jacobi DN elliptic function. It follows from Eqs. (1.112, 1.116) that:

$$N_0 \sqrt{1 - k^{-2}} + \delta n \leq |n(t)| \leq N_0 + \delta n. \quad (1.136)$$

Consequently, δ_{MQST} reads:

$$\delta_{MQST} = \sqrt{1 - (N_0 + \delta n)^2} - \sqrt{1 - (N_0 \sqrt{1 - k^{-2}} + \delta n)^2}. \quad (1.137)$$

If N_0 , δn and (n_0, ϕ_0) are known, the hypothesis of negligible momentum-shortening can be verified *a posteriori*.

1.3.3 Quantum fluctuations

The mean-field formalism is limited to the description of the expectation values, corresponding to the mean values of the phase and imbalance. In reality, the imbalance $n(t)$ and the phase $\phi(t)$ present quantum fluctuations $\Delta n(t)$ and $\Delta \phi(t)$. For the atom number of our experiment (few thousands), the TMBH Hamiltonian can be treated in the second quantization formalism to define the fluctuations of the system. We present in the following the main points of this approach detailed for example in [42, 93].

1.3.3.1 Quantum model

Similarly to the mean-field case, we resort to the two-mode approximation and write the wave function as a combination of the mean-field ground state φ_0 and mean-field first excited state φ_1 .

$$\hat{\Psi} = \hat{a}_0 \varphi_0 + \hat{a}_1 \varphi_1, \quad (1.138)$$

with \hat{a}_0 (\hat{a}_0^\dagger) and \hat{a}_1 (\hat{a}_1^\dagger) the annihilation (creation) operators for a particle in the ground state and excited state. They obey the standard bosonic commutation relation $[\hat{a}_i, \hat{a}_j^\dagger] = \delta_{ij}$.

Due to the fixed atom number, a more convenient basis to describe the wave function is the one of the Fock states, where the states have a well defined atomic population in each site. For an atom number N , the Hilbert space has the dimension $N + 1$ and the basis reads:

$$\{|N_L, N_R\rangle\} = \{|0, N\rangle, |1, N - 1\rangle, \dots, |N, 0\rangle\}. \quad (1.139)$$

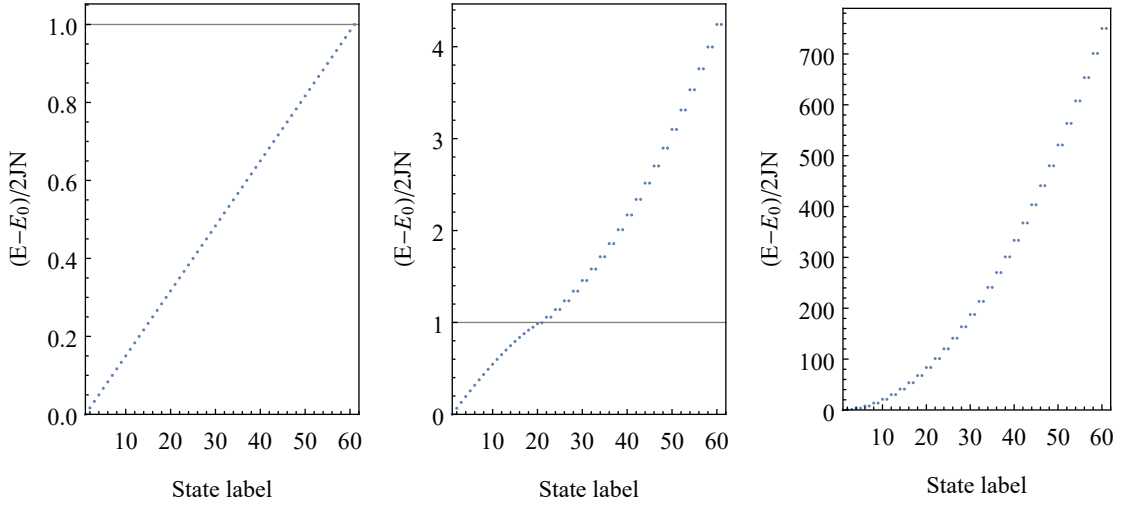


Figure 1.8: Energy spectrum in the TMBH model for $N=60$ atoms. **Left:** Non-interacting case ($U=0$). The spectrum is linear with a level spacing of $2J$. **Middle:** Josephson regime illustrated for $U/(2J) = 0.25$. The spectrum has a linear and a quadratic component. In the quadratic part of the spectrum, reached for $E - E_0 > 2JN$, the levels are pairwise degenerate. **Right:** $U/(2J) = 50$ close to the Fock regime. The spectrum is dominated by the quadratic component of the Hamiltonian.

The wave function in this basis is given by:

$$\hat{\Psi} = \hat{a}_L \varphi_L + \hat{a}_R \varphi_R, \quad (1.140)$$

with $\hat{a}_{L,R} = (\hat{a}_0 \pm \hat{a}_1)/\sqrt{2}$ and $\varphi_{L,R} = (\varphi_0 \pm \varphi_1)/\sqrt{2}$. The wave function given by Eq. (1.140) obeys the many-body Hamiltonian of Eq. (1.23), which can be written (neglecting the two-particle process) as:

$$\hat{H} = -J\hat{\alpha} + \frac{U}{2}\hat{n}^2 + \frac{UN}{4}(N-2). \quad (1.141)$$

Here, \hat{n} is the imbalance operator defined by

$$\hat{n} = \frac{\hat{a}_L^\dagger \hat{a}_L - \hat{a}_R^\dagger \hat{a}_R}{2}. \quad (1.142)$$

In a matrix notation, the imbalance operator is a diagonal matrix of dimension $(N+1)^2$ where the i -th element reads $-N/2 - 1 + i$ and i varies between 1 and $N+1$.

The operator $\hat{\alpha}$ is the tunneling operators defined by:

$$\hat{\alpha} = \hat{a}_R^\dagger \hat{a}_L + \hat{a}_L^\dagger \hat{a}_R. \quad (1.143)$$

In matrix notation, the tunneling operator is a matrix of dimension $(N+1)^2$ with non-zero terms on the super-diagonal and sub-diagonal. The i -th elements read $\sqrt{i(N-i+1)}$, with $i = 1 \dots N$.

Energy spectrum Using the matrix notations, the Hamiltonian can be diagonalized numerically to determine the eigenstates and energy spectrum. These depends strongly

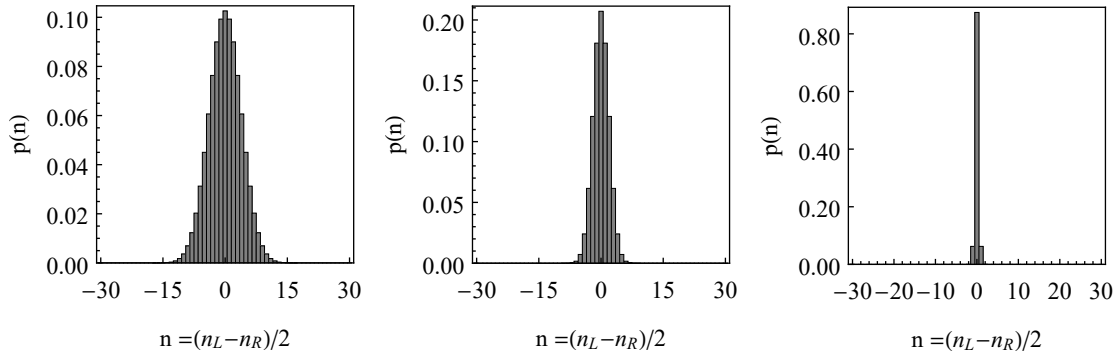


Figure 1.9: Probability distribution of the TMBH ground state in the half number imbalance basis for $\Lambda = 0, 0.25N, 50N$. The distribution is centered on $n = 0$ but its fluctuations depend on the regime. In the Rabi regime, the ground state resembles a coherent state of binomial fluctuations characterized by the width $N/4$. In the Josephson regime, the fluctuations decrease. In the Fock regime, the fluctuations are strongly reduced and the probability gets localized on a single Fock state.

on the parameter Λ . Fig. 1.8 shows the energy spectrum of $N = 60$ atoms for three values of $\Lambda = [0, 0.25N, 50N]$ with $J/h = 1$ Hz, corresponding to the Rabi regime, the Josephson regime and the Fock regime.

In the non-interacting case, the system consists of N independent particles, the energy spectrum is linear as for a harmonic oscillator with the energy level equally spaced by $2J$. The Rabi regime corresponds to $\Lambda \ll 1$ and resembles the non-interacting case.

The Fock regime corresponds to the non-tunneling limit $\Lambda \gg N^2$. It is illustrated for $\Lambda = 50N$ in the right panel of Fig. 1.8. In this case, the energy spectrum is dominated by the quadratic component of the Hamiltonian. The eigenstates are localized atom number states and the energy spectrum is similar to the energy spectrum of a free particle. Every energy, with the exception of the ground state of an even number of atoms, is a doublet with a quasi-degenerate symmetric and antisymmetric state.

In the Josephson regime, illustrated for $\Lambda = 0.25N$ in the middle panel of Fig. 1.8, the energy spectrum has a linear part for the low energy $E < 2NJ$ where the eigenstates are similar to those of a coherent state with a well defined phase. For $E > 2JN$, the eigenstates resemble the Fock states with a well defined atom number.

1.3.3.2 Ground state properties

Quantum ground state The eigenstates, and in particular the ground state, can be visualized as a probability distribution in the Fock basis. For this representation, we favor the half-number difference basis

$$|n\rangle = \left| \frac{N}{2} - n, \frac{N}{2} + n \right\rangle. \quad (1.144)$$

We define the expectation values of the i -th eigenvector $|\langle n|\psi_i\rangle|^2$. It is important to note that in this section only n refers to the half imbalance, in contrast with the normalized imbalance it corresponds to in the rest of the thesis. We display in Fig. 1.9 the fluctuations of the ground state for $\Lambda = 0, 0.25N, 50N$ associated to the parameters of Fig. 1.8. The

measure of the number of occupied states is given by the half-atom number difference:

$$\Delta n^2 = \langle \hat{n}^2 \rangle - \langle \hat{n} \rangle^2. \quad (1.145)$$

In the Rabi regime, $\Lambda \ll 1$, the ground state properties are close to the one of the non-interacting ground state. The half population imbalance of the ground state follows a binomial distribution between $-N/2$ and $N/2$. It is a product state of each atom being in the symmetric superposition left and right. The measurement projects each atom either to the left or right independently, which leads to a Poissonian distribution of standard deviation $\Delta n = N/4$ with n the half imbalance. In the Josephson regime ($1 \ll \Lambda \ll N^2$), the ground state is characterized by reduced atom imbalance fluctuations. In the Fock regime, the ground state cannot be defined by a single condensate and the states are said fragmented, meaning that they cannot be written as a product of single-particle states [94].

Semi-classical description of the ground state fluctuations In the linear part of the energy spectrum, i.e. for the states of energy $E \leq 2JN$, the Hamiltonian given by Eq. (1.141) is well approximated by a harmonic Hamiltonian and the fluctuations of the ground state are given by a simple formula [42].

To define the harmonic Hamiltonian, we start by introducing the notion of phase difference. The creation operators can be replaced by $\hat{a}_{L,R} \rightarrow \sqrt{N_{L,R}} \exp(i\phi_{L,R})$. The tunneling operator is therefore replaced by $\sqrt{N^2 - 4n^2} \cos(\phi)$. A second-order development in n and ϕ gives the Hamiltonian:

$$H = \frac{\hbar\omega_0}{2} \left(\frac{\phi^2}{2\Delta\phi^2} + \frac{n^2}{2\Delta n^2} \right), \quad (1.146)$$

with ω_0 the plasma frequency given by Eq. (1.105). $\Delta\phi$ and Δn obey the Heisenberg uncertainty principle $\Delta\phi\Delta n > 1/2$ and are defined by:

$$\Delta\phi^2 = \frac{\sqrt{1+\Lambda}}{N} \quad \text{and} \quad \Delta n^2 = \frac{N}{4\sqrt{1+\Lambda}}. \quad (1.147)$$

We represent in Fig. 1.10 the behaviors of Δn^2 and $\Delta\phi^2$ as a function of Λ . For $\Lambda \ll 1$, the imbalance fluctuations are binomial and equal to $N/4$. The phase distribution is narrow. In the Josephson regime, the imbalance fluctuations decrease and the phase fluctuations increase accordingly. The transition where the phase fluctuations reach 1 corresponds to the Fock regime, where the phase coherence vanishes. The imbalance and phase are no longer conjugate variables in this regime and the semi-classical treatment does not estimate properly the fluctuations.

1.3.4 Dynamics with fluctuations in the semi-classical picture

The dynamical response of the BJJ to low energetic excitations can be rigorously calculated in the many-body two-mode description [42]. However, we develop a simpler approach to model the dynamics of the fluctuations relying on a generalization of the equations of motion given by Eqs. (1.97, 1.98). The main limitation of this method is that the initial state must be introduced as a starting parameter.

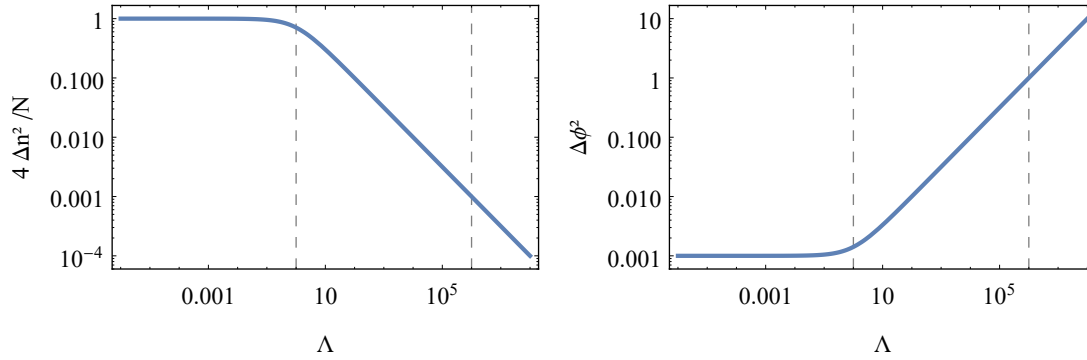


Figure 1.10: Semi-classical estimation of the fluctuations of the half imbalance and phase in the ground state. $N = 1000$. The fluctuations of the half imbalance are normalized to the coherent state fluctuations ($N/4$) and decrease from a binomial variance in the Rabi regime to a localized Fock state for large Λ . In the semi-classical picture, the phase variance increases accordingly to maintain $\Delta n^2 \Delta \phi^2 = 1/4$. Once $\Delta \phi^2$ reaches 1, the system enters the Fock regime. The semi-classical predictions are no longer valid and the imbalance and phase are no longer conjugate variables.

1.3.4.1 Principle of the Monte-Carlo like model

The initial state is characterized by the mean values of the initial imbalance \bar{n}_0 ¹ and of the initial phase $\bar{\phi}_0$ as well as by the associated fluctuations around the mean values. Contrary to the previous section n refers now to the normalized imbalance. The fluctuations of the initial state can be visualized in the (ϕ, n) plane [83] in the spirit of the Husimi Q-representation [95–97]. The surface \mathcal{S} covered by the fluctuations is centered on $\bar{\phi}_0, \bar{n}_0$ and has a given extension around the mean values.

Establishing the exact fluctuations is not trivial. However, we can access experimentally the projection of the fluctuations along the imbalance and phase axes. To do so, we repeat the measurement of the phase and imbalance (typically 50 experimental measurements) to establish their distribution and determine the standard deviations (or spread) $\Delta \phi_0$ and Δn_0 . While this does not give the exact shape of the fluctuations, a Gaussian distribution is characteristic of an elliptic shape for the fluctuations surface. It does not give indication about the orientations of the ellipse axes with respect to the phase and imbalance axes. For simplicity, we restrict this study to the case where the axes of the ellipse are oriented along the phase and imbalance axes. This corresponds either to a coherent state, to a number squeezed state or to a phase squeezed state.

The principle of the semi-classical treatment consists in simulating the initial fluctuations by a distributions of m classical points characterized by (ϕ_0^i, n_0^i) , with $i = \{1 \dots m\}$. Each ϕ_0^i (respectively n_0^i) is taken in a binomial distribution centered on $\bar{\phi}_0$ (respectively \bar{n}_0) and of width $\Delta \phi_0$ (respectively Δn_0). The m combinations (ϕ_0^i, n_0^i) are then numerically propagated in time using the mean-field equations of motion Eqs. (1.97, 1.98). This simulation is in the idea similar to a Monte-Carlo model therefore we refer to it as a Monte-Carlo (MC) like model.

Over the time evolution, the individual points visualized in the (ϕ, n) space follow

¹ n refers from now on to the normalized imbalance defined by Eq. (1.91)

different trajectories which results in a deformation of the fluctuation surface \mathcal{S} and an evolution of $\Delta\phi(t)$ and $\Delta n(t)$. The mean value of the distributions defines the average time evolution while the standard deviations reflects the evolutions of the fluctuations. The evolution of the fluctuations depends strongly on the initial conditions $\bar{\phi}_0, \bar{n}_0, \Delta\phi_0$ and Δn_0 . More precisely, it depends on the number of classical trajectories populated and on the repartition of the classical points on the trajectories. This leads to a large variety of dynamical behaviors categorized in the following sections.

1.3.4.2 Ground state and static states

For comparison with the quantum model, we test this model on the ground state, where the mean values and fluctuations obey:

$$\bar{\phi}_{\text{GS}} = 0 \text{ and } \Delta\phi_{\text{GS}} = \sqrt{\frac{\sqrt{1+\Lambda}}{N}}, \quad (1.148)$$

$$\bar{n}_{\text{GS}} = 0 \text{ and } \Delta n_{\text{GS}} = \sqrt{\frac{1}{N\sqrt{1+\Lambda}}}. \quad (1.149)$$

The upper row of Fig. 1.11 displays the reconstruction of the ground state for $N = 3000$ atoms and $\Lambda = 50$. The phase and imbalance follow Gaussian distributions obeying Eqs. (1.148, 1.149). For a good visualization of the density of points in the (ϕ, n) space, we use 10^6 classical points, but a much smaller number is enough to look at the time evolution. Figure 1.12 shows that the fluctuations and the mean values are almost constant over time. A small oscillation of phase and imbalance is visible and comes from the fact that, for a finite number of classical points, the spreads $\Delta\phi_0$ and Δn_0 cannot be exactly the ones of the ground state. Similar results are obtained for any values of J, N and Λ such that the semi-classical model is compatible with the quantum expectations.

The case of the ground state can be generalized to an entire category of states of constant fluctuations, that we refer to as static states (SS). This appears more clearly in the (ϕ, n) space by considering the fluctuations surface. For the spreads to be constant over time, the fluctuations surface must not be deformed by the propagation of the individual classical points. The classical points follow a trajectory characterized by the initial energy α and the trajectories cannot cross each other as well illustrated in the (ϕ, n) space. Therefore, for the fluctuation surface to remain unchanged, the displacement of a particle m with α_m must be compensated by the displacement of another particle m' of identical α_m . Along the trajectory labeled α_m , the individual motions are compensated if the density of particle over the trajectory is homogeneous i.e. when the particles initially fill every possible combinations of phase and imbalance corresponding to α_m given by Eq. (1.100). The reasoning applies to the entire set of α populated by the initial Gaussian distributions.

This situation occurs for Gaussian states centered on $\bar{\phi}_0 = 0, \bar{n}_0 = 0$ for which the spreads are linked by:

$$\alpha_L = \frac{\Lambda}{2}(\Delta n_{\text{SS}})^2 - \sqrt{1 - (\Delta n_{\text{SS}})^2} \cos(\Delta\phi_{\text{SS}}). \quad (1.150)$$

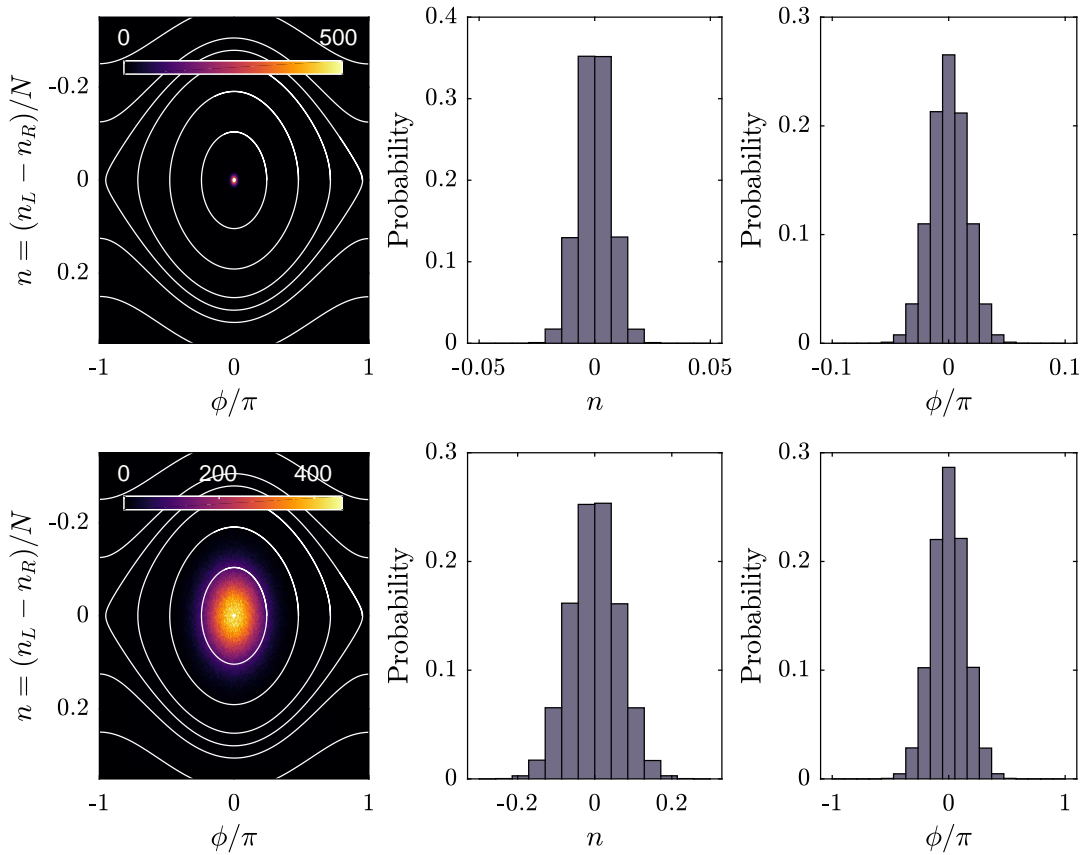


Figure 1.11: States of constant fluctuations The initial state is reproduced using 10^6 classical points sampling Gaussian distributions centered on $\bar{\phi}_0 = 0, \bar{n}_0 = 0$. **Top: Gaussian ground state** The std of the distributions is given by the fluctuations of the quantum ground state of $\Lambda = 50$ for $N = 3000$ atoms, i.e. $\Delta n_0 = 0.0068, \Delta \phi_0 = 0.0488$. **Bottom: Gaussian state with non-minimal uncertainty fluctuations.** For the same values of Λ, N , the std of the distributions is given by $\alpha_L = -0.9$, such that $n_0 = 9.16\Delta n_{GS}$ and $\Delta \phi_0 = 9.25\Delta \phi_{GS}$ and $\Delta \phi_0 \Delta n_0 = 85/N$.

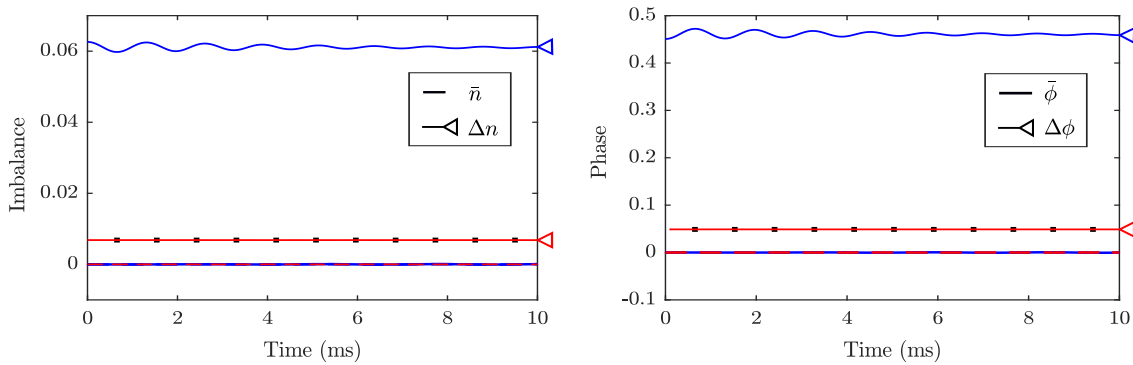


Figure 1.12: Time evolution of the imbalance and phase computed with 10^4 classical points for the parameters of Fig. 1.11. The red and blue lines relate to the ground state case and static state ($\alpha_L = -0.9$) respectively. The lines indicated by a triangle are the fluctuations by contrast the the bare ones, representing the mean values, and constantly equal to 0. The black squares represent the quantum ground state fluctuations.

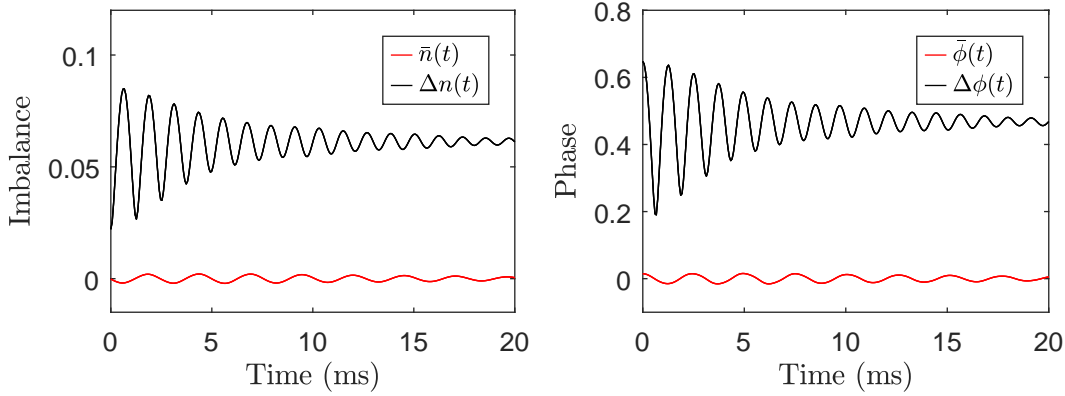


Figure 1.13: Squeezing oscillations Time evolution of an initial number-squeezed state prepared as $\bar{\phi}_0 = 0, \bar{n}_0 = 0, \Delta n_0 = \Delta n_{SS}(\alpha = -0.8)/4$ and $\Delta\phi_0 = \Delta\phi_{SS}(\alpha = -0.8)$ for $\Lambda = 50$ and $N = 3000$ atoms. The spreads display a π out-of-phase oscillations as the fluctuations surface gets deformed due to the individual time evolutions. The system alternates between number and phase squeezing. The oscillations stabilize at long time due to a dephasing mechanism appearing clearly in the (ϕ, n) space. The mean values show little to no evolution.

α_L is a value characterizing the relative width of the fluctuations such the when a point obeys $n_0^i = \Delta n_{SS}$ and $\phi_0^i = \Delta\phi_{SS}$, the associated α^i is equal to α_L . α_L can take any value such that $\Delta n_{SS} < n_c$ to make sure that the fluctuations remain in the oscillating regime.

We can express $\Delta\phi_{SS}$ and Δn_{SS} as a function of Λ and α_L only. $\Delta\phi_{SS}$ is obtained by evaluating Eq. (1.150) for $\Delta n_{SS} = 0$ which is equivalent to a projection of the fluctuations surface of the phase axis, and Δn_{SS} is established using the same equation evaluated for $\Delta\phi_{SS} = 0$ (projection on the imbalance axis). It follows that:

$$\Delta\phi_{SS} = \arccos(-\alpha_L), \quad (1.151)$$

$$\Delta n_{SS} = \frac{\sqrt{2}}{\Lambda} \sqrt{\alpha_L \Lambda - 1 + \sqrt{1 - 2\alpha_L \Lambda + \Lambda^2}}. \quad (1.152)$$

In this case, the initial fluctuation surface is an ellipsoid where the trajectories of lowest α have the highest density of points and the density decreases for larger α until the boundary α_L . For each value of α , the trajectory is homogeneously populated. An example is displayed in the lower row of Fig. 1.11 for $\alpha_L = -0.9, \Lambda = 50, N = 3000$ atoms. The evolution of this state over 10 ms is displayed in Fig. 1.12 and shows that the mean values and fluctuations do not evolve noticeably.

1.3.4.3 Squeezing oscillations

The situation changes completely when the distribution does not populate the trajectories homogeneously. This is typically realized by any squeezed state centered on $(\bar{\phi}_0 = 0, \bar{n}_0 = 0)$ and not obeying Eq. (1.150). In this case, the evolution of the classical points on their respective trajectory leads to a rotation of the surface such that the system oscillates between number squeezing and phase squeezing. As an illustration, an initial number-squeezed state is displayed in the upper row of Fig. 1.13. It corresponds to $\bar{\phi}_0 = 0, \bar{n}_0 = 0, \Delta\phi_0 = \Delta\phi_{SS}(\alpha = -0.8)$ and $\Delta n_0 = \Delta n_{SS}(\alpha = -0.8)/4$. The first

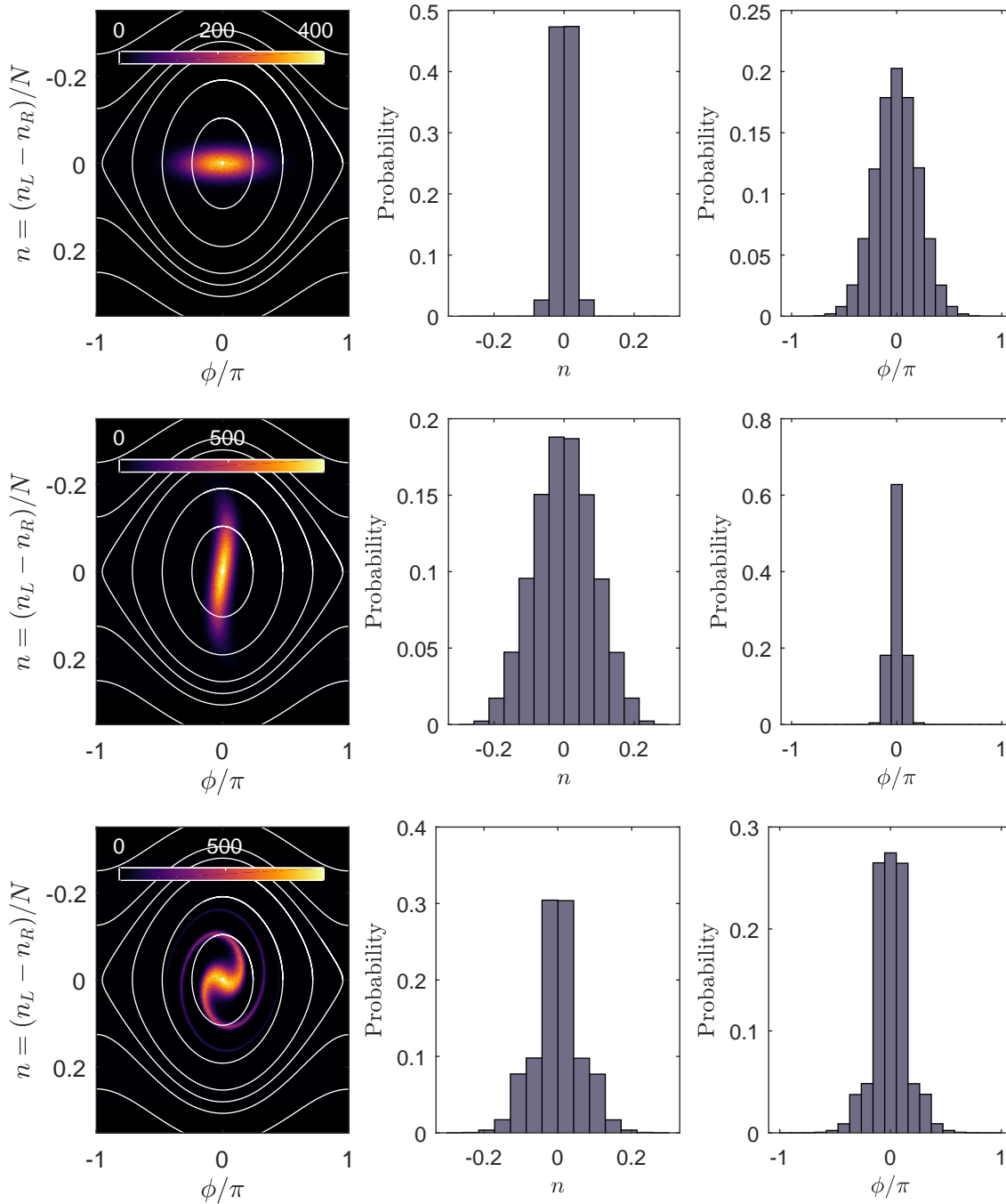


Figure 1.14: Squeezing oscillations Top to bottom: Snapshot at $t = 0$ ms, 0.5 ms and 20 ms of the fluctuations surface in the (ϕ, n) space and its projection on the imbalance and phase axes. The state is initially number-squeezed: $\bar{\phi}_0 = 0, \bar{n}_0 = 0, \Delta n_0 = \Delta n_{SS}(\alpha = -0.8)/4$ and $\Delta \phi_0 = \Delta \phi_{SS}(\alpha = -0.8)$ for $\Lambda = 50$ and $N = 3000$ atoms. Over time, the fluctuation surface undergoes a rotation around the equilibrium point, leading to a phase squeezing after 0.5 ms. The system alternates between number and phase squeezing at short times. However, the evolution is faster close to equilibrium such that a dephasing can be seen at longer time. The extremities of the surface being slower, the ellipse gets deformed as a reversed "S" and lead to a stabilization of the spreads of the phase and imbalance distributions.

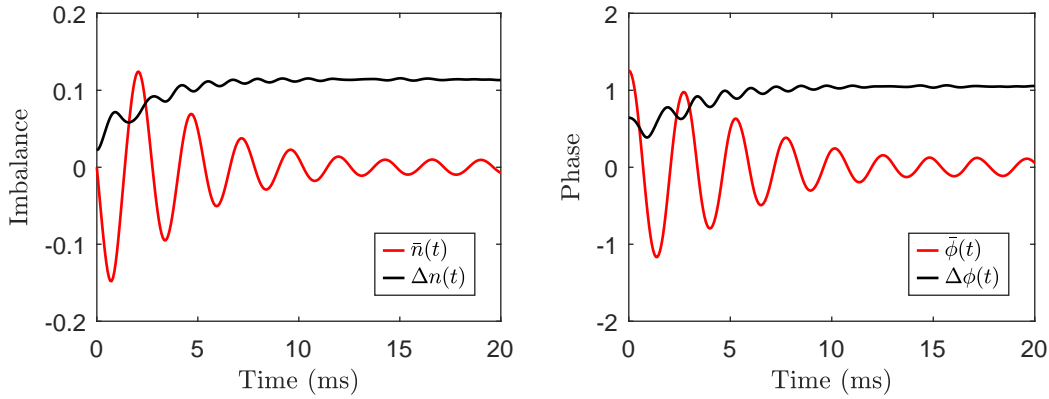


Figure 1.15: Dephasing Evolution of 10^6 classical points reproducing an initial number-squeezed state characterized by $\bar{\phi}_0 = 0.4\pi$, $\bar{n}_0 = 0$ and the std $\Delta n_0 = \Delta n_{\text{SS}}(\alpha = -0.8)/4$ and $\Delta\phi_0 = \Delta\phi_{\text{SS}}(\alpha = -0.8)$. Due to large number of trajectories populated by this initial state, the squeezing oscillations are dominated by a dephasing which increases the spreads until they reach a saturation value. The Josephson oscillations, resulting from the collective displacement of the individual points, are quickly damped due to this dephasing.

rotation of the fluctuations is displayed in the middle row of Fig. 1.13 after 0.5 ms of evolution. It clearly shows that the initially number-squeezed state has evolved into a phase-squeezed state. The evolution over 20 ms of the mean values and fluctuations is displayed in Fig. 1.13.

The squeezing oscillations are damped due to a dephasing effect. Indeed, the points of larger α (i.e. further away from equilibrium) are characterized by a slower evolution which, over time, leads to a deformation of the surface \mathcal{S} into a reversed "S" shape. This appears in the lowest row of Fig. 1.14 showing the fluctuations surface after 20 ms of evolution. The exact shape of the damping and the final value depends on the parameter Λ and on the initial distributions. Revivals of the squeezing oscillations can also be observed with a smaller amplitude than the oscillations at short time. The evolution of the mean values is quite negligible in this case as they are initially centered on $(\bar{\phi}_0 = 0, \bar{n}_0 = 0)$.

1.3.4.4 Dephasing

Without fluctuations, an initial state centered on $(\bar{\phi}_0 \neq 0, \bar{n}_0 = 0)$ exhibits Josephson oscillations for an indefinite amount of time. However, fluctuations introduce a dephasing effect which affects the time evolution of the mean values and fluctuations.

Experimentally, the case where the initial state is number-squeezed and centered on $(\bar{\phi}_0 \neq 0, \bar{n}_0 = 0)$ is especially relevant as it is the best one we can prepare to observe Josephson oscillations. The predictions of a dephasing originating from the fluctuations is therefore crucial in the context of this thesis.

When considering a number squeezed state with $(0 < |\bar{\phi}_0| \ll \pi, \bar{n}_0 = 0)$ the Gaussian fluctuations are entirely contained in the oscillating sector. However, centering the fluctuations on these mean values maximizes the number of trajectories populated. As the frequency of evolution of the various trajectories is different, the points evolve more and more slowly the further they are from equilibrium and the fluctuation surface is quickly

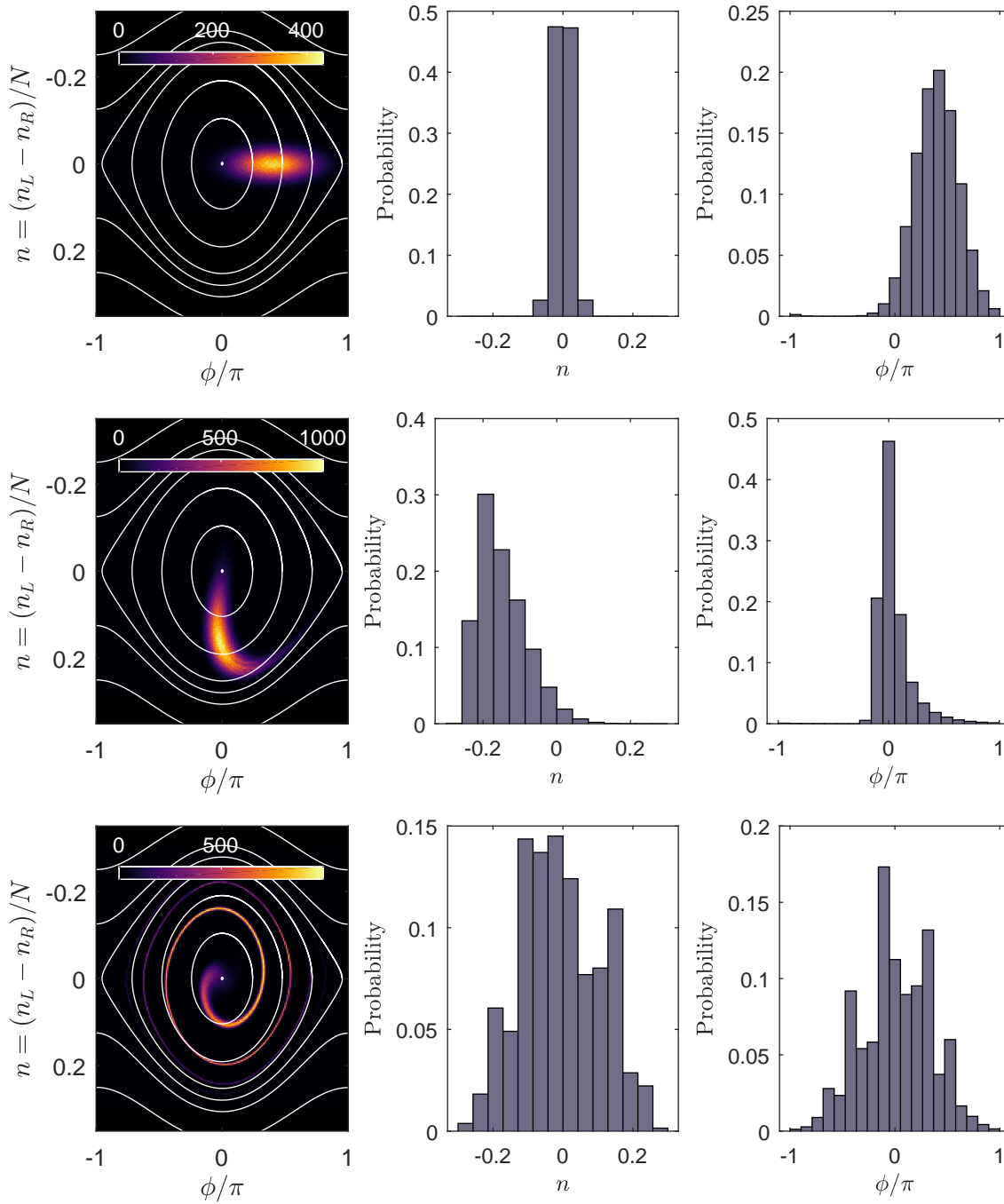


Figure 1.16: Dephasing For the initial state of Fig. 1.15, snapshots at $t = 0$ ms, 1.5 ms and 20 ms (top to bottom) of the fluctuations in the (ϕ, n) space and of its projections on the imbalance and phase axes. The evolution of the distribution leads to an oscillation between number and phase squeezing at short time, dominated by a dephasing mechanism. Due to the different propagation speeds between the points close to equilibrium and far from equilibrium, the fluctuation surface is quickly distorted in a spiral such that the projections are broad and do not show a significant evolution.

stretched until the individual points are totally scattered over the trajectories (Fig. 1.16). The distributions differ strongly from Gaussian distributions at short time such that defining standard deviations does not fully make sense. In Fig. 1.15, the spreads extracted from the distributions show a small squeezing oscillations but mainly an increase over time until they reach a saturation value. The dephasing quickly suppresses the Josephson oscillations of the mean values.

The strong increase of the spreads compared to the initial ones is a clear difference between a dephasing and a relaxation. The latest cannot be predict in the semi-classical approach presented in this section.

If similar initial distributions are centered on another value of phase or imbalance, the dephasing also occurs but possibly more slowly. The key argument defining the dephasing is the number of trajectories populated, as this effect comes entirely from the fact that particles on various trajectories evolve at different speed. The smallest dephasing for a number squeezed state occurs for $\phi_0 = 0, n_0 \neq 0$ as this situation minimizes the width of the distribution of α . However, if part of the distribution is in the self-trapping regime, the dephasing must be described differently and is known as interaction-induced phase diffusion. It is presented in the next section.

1.3.4.5 Interaction-induced phase diffusion

Interaction-induced phase diffusion is a direct consequence of the repulsive interactions in a two-mode BEC [98–100] such that an energy cost is associated to an atomic imbalance. This phenomenon can be explained in the framework of the quantum two-mode Bose-Hubbard model. In this paragraph, we recover the quantum predictions of [101, 102] using the MC-like model.

Contrary to the squeezing oscillations where the fluctuations oscillate between $\Delta\phi(t)$ and $\Delta n(t)$ before dephasing at long time, the phase diffusion is an increase of $\Delta\phi$ without evolution of $\Delta n \neq 0$. Therefore, it occurs when the system is not in the Josephson oscillating regime. In term of the classical distribution, all the initial points must deep in the MQST. This can be realized either by preparing the appropriate (ϕ, \bar{n}) far from the equilibrium point or by realizing $J = 0$.

Phase diffusion in absence of tunnel coupling For $J = 0$, the individual points $i = \{1\dots m\}$ follow the equations of motion:

$$\dot{n}_i(t) = 0, \quad (1.153)$$

$$\dot{\phi}_i(t) = \frac{NU}{\hbar} n_i(t) + \frac{\epsilon}{\hbar}. \quad (1.154)$$

Therefore the phase and imbalance evolutions of each point i of initial coordinates $(\phi_i(0), n_i(0))$ read:

$$n_i(t) = n_i(0), \quad (1.155)$$

$$\phi_i(t) = \left[\frac{NU}{\hbar} n_i(0) + \frac{\epsilon}{\hbar} \right] t + \phi_i(0). \quad (1.156)$$

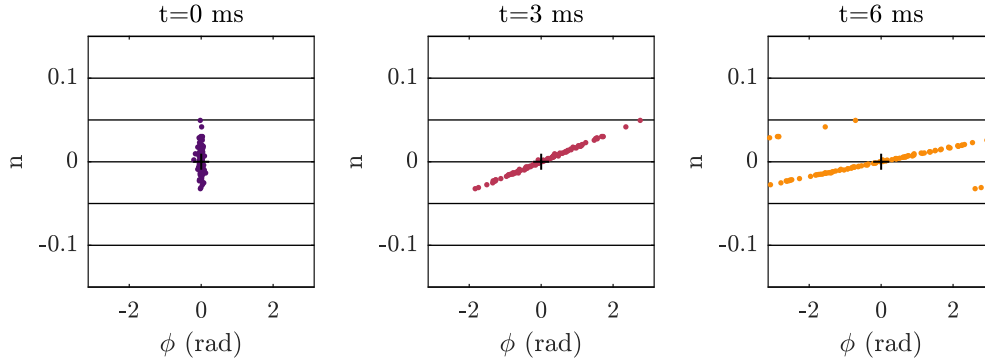


Figure 1.17: Distributions of phase and imbalance in a decoupled trap at three different times. The initial distributions are characterized by $\bar{n} = 0$, $\bar{\phi} = 0$, $\Delta n(0) = 0.017$ and $\Delta\phi(0) = 0.05$, a total atom number of $N = 3000$ atoms evolving in a trap where $J = 0$ and $\epsilon = 0$. Over time, the classical points linearly evolve toward the positive phase for the points i verifying $n_i(0) > 0$ and toward the negative phase for those obeying $n_i(0) < 0$. This result in a broadening of the phase distribution known as interaction induced phase-diffusion. The effect is faster for increasing values of $\Delta n(0)$ as the phase evolution is faster for larger n . After a linear phase diffusion, the phase is totally random.

This corresponds to the deep MQST where the imbalance is frozen and the phase accumulates linearly. We consider an initial state centered on $(\bar{\phi} = 0, \bar{n} = \epsilon/NU)$ as displayed in Fig. 1.17 for $\epsilon = 0$. In this case, the points with $n_i(0) > \epsilon/NU$ evolve toward the positive phase values while those with $n_i(0) < \epsilon/NU$ evolve toward the negative phase values. This leads to an increase of the phase fluctuations $\Delta\phi(t)$ known as phase diffusion. The simulation displayed in Fig. 1.17 considers a state with very small phase fluctuations in order to illustrate at best the stretching of the phase distribution over time. However, this result is also valid for states with larger initial phase fluctuations.

To establish the phase diffusion rate, we consider a point in the tail of the imbalance distribution with $n_+ > 0$. The phase accumulation rate is $\dot{\phi}_+ = \frac{NU}{\hbar}n_+ + \frac{\epsilon}{\hbar}$. On the other side, a point in the tail of the imbalance distribution $n_- < 0$ experiences a phase accumulation at the rate $\dot{\phi}_- = \frac{NU}{\hbar}n_- + \frac{\epsilon}{\hbar}$. The difference between the phase accumulation rate of these two points corresponds to the phase diffusion rate:

$$R = \dot{\phi}_+ - \dot{\phi}_- = \frac{NU}{\hbar}(n_+ - n_-) = \frac{NU}{\hbar}\Delta n. \quad (1.157)$$

We recover the phase diffusion rate calculated in [101, 102] for Gaussian fluctuations close to the minimal uncertainty limit. This phenomenon is known as interaction-induced phase diffusion as it arises from the term $\frac{NU}{\hbar}\Delta n$.

Equation (1.157) does not involve the detuning. This can appear surprising, as the reasoning presented previously relies on the evolutions of the two tails of the distribution toward opposite directions along the phase axis. For $\epsilon \neq 0$, the distribution might obey $n_i(0) > \epsilon/NU$ for all i such that the fluctuations evolve toward $\phi > 0$. The same reasoning applies to $n_i(0) < \epsilon/NU$ toward $\phi < 0$. In this case, the phase distribution still stretches as the points of different $n_i(0)$ present a phase evolution at different rates. This is illustrated in Fig. 1.18 for $\epsilon/\hbar = [-1500, 0, 1500]$ Hz. Therefore, the phase diffusion deep in the MQST is solely due to the repulsive interaction and Δn .

However, while $\Delta\phi(t)$ does not vary with the detuning, the latest affects the mean

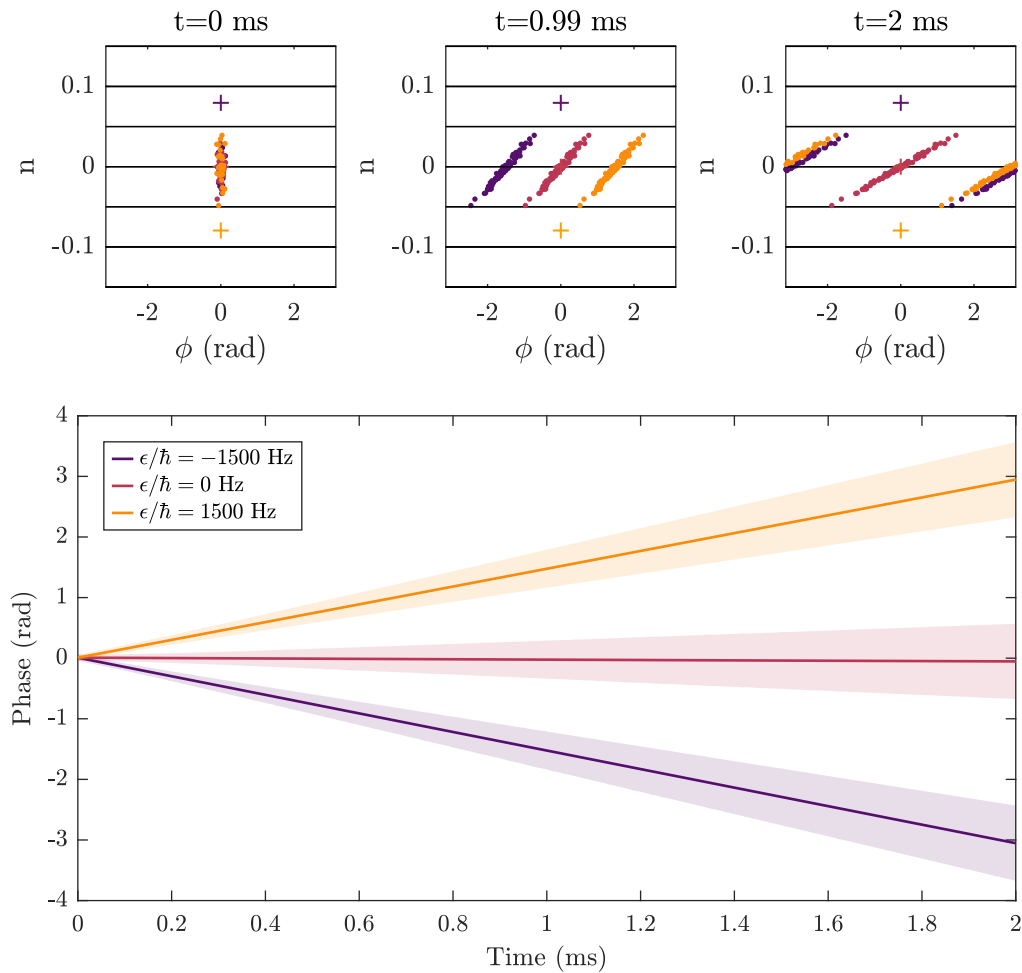


Figure 1.18: Evolution of the phase and phase spread for various detuning. For a total of $N = 3000$ atoms, the initial distributions are characterized by $\bar{n} = 0$, $\bar{\phi} = 0$, $\Delta n(0) = 0.017$ and $\Delta\phi(0) = 0.05$, a distribution of 100 points is evolved in a trap where $J = 0$ and $\epsilon/\hbar = [-1500, 0, 1500]$. **Top:** Evolution of an identical initial state in the phase portrait representation for three values of ϵ . After 1 ms of dynamics, we observe that the distribution have diffused identically but that the averaged phase is displaced, toward positive values for positive detuning (the entire distribution is initially above the equilibrium point represented by the orange cross) and toward the negative phase values for $\epsilon < 0$ (distribution initially below the equilibrium point represented by the deep purple cross). **Bottom:** Evolution of the averaged phase for the same initial distribution and three values of ϵ and corresponding spreads.

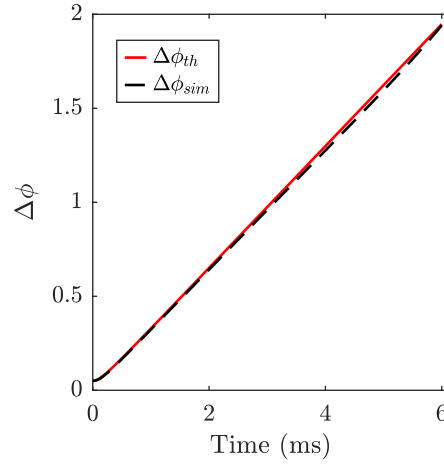


Figure 1.19: Phase diffusion. The phase fluctuations $\Delta\phi(t)$ obtained from the semi-classical model (dashed black line) are in agreement with the quantum predictions of a Gaussian state (red solid line) where the phase fluctuations evolves as $\Delta\phi(t) = \sqrt{\Delta\phi(0)^2 + R^2 t^2}$ with R the phase diffusion rate defined by $R = NU\Delta n/\hbar$.

values of the phase, which present a linear evolution with a slope $\propto \epsilon/\hbar$ (Fig. 1.18).

[101, 102] establish that the evolution of the phase fluctuations relates to the diffusion rate as:

$$\Delta\phi(t) = \sqrt{\Delta\phi(0)^2 + R^2 t^2}. \quad (1.158)$$

This equation is valid for initial distributions close to the minimal uncertainties fluctuations $\Delta n(0)\Delta\phi(0) \gtrsim 1/N$ and as long as the phase is not fully random. This equation is well verified by the MC-like simulation as illustrated by Fig. 1.19. In this case, we chose an atom number of $N = 3000$ atoms with the initial distributions $\Delta n(0) = 0.017$, $\Delta\phi(0) = 0.05$, we obtain a phase diffusion rate of $R = 325$ mrad/ms. The $\Delta\phi(t)$ obtain by the MC-like model and by the analytical expression given by Eq. (1.157) are in very good agreement.

Phase diffusion in presence of a weak finite tunnel coupling Experimentally, the tunnel coupling always has a finite value, even if this one is very small. In the case of a finite but small tunnel coupling J , the description of the phase diffusion is modified when part of the distribution is in the oscillating regime.

We presented in Sec. 1.3.4.3 that the evolution of a distribution in the oscillating regime mainly consists in squeezing oscillations, where the widths of the phase and imbalance distributions oscillate π out-of-phase until a dephasing dominates.

In the case of a finite small coupling, the initial fluctuations are divided between the JO and the MQST regimes, resulting in two dynamical behaviors. The part in the oscillating regime shows an oscillation of the fluctuations as explained in Sec. 1.3.4.3 while the part in the MQST shows a phase diffusion. At short time, both effects are equivalent as all points with $n_i(0) > 0$ evolve toward larger positive values of ϕ and those of $n_i(0) < 0$ evolve toward larger negative values of ϕ . Therefore, the system follows the predictions of Eq. (1.158). However, after the part in the oscillating regime reaches its highest phase value, it evolves toward lower phase values which leads to a saturation of $\Delta\phi$ at long time.

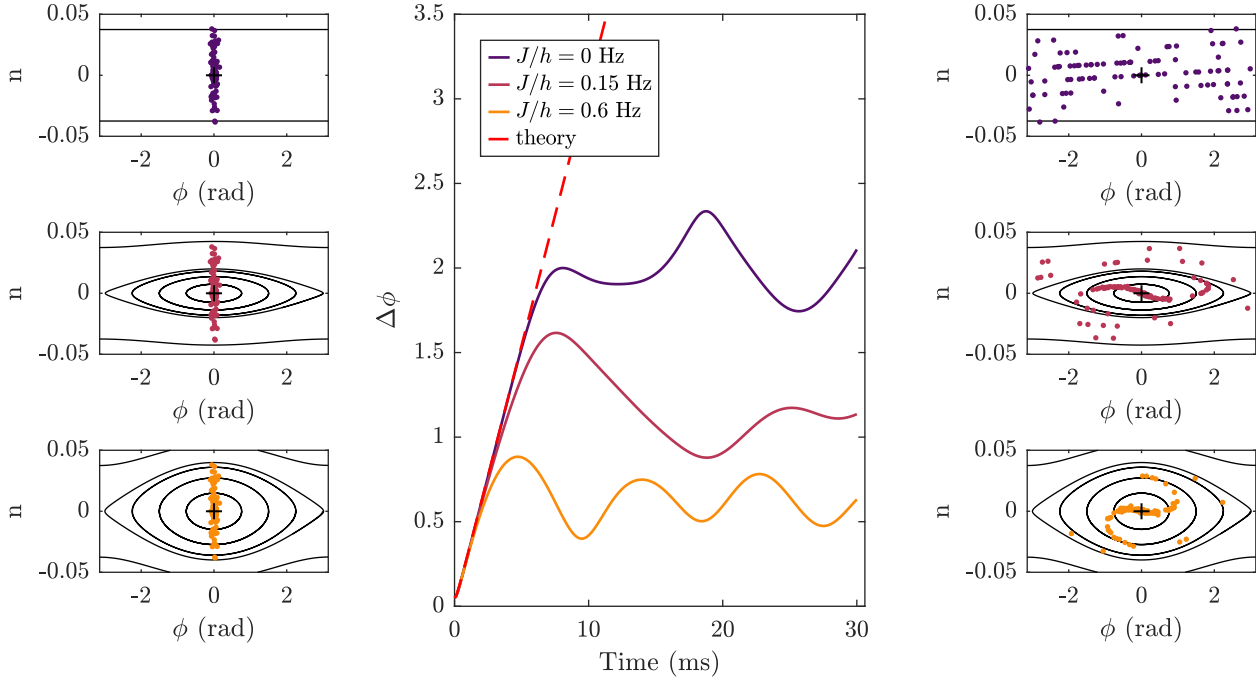


Figure 1.20: Phase diffusion for a finite tunnel coupling. Evolution of the phase spread for three values of the tunnel coupling $J/h = [0, 0.15, 0.6]$ Hz and identical initial number and phase fluctuations. The left panel represents the initial fluctuations in the (ϕ, n) space and illustrates that, under a change of J , the distribution can be entirely in the MQST, divided between the MQST and the JO regime or fully in the JO regime. This affects the phase diffusion. The distribution in the MQST follows the prediction of phase diffusion up to the point where the phase is random (purple line). The distribution divided between MQST and JO follows the prediction of the interaction-induced phase diffusion at short time and saturates before the phase gets random. For a distributions totally in the JO, the predictions of the interaction-induced phase diffusion are followed for an even shorter time after which the phase spread oscillates close to a saturation value.

This behavior is illustrated in Fig. 1.20 which displays the typical time evolutions when Δn is varied from $\Delta n \gg n_c$ to $\Delta n = n_c$ by a change of $J/h = [0, 0.15, 0.6]$ Hz.

Phase diffusion as a sensitive measurement of the trap symmetry An interesting consequence from the experimental point of view is that, even though we cannot reach a zero tunnel coupling, a small detuning is enough to realize an effective decoupled trap where J_{eff} depends on J and ϵ . Indeed, for a finite value of J , the mean position of the distribution with respect to the equilibrium position determines the proportion of the fluctuations in the JO and in the MQST regimes. As discussed in the previous section, this changes the value at which the phase spread saturates. A change of detuning results in a displacement of the equilibrium point and changes the proportion of the fluctuations in both dynamical regimes.

Therefore, the phase diffusion can be used as a calibration tool for the trap symmetry. Two requirements are important to use this method.

- The minima of phase diffusion is reached when \bar{n} coincides with the equilibrium

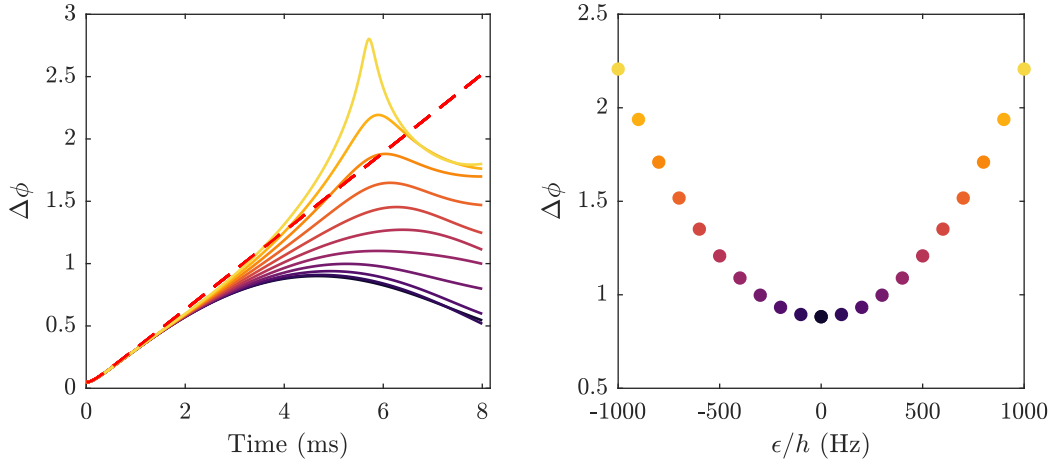


Figure 1.21: Phase diffusion in an asymmetric trap. Left: Time evolution of the phase spread for a detuning varied between $\epsilon/\hbar = -1000 : 1000$ Hz. The interaction-induced phase diffusion does not depend on the detuning for $J = 0$. However, for finite J , ϵ realizes the transition between MQST and JO regime. At short time, JO and MQST follow the predictions of the phase diffusion at $J = 0$. However, at longer time, the dephasing saturates at a value depending on ϵ . **Right:** Phase spread after saturation as a function of the detuning. The phase spread presents a minimum reached for the symmetric trap. Experimentally, this allows a determination of the symmetric trap for finite J .

imbalance. Therefore, the imbalance distribution must be centered on $\bar{n} = 0$. If not, the minima of phase diffusion will be obtained for the detuning value ϵ_{off} matching $\bar{n} = \epsilon_{\text{off}}/NU$.

- This method yields better results for typical values of $\Delta n(0)$ smaller than n_c i.e. when the initial distribution is entirely in the oscillating regime of the symmetric trap. For small J , the use of a number squeezed state is the most promising choice.

In this case, a change of ϵ realizes smoothly the transition between squeezing oscillations and phase diffusion. The phase spread over time is illustrated in the left panel of Fig. 1.21 for $\epsilon/h = [0 : 200 : 1000]$ (purple to yellow). The behavior is identical for ϵ/h and $-\epsilon/h$. The phase spreads measurement at a time t of the dynamics for various ϵ/h allows to determine the minimum of phase spread. This is displayed in the right panel of Fig. 1.21 for $t = 5.6$ ms. The minima is clearly obtained for $\epsilon = 0$.

At any time of the dynamics, the minimal phase spread is obtained for the symmetric trap. However, the evolution at short time is not the most suitable to evaluate the minimal phase spread as we explained that for a finite J the squeezing oscillations and phase diffusion present an identical behavior at short time. At long time, the phase is random and the phase spread versus ϵ/h is not a simple parabola but presents noise. A time briefly before the phase randomizes fully for the highest ϵ/h is the most suitable time to evaluate $\Delta\phi$.

1.3.4.6 Adiabatic squeezing generation by linear ramp

Experimentally, the coherent manipulation of the atomic cloud relies on the continuous modification of the trapping geometry and uses the repulsive interactions and tunneling

to prepare a broad variety of initial states. In this section, we investigate the modification of the trap allowing the generation of states with small imbalance fluctuations (number-squeezed state). The amount of the number-squeezing is quantified by the number-squeezing factor defined by:

$$\xi_N = \sqrt{N}\Delta n, \quad (1.159)$$

with N the total atom number and Δn the fluctuations of the normalized imbalance. A number-squeezed state is characterized by $\xi_N < 1$ and the number-squeezing is as high as the associated squeezing factor is small. In the previous section, we explained that a low number squeezing factor is beneficial as it limits phase diffusion rate and ensures a coherent evolution over longer times.

Figure. (1.10) shows that the quantum ground state of a double-well in the Josephson regime is always number-squeezed and that its quantum fluctuations decrease with the tunnel coupling strength (equivalently when increasing Λ). Therefore, small number-squeezing factors can be reached by various manipulation of the barrier height. We focus in this section on ramps leading to an adiabatic generation of number-squeezing [103–107].

To realize a ramp of tunnel coupling, we introduce the following dependence of J with a control parameter I :

$$J(I) = h \times 87 \exp \left[- \left(\frac{I - 0.42}{0.1} \right)^{5/2} \right]. \quad (1.160)$$

This expression will be justified in Sec. 2.3.2.6, in which we detail the experimental control of the trap geometry. In this section, we consider I as a generic parameter taking values between 0 and 1 to modify the transverse geometry of the trapping potential. For $I = 0$, the trap geometry is a harmonic single well. When I increases up to 0.42, the trap is decompressed until it reaches a quartic single trap. $I = 0.42$ is the lowest value of I defining two trap minima and defining a double-well. This explains the offset of 0.42 in Eq. (1.160). From 0.42 on, the barrier height and inter-well spacing increase with I . The ramps of tunnel coupling that we consider in the simulations always consist in a continuous modification of I bounded by $0.42 < I < 1$.

The protocol we investigate relies on a linear ramp of the parameter I and is therefore referred to as linear splitting, even though it is not linear for J . This protocol was proposed by [102, 103] as a way to adiabatically follow the ground state of the potential and generate strongly number-squeezed states. The simplified picture is used in [107] to explain their measured number squeezing. Using an experimental protocol identical to our experimental sequence, [107] explains that the system follows the quantum ground state of Fig. 1.10 until the adiabaticity is broken after which the fluctuations Δn are frozen and $\Delta\phi$ increases due to phase diffusion.

Here we investigate the adiabatic squeezing generation using the MC-like model and improve this simplified picture.

Adiabaticity criteria We consider a point i of initial coordinates $(\phi_i(0), n_i(0))$ and energy α_i . Its evolution is under a change of J if it remains on the trajectory of constant α_i . Due to the change of J , this trajectory is no longer a closed ellipse. However, for a linear ramp, the adiabaticity can hardly be maintained all over the ramp. Indeed, while the

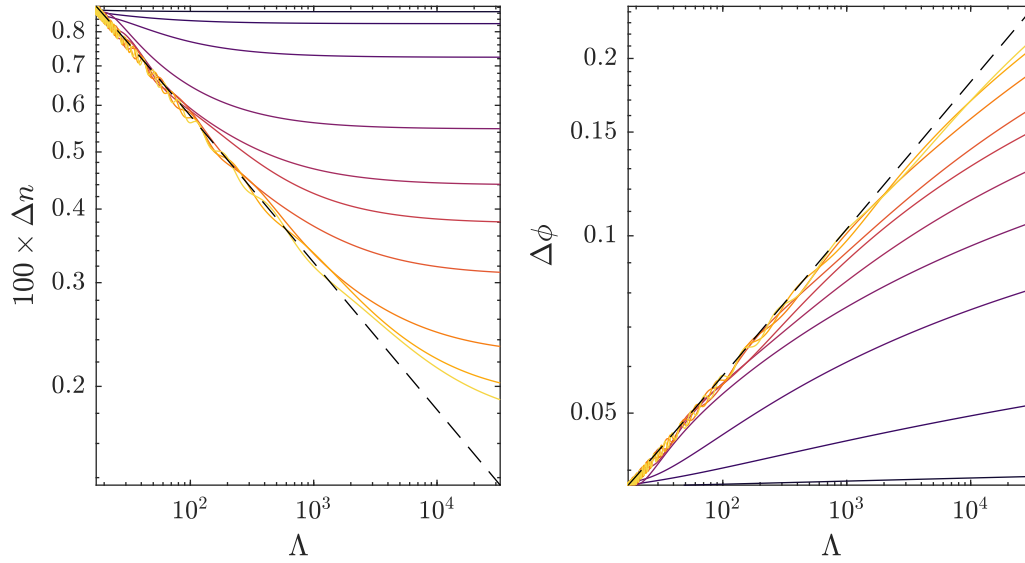


Figure 1.22: Evolution of the phase and imbalance fluctuations of an initial ground state when ramping down the tunnel coupling at various rates. The initial state is obtained by sampling the Gaussian distributions of the ground state of $J/h = 87$ Hz, $U/h = 1$ Hz, $N = 3000$ atoms with 10^4 points. The points are propagated numerically in time while decreasing the tunnel coupling to $J \approx 0$ over different durations. The dashed black line indicates the ground state fluctuations when changing Λ through J . The color curves (black to yellow) correspond to a splitting in the times $T_{\text{tot}} = [1, 4, 10, 20, 40, 60, 100, 200, 300, 400]$ ms. During the splitting, the imbalance fluctuations decrease while the corresponding phase fluctuations increase. The fluctuations of the state smoothly deviate from the ground state predictions. At longer times the imbalance fluctuations are frozen and the phase fluctuations linearly increase under the effect of phase diffusion. This corresponds to the time where the loose adiabaticity criterion is broken. This point is reached for higher Λ as the splitting duration increases. Therefore, the longer the splitting duration the lower the imbalance fluctuations and improves the number-squeezing.

rate with which I increases is constant, the characteristic tunneling time defined by the plasma frequency increases for smaller J . It means that as the tunneling gets weaker, the aptitude of the system to remain on the trajectory of constant α degrades. We can therefore define the general adiabaticity criterion:

$$|\dot{J}(t)| \ll \omega_p(t)J(t), \quad (1.161)$$

which compares the rate at which the trap is modified to the timescale of the tunneling dynamics. When α exceeds 1, the atom undergoes a transition to the MQST and the behavior changes radically, undergoing phase diffusion. For this reason, we define a loose adiabaticity criterion as:

$$\alpha_i < 1. \quad (1.162)$$

Ground state Experimentally, the splitting is performed between $I = 0$ and $I = 0.65$ over a duration T_{tot} while the simulation can only be performed starting at $I = 0.42$. As the splitting rate is linear, the duration of the simulation is adjusted to last

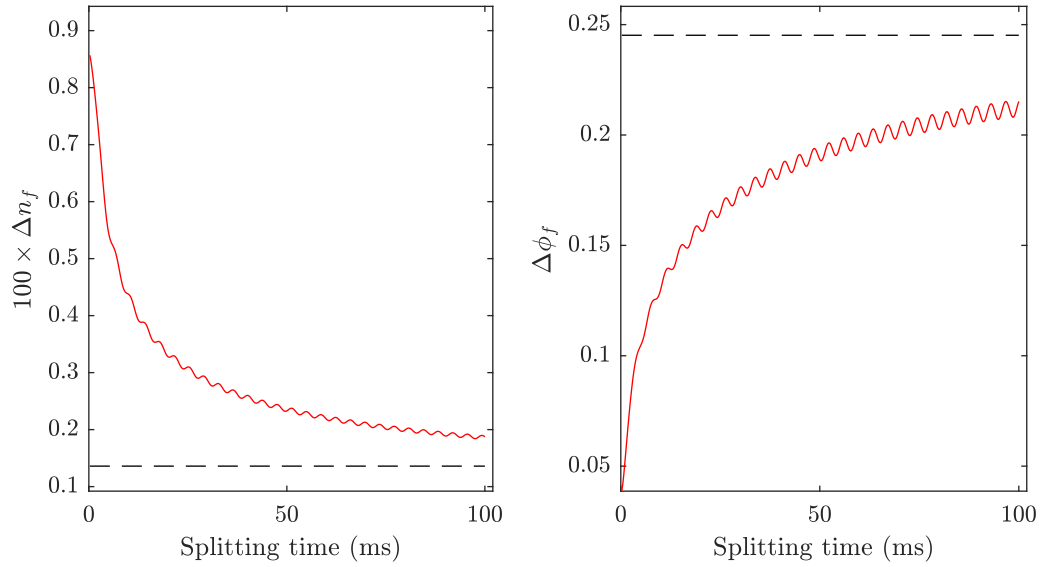


Figure 1.23: Final values of the imbalance and phase fluctuations for various splitting times. The initial state is obtained by sampling Gaussian distributions of the ground state of $J/h = 87$ Hz, $U/h = 1$ Hz, $N = 3000$ atoms with 10^4 points. The points are propagated in time using the TMBH where the tunnel coupling is decreases to ≈ 0 in various durations $T_{\text{tot}} = [1 : 100]$ ms. The final imbalance fluctuations decrease when the splitting is performed in a longer time, as the adiabaticity is maintained until smaller values of the tunnel coupling. However, decreasing the fluctuations requires increasingly long splitting time and the ground state of the final trap (dashed lines) is not reached even with a 100 ms splitting. The final fluctuations exhibit small amplitude oscillations that we attribute to an initial small discrepancy between the classical distribution of points and the Gaussian ground state.

$t = T_{\text{tot}}(1 - 0.42/0.65)$. For comparison with experimental conditions, we tend to discuss the splitting according to the total splitting time T_{tot} .

We consider the splitting of a condensate initially in the ground state of $I = 0.42$, for which $J/h = 87$ Hz and compute the ground state fluctuations of N atoms for a given value of U/h using Eqs. (1.148, 1.149)

As an example, we consider the ground state fluctuations $\Delta \phi_{\text{GS}}, \Delta n_{\text{GS}}$ of $N = 3000$ atoms and $U/h = 1$ Hz such that $\Lambda = 17$. Figure 1.22 displays the evolution of the fluctuations $\Delta n(t)$ and $\Delta \phi(t)$ as a function of Λ for 10 ramp durations $T_{\text{tot}} = [1, 4, 10, 20, 40, 60, 100, 200, 300, 400]$ ms. The ground state predictions from Eqs. (1.148, 1.149) are displayed as a black dashed line. When decreasing the tunnel coupling (increasing Λ), the system follows the ground state in the first stage of the dynamics: the spread of the imbalance distribution decreases while the phase distribution gets broadened. However, contrary to [107], the adiabaticity is not broken suddenly but the fluctuations of the system smoothly differ from the ground state predictions. When increasing the ramp duration, the final imbalance fluctuations are smaller (the phase fluctuations accordingly larger). This means that the adiabaticity is broken for a smaller tunnel coupling, resulting in a better number squeezing.

However, we notice that very long splitting times do not allow to improve the final squeezing significantly. This appears clearly in Fig. 1.23, which displays the final value of the fluctuations as a function of the splitting time.

In addition, $\Delta n, \Delta\phi$ present oscillations of small amplitude that we can relate to the oscillations in Fig. 1.22. Indeed, the fluctuations present an oscillation of small amplitude over time resembling squeezing oscillations. This is mainly due to the fact that the simulated ground state does not perfectly reproduce the ground state. As the distribution of classical points is obtained by sampling the ground state Gaussian distribution, a small discrepancy can occur, resulting in squeezing oscillations of small amplitude. This feature is suppressed when increasing significantly the number of propagated points. The oscillating feature is nonetheless important because, experimentally, we are likely to work with a state that has larger fluctuations than the ground state.

Realistic initial state Experimentally, the fluctuations of the initial state exceed those of the quantum ground state, in particular for the phase. Therefore, the splitting of a realistic initial state is likely to present a more complex dynamics as the tunnel coupling decreases, combining the effects described in Sec. 1.3.4.3, 1.3.4.4, 1.3.4.5. We illustrate this for a initial state $\Delta n_0 = \Delta n_{\text{GS}}$ and $\Delta\phi_0 = 5\Delta\phi_{\text{GS}}$. We recall that Δn_{GS} and $\Delta\phi_{\text{GS}}$ refer to the ground state fluctuations in the most coupled double-well that we can define ($I = 0.42, J/h = 87\text{ Hz}$) where we chose $N = 3000$ atoms and $U/h = 1\text{ Hz}$ as simulating parameters.

Figure 1.24 displays the evolution of $\Delta n(t)$ and $\Delta\phi(t)$ when the tunnel coupling is decreased from $J/h = 87\text{ Hz}$ to $J/h \approx 0\text{ Hz}$ in a splitting time $T_{\text{tot}} = 0\text{ ms}$ to $T_{\text{tot}} = 100\text{ ms}$. One row in Fig. 1.24 corresponds to one splitting ramp in a given duration. The duration increases from the upper to the lower rows. The fastest splitting ramp does not allow much evolution of the fluctuations. However, as the duration increases, oscillating features appear. The oscillation frequency seems to increase for longer splitting durations as more oscillations emerge. It is due to the rescaling of the times to the splitting duration.

The most right column represents the fluctuations at the end of the splitting for the various durations considered. This is displayed in Fig. 1.25 and shows that the final fluctuations oscillate with the splitting duration. Therefore, contrary to the ground state case, where the imbalance fluctuations only decrease for slower splitting rate, the state having larger phase fluctuations does not necessarily benefit from a longer splitting. The highest number squeezing is obtained by choosing a splitting duration targeting a minimum of $\Delta n(t)$. The minima of the oscillations do not reach equally low values. The value of the first few minima continue to decrease, after which the value is stable. Therefore, in this case, the fastest splitting allowing the highest number squeezing is typically 20 ms.

The number squeezing does not reach values below $\Delta n = 0.005$ while the splitting of the ground state was reaching significantly lower values. For comparison, $\Delta n = 0.003$ for a splitting in 20 ms. However, the initial fluctuations were chosen much larger than the ground state ones $\Delta n_0 \Delta\phi_0 = 5\Delta n_{\text{GS}} \Delta\phi_{\text{GS}}$. The squeezing oscillations implies that the splitting duration affects strongly the final number squeezing. For a splitting duration below 20 ms, changing the splitting duration by 1 ms increases the final Δn by up to a factor 7 in the example considered. Therefore, it is important to simulate the experimental initial state rather than assuming the ground state as the ramp duration must be adjusted to the experimentally feasible initial state.

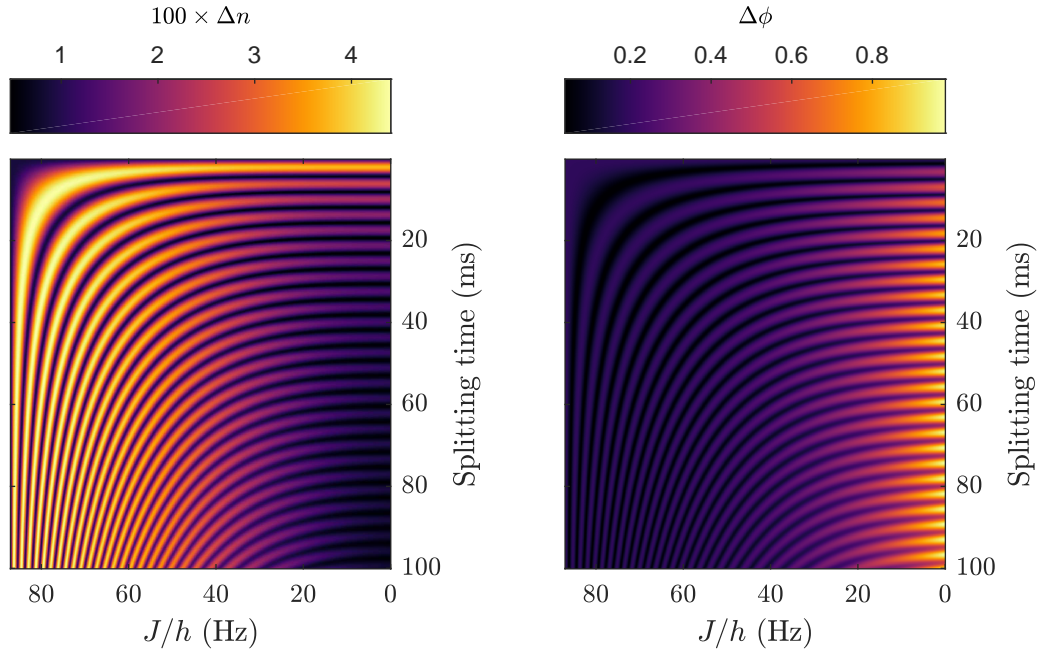


Figure 1.24: Evolution of the phase and imbalance fluctuations of an initial state obeying $\Delta n_0 \Delta \phi_0 = 5 \Delta n_{\text{GS}} \Delta \phi_{\text{GS}}$ when decreasing the tunnel coupling over different durations. The initial state is obtained using 10^4 points sampling Gaussian distributions of width $\Delta n_0 = \Delta n_{\text{GS}}$ and $\Delta \phi_0 = 5 \Delta \phi_{\text{GS}}$, with Δn_{GS} and $\Delta \phi_{\text{GS}}$ the ground state fluctuations of $J/h = 87$ Hz), $N = 3000$ atoms and $U/h = 1$ Hz.

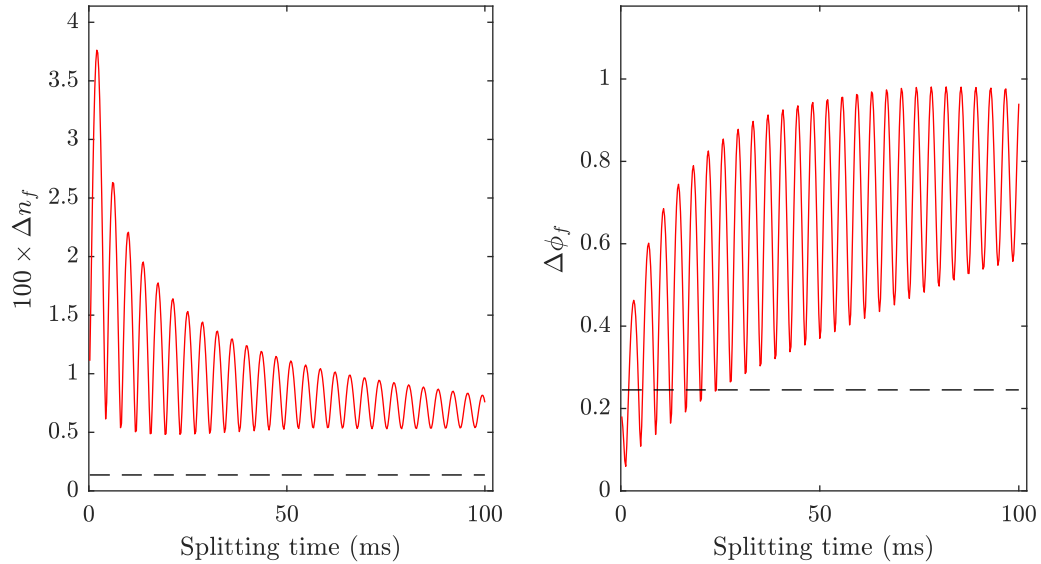


Figure 1.25: Final values of the imbalance and phase fluctuations for the parameters of Fig. 1.24. The fluctuations show an oscillation of large amplitude such that the best number squeezing is not necessarily obtained by increasing the splitting duration. The dashed black line corresponds to the fluctuations of the ground state of the final trap.

1.3.4.7 Improved squeezing generation protocols

The linear ramp is the simplest way to prepare a number-squeezed state but it is far from optimal. The main advantage of this protocol is that the long ramp durations and slow trap deformation strongly limit both collective and longitudinal excitations. However, the number-squeezing is limited by the ground state fluctuations and the long ramp duration is the main limitation of this method. While the previous paragraph does not show any restrictions on the ramp duration, additional effects play a role when the timescale exceeds ≈ 10 ms, the main one being the relaxation which is the focus of this thesis.

Several protocols have been proposed as a shortcut to adiabaticity. They include schemes such as the parametric amplification of the number squeezing based on the modulation of the tunnel barrier height [108], ramps determined by optimal control [109]. Other schemes rely on the fluctuations dynamics around the unstable fixed point [110] and use a twist-and-turn scheme [111]. They predict or measure a stronger number squeezing reached in a shorter time.

To understand why these protocols can yield better number squeezing, one must understand the limitation of the linear splitting and the reason why the adiabaticity is broken. As explained by the loose adiabaticity criterion established in Sec. 1.3.4.6, the adiabaticity is broken when a significant part of the fluctuations undergoes a transition to the MQST regime, as the system is no longer able to adjust to the change of J to remain in the oscillating regime. In a linear splitting from strong coupling to negligible coupling, breaking the adiabaticity is almost unavoidable. However, we can imagine other ramp shapes which prevents the transition to the MQST. One of them is the "two-step" splitting that we explain in the framework of the MC-like model.

Two-step splitting The simplest protocol susceptible to improve the number squeezing is a two-step splitting, which consists in several linear ramps of I adjusted to use the system dynamics to optimize the number squeezing. We illustrate this on the ground state of the most coupled trap, even though we know that this state would be challenging to realize experimentally. It illustrates very well the principle of the two-step splitting in the framework of the MC-like model.

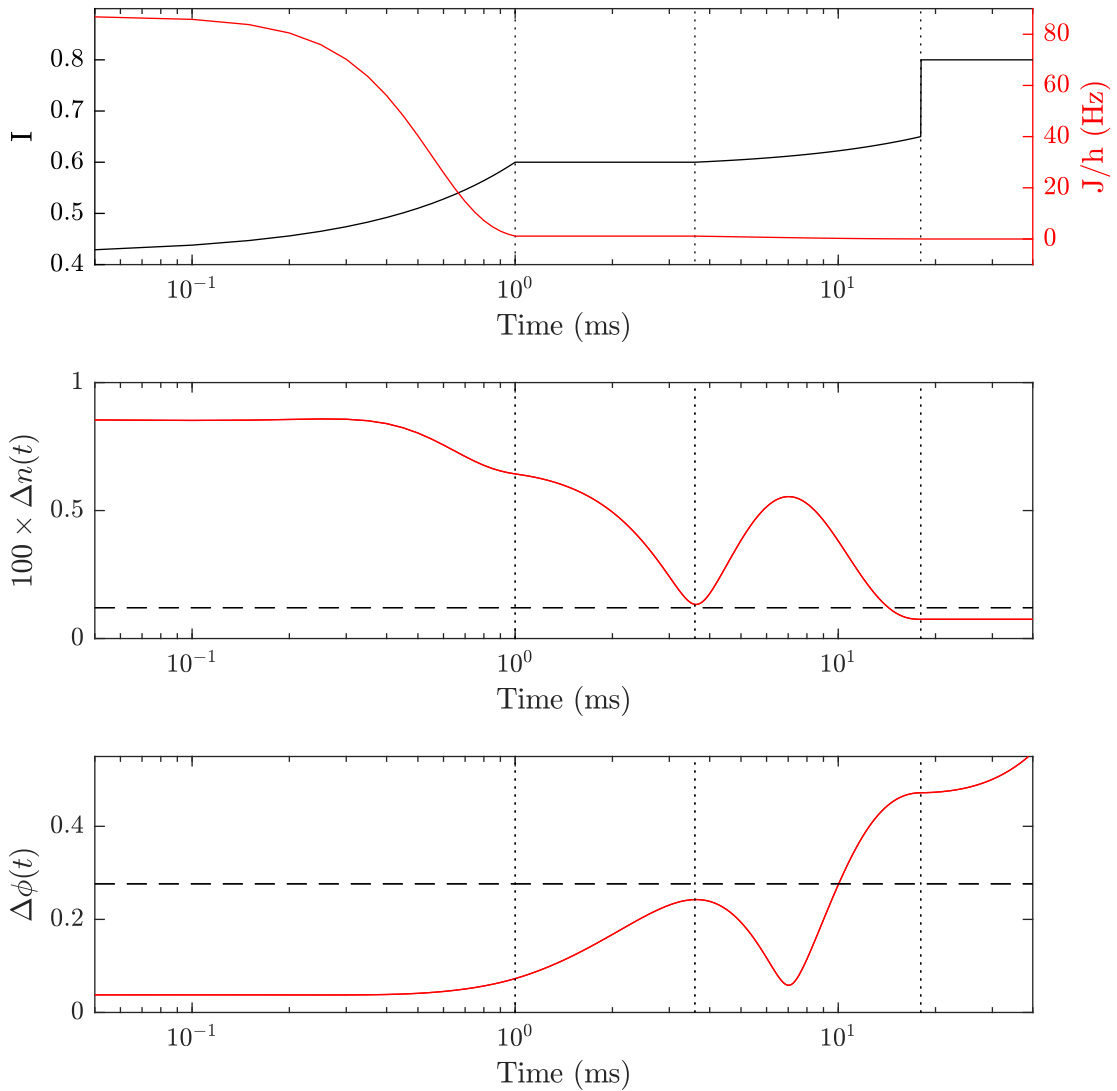


Figure 1.26: Evolution of the fluctuations during a two-step splitting. Top panel: Evolution of the parameter I and J over the splitting sequence in semi-log scale. A first ramp is performed until $T_1 = 1$ ms (first vertical dotted line) between $I = 0.42$ and $I = 0.6$. During this first ramp, the imbalance fluctuations (middle panel) and phase fluctuations (lower panel) do not evolve significantly. The coupling is maintained to let Δn undergoes half an oscillation and reach its minimal value at $T_2 = 3.6$ ms (second vertical dotted line). After this, the coupling is decreased more slowly to (I is increased to 0.65). After $T_3 = 18$ ms (third vertical dotted line), Δn is minimal again. To prevent further evolution of the fluctuations we break the adiabaticity at this instant and decrease the coupling to $J/h \approx 0$ Hz ($I = 0.8$).

- The initial fluctuations are $\Delta n_{\text{GS}} = 0.009$ and $\Delta \phi_{\text{GS}} = 0.038$ the ground state fluctuations in the most coupled double-well that we can define ($I = 0.42$, $J/h = 87$ Hz). As previously, we consider $N = 3000$ atoms and $U/h = 1$ Hz and perform the simulation with 10^4 points as in Sec. 1.3.4.6 to allow an unbiased comparison.
- A first ramp is performed very quickly to a trap of finite and lower coupling. The coupling is high enough such that $\Delta n_0 < n_c$ the imbalance threshold to the MQST given by Eq. (1.103). This ensures that the distribution remains in the oscillating regime. The coupling is on the other side as low as possible to correspond to the highest possible number squeezing. Ideally this coupling corresponds to $\Delta n_0 = n_c$ but due to outliers in the distributions, we consider a coupling slightly larger than this. We consider a fast splitting in $T1 = 1$ ms to $I = 0.6$. This corresponds to $J/h = 1.13$ Hz and $n_c = 0.055$ which is larger than Δn_{GS} .
- The prepared ground state does not corresponds to the ground state of the trap reached after this first ramp. As a consequence, the fluctuations start to evolve toward squeezing oscillations. When the first minimum of the imbalance fluctuations is reached, we perform a second slower ramp to a trap of negligible coupling. In this example, the minimum is reached at the time $T2 = 3.6$ ms. From this point, a splitting to $I = 0.65$ is performed such that this value is reached at the time $T3 = 18$ ms. Δn reaches the ground state fluctuations which is the best squeezing reachable by the linear splitting. In this case, the system reach the best number-squeezing achievable by linear splitting in a much shorter duration (3.6 ms). The dynamics continues to occur during this second ramp and another minimum can be reached after 18 ms. In this case, the number squeezing is lower that the ground state fluctuations of the trap $I = 0.65$ and therefore outperforms the results of the linear splitting scheme.
- We perform an additional ramp which is not in the "two-step" proposal. The fluctuations after 18 ms would continue to evolve. To prevent this, we brutally increase I to 0.8 to undergo the transition to the MQST and freeze the imbalance fluctuations and break the adiabaticity brutally when the number squeezing is the best.

Parametric amplification The idea of the two step splitting can be generalized. It consists in manipulating the coupling according to the squeezing oscillations. In particular, the coupling could be modulated at the same frequency as the fluctuations oscillations. The idea is to bring the individual classical points closer to the equilibrium position of the final trap until the fluctuations resemble the ground state. This avoids a drawback of the previous method, namely that, while the imbalance fluctuations are strongly reduced, the phase fluctuations are much larger than those of the ground state, such that the statistical phase coherence is strongly decreased.

Limitations Fast protocols have their own drawbacks. One of them is the generation of collective excitations which modify the number squeezing. This will be presented in the outlook chapter 5 as a preliminary result. The second issue is the impossibility to include

a relaxation in any of the current proposals. In chapter 5, we discuss the potential impact of the relaxation on the description of the splitting of a condensate.

1.4 Conclusion of the theoretical chapter

In this chapter, we have treated separately the longitudinal and transverse dynamics of elongated Bose gases. The longitudinal dynamics has been treated in the GPE formalism. The transverse dynamics of a Bosonic Josephson junction has been treated in the two-mode approximation where the two-mode Bose-Hubbard model provides an extensive description of the dynamics. We have seen that the BJJ can undergo various dynamics depending on the ratio of the atom-atom interaction and tunnel coupling and on the initial state, characterized by the phase difference and atomic imbalance. In particular, we have distinguished in the Josephson regime an oscillating dynamics and a self-trapped dynamics. We established the analytical solutions based on the analogy of a BJJ with a mechanical pendulum and established the range of validity of the rigid pendulum approximation.

A generalization of the TMBH model is also presented to include fluctuations of the phase and imbalance independently of their origin. Using this approach, we could describe additional features of the dynamics, include squeezing oscillations and interaction-induced phase diffusion. The last section was investigating the splitting of a Bose gas in two halves where the splitting is performed by decreasing the tunnel coupling in various ways in order to minimize the imbalance fluctuations.

2 Experimental setup and measurement of the observables

This chapter presents the experimental tools and procedures to access the physics of two coupled 1D condensates. It begins with an overview of the experimental sequence we follow to generate, manipulate, and image Bose-Einstein condensates. It continues with a description of the different building blocks of the experiment. The experimental highlights of this setup are the atom chip and the imaging systems. Consequently, the third section focuses on magnetic trapping with an atom chip, involving static and oscillating fields, and details both the physical concepts and the experimental implementation. Finally, we present the imaging systems used to probe the system and the analysis of the images giving access two observables of the system: phase difference and atomic imbalance.

2.1 Overview of the experimental sequence

The experiment takes place in a science chamber maintained under ultrahigh vacuum and equipped with windows for optical access.

Loading of the magneto-optical trap The experimental cycle starts with the desorption of a vapor of ^{87}Rb and ^{85}Rb atoms in the chamber during 17 s. The ^{87}Rb atoms are trapped and pre-cooled into a magneto-optical trap (MOT) situated ≈ 2 cm below the atom chip. The MOT involves four laser beams tuned close to the cycling transition $F = 2 \leftrightarrow F' = 3$ of the D2 line of the atoms. One direction of space is obstructed by the atom chip and prevents the usual six laser beams configuration. Therefore, we make use of a reflection MOT where two laser beams of polarization σ^\pm are sent with an angle of 45° on the chip surface. The chip reflects the beam and changes its polarization to σ^\mp such that the beams and their reflection complete the three dimensional trapping. The spatial trapping also requires magnetic fields. The usual coil-based quadrupole field is substituted by the combination of an external homogeneous field produced by coils located outside the science chamber and of a field obtained by sending a current through a copper wire underneath the chip surface. A second laser beam is superimposed to the MOT beams. It allows to repump the atoms which decayed to the $F = 1$ level into the cooling transition.

The residual background atoms are pumped away during an additional 1.5 s to avoid collisions with the trapped atoms and the power in the MOT beams is reduced to suppress light-induced collisions.

MOT displacement and optical cooling The MOT is then compressed and moved closer to the chip. The laser beams are detuned to perform a sub-Doppler polarization

gradient cooling (optical molasses) and the external fields are used to cancel magnetic fields of the environment. Over time, the molasses inevitably increase the size of the cloud due to the absence of magnetic fields. In order to transfer the cloud to a magnetic trap afterward, the duration of the molasses phase is limited to 4 ms after which the size of the cloud exceeds the area trappable by the magnetic trap, leading to significant losses.

Optical pumping and transfer into the Z-trap After optical cooling, the atoms are in the $F = 2$ Zeeman manifold with a random distribution over the Zeeman states. In order to trap them magnetically, they must be transferred into the state $|F = 1, m_F = -1\rangle$ by two successive transitions. We first realize the transition $F = 2 \leftrightarrow F' = 2$ using a depumping laser beam resonant with this transition. To address all magnetic orientations, we define a quantization axis along y and send a circularly polarized laser beam along x . Part of the atoms decay into $F = 1$ where a second beam tuned on $F = 1 \leftrightarrow F' = 1$ with a σ^- polarization along y pumps the atoms in the state $|F = 1, m_F = -1\rangle$. The rest of the atoms decay into $F = 2$ where they are pumped again into $F' = 2$ with the first beam until they eventually decay into $F = 1$ (laser scheme displayed in Fig. 2.3).

The atoms are then transferred into a magnetic trap referred to as Z-trap because it is generated by a copper wire with a Z-shape situated underneath the chip and by external fields. The Z-trap is then compressed and a first stage of evaporative cooling is performed.

Chip trap and coherent manipulation The atoms are then transferred into a magnetic trap created by the chip. An additional stage of evaporative cooling is performed during 3 s. The magnetic fields are then modified to obtain an elongated single-well trap where a last stage of evaporation is performed to obtain a 1D-quasi BEC. At this stage, the properties of the 1D-quasi BEC can be coherently manipulated using the atom chip. The timescale of this coherent manipulation is in the millisecond range.

Imaging The BEC is finally released by switch-off of the trapping fields and imaged after a time-of-flight expansion. We make use of either an absorption imaging system after short time-of-flight or a fluorescence imaging system after long time-of-flight to probe the system along different spatial directions.

An experimental cycle takes 36 s (dominated by the duration of the MOT loading) and ends by a destructive measurement after time-of-flight.

Previous work and detailed descriptions Extensive descriptions of the experimental sequence and associated hardware can be found in previous works performed on this experimental apparatus. The early work is reported in [112–117] and the important updates realized after 2002 are detailed in [118, 119]. More specifically, information about the chip manufacturing and characterization are found in [118, 120], the radio-frequency dressing is explained in great details in [47–49, 121, 122], the imaging systems have been reported in [27, 123, 124] and the experimental control is detailed in [125, 126].

2.2 Experimental apparatus

2.2.1 Vacuum chamber and Rubidium dispensers

The experiment takes place in a single stainless steel ultrahigh vacuum chamber.

The upper part of the chamber contains the instruments required to maintain the ultrahigh vacuum. It consists in an ion pump (Varian StarCell, 500 L/s), a passive non-evaporative getter pump (SAES Getters) and a titanium sublimation pump (TSP). The first two are permanently used while the filaments of the TSP are heated every few weeks. On the top is a large flange which was used to insert the chip mounting such that the chip reaches the lower part of the chamber, called science chamber.

The science chamber is equipped with a large window on its bottom part, providing optical access for the MOT beams oriented at 45° and for the fluorescence imaging. In the horizontal plane, the science chamber has an octagonal shape. Seven of its faces are equipped with anti-reflection coated view ports with at least 1 inch of clear aperture diameter to allow optical access for the two MOT beams, optical pumping beams and imaging beams. The eighth face is used to mount the Rubidium dispensers.

For each experimental cycles, a current is pulsed through three dispensers connected in parallel to desorb a vapor of Rubidium at few 100°C . The duration of the pulse and the value of the current play a crucial role for the rest of the sequence. The loading of the MOT requires a Rubidium background pressure of about 10^{-9} mbar. However, a pressure above 10^{-11} mbar leads to collisions with the background gas at room temperature resulting in additional losses during the evaporative cooling stage. The balance between these constrains is reached by pulsing the current over the first 17 s of the sequence and using two consecutive stages, at 29 A and 22.7 A respectively. The duration of the stage at high and low current values has been modified over this thesis to account for the depletion of Rubidium in the dispensers. Additionally, the untrapped atoms are pumped for 1.5 s after switch-off of the dispenser current before continuing the cooling sequence to decrease the background pressure.

2.2.2 Copper structure and atom chip

The inhomogeneous magnetic fields are generated inside the science chamber either by a copper structure consisting of macroscopic copper wires or by the atom chip. These elements share a water-cooled mounting which was introduced in the vacuum chamber through the top flange to reach the science chamber as displayed in the schematic of Fig. 2.1. This configuration results in a trapping of the atoms below the chip surface and allows a time-of-flight imaging.

To bring the current to the copper structure, high DC current (up to 60 A) is sent through ten feedthroughs of the flange and along copper rods to the macroscopic wires embedded in a ceramic mounting block. The mounting block provides good heat conductivity and electrical insulation.

The DC chip wires are driven by custom-designed current sources supplied by car batteries to avoid noise from the power network. They are connected to a 36-pin connector inside the chamber. From there, thin Kapton-insulated wires lead the current ($I \leq 2$ A)

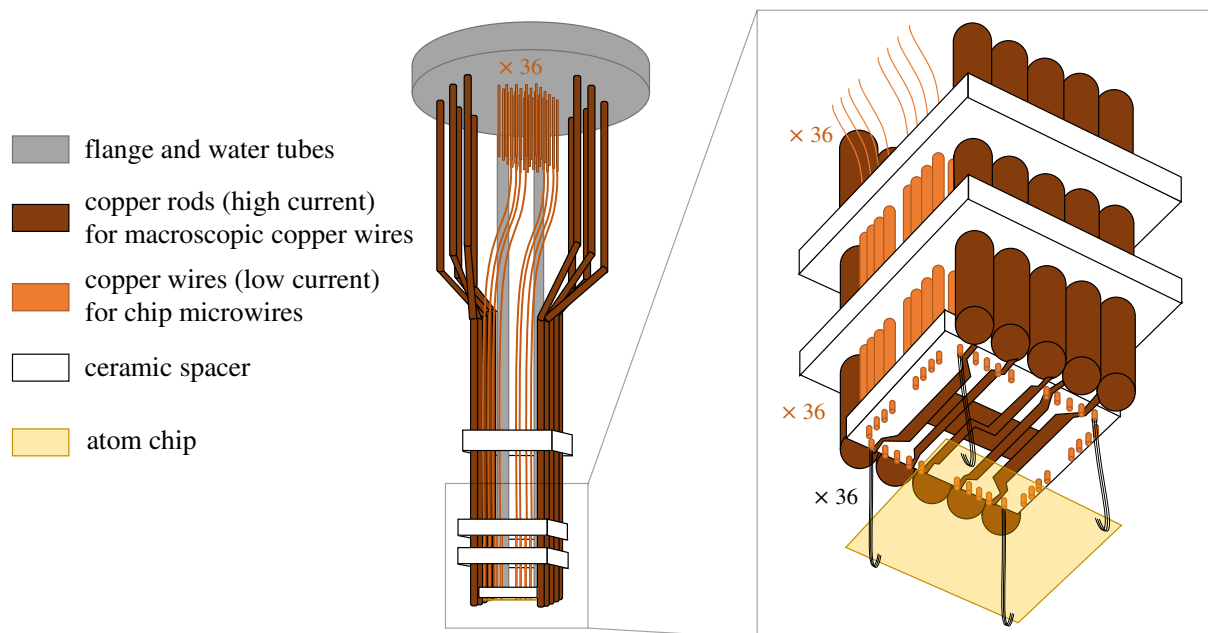


Figure 2.1: Schematic drawing of the chip mounting and zoom on the copper structure and atom chip. The high current is sent along tens copper rods (brown) to supply macroscopic copper wires (brown structure in zoom view) embedded in an insulating ceramic block. Lower currents are sent along thin Kapton-insulated wires (orange) to the same ceramic block as for the copper structure. From there the wires are bonded to the chip surface (yellow) situated 1 mm below the copper structure (drawing not to scale). The structure is water cooled through two tubes (gray).

to the lowest part of the mounting. Each wire is attached to a chip wire connection pin, which is in turn attached to the chip by ultrasonic bonding of aluminum wires. The bonding process does not damage the chip surface and the aluminum bonds (about 20 per pads) can carry high current density. The chip is glued on the ceramic block and is located about 1 mm below the copper structure (schematic not to scale).

Copper structure The copper structure refers to a set of macroscopic wires displayed in the left panel of Fig. 2.2 with a color coding. The largest wire has an H-shape and is electrically connected as a U-wire (light blue line). In association with an external homogeneous magnetic field, the wire creates a quadrupole field needed for the MOT approximately 1 cm below the chip surface. It is also used as a radio-frequency antenna for the evaporative cooling.

In the center of the copper structure, a Z-wire (light green line) is used in combination with external fields to create the Ioffe-Pritchard magnetic trap few millimeters below the chip surface.

The I-wires (red lines) are located on each side of the Z-wire and any of them can be used to create a magnetic gradient. We make use of this feature to perform a Stern-Gerlach separation of the magnetic Zeeman states during the time-of-flight measurement.

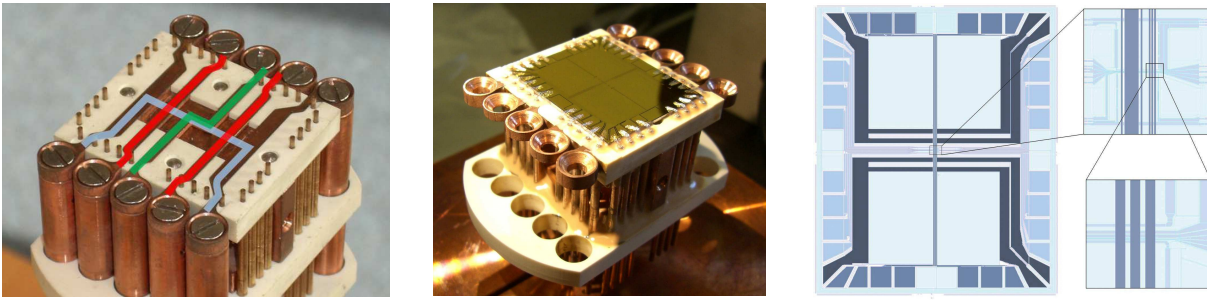


Figure 2.2: **Left:** The copper macroscopic wires are embedded in an insulating ceramic mount and are used to produce inhomogeneous magnetic fields. They are connected as a U-wire (blue), a Z-wire (green) and I-wires (red). **Middle:** The atom chip is glued on the ceramic block and bonded to the pins by aluminum wires. **Right:** Taken from [120]. Layout of the double layer atom chip. The general view (25×30 mm) shows the connection pads arranged along the edges of the chip. The longitudinal confinement is due to four $500 \mu\text{m}$ wide wires (dark blue). Two additional zooms are displayed over $600 \times 600 \mu\text{m}$ and over $100 \times 100 \mu\text{m}$.

Atom chip The atom chip consists of a large structure able to carry sizable currents of a few amps to create deep traps as well as small structure carrying high current densities for tight confinement. In addition, it allows the generation of radio-frequency fields shaping the magnetic trap into different configurations.

To fulfill these constraints, the atom chip consists of a $700 \mu\text{m}$ thick silicon substrate ensuring a good thermal conductivity and low thickness variation, covered by a layer of 100 nm thickness of silicon oxide for electric insulation. The current is carried by gold wires created by a combination of traditional optical ultraviolet lithography and electron beam lithography. Gold allows less defects on the wire edges and less reactivity with other atoms both during fabrication and in the vacuum chamber. The double layer structure allows crossed wire configurations, which increases the versatility of the trapping potential geometries. The two layers are separated by a layer of polyimide allowing electric insulation. Its thickness is decreased to 500 nm to allow sufficient heat transfer from the wires to the water-cooled substrate. The use of gold for the chip also allows to use its surface as a mirror for the reflection MOT as shown in the middle panel of Fig. 2.2.

The chip layout is represented in the right panel of Fig. 2.2 and allows to design many trapping potentials. The current work targets an elongated trap geometry, which makes use of a trapping wire of width $80 \mu\text{m}$ responsible for the strong confinement (referred to as primary trapping wire), combined with two wires of $500 \mu\text{m}$ positioned perpendicularly to the $80 \mu\text{m}$ wire and imposing a weak confinement along the direction of elongation (referred to as secondary trapping wires). Two wires of $10 \mu\text{m}$ width are located on each side of the $80 \mu\text{m}$ wire. They are used to apply radio-frequency fields and deform the trapping potential into an elongated double-well potential by radio-frequency dressing. Perpendicular to the primary trapping wire, a $10 \mu\text{m}$ -width wire enables a local deformation of the trap along the direction of elongation referred to as "dimple" trap. This feature is used during the trap calibration to measure the longitudinal trap frequency.

2.2.3 External coils

During the sequence, homogeneous offset fields are required to complement the inhomogeneous fields created by the chip and copper structure. They are created by six pairs of coils located outside the chamber. Along each of the three directions of space, the science chamber is situated between two pairs of coils operated close to Helmholtz configuration to generate a homogeneous magnetic field close to the center of the chamber. One pair of coils is made of thick copper wires to create magnetic fields up to tens of Gauss and the second one is made of thinner wires to provide fields of few Gauss. Using two sets of coils allows to switch the fields magnitude and direction faster than with a single set, where the timescale is limited by the high inductive load of the current sources. It also enables to use of unipolar current supplies¹ and to match the voltage and current range to the requirement of each coil. The coils are switched off in a short time (below 0.1 ms) by using field-effect transistor (FET) switches which stand currents up to 60 A and induced voltages up to 400 V.

2.2.4 Lasers system and optics

The experiment requires two laser systems, the wavelength of which is approximately 780.2 nm to address the D2 line, i.e. the transition of the ^{87}Rb electronic ground state ($5^2S_{1/2}$) and the excited state ($5^2P_{3/2}$) as represented in Fig. 2.3. We note F the hyperfine state of the ground state and F' the one of the excited state. The laser frequencies differ by $\nu \approx 6.83$ GHz corresponding to the hyperfine level spacing between $F = 1$ and $F = 2$ [68].

Both lasers are external cavity diode lasers (ECDLs) and are independently locked to Doppler-free saturation spectroscopies using Rubidium vapor cells. The beams are distributed between different paths using half wave-plates and polarization beam splitters and the frequency of each paths is shifted using acousto-optical modulators (AOMs) represented in the right panel Fig. 2.3. The left panel of Fig. 2.3 summarizes the transitions addressed by the two lasers after the beams are separated and independently detuned.

One of the laser systems, represented in blue in Fig. 2.3 mainly serves to drive the cooling transition. As this requires high power, it is mounted in a Master Oscillator Power Amplifier (MOPA) configuration, which combines an ECDL and an amplifier (TA)². The beam is then distributed and the power in the cooling path is increased by an external amplifier BoosTA³. The frequency is dynamically detuned during the cycle using an AOM in double-pass configuration. During the MOT stage, the AOM shifts the frequency to reach a -20 MHz detuning with respect to the $F = 2 \leftrightarrow F' = 3$ transition while for the molasses stage, the AOM leads to a detuning of -70 MHz with respect to the transition. The remaining beam is divided between the imaging beam, the frequency of which is shifted to address the cycling transition $F = 2 \leftrightarrow F' = 3$ and the optical repumping beam requires for magnetic trapping after the molasses stage. The AOMs also enable a rapid switch-off of the beams.

¹HP/Agilent 65xx series, except for the small vertical coils using the bipolar supply High-Finesse BCS-5/5

²Toptica Photonics TA100

³Toptica Photonics BoosTA

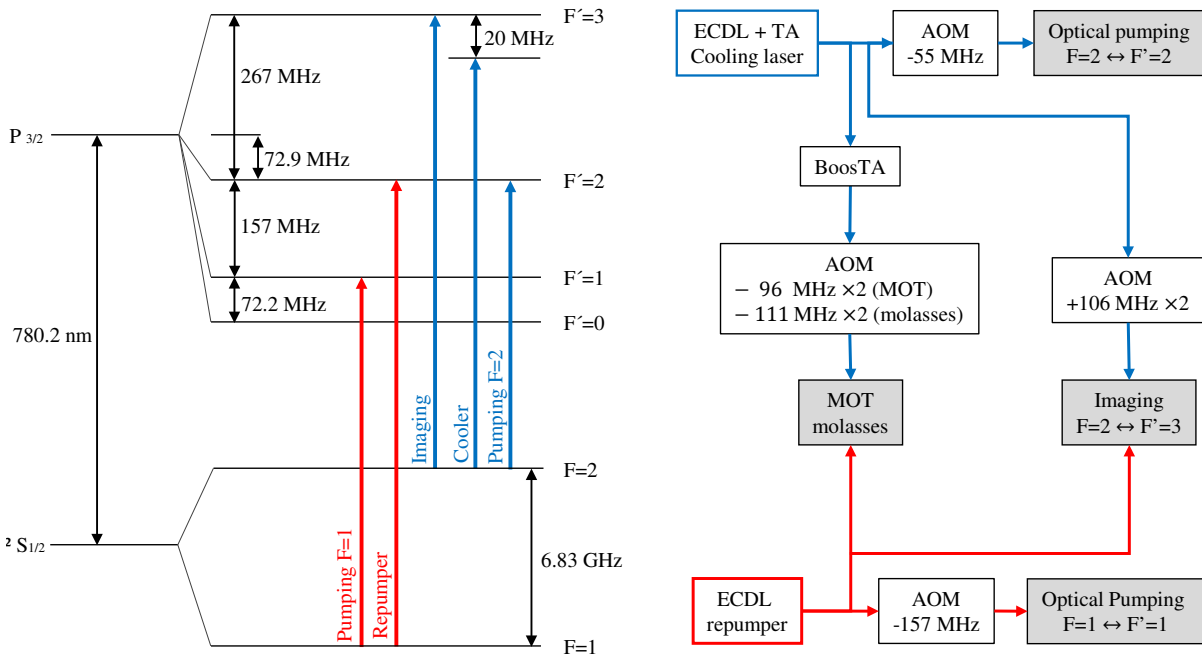


Figure 2.3: Hyperfine structure of the D2 line of Rubidium 87 (left) and simplified scheme of the laser beams distribution (right). The experiment involves two laser systems represented in blue and red. The initial beams are distributed along various paths using half wave-plates and polarizing beam splitters. The frequency of each beam is shifted using acousto-optical modulators in single or double-pass such that the light is resonant with a given optical transition.

The second laser system consists of a single ECDL⁴ locked on the $F = 1 \leftrightarrow F' = 2$ using a digital laser locking module⁵. This beam is also distributed between different paths. One path addresses the transition $F = 1 \leftrightarrow F' = 1$. The repumper beam is used during the MOT and molasses stage to pump the atoms which decayed to $F = 1$ to the cooling transition. It is also used in the imaging to bring the atoms into $F = 2 \leftrightarrow F' = 3$.

2.2.5 Radio-frequency generators

Radio-frequency (rf) fields are used for the evaporative cooling and for the rf-dressing of the atoms. The source of rf signals is a digital arbitrary waveform generator which executes a series of arbitrary waveforms after reception of a TTL trigger. During the various evaporation stages, the rf field frequency ranges from several MHz to a few hundred kHz over several seconds. To avoid exceeding the ability of the internal memory of the generator, we program a series of one-period cosine waveforms each differing by its frequency. Over a range of constant frequency, the cosine is looped to form units of constant frequency. The units are then concatenated to form a ramp of decreasing frequency without phase jump. The length of each unit is set to obtain several exponential ramps of frequencies as depicted in Fig. 2.4.

⁴Toptica Photonics DL100

⁵DigiLock 110

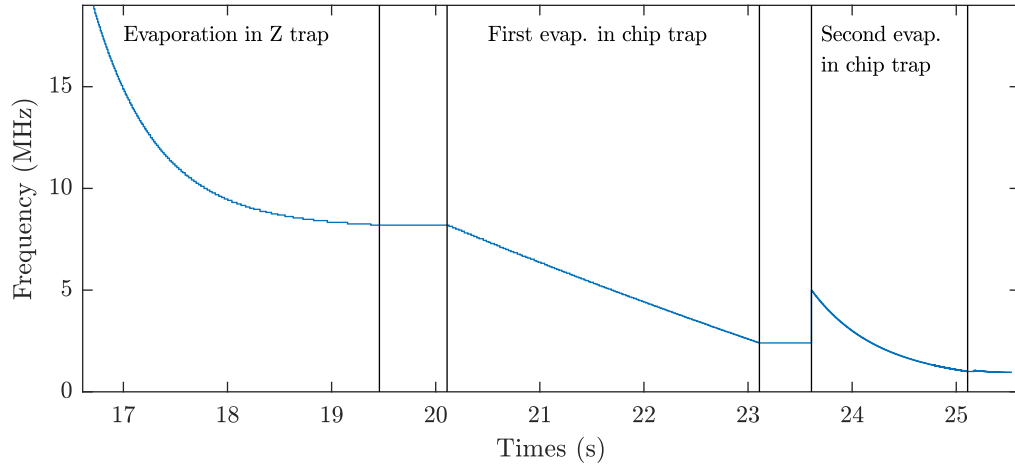


Figure 2.4: Evaporation sequence After 16.7 s, a first evaporation with coarse frequency steps is performed in the Z trap over 3 s. After compression and transfer to the chip trap, the atoms experience a first evaporation ramp in the chip over 3 s. The chip trap is then compressed and displaced closer to the chip ($\approx 60 \mu\text{m}$) to benefit from the strong magnetic gradient and the strong confinement in two directions of space. We then perform a second evaporation ramp with a very fine frequency step to approach smoothly the Larmor frequency at the center of the trap. After the second evaporation in the chip trap, a final evaporation can be programmed to perform various trap characterizations.

At the beginning of each cycle, the generator receives an instruction sequence containing the basic waveforms such as the initial and final frequency, as well as the ramp duration. The curvature of the exponential and the amplitude of the signal is set independently for each frequency ramp. The step in frequency is changed over the ramp duration to be coarse at the beginning of the evaporation and fine at the end, when approaching the trap bottom frequency ($\approx 2\pi 900 \text{ kHz}$). The U-wire presented in Sec. 2.2.2 is used as a rf antenna.

2.2.6 Computer control and acquisition

With only few exceptions, the behavior of every device during the experimental cycle is centrally controlled via a stand-alone real-time computer⁶. It consists in 32 analog voltage channels (16 bits, $\pm 10 \text{ V}$) and 64 digital TTL channels (0-5 V). The analog channels are typically used for the dispenser current, the coils power supplies, the current drivers for the chip and copper structure and for the amplitude and detuning in the AOMs. The digital outputs trigger various switches (coils, RF, chip), mechanical shutters, AOM as well as signals for the cameras and acquisition.

The behavior of each channel is coded by the user through a MatlabTM graphic interface and consists in a sequence of timings (with a minimal time step of $25 \mu\text{s}$) and values. For a digital channel, the value alternates between 0 and 1 between two successive timings and the user decides whether to start with 0 or 1.

For the analog channel, each timing is associated to a voltage value. In practice, we prefer to enter variables in physical units such as Gauss for the channel controlling

⁶Jäger ADwin Pro

magnetic fields. We therefore associate a calibration script to each channel converting the variable into a voltage. In addition, the value can be ramped linearly or remain constant over a time interval.

The timings and analogue values are either entered manually in a channel sequence or calculated aside in order to affect several channels in a similar way. This avoids inconsistencies between the channels. For example, two different coils playing a role in the MOT loading should have similar timings. More generally, as we have two imaging system relying on different protocols, the imaging system is a variable (0 for absorption, 1 for fluorescence) which affects at once every channels involved in the imaging.

Timings and analog values can also be scanned over a range that we define by its step, initial and final value. This defines a scan, which contains a number of cycles equal to the number of values taken by the scanned parameters. This feature allows to realize repeats with various parameters automatically.

Once the sequence of instructions is defined, it is transmitted to the experiment via an Ethernet connection at the beginning of each cycle and executed autonomously. The devices which are not directly controlled by the sequencer are the rf sources and the imaging cameras. Information between the sequencer and the various codes controlling these devices are exchanged between six computers and the sequencer through an internal network via shared folders and UDP connections. The parameters of the sequence and the pictures are saved automatically.

2.3 Magnetic trapping of atoms with an atom chip

2.3.1 Magnetic trapping with static fields

2.3.1.1 Magnetic interaction

The basic concepts of magnetic trapping are reported for example in [23]. A magnetic field $\vec{B}(\vec{r})$ interacts with the magnetic moments of the nucleus and of the electrons of a neutral atom. In the case of an alkali atom such as ^{87}Rb , only the outer electron contributes to the electron magnetic moment. Due to this coupling, an atom of magnetic moment $\vec{\mu}$ experiences a splitting of its fine structure into sublevels, the energy of which are shifted by the local interaction energy:

$$\Delta E(\vec{r}) = -\vec{\mu} \cdot \vec{B}. \quad (2.1)$$

For a magnetic field weak enough, i.e for an energy shift $\Delta E(\vec{r}) \ll \Delta E_{\text{HFS}}$ the hyperfine splitting energy, the magnetic moment reads $\vec{\mu} = g_F \mu_B \vec{F}$ with \vec{F} the total angular momentum of the atom, g_F the Landé factor and μ_B the Bohr magneton. Under the effect of the magnetic field, the hyperfine levels characterized by F are split into equally spaced sublevels labeled by the quantum number $m_F = \{-F : 1 : F\}$ and the shift of energy due to the magnetic interaction depends linearly on the field intensity:

$$\Delta E(\vec{r}) = m_F g_F \mu_B |\vec{B}(\vec{r})|. \quad (2.2)$$

This is known as the linear Zeeman regime. The energy shift can be expressed in terms of the frequency ω_L :

$$\Delta E(\vec{r}) = \hbar \omega_L, \quad (2.3)$$

with \hbar the reduced Planck constant and ω_L the Larmor frequency of the atoms defined by $\omega_L = m_F g_F \mu_B |\vec{B}(\vec{r})|/\hbar$.

Assuming that the atoms remain in a fixed m_F state, those in the m_F states obeying $g_F m_F > 0$ minimize their energy ΔE at a field minimum, resulting in a trapping in the region of space where the field is minimum. However, if the field amplitude changes faster than the Larmor frequency of the atoms, the adiabaticity criterion:

$$\frac{d\vec{B}}{dt} < \omega_L |\vec{B}| \quad (2.4)$$

is violated and the atoms undergo a spin flip to reach an untrapped state ($m_F = 0$) or a high field seeking state ($g_F m_F < 0$). As Maxwell's equations forbid a maximum of magnetic field in free space, the high field seeking states are not trappable. The adiabaticity criterion is violated in regions of very small magnetic fields, which makes it necessary to shift the minimum of magnetic fields from zero.

As reported in [68], the Landé factor for the $F = 1$ hyperfine state of the ^{87}Rb ground state ($5^2S_{1/2}$) reads $g_F \approx -1/2$ such that only the state $m_F = -1$ can be trapped. Assuming that the field is weak enough to be in the linear Zeeman regime and that the adiabaticity criterion is fulfilled, we commonly consider that Eq. (2.2) defines a magnetic potential, even though it is in truth an energy shift from the hyperfine energy at $B = 0$. In this thesis, we regularly refer to the potential V , which is obtained by the conversion $V(x, y, z) = \kappa |B(x, y, z)|$ with $\kappa = |g_F| \mu_B = h \times 0.7 \text{ MHz/G}$.

This approach is limited to small magnetic fields. For large fields, the magnetic field couples independently to the electron and nuclear spins and the total spin F does no longer make sense.

2.3.1.2 Transverse confinement in a wire-guide

Atom chips produce strong magnetic field gradients in the vicinity of the current carrying microstructures which allows strong confinement while offering a high degree of robustness and control. In our setup, we make use of this feature to produce an anisotropic confinement, distinguishing between a strong confinement along the transverse directions (x and y) and a weaker longitudinal confinement (along z). The coming section mainly uses concepts explained in the book [45] and in the review [46].

Quadrupole trap The simplest trapping geometry is a wire-guide, obtained by a single current-carrying wire and an homogeneous bias field perpendicular to the wire.

By sending a DC current I through a wire oriented along z and supposed both infinitely thin and infinitely long, one generates a circular magnetic field:

$$\vec{B}_w(\vec{r}) = \frac{\mu_0 I}{2\pi} \frac{1}{r} \vec{e}_\theta = \frac{\mu_0 I}{2\pi} \left[-\frac{y}{x^2 + y^2} \vec{e}_x + \frac{x}{x^2 + y^2} \vec{e}_y \right], \quad (2.5)$$

with $\mu_0 = 4\pi \times 10^{-3} \text{ G.m/A}$ the vacuum permeability. We assume the wire to define the center of the reference frame and therefore to be located in $(x = 0, y = 0)$. When

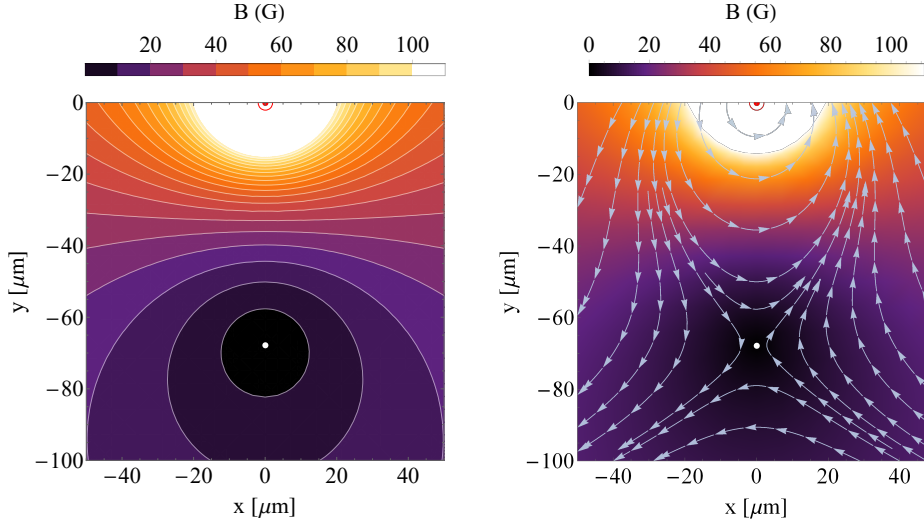


Figure 2.5: Magnetic fields in a wire-guide An infinite wire located at $(x = 0, y = 0)$ carries the current $I = 1$ A oriented along $-z$. A uniform external field of amplitude $|B_b| = 29.5$ G is oriented along x . The fields cancel along the line $(x = 0, y = -d)$ with $d = 68$ μm . **Left:** Magnitude of the magnetic field (saturated at 110 G) and equipotential lines in the (x, y) plane. The red dot represents the wire and the white dot is the trap minimum. **Right:** Field magnitude and field lines illustrating the quadrupole configuration around the trap minimum.

combining this field to an homogeneous bias field $\vec{B}_b = -|B_b|\vec{e}_x$, the fields cancel along the line $(x = 0, y = -d, z)$ with d defined by:

$$d = \frac{\mu_0 I}{2\pi |B_b|} = 2000 \mu\text{m} \frac{I[\text{A}]}{B_b[\text{G}]} \quad (2.6)$$

This is illustrated in Fig. 2.5 for the experimental parameters $I = 1$ A, $|B_b| = 29.5$ G, leading to a field minimum at the distance $d \approx 68$ μm below the wire.

In the vicinity of the minimum $(x = 0, y = -d)$, the field presents a quadrupole configuration such that the variation of fields are linear in space with a slope $\frac{|B_b|}{d}$ and the field can be approximated by the function:

$$\vec{B} \approx \frac{|B_b|}{d} \vec{e}_\theta = \frac{|B_b|}{d} (-(y-d)\vec{e}_x + x\vec{e}_y) \quad (2.7)$$

Equation (2.7) shows that increasing B_b displaces the trap minimum closer to the wire. However, too close to the wire, the approximation of an infinitely thin wire does no longer describe practical realizations.

Ioffe-Pritchard trap The quadrupole trap presents a zero field in its minimum which inevitably leads to spin-flips. To solve this, we add a field along the wire axis $\vec{B}_0 = |B_0|\vec{e}_z$, referred to as Ioffe-Pritchard field, to create a Ioffe-Pritchard trap [127, 128]. The field magnitude now reads:

$$B_{\text{IP}} = \sqrt{\left(-\frac{\mu_0 I}{2\pi} \frac{y}{x^2 + y^2} - |B_b|\right)^2 + \left(\frac{\mu_0 I}{2\pi} \frac{x}{x^2 + y^2}\right)^2 + |B_0|^2} \quad (2.8)$$

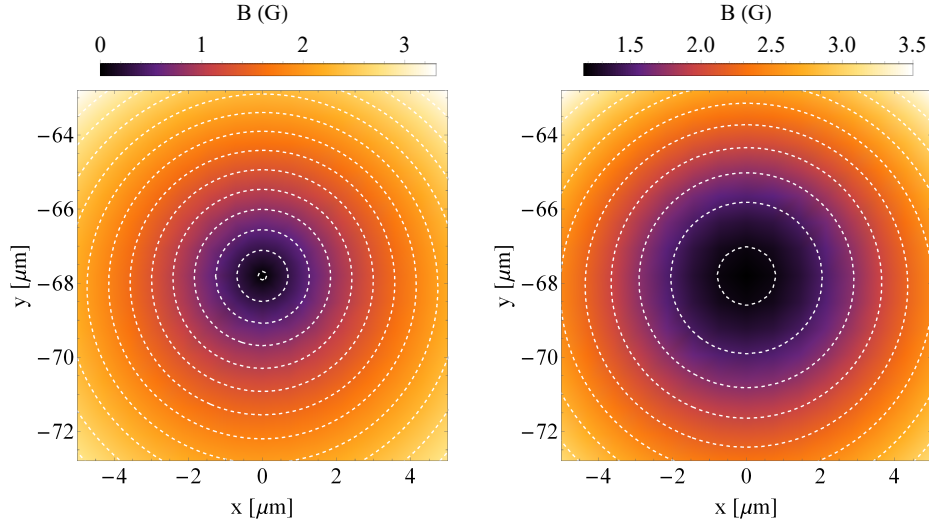


Figure 2.6: Left: Quadrupole trap In the vicinity of the trap minimum, the magnitude of the field varies linearly and the field magnitude at the trap minimum is 0. The equipotential lines for linearly spaced values of small B are equidistant circles around $(x = 0, y = -d)$. **Right: Ioffe-Pritchard trap** The addition of a field of magnitude $|B_0|$ in the direction of the wire changes the field in the vicinity of the trap minimum to a harmonic confinement. The equipotential lines are therefore no longer equidistant. The position of the trap minimum is unchanged and its magnitude is increased from 0 to $|B_0|$.

with $y' = y - d$. In this field configuration, the position of the trap minimum is unchanged compared to the quadrupole trap but its magnitude is shifted to B_0 . Additionally, the field variations are harmonic in the vicinity of the minimum as can be seen when comparing the magnitudes of the fields in Fig. 2.6.

In the vicinity of the trap minimum, the field can be approximated by the shifted harmonic function:

$$B(x, y) = B_0 + \frac{1}{2} \left(\frac{2\pi B_b^2}{\mu_0 I B_0} \right)^2 (x^2 + y^2). \quad (2.9)$$

We work more commonly with the potential energy, deduced from the field amplitude using the conversion factor $\kappa = |g_F| \mu_B = h \times 0.7 \text{ MHz/G}$ with h the Planck constant. The potential therefore reads:

$$V_{\perp}(x, y) = \hbar \omega_{L,0} + \frac{1}{2} m \omega_{\perp}^2 (x^2 + y^2), \quad (2.10)$$

where $\omega_{L,0}$ is the Larmor frequency at the trap center given by $\omega_{L,0} = 2\pi \kappa B_0 / h$ and the transverse trap frequency defined by

$$\omega_{\perp} = \sqrt{\frac{\kappa}{m} \frac{2\pi B_b^2}{\mu_0 I \sqrt{B_0}}}, \quad (2.11)$$

The comparison of these two quantities allows to check whether the experimental settings satisfies to the adiabaticity criterion. Experimentally, $B_0 = 1.17 \text{ G}$ such that $\omega_{L,0} \approx 2\pi \times 819 \text{ kHz}$ is much larger than $\omega_{\perp} \approx 2\pi \times 3.6 \text{ kHz}$.

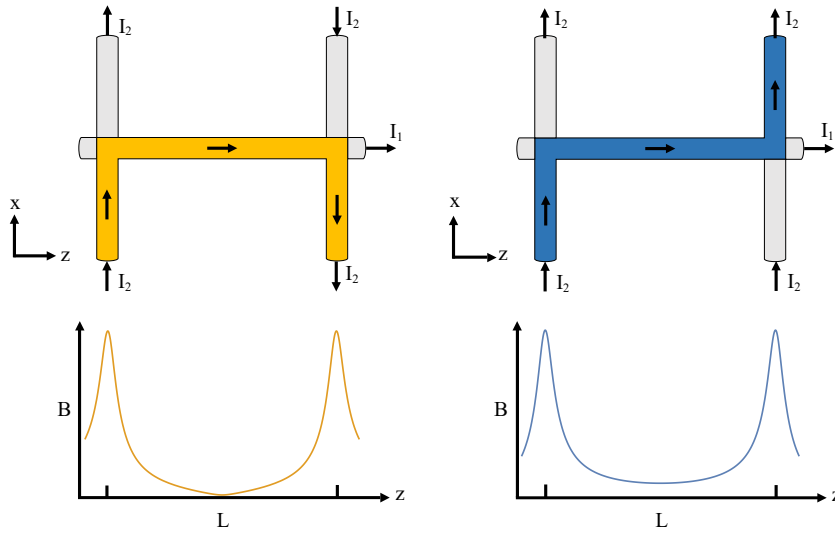


Figure 2.7: *U*- and *Z*-wire geometries obtained by a main trapping wire and two orthogonal wires spaced by L carrying identical intensities. **Left:** *U*-shape conductor obtained by sending currents with opposite orientation into the two wires at the extremities. The total field cancels in the center of the trap ($x = 0, y \approx -d, z = L/2$) forming a quadrupole trap. **Right:** *Z*-shape conductor obtained by sending currents with identical orientation in the two wires at the extremities. The fields amplitudes add up and the minimum at the trap center is non-zero, resulting in a Ioffe-Pritchard configuration. The lower panels sketches the field along ($x = 0, y = -d, z$) using a simplified Biot-Savart calculation.

2.3.1.3 Longitudinal confinement in an H trap

The straight wire with homogeneous external fields creates a cylindrical guide along the line ($x = 0, y = -d, z$). Adding a longitudinal confinement requires to change the wire geometry in the xz -plane such that the wire resembles either a *U*, in which case it is called *U*-shape conductor, or a *Z*, in which case it is named a *Z*-shape conductor. To have the best flexibility, we experimentally realize these geometries by adding two secondary wires orthogonal to the primary wire to form the *H* configuration represented in Fig. 2.7. The direction of the current in the secondary wires determines the effective geometry of the wire: currents of opposite orientation realize a *U*-wire, while currents of identical orientation realize a *Z*-wire.

While we previously had a translation invariant field minimum along the axis ($0, -d, z$), the secondary wires, separated by the distance L , define a field minimum along z . The magnitude of the minimum depends on the currents orientation as represented in Fig. 2.7.

For the effective *U*-wire, the field deformation is anti-symmetric. Therefore, the fields cancel at equal distance from the wires and form a quadrupole trap. The *U*-wire configuration is realized using the macroscopic copper structure underneath the chip trap and used during the MOT stage.

For an effective *Z*-wire, the field deformation is symmetric and the fields are added at the location of the minimum, which results in a Ioffe-Pritchard trap. This configuration can be realized using the micro-wires of the chip. The longitudinal confinement using a *Z*-wire changes the Larmor frequency and the distance between the chip and the minimum compared to the ones defined for the wire-guide. The Larmor frequency at the trap center

now reads:

$$\omega_{L,0} = \frac{\kappa}{\hbar} \left(B_0 + \frac{4d\mu_0 I_h}{\pi L^2} \right), \quad (2.12)$$

with I_h the current in the two wires and L the distance separating them. In our setup, $I_h = 0.5$ A and $L = 2$ mm. The resulting Larmor frequency at the trap minimum is $\omega_{L,0} = 2\pi \times 914$ kHz.

2.3.1.4 Trap simulation with realistic wires

The previous section presented the concepts of three dimensional magnetic trapping assuming infinite long and thin wires. This approximation allows to understand basic trap behaviors and provides estimates of the trap parameters. However, the chip trap is a Ioffe-Pritchard trap for which the distance between the trap minimum and the wire is of the order of the wire width itself such that finite size effects are not negligible. At such scale, the trap is affected by the rectangular shape of the wires and the inhomogeneities in current density, in particular close to the wire crossings.

Therefore, a more realistic approach consists in modeling the chip layout and computing analytically the field produced by rectangular three dimensional wires [122]. The simulation provides the trap frequencies along the eigenaxes of the potential by diagonalizing the Hessian matrix at the center of the trap. It also takes into account the spatial shift of the potential along the vertical axis due to the gravitational sag. For this, the precise measurement of the currents in the wires is necessary. It also requires the measurement of the magnitudes of the external fields, which are deduced from the measurement of ω_0 and ω_{\perp} .

2.3.1.5 Trap characterization

Larmor frequency at the trap center The value of the Larmor frequency ω_0 at the trap center (referred to as "trap bottom") is determined by radio-frequency (rf) spectroscopy. A 20 ms rf pulse is used to transfer atoms out of the trap by resonant coupling of the $m_F = -1$ and $m_F = 0$ states. To realize the pulse, we use the electronics of the evaporative cooling presented in Sec. 2.2.5 with a strongly reduced intensity. The rf frequency is constant for a pulse after which the atoms remaining in the trap are imaged. This is repeated for various values of ω_{rf} .

A simplified picture is presented in Fig. 2.8 in the 1D case along with a typical measurement of the trapped atom number versus the rf frequency. As long as $\omega_{\text{rf}} < \omega_0$ (a), all the atoms remain trapped in the $m_F = -1$ state and the measured atom number is constant. For $\omega_{\text{rf}} = \omega_0$ (b), the coupling is maximally resonant and all the atoms are outcoupled (measured atom number ≈ 0). For $\omega_{\text{rf}} \gtrsim \omega_0$ (c), the atoms with an energy above $\hbar\omega_{\text{rf}}$ are outcoupled. Therefore, as ω_{rf} increases, the number of outcoupled atoms decreases and we measure more atoms. In principle, the slope $N(\omega_{\text{rf}} > \omega_0)$ gives an estimate of the temperature of the atoms. When $\hbar\omega_{\text{rf}}$ exceeds the energy of the hottest atoms (d), the atoms are transparent to the rf pulse and the measured number of atoms remaining in the trap is constant.

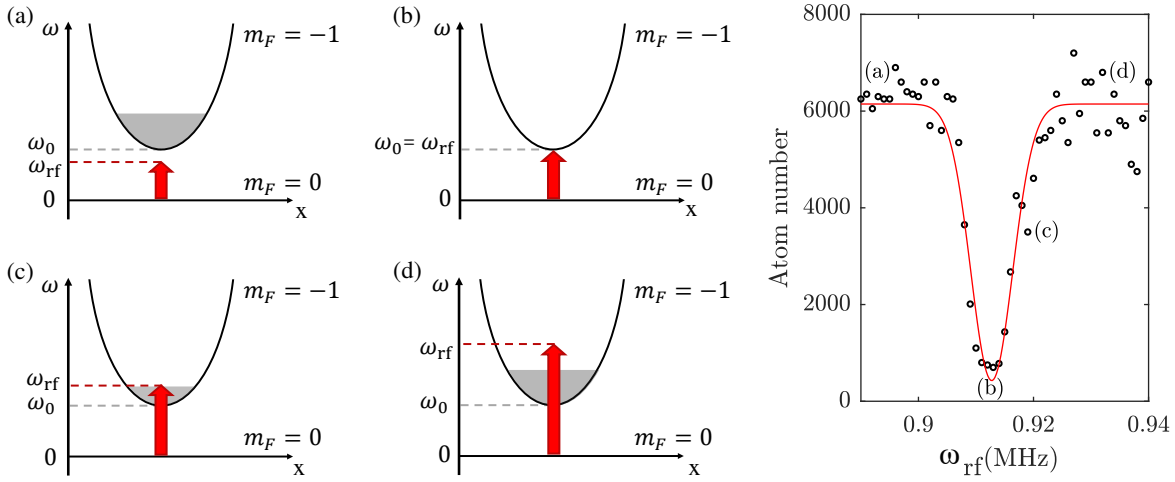


Figure 2.8: Trap bottom spectroscopy and illustration in a simplified 1D model. Left: The spatial dependence of the energy of the $m_F = -1$ state is assumed harmonic and the potential is filled up to a given energy. (a) For $\omega_{rf} < \omega_0$, the atoms remain trapped in the $m_F = -1$ state. (b) For $\omega_{rf} = \omega_0$, the coupling is maximally resonant and almost all the atoms are outcoupled from the trap. (c) For $\omega_{rf} > \omega_0$, the atoms with an energy above $\hbar\omega_{rf}$ are outcoupled. (d) When $\hbar\omega_{rf}$ exceeds the energy of the hottest atoms, the atoms are transparent to the rf pulse. **Right:** Atoms number remaining in the trap after an rf pulse frequency varied between $\omega_{rf} = 0.89$ MHz and $\omega_{rf} = 0.94$ MHz. The various qualitative behaviors described in (a,b,c,d) are reported on the measurement. The asymmetry of the plot is limited here as the temperature in the trap is very low.

Trap frequencies The trap frequencies are measured by triggering a collective dipolar motion of the atoms along the eigen-axes of the trap. The measurement of ω_{\perp} relies on a rapid change of the current I in the primary wire. The current is decreased by 1% over 11 ms before being ramped suddenly to its original value ($I = 1$ A) resulting in a vertical displacement of the trap center and a vertical motion of the cloud. The oscillation of the atoms is imaged in the yz -plane after 17 ms time-of-flight as illustrated in the left panel of Fig. 2.9.

To measure the longitudinal trap frequency ω_z , the longitudinal confinement is slowly increased over 10 ms before being brought back suddenly to its original geometry. The deformation is obtained using the "dimple" wire presented in Sec. 2.2.2 and located at 710 μm from one of the secondary wire of the chip. The brutal deformation along z leads to an oscillation than we measure in time-of-flight. The oscillations are slowly damped by a heating process.

The calibration of the simulations using $\omega_0 \approx 2\pi \times 913$ kHz and $\omega_{\perp} \approx 2\pi \times 2.938$ kHz leads to $I = 1$ A, $I_h = 0.5$ A, $B_b = 29.9$ G, $B_0 = 1.17$ G and $d \approx 62$ μm . However, for these parameters, the simulated longitudinal frequency is $\omega_z \approx 2\pi \times 8.5$ Hz while the measured frequency is $\omega_z \approx 2\pi \times 22.2$ Hz. This discrepancy is attributed to the defects of the wires (inhomogeneity of bulk density and roughness of its surface and edges) which distort the current densities and consequently the magnetic field along z . This is known as corrugation of the longitudinal potential and cannot be easily included in the finite-size wire simulations. The measured frequency is larger than the simulated one, which

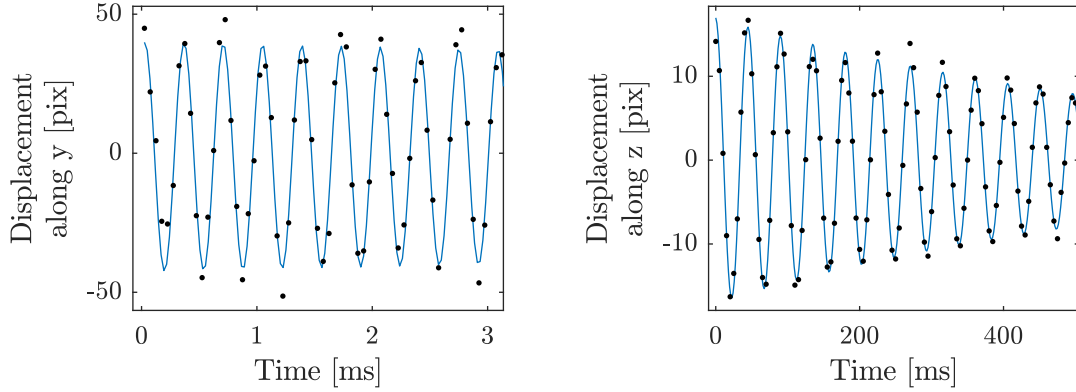


Figure 2.9: Measurement of the trap frequencies. **Left:** Vertical displacement of the center of mass of the cloud to measure the transverse frequency $\omega_{\perp} \approx 2\pi \times 2.938$ kHz. **Right:** Longitudinal displacement of the center of mass to measure the axial frequency $\omega_z \approx 2\pi \times 22.2$ Hz.

indicates that the condensate is trapped in a local minimum created by the wire corrugation [129–131]. The field inhomogeneities along z are much smaller than the magnitude of the Ioffe field B_0 such that the trap bottom is not affected by the corrugation.

2.3.2 Magnetic trapping with radio frequency fields

For the general concepts, the coming section is inspired from the book of [132] while the part related to the double-well potentials recovers the results of [48].

2.3.2.1 Magnetic resonance and coupling to a classical rf field

We consider neutral atoms trapped in a non-uniform static field such as described in Sec. 2.3.1. Here again, we consider a static field weak enough for F to remain a good quantum number, such that the description in term of Zeeman sublevels presented in Sec. 2.3.1 still holds true. We now superimpose a general magnetic field oscillating at the frequency ω near resonance with ω_L , placing ω in the radio frequency domain. We will show in this section that, through the magnetic dipolar interaction, the oscillating magnetic field couples to the atomic spin, resulting in a coupling of the so-called "bare" Zeeman m_F states. This defines new m_F states, which are called "dressed" by the rf field. The amplitude of the rf field is usually larger than a mG such that the atomic spins interact with enough rf photons to describe the rf field by a classical coherent field.

The magnetic field reads:

$$\vec{B}(\vec{r}, t) = \vec{B}_s(\vec{r}) + \vec{B}_{\text{rf}}(\vec{r}) \cos(\omega t), \quad (2.13)$$

with $\vec{B}_s(\vec{r})$ the static field and $\vec{B}_{\text{rf}}(\vec{r}) \cos(\omega t)$ the near resonant rf field. The atom-field coupling is described by the Hamiltonian:

$$H(\vec{r}, t) = g_F \mu_B \left[\vec{B}_s(\vec{r}) \cdot \vec{F} + \vec{B}_{\text{rf}}(\vec{r}) \cos(\omega t) \cdot \vec{F} \right]. \quad (2.14)$$

We consider first the case of homogeneous fields. The situation where the fields are spatially varying is treated in the following section, as it corresponds to the realisation of adiabatic potentials.

We define the quantization axis \vec{e}_z as the local direction of the static field, such that $\vec{B}_s = B_s \vec{e}_z$. We restrict ourselves to the case where \vec{B}_{rf} is linearly polarized and orthogonal to \vec{e}_z (known as π polarized) and set the \vec{e}_x axis parallel to the rf field: $\vec{B}_{\text{rf}} = B_{\text{rf}} \cos(\omega t) \vec{e}_x$. The Hamiltonian now reads:

$$H(t) = s [\omega_L F_z + 2\Omega_{\text{rf}} \cos(\omega t) F_x], \quad (2.15)$$

with s the sign of g_F and Ω_{rf} the Rabi frequency defined by

$$\Omega_{\text{rf}} = \frac{\kappa}{2\hbar} B_{\text{rf}}. \quad (2.16)$$

To make the coupling of the m_F states appear, we introduce the rising and lowering operators F_+ and F_- defined as

$$F_{\pm} = F_x \pm iF_y, \quad (2.17)$$

which increase and decrease m_F by one unit respectively. The Hamiltonian given by Eq. (2.15) reads:

$$H(t) = s\omega_L F_z + s\frac{\Omega_{\text{rf}}}{2} \left[e^{-i\omega t} (F_+ + F_-) + e^{i\omega t} (F_+ + F_-) \right]. \quad (2.18)$$

The first term describes the precession of the spin around the quantization axis at the Larmor frequency with the orientation given by s as in the static case. The second term describes the coupling between the bare states and the resulting transitions. To diagonalize the Hamiltonian, we rotate the basis at the magnetic field frequency $s\omega$ around z such that the rotated state are described by the Hamiltonian:

$$H(t) = -s\delta F_z + s\frac{\Omega_{\text{rf}}}{2} \left[e^{i(s-1)\omega t} F_+ + e^{-i(s-1)\omega t} F_- + e^{i(s+1)\omega t} F_+ + e^{-i(s+1)\omega t} F_- \right], \quad (2.19)$$

with δ the detuning defined by $\delta = \omega - \omega_L$. Depending on the sign of s , two terms of the previous equation becomes static while the two others oscillate at 2ω in the rotating frame. In the near resonant limit ($\delta \ll \omega_L$) and assuming that $\Omega_{\text{rf}} \ll \omega_L$, we can apply the rotating wave approximation (RWA), which consists in neglecting the terms oscillating at 2ω in Eq. (2.19). It results in a stationary Hamiltonian:

$$H_{\text{eff}} = -s\delta F_z + s\frac{\Omega_{\text{rf}}}{2} (F_+ + F_-) = s(-\delta F_z + \Omega_{\text{rf}} F_x). \quad (2.20)$$

This effective Hamiltonian can be expressed using a spin projection F_{θ} :

$$H_{\text{eff}} = \Omega F_{\theta}, \quad (2.21)$$

with the frequency splitting defined by the generalized Rabi frequency:

$$\Omega = \sqrt{\delta^2 + \Omega_{\text{rf}}^2}, \quad (2.22)$$

and F_θ the spin projection on \vec{e}_θ such that $F_\theta = \cos(\theta)\vec{e}_z + \sin(\theta)\vec{e}_x$. The angle θ is defined by

$$\theta = \arccos\left(-\frac{\delta}{\Omega}\right) + \frac{(s-1)\pi}{2}. \quad (2.23)$$

Equation (2.21) resembles the first term of Eq. (2.15), which shows that H_{eff} is the Hamiltonian of an effective static field defined by:

$$\vec{B}_{\text{eff}} = s\frac{\hbar}{\kappa}\Omega\vec{e}_\theta. \quad (2.24)$$

The eigenstates $|m'\rangle$ of the effective Hamiltonian are the dressed states. In the rotated frame, they are obtained by rotation of the bare states $|m\rangle$ in the rest frame and their energy is

$$E_{m'} = m'\hbar\Omega. \quad (2.25)$$

The previous calculation has been performed for a linear polarization. A similar reasoning can be done for any polarization. Considering \vec{e}_z defined by the direction of the static field, the rf field reads:

$$\vec{B}_{\text{rf}} = B_x \cos(\omega t + \phi_x)\vec{e}_x + B_y \cos(\omega t + \phi_y)\vec{e}_y + B_z \cos(\omega t + \phi_z)\vec{e}_z. \quad (2.26)$$

The coupling between the Zeeman states due to the component of the rf field aligned with the quantization axis is extremely small if the corresponding Rabi frequency Ω_z verifies $\Omega_z \ll \omega$. In this case, the RWA holds true and B_z plays a negligible role. After performing rotations around $s\omega$, terms get negligible in the RWA and we define an effective Hamiltonian of the same form as in the linear case and a Rabi frequency:

$$|\Omega_{\text{rf}}| = \frac{\kappa}{2\hbar}\sqrt{B_x^2 + B_y^2 + 2sB_xB_y\sin(\phi_x - \phi_y)}. \quad (2.27)$$

For a linearly polarized field in the plane perpendicular to \vec{e}_z , $\phi_x = \phi_y$ and we recover the expression of the Rabi frequency given by Eq. (2.16).

2.3.2.2 Adiabatic potential for rf dressed atoms

When the static and rf fields vary in space, the previous reasoning must be done in every point of space \vec{r} and the various rotations leads to local definitions of the detuning $\delta(\vec{r})$ and of the generalized Rabi frequency $\Omega(\vec{r}) = \sqrt{\delta(\vec{r})^2 + |\Omega_{\text{rf}}|^2}$.

For space dependent fields, the total Hamiltonian includes a kinetic term as the spin Hamiltonian is now coupled with the external degrees of freedom of the atom. The unitary transformations applied previously to diagonalize the spin Hamiltonian do not commute with the kinetic term. This effect can be ignored when the spatial dependence of the fields are weak enough (small angular velocities or large rf splitting). This is the adiabatic limit, in which an atom prepared in a state $|m\rangle$ follows adiabatically this local eigenstate called adiabatic state. Using an effective field B_{eff} as introduced in the previous section, the adiabaticity criterion can be expressed as a comparison between the variation of the

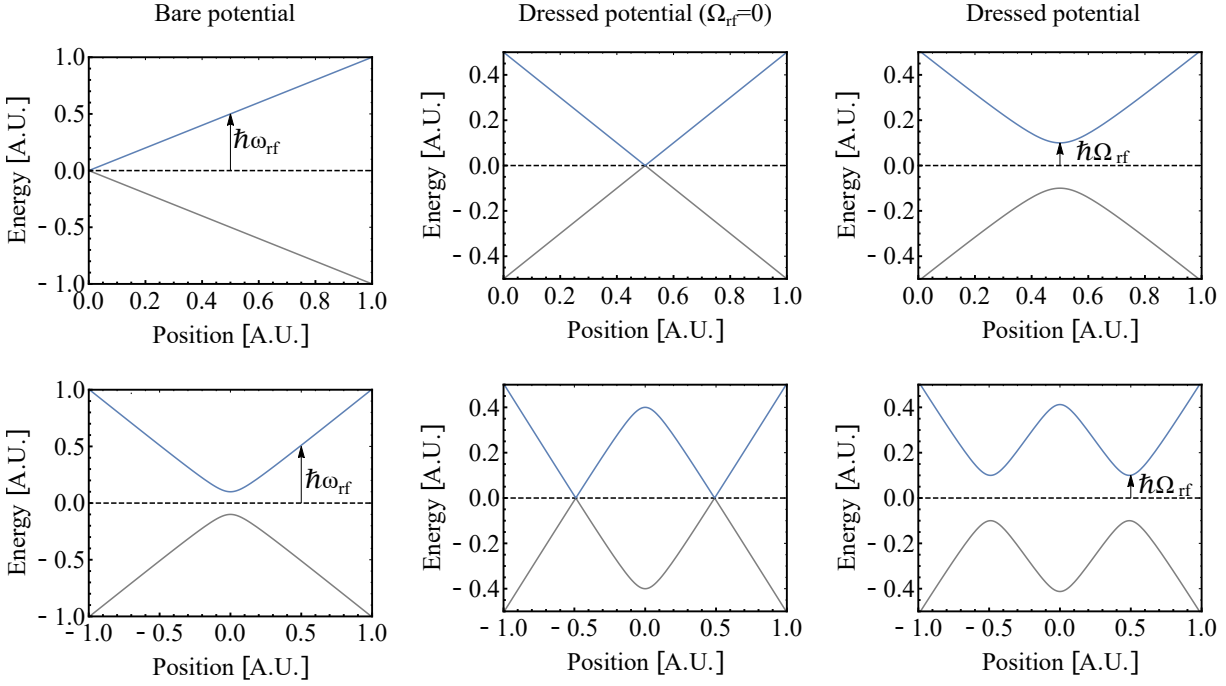


Figure 2.10: Example of adiabatic potentials in $F=1$ in the case of a linear static trap (top) and a Ioffe-Pritchard (IP) static trap (bottom). **Left:** Energy of the bare m_F state $m_F = -1$ (blue), $m_F = 0$ (black dashed), $m_F = 1$ (grey). The static field is then dressed by the field oscillating at the frequency ω_{rf} . **Middle:** For negligible magnitude of the rf field, only the resonance term plays a role. The energy of the dressed $m_F \neq 0$ states is obtained by shifting the bare energies by the photon energy $\pm\hbar\omega_{\text{rf}}$ for the $m_F = \mp 1$ respectively and taking the absolute value. This defines a minimum at the resonance position $\omega_{\text{rf}} = \omega_L$. It results in a quadrupole trap with one minimum when the static field is linear, and two minima for a IP static trap. **Right:** The magnitude of the rf field causes a level repulsion and an avoided crossing of energy $2\hbar\Omega_{\text{rf}}$. For a linear static field, the coupling term plays the role of an effective Ioffe field. For a IP static trap, this leads to a double-well geometry.

orientation of the effective field (now called adiabatic state) compared to the effective Rabi frequency:

$$|\dot{\theta}| \ll \Omega. \quad (2.28)$$

When the adiabaticity criterion is fulfilled, the local eigenenergies of the dressed states lead to an effective adiabatic potential:

$$V_{\text{eff}} = m'\hbar\Omega = m'\sqrt{\left(\hbar\omega - \kappa|\vec{B}_s|\right)^2 + \left(\frac{1}{2}\kappa|\vec{B}_{\text{rf}}|\right)^2}, \quad (2.29)$$

where $|\vec{B}_{\text{rf}}|$ is the field component orthogonal to the orientation of \vec{F} . The first term of the square root shifts the energy of the bare potential by the photon energy $\pm\hbar\omega$ (positive for $mg_F > 0$ and negative $mg_F < 0$) and is named detuning term. The second term, known as coupling term, describes the strength of the coupling of the rf field with the atom. It couples the bare Zeeman sublevels and causes avoided crossings where the m_F states are resonant.

This is illustrated by the schematic of Fig. 2.10 for $F = 1$ where the static field varies linearly in space and for a Ioffe-Pritchard configuration.

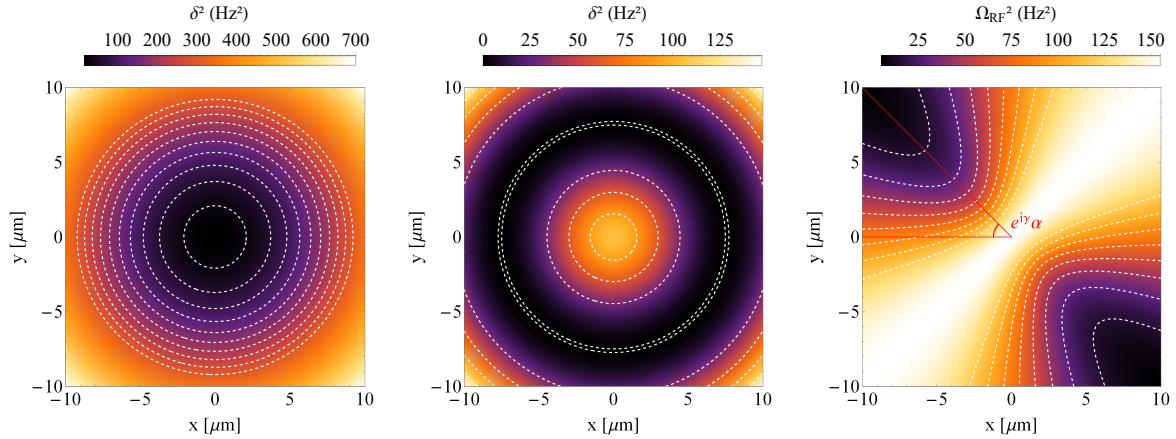


Figure 2.11: Detuning squared and Rabi frequency in the xy plane for a linear polarization. **Left:** $\delta < 0$ corresponds to $\omega < \omega_0$ and results in a simple shift to lower energy of the static Ioffe-Pritchard potential by $\hbar\omega$. In this case, $\omega = 0.2\kappa B_0/\hbar$. **Middle:** For $\delta > 0$, the detuning changed the potential shape and defined the minimum over a ring. In this case $\omega = 3\kappa B_0/\hbar$. **Right:** Rabi frequency showing two minima at the angles $e^{i\gamma}\alpha$ and $e^{i\gamma}(\alpha + \pi)$.

2.3.2.3 The dressed Ioffe-Pritchard trap

This section presents an analytical calculation of the rf potential considering idealized fields. This is very close to the experimental situation presented in the next section. We limit the calculation to the xy -plane as the effect on the longitudinal component results in negligible modifications. As presented in Sec. 2.3.1.2, the trap in the xy -plane can be approximated, in the vicinity of the minimum, by the static field:

$$\vec{B}_s(\vec{r}) = G\rho[-\sin\theta\vec{e}_x + \cos\theta\vec{e}_y] + B_0\vec{e}_z, \quad (2.30)$$

with G the gradient defined by $|B_b|/d$, $\rho = \sqrt{x^2 + y^2}$ and $\theta = \arctan y/x$ in polar coordinates. The field magnitude is $|B_s(\vec{r})| = \sqrt{G^2\rho^2 + B_0^2}$.

The rf field is written as a superposition of two perpendicular linear fields:

$$\vec{B}_{\text{rf}}e^{i\omega t} = [B_x\vec{e}_x + B_ye^{i\gamma}\vec{e}_y]e^{i\omega t}. \quad (2.31)$$

Here $B_{x,y} > 0$ and γ is the phase shift between the two components of the rf field.

Using the unitary transformations as presented above and the RWA, we define, after some calculation the adiabatic rf potential:

$$V = m'\hbar\sqrt{\delta(\vec{r})^2 + \Omega_{\text{rf}}(\vec{r})^2}, \quad (2.32)$$

with $\delta(\vec{r})$ the detuning defined as:

$$\delta(\vec{r}) = \omega - \frac{\kappa}{\hbar}|B_s(\vec{r})| \quad (2.33)$$

and $\Omega_{\text{rf}}(\vec{r})$ the Rabi frequency defined as:

$$\Omega_{\text{rf}}(\vec{r})^2 = \frac{\kappa^2}{\hbar^2} \frac{B_x^2 + B_y^2}{8|B_s(\vec{r})|^2} [2B_0(B_0 + |B_s(\vec{r})| \sin(2\alpha) \sin\gamma^*) \quad (2.34)$$

$$+ G^2\rho^2[1 - \cos(2\alpha) \cos(2\theta) + \sin(2\alpha) \sin(2\theta) \cos\gamma^*]], \quad (2.35)$$

with $\alpha = \arctan(B_y/B_x)$.

Linear polarization: double-well adiabatic potential The geometry of the adiabatic potential depends on three parameters: the detuning δ (in particular its sign), the orientation of the rf field in the xy -plane given by α and the amplitude of the rf field $B_{\text{rf}}^2 = B_x^2 + B_y^2$. While it is not possible to report all configurations, we illustrate the effect of each parameter in a set of representative examples.

In case of an infinitesimal rf field amplitude $\Omega_{\text{rf}} \approx 0$, the detuning is solely responsible for the adiabatic potential. The case $\delta < 0$ corresponds to $\omega < \omega_0$, the Larmor frequency at the center of the trap defined by $\omega_0 = \kappa/\hbar B_0$. As a consequence, the detuning does not change the shape of the static trap but merely lowers its energy by $\hbar\omega$ as displayed in the left panel of Fig. 2.11. For $\delta > 0$, $\omega > \omega_0$ such that δ^2 defines new minima as was illustrated in the 1D case in Fig. 2.10. Due to the rotational invariance of the Ioffe-Pritchard trap, the new minimum forms a ring as displayed in the middle panel of Fig. 2.11. Regardless of the detuning value, the detuning preserves the rotational invariance.

The rotational invariance is broken by the Rabi frequency. For a linear polarization, $\gamma = 0, \pi$ and the expression of the Rabi frequency given by Eq. (2.35) reads:

$$\Omega_{\text{rf}}(\vec{r})^2 = \frac{\kappa^2}{\hbar^2} \frac{B_x^2 + B_y^2}{8|B_s(\vec{r})|^2} [2B_0^2 + G^2\rho^2[1 - \cos(2\alpha)\cos(2\theta) \pm \sin(2\alpha)\sin(2\theta)]] \quad (2.36)$$

where the \pm term corresponds to $\gamma = 0$ and π respectively. The Rabi frequency in this case has two minima in space located at the angles $e^{i\gamma}\alpha$ and $e^{i\gamma}(\alpha + \pi)$ as illustrated on the right panel of Fig. 2.11. Equation. (2.32) shows that the adiabatic potential involves the sum of δ^2 and Ω_{RF}^2 such that the adiabatic potential will present minimal energy along the angles $e^{i\gamma}\alpha$ and $e^{i\gamma}(\alpha + \pi)$. Therefore, changing α by changing the ratio B_y/B_x while maintaining the rf field amplitude $B_x^2 + B_y^2$ constant leads to a rotation of the adiabatic potential by the angle $e^{i\gamma}\alpha$ in the xy -plane. We note that, for $\alpha = 0$, the Rabi frequency simplifies to

$$\Omega_{\text{rf}}(\vec{r})^2 = \left(\frac{B_{\text{rf}}}{2|B_s(\vec{r})|} \right)^2 [B_0^2 + G^2\rho^2 \sin^2(\theta)] \quad (2.37)$$

and we recover the formula of [48].

Having established that α simply rotates the adiabatic potential in the xy -plane, we investigate the roles of the field magnitude and of the detuning in the case where $\alpha = 0$ (horizontal double-well) without loss of generality.

For $\delta < 0$, the geometry depends on the amplitude of the rf field as shown in Tab. 2.1. Below a critical value of the field, the potential remains a single-well for which the energy at the minimum increases with B_{rf} . The rf amplitude introduces an anisotropy and anharmonicity along the axes $e^{i\gamma}\alpha, e^{i\gamma}(\alpha + \pi)$. The critical field below which such a behavior is observed is defined by:

$$B_c^2 = -2B_0 \frac{\hbar\delta_0}{\kappa}, \quad (2.38)$$

with δ_0 the detuning at the minimum defined by

$$\delta_0 = \omega - \frac{\kappa}{\hbar} B_0. \quad (2.39)$$

For $B_{\text{rf}} > B_c$, we can define two minima located at $e^{i\gamma}\alpha$ and $e^{i\gamma}(\alpha + \pi)$ and therefore define a double-well potential. When increasing B_{rf} further, the inter-well spacing and the barrier height increase. Along the axis joining the minima, we can approximate the potential by the following expression as long as $\rho \ll B_0/G$:

$$V_{\text{DW}} = m'_{\text{F}} g_{\text{F}} \mu_{\text{B}} \sqrt{\frac{G^4}{B_0^2} \left(\frac{x^2 - x_0^2}{2} \right)^2 + B_0'^2} \quad (2.40)$$

with x_0 the position of the potential minimum:

$$x_0 = \frac{1}{G} \sqrt{\frac{B_{\text{rf}}^2 - B_c^2}{2}} \quad (2.41)$$

and B'_0 the amplitude at the minimum:

$$B'_0 \approx \frac{|\vec{B}_{\text{rf}}|}{2} \sqrt{1 - \frac{\hbar\delta_0}{\kappa B_0}}. \quad (2.42)$$

In addition, we define the double-well frequency as:

$$\omega_{\text{dw}} = \sqrt{\frac{\kappa}{m B'_0} \frac{G^2 \rho_0}{B_0}}. \quad (2.43)$$

For $\delta > 0$, any amplitude of the rf field breaks the rotation invariance of the ring geometry and results in a double-well potential as illustrated in Tab. 2.1. In this thesis, we create double-well potentials with $\delta < 0$ in order to change smoothly the geometry from a single harmonic trap to a double-well.

Arbitrary polarization Before focusing on the double-well geometry, we briefly discuss the case of an arbitrary polarization. The Rabi frequency Ω_{rf} given by the general Eq. (2.35) still applies and leads to a large number of configurations. We restrict the description to the case of a negative detuning $\delta < 0$ for $B_x = B_y > B_c$, which is relevant to understand how we generate a linear polarization. For $B_x = B_y > B_c$ and $\delta < 0$, a double-well obtained by $s\gamma = 0, \pi$ will turn into either a ring or a single-well as displayed in Fig. 2.12. In addition, the trap bottom depends on the polarization as illustrated in the middle panel of Fig. 2.12. The effect of the polarization on the trap bottom is a feature used to calibrate the polarization of the rf field.

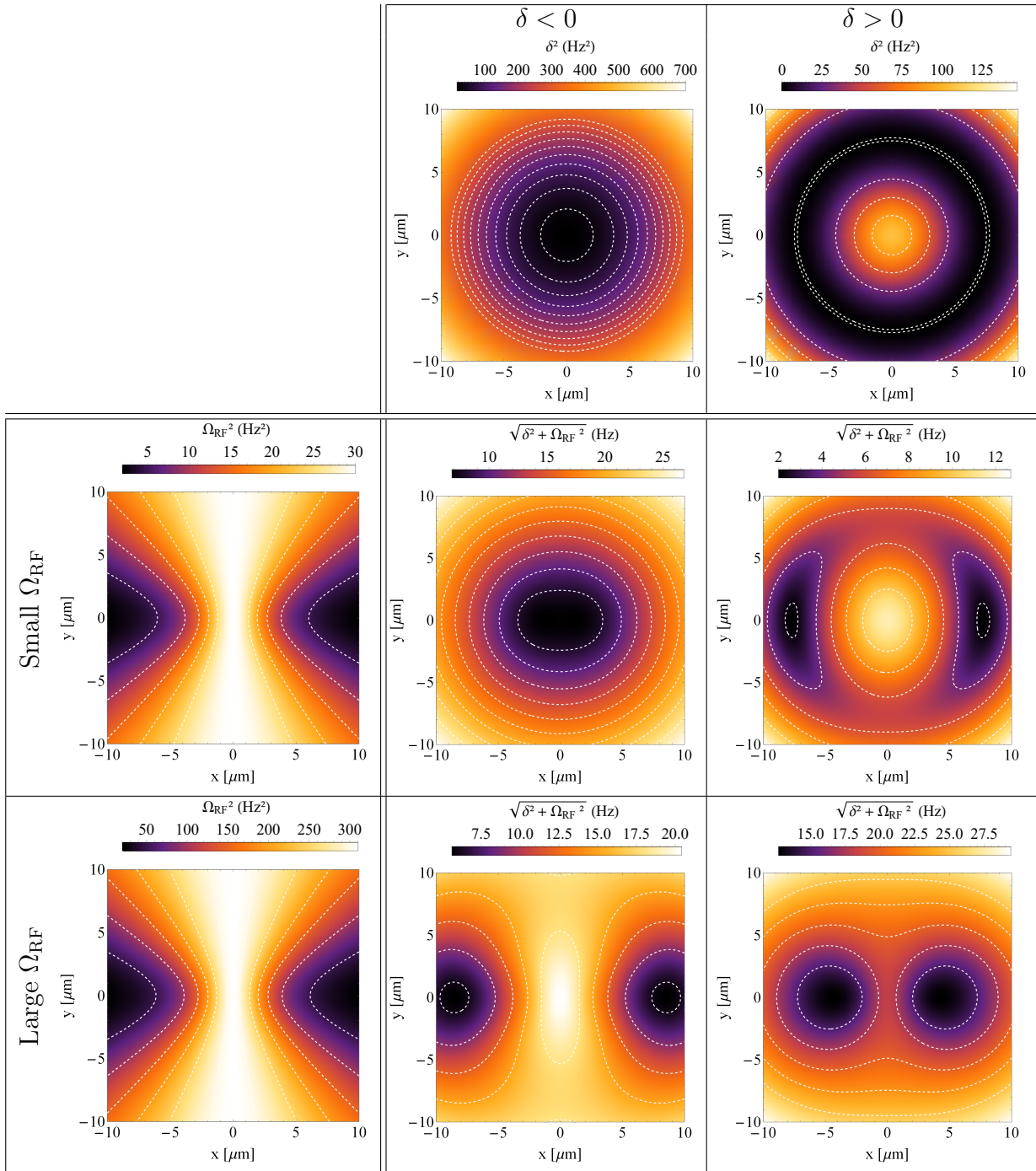


Table 2.1: Adiabatic potentials obtained by different combinations of rf field amplitudes and detunings. The top line represents the squared detuning for $\delta < 0$ and $\delta > 0$. The first column shows the squared Rabi frequency for weak field amplitude and large field amplitude. The table shows the adiabatic potentials (normalized by $m'\hbar$) obtained by combining the various rf field amplitudes and the detunings. For $\delta < 0$, increasing the rf field first leads to an anisotropy until it reaches a critical value above which two minima are defined. Therefore, we observe a smooth transition between single and double-well. For $\delta > 0$, an arbitrary rf field amplitude breaks the rotation invariance of the minimum and defines two minima. For $\delta > 0$, the adiabatic potential at finite Ω_{rf} is always a double-well.

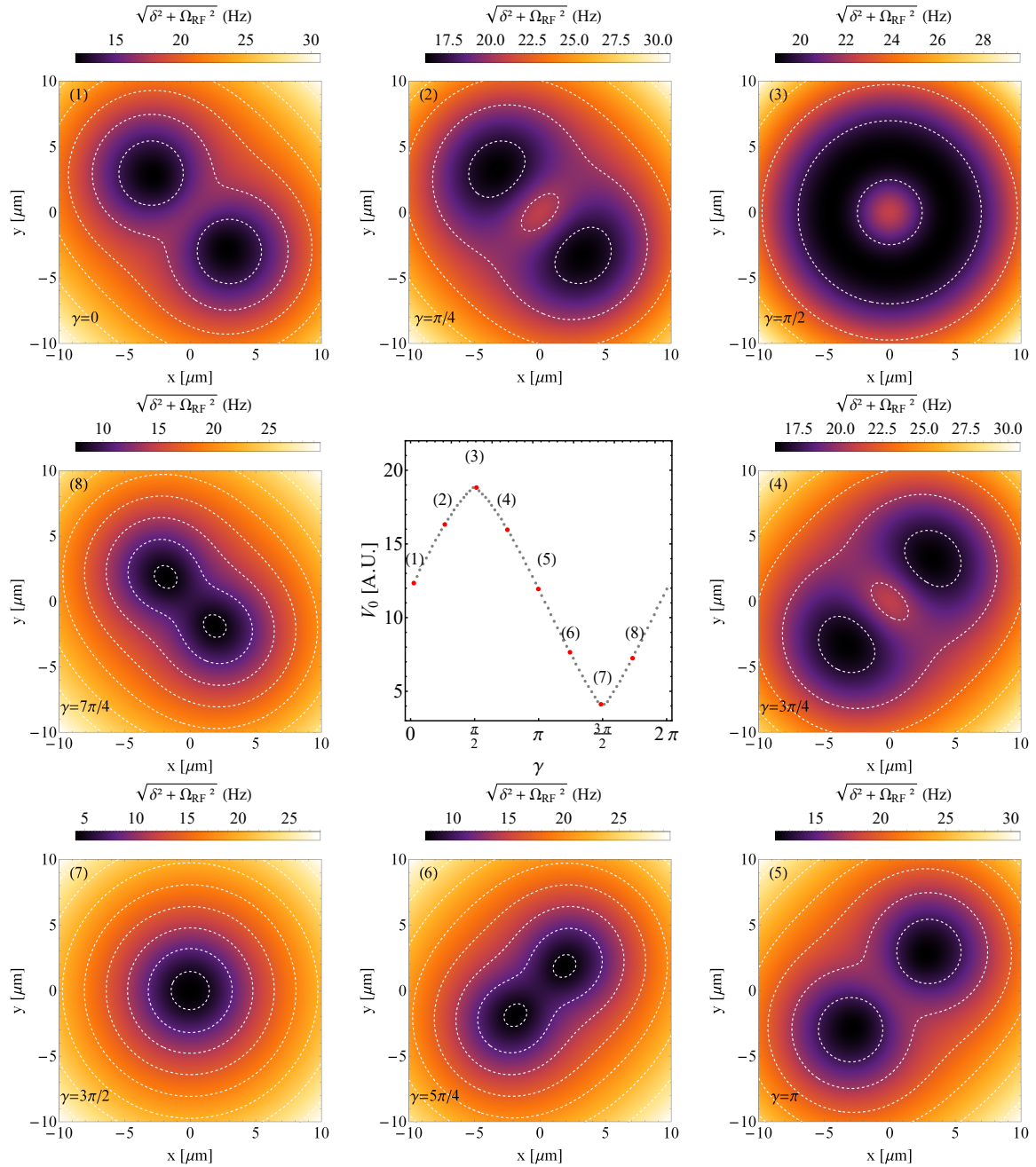


Figure 2.12: Arbitrary polarization for negative detuning and identical values of the field components. Outer figures: Adiabatic potential for polarization varying between 0 and 2π (clockwise). The geometry of the trap varies between a double-well, a ring and a single-well depending on the value of γ^* . **Center:** Minimal energy (trap bottom) as a function of the polarization.

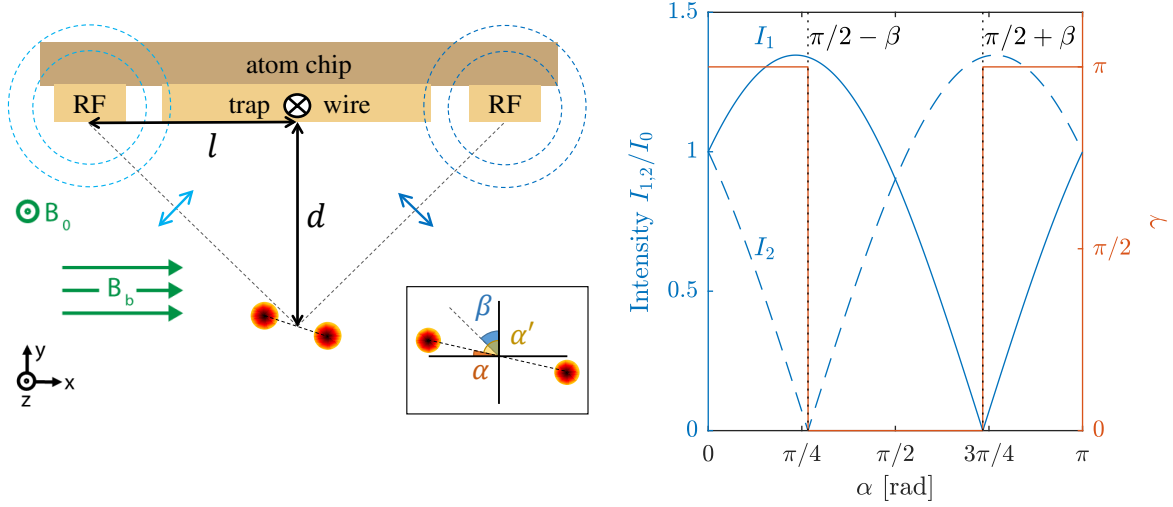


Figure 2.13: Schematic of the three-wires configuration. **Left:** The minimum of the static Ioffe Pritchard is formed under the trapping Z -wire at a distance d . Two additional wires located on each side at the distance l allow to add an rf field of arbitrary polarization and orientation in the xy -plane. The double-well is obtained for a linear polarization and the independent control of the AC current amplitudes allows the rotation of the double-well in the xy -plane by the angle α . The insert shows the angle $\beta = \arctan(l/d)$ giving the orientation of the rf field components and α the tilt angle that we control. **Right:** Relative phase and relative current amplitudes $I_{1,2}$ required to perform a rotation of the trap by α without modification of the inter-well distance. This results in a vertical tilt of the trap and an asymmetry of the minima energies.

2.3.2.4 Implementation of a double-well with an atom chip

The adiabatic potentials are implemented using a three-wires configuration represented in the schematic of Fig. 2.13. The static trap is a Ioffe-Pritchard trap generated, as previously described, by the Z -wire combined with homogeneous static external fields. The rf magnetic field is induced by sending AC currents through two additional wires located on each side of the main wire and separated by $2l = 100 \mu\text{m}$. The intensities read:

$$I_{\text{RF},1} = I_1 e^{i\omega t} \quad (2.44)$$

$$I_{\text{RF},2} = I_2 e^{i\gamma} e^{i\omega t}, \quad (2.45)$$

$I_{1,2}$ (positive by convention) are controlled independently, such that an rf field of arbitrary orientation in the xy -plane is possible. The relative phase γ is also a controllable parameter, realizing any polarization. Therefore, any configuration of the dressed Ioffe-Pritchard trap is achievable with the three wires layout.

We now focus on the double-well potentials realized for $\gamma = 0, \pi$. A key feature for the manipulation of the BEC is the possibility to introduce an energy difference ϵ between the two minima by changing their vertical position while maintaining the inter-well spacing almost constant. As presented in Sec. 2.3.2.3, the rotation of the adiabatic potential in the xy -plane corresponds to a change of the ratio between the rf field components. Experimentally, it consists in changing the intensities $I_{1,2}$. We define the tilt angle α as the angle between the x -axis and the axis joining the trap minima. In order to maintain

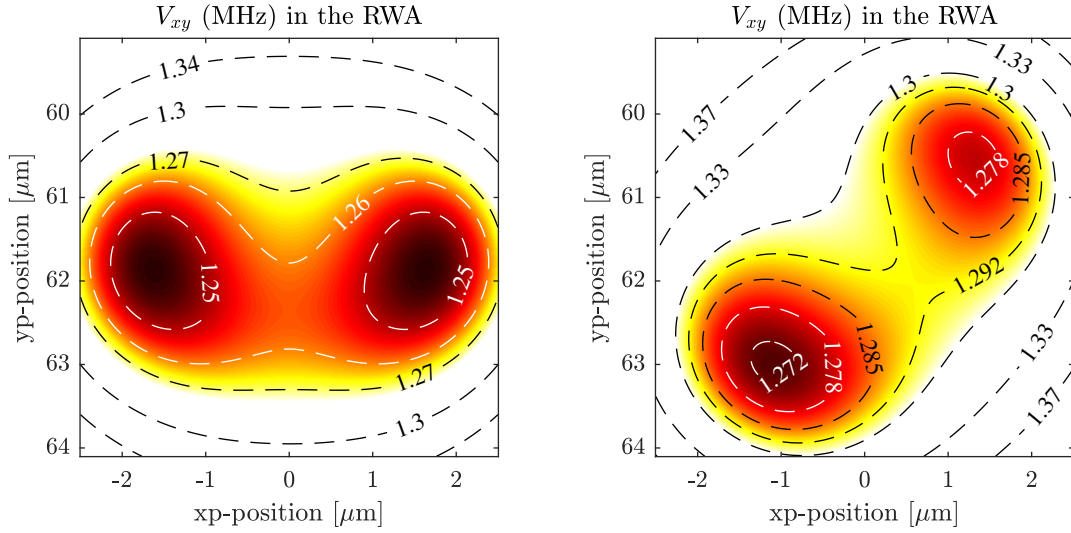


Figure 2.14: Double-well potential in the xy -plane (RWA) for realistic wires. **Left:** Horizontal and symmetric double-well obtained for $\alpha = 0$. The two minima are at the same distance from the chip and have the same energy. **Right:** Tilted double-well obtained for $\alpha = \pi/4$. The two minima form the angle α with the x axis such that the potential is called tilted. The two minima also differ by the energy ϵ and the trap is called asymmetric.

a constant well-spacing, the intensities and polarization must obey:

$$\begin{aligned}
 I_1 &= I_0 |\tan(\beta) \cos(\alpha') + \sin(\alpha')| \\
 I_2 &= I_0 |\tan(\beta) \cos(\alpha') - \sin(\alpha')| \\
 \gamma &= \pi \text{ for } \alpha' \in [-\beta, \beta] \text{ and } 0 \text{ otherwise,}
 \end{aligned} \tag{2.46}$$

with $\beta = \arctan(l/d)$ and $\alpha' = \pi/2 - \alpha$ illustrated in the left panel of Fig. 2.13. The intensities and polarization required to perform a rotation by α are represented in the right panel of Fig. 2.13. I_0 is an intensity identical for both wire. For any $\alpha \neq 0$, either I_1 or I_2 is larger than I_0 , by an amount depending on β , i.e. on the distance between the chip and the static Ioffe Pritchard minimum. Larger values of $I_{1,2}$ correspond to smaller distances d . Therefore I_0 is chosen such that $I_{1,2}$ do not exceed the maximal current allowed by the wire. The AC currents have peak-to-peak amplitudes up to 100 mA resulting in magnetic field amplitudes up to 2.5 G. This field is considered uniform in the vicinity of the minima.

The rotation by α , defining $I_{1,2}$ as in Eqs. (2.46) modifies the energy of the minima and introduces an energy difference ϵ as represented in Fig. 2.14 for $\alpha = 0$ (left) and $\alpha = \pi/4$ (right). This feature of the double-well allows various manipulations of the BEC. For a fixed I_0 , increasing the tilt angle α increases the energy difference between the two double-wells without changing the inter-well spacing. Such scheme, illustrated in the left panel of Fig. 2.15, is a key feature to prepare two BECs with a well-controlled phase difference. One can also perform the deformation from a single to a tilted and asymmetric double-well. This is achieved by ramping I_0 from 0 to a final value I_f for a fixed value of the angle α as represented in the right panel of Fig. 2.15. The atoms are preferentially trapped in the site of lowest energy therefore preparing an atomic imbalance between two BECs.

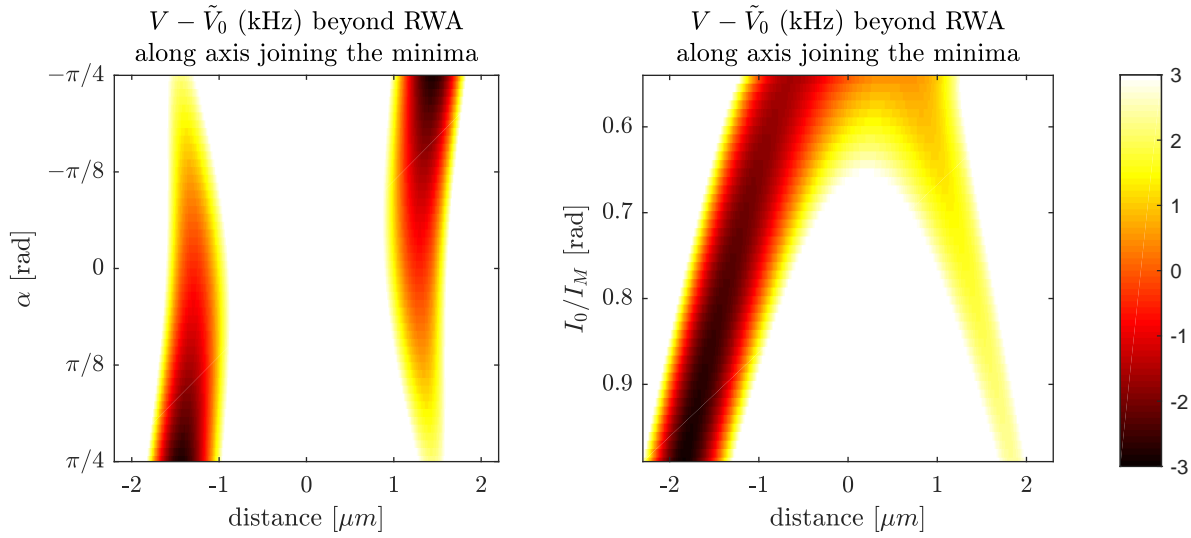


Figure 2.15: Potential cut along the axis joining the minima beyond the RWA (color scale saturated at -3 and 3 kHz). **Left:** Potential along the axis joining the minima as a function of the splitting angle α for $I_0/I_M = 0.9$. α is limited to $-\pi/4, \pi/4$ beyond which the deformation of the trap is such that two minima are no longer defined. The potential is shifted by \tilde{V}_0 defined as the average of energy of the two trap minima. The offset by \tilde{V}_0 allows to see clearly the asymmetry between the two sites. While the two sites have identical energy for $\alpha = 0$, one clearly sees that the energy of both sites is shifted for $\alpha \neq 0$. **Right:** Transition of a single-well to an asymmetric double-well for $\alpha = \pi/4$ and $I_0/I_M = 0.55 : 1$. The lower bound of I_0 corresponds to the minimal intensity at which two minima are defined.

The characteristics of the adiabatic potential are well described by the analytical model we presented in Sec. 2.3.2.3. However, the determination of ϵ as a function of α requires more realistic calculations. As for the static trap, we model the chip layout with rectangular wires and include the longitudinal confinement. This more elaborated model is used to obtain Fig. 2.14.

An additional improvement of the description consists in computing the potential beyond the RWA. While the RWA gives very reasonable results for low I_0 , the validity conditions are violated for large I_0 where $\Omega_{\text{rf}} \gtrsim \omega_{L,0}$. The physical meaning of the terms beyond the RWA appears clearly when considering a quantized description of the rf field. The coupling involve processes exchanging more than one rf photon, leading to a coupling with additional m_F states and therefore modifying the shape of the adiabatic potential compared to the RWA. For large rf field amplitudes, the RWA tends to underestimate the barrier height [132]. As for the static case, the simulations require various calibrations performed by a set of measurements.

2.3.2.5 Calibration and double-well characterization

Equalize the RF currents The rf generator produces a given AC voltage. Due to the resistance in the wires (leads and rf electronics for each output port), the currents have to be balanced using a common probe, which in our case is the trap bottom. We perform a series of rf-spectroscopy measurement of the trap bottom following the same procedure as presented in Sec. 2.3.1.5 for the single trap. We first send an arbitrary current I_1 in one of the wires with the frequency $\omega = 2\pi \times 885$ kHz and measure the effective trap bottom

$\omega_{\text{TB},1}$. In a second step, we set I_1 to zero, maintain the rf-spectroscopic field to match the effective trap bottom $\omega_{\text{TB},1}$ and scan the current in the second wire I_2 (the frequency is also $\omega = 2\pi \times 885$ kHz). When scanning I_2 , the atom number will present a minimum when the current matches I_1 .

After calibration, the measured trap bottom (in our case $\omega_{\text{TB}} = 2\pi \times 1.216$ MHz) allows to calibrate the simulations introduced in Sec. 2.3.1.4. This allows to determine the absolute value of the currents, which was found to be $I_{\text{M}} = 80.25$ mA .

Calibration of the relative phase Various delays can modify the phase defined by the rf generator. We have seen in Sec. 2.3.2.3 that for identical field amplitudes ($I_1 = I_2$), a change of polarization leads to different trap geometries and in particular to different trap bottoms. Therefore, we perform rf spectroscopies to determine the trap bottom as a function of the relative phase γ . The general feature resembles the middle panel of Fig. 2.12. The curve is simulated beyond the RWA and matches the measurements after correcting the simulations by a phase offset. This offset is the correction to apply on the phase of the rf generator to produce a linearly polarized field. In our case, it was evaluated to 7° .

Trap characterization In principle, after the calibration procedure presented above, we expect the simulations to reproduce the trap with a very good agreement. Additional quantities can nonetheless be measured to confirm that the experimental parameters have the effect we expect. From now on, we consider the normalized dressing amplitude $I_{\text{rf}} = I_0/I_{\text{M}}$ with $I_{\text{M}} = 80.25$ mA evaluated from simulations and I_0 introduced in Eqs. (2.46).

The trap frequencies along the three eigenaxes of the potential are experimentally accessible.

The transverse horizontal frequency is measured using the fringe spacing. The inter-well spacing can be measured by studying interference patterns obtained by time-of-flight measurement. Neglecting the inter-atom interaction, the fringe spacing λ characterizing the interferences related to the inter-well spacing $2x_0$ through:

$$\lambda \approx \frac{h}{2x_0 m} t \quad (2.47)$$

with h the Planck constant, m the mass of the atom and t the time-of-flight duration. A transverse oscillation results in an oscillation of the fringe spacing, that we use to measure the transverse horizontal trap frequency. For this, we modify slightly the dressing amplitude before decreasing it back to its initial value to trigger a small amplitude dipolar oscillation of the atoms. We notice that the frequency drops very brutally around $I_{\text{rf}} = 0.4$. This corresponds to the dressing amplitude where the trap is quartic along the transverse direction and therefore a frequency cannot be defined.

The transverse vertical trap frequencies ω_y and longitudinal trap frequencies ω_z are measured as in the static trap by inducing a dipolar motion either along y by a quick displacement along the vertical axis or along z by a slight deformation of the trap along the longitudinal direction. We attribute the small discrepancy between the measurements and the simulations to the corrugation effect.

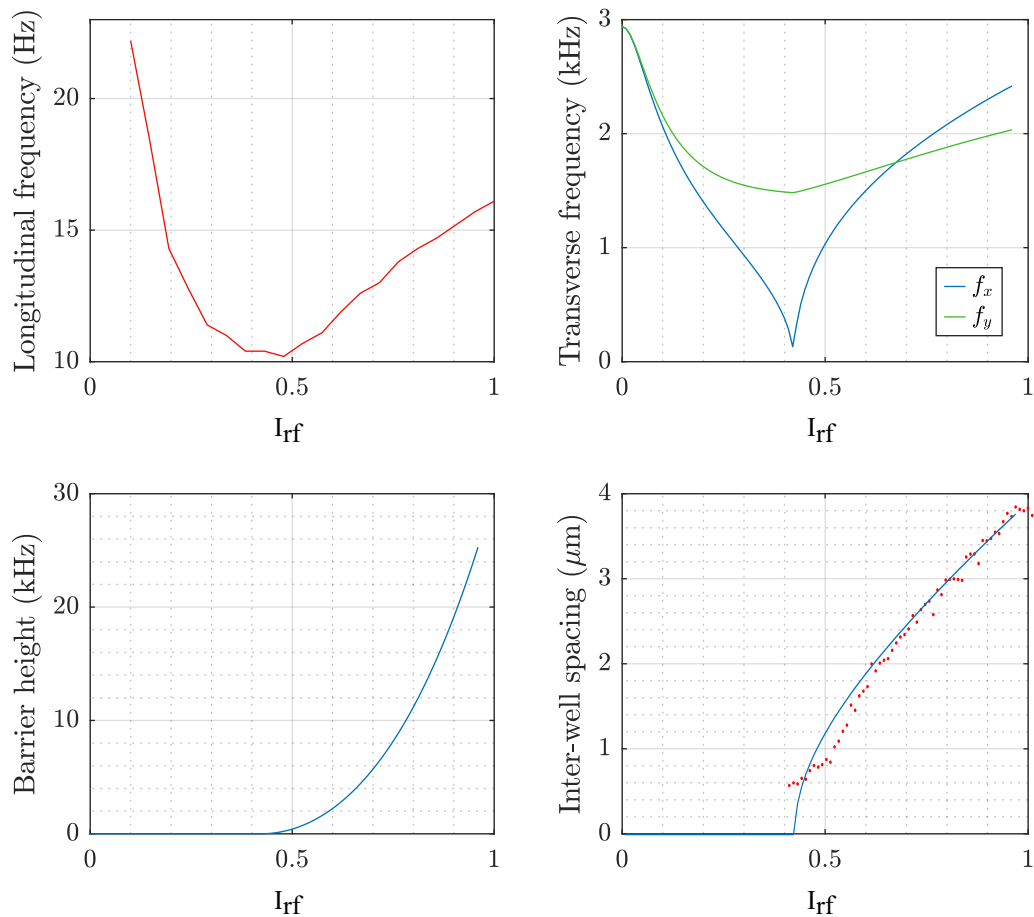


Figure 2.16: Simulations and measurement of the double-well characteristics. **Top:** Trap frequencies along the longitudinal direction (measured) transverse directions (simulated). The strong decrease of the horizontal transverse frequency around $I_{\text{rf}} = 0.4$ indicates a quartic regime where the frequency is not defined. When increasing the dressing amplitude, the trap first undergoes a decompression followed by a compression. **Bottom:** Barrier height and inter-well spacing deduced from simulations and comparison with measurements. These two parameters are not tuned independently in an atom chip setup. Both quantities show that a double-well is defined for dressing amplitudes exceeding $I_{\text{rf}} = 0.42$. Experimentally, we investigate the tunneling dynamics for I_{rf} between 0.5 and 0.6, where the barrier height is below 2 kHz and the inter-well spacing is below $2 \mu\text{m}$.

2.3.2.6 Estimation of the tunnel coupling

In order to perform simulations as in Sec. 1.3.4.6, it is necessary to evaluate the tunnel coupling strength as a function of the dressing amplitude I_{rf} . For simplicity, we define the left and right modes as the non-interacting Gaussian ground states centered on $\pm x_0$ in a harmonic double-well. The tunnel coupling therefore reads:

$$J = \frac{\hbar\omega_0}{2} \left(\frac{x_0^2}{a_{\text{ho}}^2} - 1 \right) \exp \left[- \left(\frac{x_0}{a_{\text{ho}}} \right)^2 \right]. \quad (2.48)$$

In the RWA, the double-well potential is described by Eqs. (2.41, 2.43), from which we deduce $x_0(I_{\text{rf}})$ and $\omega_0(I_{\text{rf}})$. The tunnel coupling is therefore proportional to $\exp[-(I_{\text{rf}}^2 - I_{\text{rf},c}^2)^{3/2}]$ with $I_{\text{rf},c}$ the lowest amplitude where two minima can be defined. The tunnel coupling as a function of the dressing amplitude reads:

$$J(I_{\text{rf}}) = J_0 \exp \left[- \left(\frac{I_{\text{rf}} - I_{\text{rf},c}}{\sigma} \right)^{5/2} \right]. \quad (2.49)$$

The critical amplitude reads $I_{\text{rf},c} = 0.42$ while $J_0/h = 87$ Hz and $\sigma = 0.10$ are deduced from a fit of Eq. (2.48) using Eq. (2.49).

2.4 Imaging and data analysis

2.4.1 Imaging systems

The information about the different observables of the system are obtained by optical measurement. Because of the light reflection on the chip surface, the system cannot be imaged *in-situ* and we perform a destructive time-of-flight (TOF) measurement [23].

Two imaging techniques are implemented on the setup and rely on a same principle. A laser light resonant with a cycling transition of the atoms is sent through the dilute cloud of atoms. The atoms will successively absorb photons from the incoming light and re-emit them in all directions of space.

2.4.1.1 Absorption imaging

The absorption imaging illustrated in Fig. 2.17 relies on measuring the attenuation of the incoming laser beam to measure the atom number integrated along the direction of the beam. This system is implemented to measure the atoms in the xy -plane after a TOF varying between 2 ms and 25 ms. At shorter time-of-flights, the atoms are so close to the chip surface that the images are distorted by the reflection and refraction of the beams on the chip. The longest duration of the time-of-flight is limited by the field of view of our camera. In the context of this thesis, the absorption is mainly used to calibrate the fluorescence imaging system.

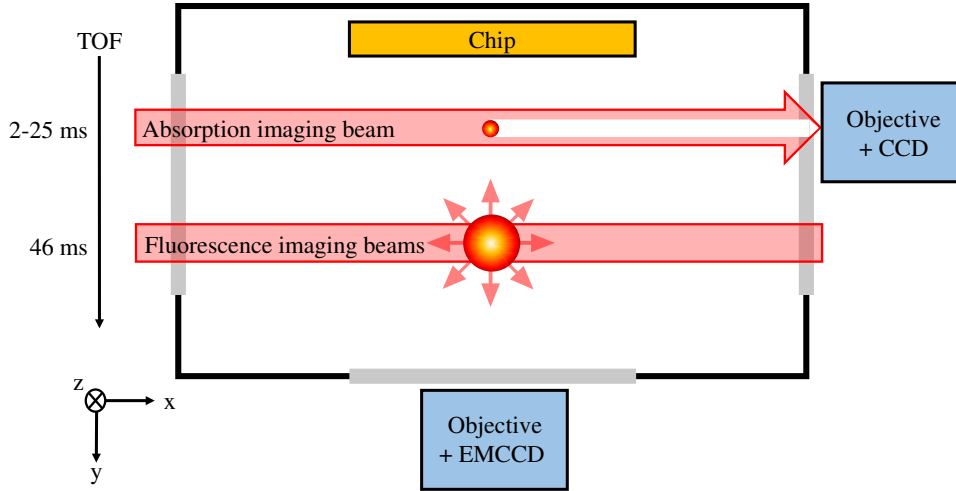


Figure 2.17: Schematic of the imaging systems. An absorption system images the atoms in the xz -plane for TOF adjustable between 2 ms and 25 ms. The fluorescence imaging system images the atoms in the xz -plane after a fixed TOF of 46 ms.

Principle When an atomic cloud is illuminated by a light resonant with one of the atomic optical transitions, the atoms cycle between the ground state and the excited state of this transition by successive absorption and emission of photons. In a two-level approach, the photon scattering rate on resonance reads:

$$\dot{N}_{\text{ph}} = \frac{\Gamma}{2} \frac{I/I_{\text{sat}}}{1 + I/I_{\text{sat}}}, \quad (2.50)$$

with Γ the natural line width of the optical transition and I_{sat} the saturation intensity. The saturation is defined as the intensity at which the scattering rate drops to half its maximal value such that:

$$I_{\text{sat}} = \frac{\hbar\omega\Gamma}{\sigma}, \quad (2.51)$$

with σ the scattering cross section.

However, experimental deviations to the two-level system are unavoidable and reduce the scattering cross section. They originate from the imperfection of the probe beam polarization, from the misalignment of the light wave vector with the quantization magnetic field, from optical pumping effects as well as from the multiple Zeeman levels involved in the transition. Therefore, we define an effective cross section:

$$\sigma_{\text{eff}} = \frac{\sigma}{\alpha}, \quad (2.52)$$

with $\alpha \geq 1$. Without calibration (α assumed equal to 1), the scattering cross-section is over-evaluated. Therefore, it requires less atoms to obtain the measured signal and the atom number is under-evaluated.

The attenuation of the beam is deduced from Eq. (2.50). After passing through an infinitesimal distance dx of the cloud of density $n(\vec{r})$, the beam is attenuated by:

$$dI = -\frac{\sigma}{\alpha} \frac{I}{1 + I/I_{\text{sat}}^{\text{eff}}} n(\vec{r}) dx, \quad (2.53)$$

with $I_{\text{sat}}^{\text{eff}} = \alpha I_{\text{sat}}$. This considers that every photon scattered by the cloud is lost for the beam, which neglects the photons scattered in the same direction as the incoming light. In the most general case, the density column is obtained by integration of Eq. (2.53) and reads:

$$\sigma \tilde{n}(y, z) = \alpha \ln \left(\frac{I_i}{I_t} \right) + \frac{I_i - I_t}{I_{\text{sat}}}. \quad (2.54)$$

The number of transitions occurring at the rate \dot{N}_{ph} is given by the duration and intensity of the probe pulse and is limited by Doppler shift. The absorption of resonant photon transfers a recoil momentum to the atom which modifies the atom velocity and Doppler shifts its frequency. The emission of a photon being isotropic, its averaged effect is negligible. The successive absorption of photons changes the atom frequency until it stops being resonant with the imaging beam. The Doppler shift changes the effective scattering cross-section by pushing the atoms away from resonance. It is an important limitation for imaging above saturation but is negligible far below saturation. The principal limitation below saturation comes from the lifetime of the cycling transition.

Implementation The imaging transition we consider is the D2 line of ^{87}Rb where $\Gamma = 2\pi \times 6.07 \text{ MHz}$. In order to maximize the absorption signal, we address the cycling transition $F = 2, m_F = 2 \leftrightarrow F' = 3, m_F = 3$ using σ^+ polarized light. To be as close as possible to a two level system, we must make sure that the atoms experience a σ^+ polarization, we apply a uniform magnetic field parallel to the optical imaging axis to define a quantization axis.

The cross section for this transition is $\sigma = 2.91 \times 10^{-9} \text{ cm}^2$ and the saturation intensity is $I_{\text{sat}} = 1.67 \text{ mW/cm}^2$ [68]. Experimentally, we access the imaging transition by first repumping the atoms from $F = 1$ to $F = 2$ using a laser pulse lasting $\approx 200 \mu\text{s}$.

On our experiment, the transmitted signal reaches a back illuminated Charge Coupled Device camera (CCD), after passing through an objective consisting of two doublet lenses operating at near infinite conjugate ratio. The magnification is adjusted to $\times 3.78$. The corresponding pixel size in object space is $A = (3.4 \mu\text{m})^2$. We deduce the incoming and transmitted intensities from the signal S_i deposited on the pixel i , knowing the imaging pulse duration and having established that the camera has a linear behavior. The mechanical vibrations are corrected for each pixel by using a reference picture. It is taken with a short delay of the order of ten ms using the fast frame-transfer readout of the camera. The incoming intensity is taken from a second picture without atoms, assuming that the two intensities were identical before reaching the camera. To correct possible mismatches, a correction factor is computed in a region without atoms.

The deduced signal is the uncalibrated number of atoms. Experimentally, the imaging is performed at intensity far below saturation ($I \ll I_{\text{sat}}$). In this case, the optical density $\sigma \tilde{n}$ obtained by integration of Eq. (2.53) follows the Beer Lambert law and the total atom number reads:

$$N = A^2 \frac{\alpha}{\sigma} \ln \left(\frac{I_i}{I_t} \right), \quad (2.55)$$

where A^2 is the surface of a camera pixel, $I_{i,t}$ refer to the incoming beam intensity and the transmitted one after propagation through the cloud respectively. Far below saturation, the atom number depends linearly on α .

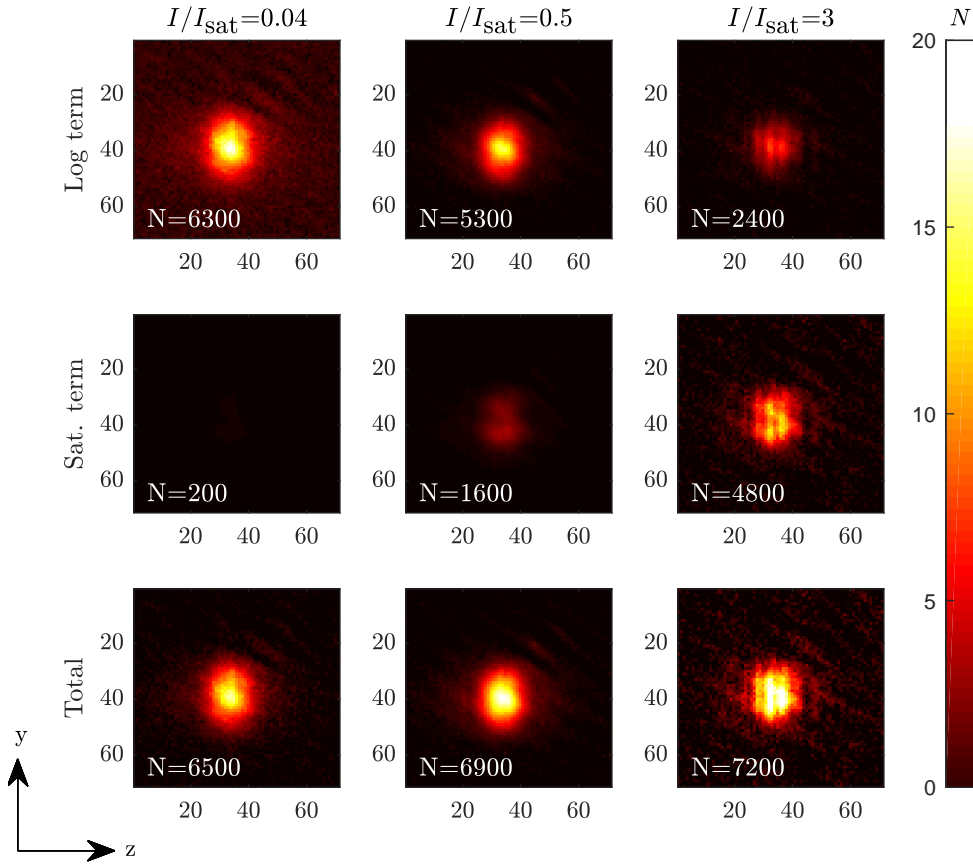


Figure 2.18: Typical absorption images at various imaging intensities. The pictures are computed after 6 ms TOF for a number of scattered photons $N_{\text{ph}} = 200$ photons/at. The axes are in pixels. **Top row:** Contribution of the calibrated logarithmic term of Eq. (2.54) to the atom number. We observe that the contribution decreases at higher intensities. **Middle row:** Contribution of the saturation term of Eq. (2.54) to the atom number. This contribution increases with the imaging intensity. **Bottom row:** Total atom number obtained by summing the logarithmic and saturation term and equal to $N \approx 6800$ atoms. The slight increase in atom number is principally due to the increasing noise at high intensity. The fringes originate from the beam diffraction on the chip.

The calibration parameter α has been determined using two techniques. A first one relies on imaging at high intensity. The second one consists in deducing the total atom number from the length of the atomic cloud along the direction of elongation.

Calibration of the atom number by imaging above saturation Equation (2.54) shows that the two contributions to the beam absorption present a different dependence on α . While the first term, dominant at low intensity, presents a linear dependence, the second term, dominant above saturation, is independent of α . When changing the imaging intensity, the contribution of both terms is modified as displayed in Fig. 2.18 for $I = [0.04, 0.5, 3]I_{\text{sat}}$. For a constant atom number and a constant number of emitted photons, the sum of both terms must remain constant under a variation of imaging intensity, which is only the case for the calibrated value of α .

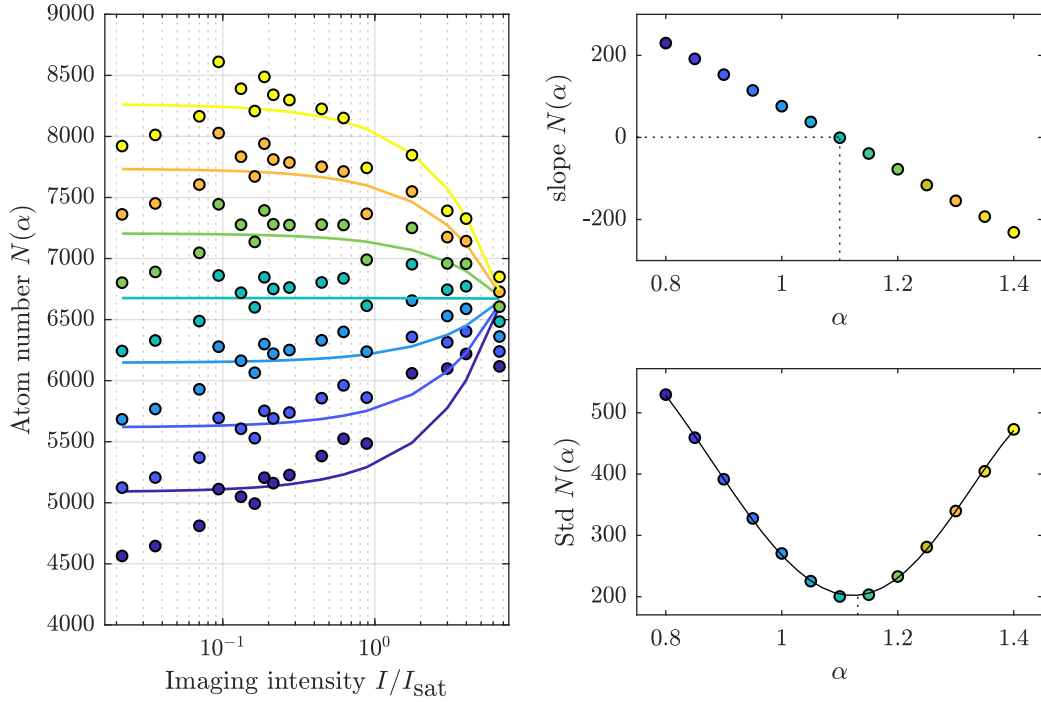


Figure 2.19: Calibration of the absolute atom number in absorption. **Left:** Total atom number versus the imaging intensity computed using Eq. (2.54) for various values of α . α is varied between 0.8 (blue dots) and 1.4 (yellow dots). The lines are the associated linear fit. The calibrated value of α is the one maintaining the atom number constant. **Top right:** Slopes of the linear fit of $N(\alpha)$ showing that a constant atom number is reached for $\alpha = 1.1$. **Bottom right:** Width obtained from a Gaussian fit of the atom number distributions at the various imaging intensities for various values of α . The calibrated value of α is the one minimizing the width. A clear minimum is found at $\alpha = 1.12$. In this case, the atom number is $N = 6764$ atoms.

The calibration measurement used in [133] consists in changing the imaging intensity between $0.02I_{\text{sat}}$ to $8I_{\text{sat}}$ maintaining the number of scattered photons constant by adjusting the pulse duration. We verify that the CCD camera presents a linear behavior when changing the intensity and we adjust the pulse duration to maintain the photon number unchanged according to Eq. (2.50). We make sure that the Doppler shift is negligible.

The determination of α is presented in Fig. 2.19 for $N_{\text{ph}} = 200$ photons/at. We determine the atom number $N(\alpha, I)$ using Eq. (2.54) and modify α . The atom number as a function of the imaging intensity presents a slope depending on α (top panels). The calibrated value of α is the one giving a zero slope. Equivalently, the distribution of $N(\alpha, I)$ can be fitted by a Gaussian and the calibrated value of α is the one minimizing the Gaussian width (lower panels). The measurement has been repeated for various numbers of scattered photons below the Doppler limit and resulted in comparable values of α .

Calibration of the atom number using the condensate extension An independent calibration method consists in deducing the atom number from the longitudinal extension of the condensate using the mean-field formalism of Sec. 1.2.4.

We briefly justify the validity of a mean-field treatment in that case. It applies to

a condensate at equilibrium. In our system, degeneracy is reached by performing an evaporative cooling using radio-frequency fields susceptible to excite a breathing mode of the condensate. This mode expands and shrinks the size of the cloud and would result in an error of the estimate of the cloud size and atom number. We measure the breathing amplitude by holding the condensate in the trap for various durations after evaporation. The condensate extension only showed negligible variation over time such that we consider the cloud at equilibrium.

The mean-field model is an *in-situ* description, which can be used as long as the expansion of the cloud is negligible. For this, we limit the time-of-flight to 2 ms, which is the shortest value reachable without distortion of the image due to the diffraction of the imaging light on the chip.

We also assume a pure BEC. For this, we measure the thermal fraction and place ourselves in a regime where it is below 10%. This was done using the single atom sensitivity fluorescence imaging described in the next section.

In the mean-field formalism, we establish in Sec. 1.2.4 that the density distribution of a condensate elongated along the z -axis reads:

$$n_{1D}(z) = \frac{\beta}{16a_s} \left[\beta \left(1 - \frac{z}{L(\beta)} \right)^2 + 4 \right] \left[1 - \left(\frac{z}{L(\beta)} \right)^2 \right]. \quad (2.56)$$

β obeys⁷

$$\beta^3(\beta + 5)^2 = \left(15 \frac{Na_s}{a_{\perp}a_{\parallel}} \right)^2, \quad (2.57)$$

with N the total atom number, a_s the s-wave scattering length, $a_{\parallel,\perp}$ the longitudinal and transverse harmonic oscillator lengths respectively. In Eq. (2.56) L is the half-length of the condensate defined by:

$$L(\beta) = \sqrt{\beta} \frac{a_{\parallel}^2}{a_{\perp}}. \quad (2.58)$$

β , and therefore the atom number, affects both the condensate length and the peak density n_0 obtained by evaluating Eq. (2.56) for $z = 0$:

$$n_0 = \frac{\beta}{16a_s}(\beta + 4). \quad (2.59)$$

Therefore, the longitudinal density profile allows to determine the atom number and only requires to know the pixel size in object space and the trap frequencies $a_{\perp,\parallel}$.

The longitudinal profiles, such as displayed in Fig. 2.20 are obtained after integration of the absorption picture along the y -axis. The z -axis is expressed in microns and the atomic density profile is obtained in counts/microns. The fit function is:

$$n_{1D}(z) = \max \left[n_{\text{off}}, \kappa \frac{\beta}{16a_s} \left[\beta \left(1 - \frac{a_{\perp}(z - z_0)}{\sqrt{\beta}a_{\parallel}^2} \right)^2 + 4 \right] \left[1 - \left(\frac{a_{\perp}(z - z_0)}{\sqrt{\beta}a_{\parallel}^2} \right)^2 \right] + n_{\text{off}} \right], \quad (2.60)$$

⁷ β is noted α in Sec. 1.2.4 and [74]. We replace the notation for clarity.

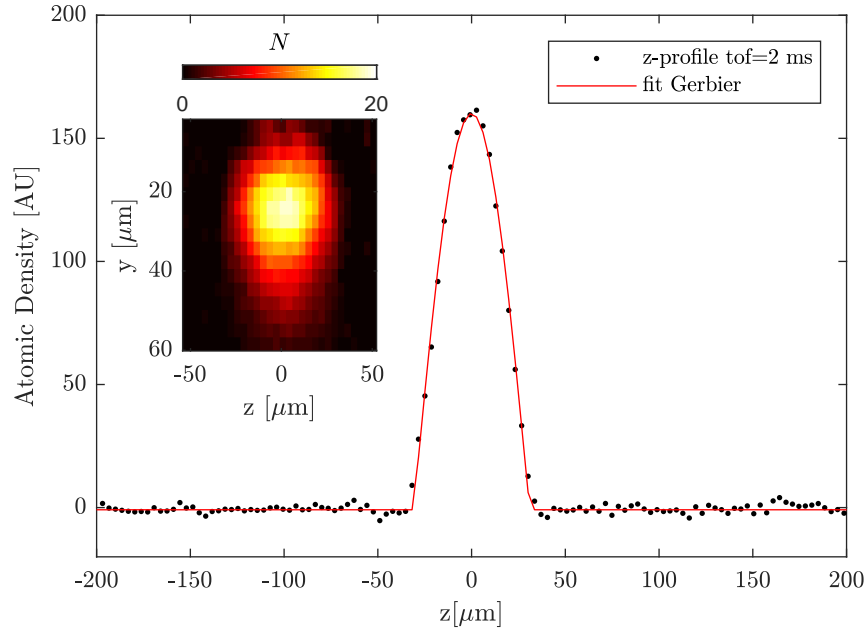


Figure 2.20: Longitudinal profile after TOF=2 ms averaged over 20 individual realizations. The profile is fitted with Eq. (2.60) to obtain the length of the condensate (in this case $L = 31 \mu\text{m}$) and the total atom number $N = 3500$ atoms. **Inset:** Averaged absorption picture before integration along the y -axis.

where the fit parameters are β , n_{off} the baseline signal, z_0 the center of the profile and κ a conversion factor between counts and atoms. κ accounts for the deviations to the two-mode model at short time-of-flight. While the length of the condensate is very well determined at such short TOF, the cloud is very dense and the quantization axis is not fully established such that the total integrated signal is not suitable to deduce the atom number. The parameter β extracted from the fit provides the calibrated atom number.

The uncalibrated atom number is obtained from the total absorption signal measured at longer TOF, where the two-level approximation is better realized. The comparison of the calibrated and uncalibrated values of the atom number yields $\alpha = 1.13(15)$, which is compatible with the value obtained by the imaging above saturation technique.

2.4.1.2 Light sheet fluorescence imaging

The fluorescence imaging illustrated in Fig. 2.17 consists in measuring the photons emitted by the atoms when they are illuminated by a resonant laser beam. After a fixed TOF of 46 ms, the atoms pass through a thin resonant light obtained by two counter propagating beams, referred to as light sheet. The emitted photons are imaged through the bottom window of the science chamber. Due to the imaging in the xz -plane, the fluorescence imaging system is used to probe the physics of atoms in a double-well potential.

Imaging beams and atom trajectory To perform a 46 ms TOF, we superimpose two counter-propagating laser beams approximately 1 cm below the atom chip. The beams are resonant with the cycling transition of the atoms and a repumper beam is superimposed

to one of the imaging beams to transfer the atoms into the imaging transition. To reduce the time the atoms spend in the imaging beams, the latter are made very thin along the vertical axis and are consequently called light sheet (LS). The anisotropy is obtained by using an optical fiber, leading to a collimated beam of waist 4.5 mm, followed by a cylindrical lens to obtain a vertical waist of 20 μm . The intensity in the counter-propagating beams is identical to cancel the net radiation pressure. The intensity is controlled by an AOM and is stabilized every second cycles by measuring a fraction of the optical power and automatically re-adjusting the AOM amplitude accordingly.

Each atom takes about 100 μs to cross the LS and scatters few hundreds of photons. In the LS, the atoms perform a random walk in momentum space due to stochastic absorption and emission events. It follows that each atom appears as an irregular and blurred shape. The detail of the trajectory is a complex problem investigated in detail in [27]. Assuming that the LS beams are well balanced, the trajectory of the atoms in the xz -plane can be summarized by three major contributions which have been estimated by comparison of experimental data and Monte-Carlo simulations.

The first one is the centroid deviation. It accounts for the fact that all scattering events lead to a displacement of the undisturbed atom in the xz -plane. On average, the displacement is $\bar{R}_c \approx 10 \mu\text{m}$ with an isotropic probability. The deviation itself is a normal distribution of standard deviation $\Delta R_c \approx 3 \mu\text{m}$. From the centroid deviation only, it results that a large number of atoms of undisturbed position ($x = 0, y = 0$) would be imaged as a ring or radius \bar{R}_c and RMS width ΔR_c . In addition, each atom is imaged as a optical point spread function of rms width 7 μm . The collected photons are spread over this normal distribution (rotation invariant in the xz -plane). Finally, the number of photons emitted per atoms fluctuates due to the photon shot noise. The number of fluoresced photons per atoms follows a normal distribution centered on \bar{p} and of RMS width $2\sqrt{\bar{p}}$. All these effects tend to limit the resolution, allowing nonetheless a single-atom sensitivity [27].

EMCCD and picture analysis About 2% of the emitted photons are collected by high-numerical aperture lens system and reach a CCD chip where they are converted into primary photoelectrons with a quantum efficiency of 72%. The main technical noise caused by the camera originates from the clock-induced electrons due to the pixel row shifting during read-out. They are inherently indistinguishable from real photons and are corrected for each image taken by a second picture taken without light.

The primary electrons are then amplified to typically 250 secondary electrons. The amplification process is stochastic and has to be described by a probability distribution function of secondary electrons for a given count of primary electrons. Finally, the secondary electrons are converted to a voltage and digitized by a readout unit (RU). The analogue to digital conversion contributes to the readout noise and converts the signal in counts with a conversion factor of $C2E = 10.63$ counts/secondary electron.

To retrieve the number of photons from the counts, one must determine on the probability distribution the gain, baseline and read-out noise by a fit of the distribution following [27]. To avoid the light scattered by the atoms, the analysis is done on the picture of the clock-induced charges used as calibration image and resembles Fig. 2.21(a).

The main peak is a baseline contribution and corresponds to an offset set by the RU to

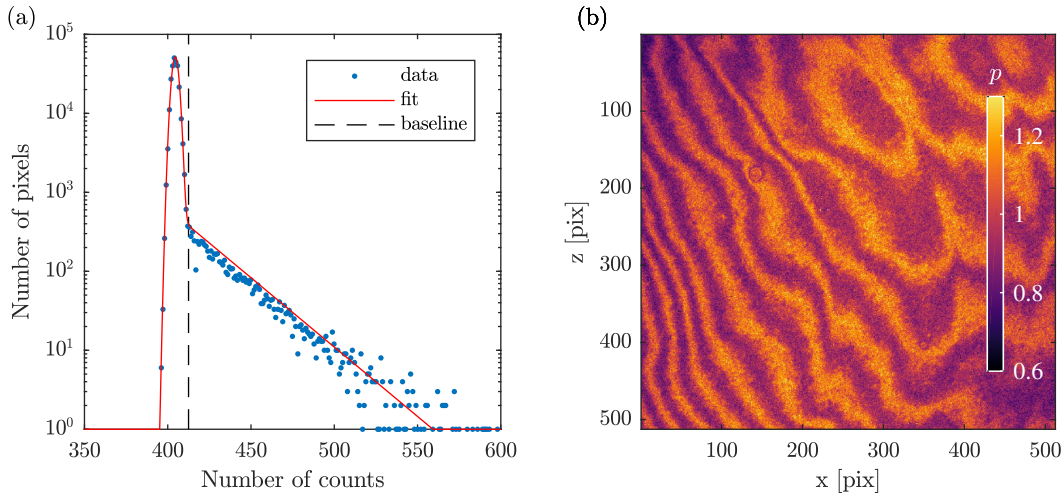


Figure 2.21: Correction of the fluorescence pictures: (a) Distribution of the number of counts per pixel for a calibration picture taken without light. On every picture, the determination of the amplification gain, of the baseline and of the readout noise relies on a fit using Eq. (2.61) (red line). The vertical dashed line delimit the readout cutoff. (b) Etaloning map considered as a pixel dependent gain factor.

avoid negative values of counts. It is centered on a baseline b , typically equal to 400. The width of this contribution is the readout noise σ_{ro} and is typically of 2 counts. The gain is then estimated for counts higher than $b + 2\sigma_{\text{ro}}$. The typical gain is 25. These values are extracted by a fit of the distribution using the fit function:

$$f(x) = \frac{A}{\sqrt{2\pi}\sigma_{\text{ro}}} \times \exp\left(-\frac{(x-b)^2}{2\sigma_{\text{ro}}^2}\right) + \frac{A_2}{2G} \times \exp\left(\frac{\sigma_{\text{ro}}^2}{2G^2} - \frac{x-b}{G}\right) \times \left[1 + \text{Erf}\left(\frac{x-b-\sigma_{\text{ro}}^2/G}{\sqrt{2}\sigma_{\text{ro}}}\right)\right], \quad (2.61)$$

with $A_2 = 0.01 \times A \times \sqrt{2\pi}\sigma_{\text{ro}}$. Erf is the Error Function such that the second contribution of Eq. (2.61) smoothly contributes after the baseline. Identical values of b , σ_{ro} and G are used to recover the photons from the picture with atoms.

An additional background noise is due to the stray light of the light sheet beams. It is evaluated for each shot on the picture with light by measuring the background signal in the four corners of the picture and reconstructing a gradient linking these values. The 2-dimensional mask thus obtained is subtracted from the picture with atoms. Typically, the value in the left corner is $p(1, 512) = 0.063$ while the value in the top right corner is $p(512, 1) = 0.071$. The gradient of background follows the orientation of the light sheet beams, oriented at 45° with respect to the imaging axis.

Finally, the pictures are corrected from the interferences of coherent light on the CCD chip which distort the images. As this effect does not evolve over time, we measure the picture with a uniform illumination, using for this a hot thermal cloud and hundreds of repeat and obtain the Fig. 2.21(b). The processed pictures are divided by the etaloning picture and the final picture is in photon/pixel.

The total number of measured photons is compared to the atom number measured in absorption to determine the averaged number of photon per atom \bar{p} . Typically, $\bar{p} = 12$.

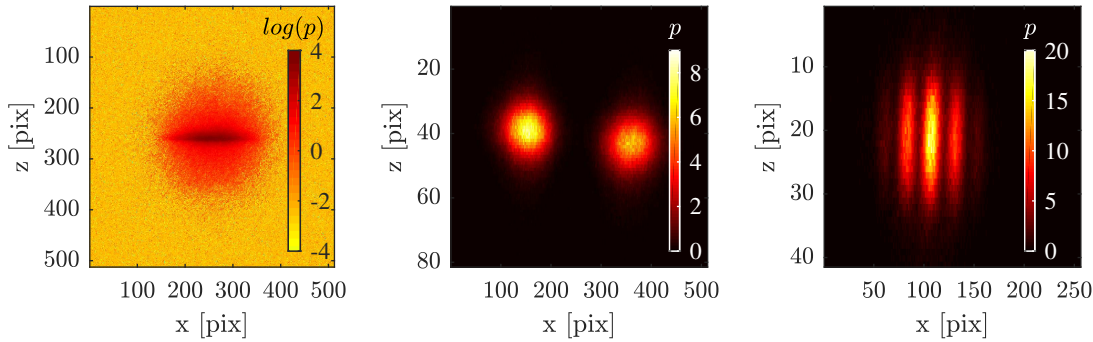


Figure 2.22: Typical fluorescence pictures. Left: Image in logarithmic scale of a single condensate with $\sim 50\%$ thermal fraction. The Gaussian fit along x and z of the thermal fraction gives an estimate of the temperature. Middle: Image of two separated clouds. The difference of intensity gives the atom number difference between the clouds. Right: Interference pattern obtained from the overlap of the wave functions of two condensates. The contrast of the fringes and the position of the maximum of intensity provide informations about the global phase and longitudinal phase coherence.

While this value can be increased by increasing the beam intensity in the LS, this increases the point spread function and decreases the spatial resolution.

This imaging system is used in three situations. In a single-well potential, it provides an accurate measurement of the thermal fraction (left panel of Fig. 2.22) In a double-well potential, the fluorescence imaging allows to image either the individual condensates (middle panel of Fig. 2.22) to access the atom number imbalance or to image the superimposed condensates (right panel of Fig. 2.22) to access phase properties.

Light sheet alignment To cancel the net radiation pressure, the atoms must experience two identical beams propagating in opposite directions. Therefore, this requires identical beams intensity and a good overlap of the beams and of their focuses. The intensity of an incoming beam is divided between the two beams by a wave plate. If the intensity is uneven, the atoms preferentially absorb from one direction and get a corresponding recoil. If the focuses of the Gaussian beams do not perfectly overlap, the picture shows a "tail" as a gradient of intensity along the beam axis (Fig. 2.23). This effect had to be corrected very carefully in the framework of this thesis. Indeed, Fig. 2.23 shows that the alignment can strongly tilt the fringes and decreases the integrated fringes contrast.

The balance of the intensity can be done easily by measuring the photons emitted by a constant number of atoms using each beam in turn. The intensity of both beams is identical when we measure an identical number of photons from each beam. The overlap of the beams is achieved by mechanically translating and rotating one fiber outcoupler while using the other one as fixed reference. A first overlap is obtained by maximizing the intensity transmitted to the reference fiber. A fine tuning is achieved by the analysis of the fluorescence pictures. While a single elongated condensate is sufficient to illustrate the principle, we present the case of interference fringes between two condensates where two quantities allow the beam alignment.

The first one is the asymmetry of the longitudinal profile as observed in the middle

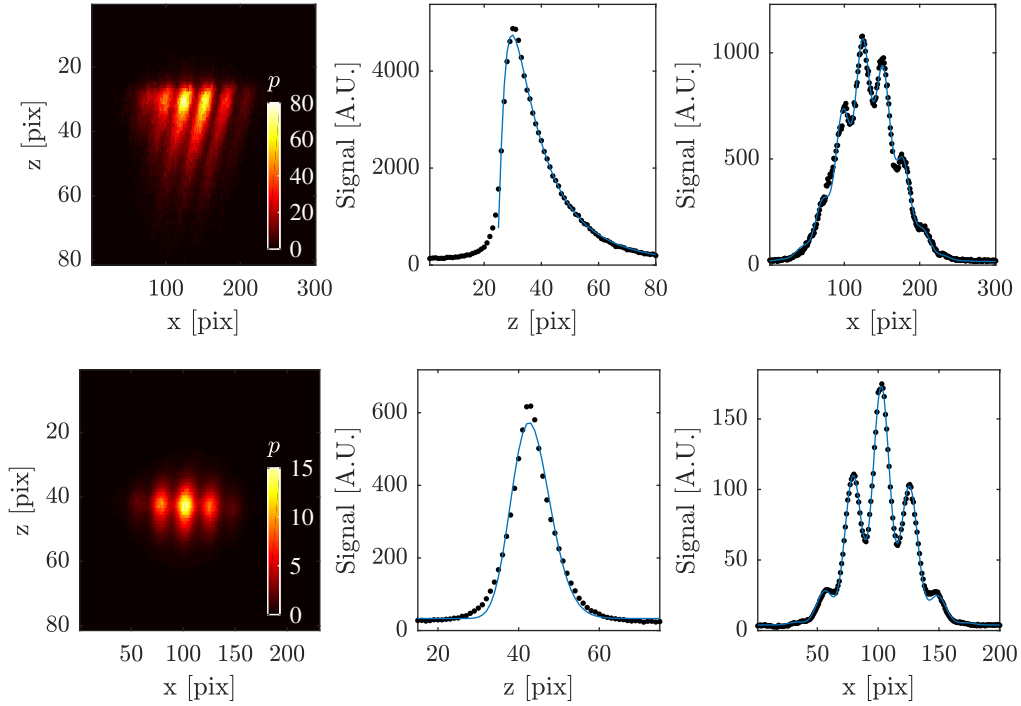


Figure 2.23: Fluorescence images and integrated profiles of two condensates before (top) and after (bottom) alignment of the LS beams. Left: The image with misaligned beams shows a tail of photons as atoms diffused preferentially along one direction. **Center:** Longitudinal profiles showing a strong asymmetry in the misaligned case. The alignment aims at reducing the asymmetry. **Right:** Transverse profiles showing the interference fringes. The misalignment decreases the integrated fringes contrast. The alignment aims at maximizing the contrast.

panels of Fig. 2.23. The asymmetry is quantified by the ratio

$$A = 1 - \frac{z_R - z_0}{z_L - z_0}, \quad (2.62)$$

with z_0 the index of the maximum and $z_{L,R}$ the position of the middle height on the left and right side respectively. In Fig. 2.23, the case where the beams are misaligned leads to $A = 1.3$ while $A = 0$ after beams alignment. The profile can be fitted by an asymmetric fit function inspired from the log-normal distribution. It involves a polynomial growth on one hand competing with an exponential decay which dominates at long time.

The alignment can also be performed using the interference fringes integrated along z . The diffusion is oriented at 45° compared to the direction of integration. The diffusion therefore decreased the integrated fringe contrast as can be seen in Fig. 2.23. The precise determination of the contrast is presented in Sec. 2.4.2.2. An estimate is done by fitting the transverse profile with a modulated Gaussian envelope:

$$p(x) = A \times \exp\left[-\frac{(x - x_0)^2}{2\sigma^2}\right] \times \left[1 + C \cos(2k_0(x - x_0) + \phi_0)\right] + p_b, \quad (2.63)$$

with the fit parameters A , the amplitude of the profile, x_0 , its center, σ the width of the Gaussian envelope, C the fringes contrast, k_0 the wave vector, ϕ_0 the phase and p_b the

background noise. The integrated fringes contrast improved from $C = 0.11$ to $C = 0.43$ after alignment.

2.4.2 Estimation of the relative phase

The state of two condensates in a double-well can be in part characterized by the phase difference and the atomic imbalance. As outlined in the theory chapter, they are the main observables of the tunneling dynamics in the mean field TMBH model. We can experimentally measure the phase difference using atom interferometry [134].

2.4.2.1 Experimental implementation

The measurement is performed by a rapid switch-off of the confining trap, which results in an expansion of the atomic clouds during 46 ms TOF. The atoms expand faster in the transverse direction, for which the trap confinement is stronger. After 46 ms, the distance between the two sites of the trap is negligible compared to the transverse size of the expanded clouds, which results in a full overlap of the wave functions. The phase difference modulates the intensity and results in interference fringes that we image in fluorescence.

The switching-off of the trap involves the rf dressing, the trapping wire and the bias field which unavoidably switch-off with a time mismatch. The atoms therefore experience a strongly changing magnetic field and are projected onto the states $m_F = 0, \pm 1$. During the TOF, the atoms of different m_F states experience residual fields shifting their transverse position. In consequence, the signal is blurred and the fringes are not visible. To address this problem, we apply a longitudinal magnetic field gradient to realize a Stern-Gerlach separation of the three m_F clouds. This is achieved by pulsing a current in the I-wire of the chip mount. The fraction of atoms in each state depends on the exact configuration of the fields during the switch off. We can vary the population by changing the phase of the rf-dressing field at the switch-off. We adjust the phase of the rf-field such that the population of atoms in the $m_F = 0$ state remains constant over the study and preferentially work with this cloud as it is insensitive to magnetic fields during switch-off. The highest constant value reached is 50% of the total atom number in $m_F = 0$.

We define a region of interest including the entire signal of the cloud. The phase is deduced from the fringes integrated along the z -direction, either over the entire region of interest, in which case we speak of integrated phase difference or along parts of the cloud to access local information.

2.4.2.2 Determination of the phase

The most general description of the transverse density profile after TOF consists in a generic envelope $g(x)$ modulated by an interference term.

$$n(x) = g(x - x_0) \left[1 + C \cos \left(k_0(x - x_0) + \phi \right) \right]. \quad (2.64)$$

The pixel x_0 indicates the center of the envelope. The modulation term consists of a cosine contribution with a contrast C between 0 and 1. The fringe spacing is characterized

by the wave vector k_0 . k_0 depends on the distance between the minima of the double-well and on the duration of the expansion. As our experimental TOF duration is fixed at 46 ms, we note k_0 the wave vector evaluated at $t = 46$ ms. ϕ is the relative phase between the two condensates and corresponds to the phase between the modulation and the envelope. Visually, ϕ appears as a displacement of the fringes maximum compared to the envelope maximum.

The parameters C , ϕ , k_0 and x_0 can be deduced from the modulus and argument of the Fourier transform of Eq. (2.64). The latest reads:

$$F(k) = \sqrt{2\pi}G(k)e^{ik \cdot x_0} * \left[\delta(k) + \frac{C}{2}e^{i\phi}\delta(k - k_0) + e^{-i\phi}\delta(k + k_0) \right], \quad (2.65)$$

with $G(k)$ the Fourier transform of the generic envelope, $\delta(k)$ the Dirac distribution and $*$ the convolution product. The contribution $e^{ik \cdot x_0}$ results from the translation in space by x_0 .

Determination of the wave vector and contrast The modulus $|F(k)|$ consists in three peaks of identical width. The central peak is centered on $k = 0$ and corresponds to the envelope term. Its height and width relate to those of the envelope. Two identical side peaks are located in $k = \pm k_0$ and correspond to the modulation term. Their height relates to the fringe contrast.

The accurate determination of the wave vector k_0 requires a fit of $|F(k)|$. In the harmonic approximation, $g(x)$ is a Gaussian such that $|F(k)|$ consists of three Gaussian peaks, the fit of which allows a more precise determinations of the side peaks maximum and the value $\pm k_0$ for which it is reached.

From Eq. (2.65), we deduce that the contrast determines the relative height of the peaks:

$$C = 2 \frac{|F(k_0)|}{|F(0)|}. \quad (2.66)$$

Experimentally, we favor the determination of C_{exp} by averaging the modulus of $F(k)$ over an interval of values of k . The three Gaussian fit provides a good estimate of the width σ of the peaks. We define $\Delta k = 2\ln(2)\sigma$ and deduce the fringe contrast from

$$C_{\text{exp}} = 2 \frac{\left| \int_{k_0 - \Delta k}^{k_0 + \Delta k} F(k) dk \right|}{\left| \int_{-\Delta k}^{\Delta k} F(k) dk \right|}. \quad (2.67)$$

Determination of the phase and influence of the envelope center Following Eq. (2.65), the phase can be deduced from the argument of the Fourier transform evaluated at $k = k_0$

$$\arg [F(k_0)] = \phi + k_0 \cdot x_0. \quad (2.68)$$

The contribution of the envelope center is eliminated by a translation of the x -axis leading to $x_0 = 0$. However, the central pixel is difficult to determine on a single shot and we call δx the error on the determination on x_0 leading to:

$$\arg [F(k_0)] = \phi + k_0 \cdot \delta x. \quad (2.69)$$

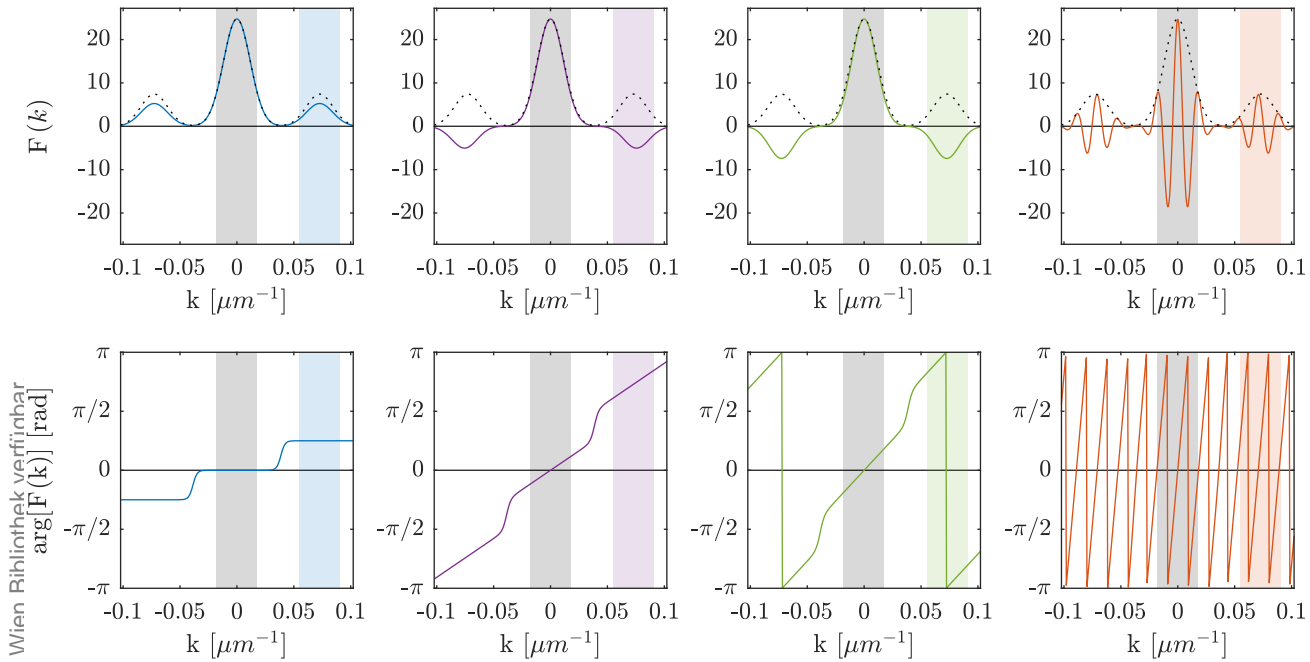


Figure 2.24: Fourier transform of simulated interference patterns. A Gaussian envelope centered on $x_0 = 0$ pix and characterized by $\sigma = 35$ pix, a height 1 is modulated by $k_0 = 0.25$ pix $^{-1}$, $C = 0.6$ and $\phi = \pi/4$. To reproduce the effect of an error of the determination of x_0 , we introduce an offset δx in the Fourier transform. From left to right, δx takes the values $\delta x = 0, 6, 9, 150$ pix. The upper panels display the Fourier transform $F(k)$ (color plain line) and its modulus $|F(k)|$ (dashed black line). The modulus is not affected by δx such that k_0 and C are well determined. The lower panels display the corresponding arguments of $F(x)$. For $\delta x = 0$ the argument presents three plateaus in $-\phi, 0$ and ϕ for the ranges of k corresponding to the three peaks of the modulus. The phase can be read as the value of the argument evaluated in $k = k_0$ or over an interval of k corresponding to the side peak for $k = [k_0 - \Delta k, k_0 + \Delta k]$ (color area). For $\delta x \neq 0$, the argument presents an additional slope δx such that the evaluation of the argument in k_0 or over $k = [k_0 - \Delta k, k_0 + \Delta k]$ does not give direct access to ϕ .

To illustrate the effect of δx , we simulate an interference pattern assuming a Gaussian envelope. Figure 2.24 displays the Fourier transform with its modulus and argument for a simulated Gaussian envelope of width $\sigma = 35$ pix and height 1 centered on the pixel $x_0 = 0$ pix. The modulation of the envelope is characterized by the wave vector $k_0 = 0.25$ pix $^{-1}$, the contrast $C = 0.6$ and the phase $\phi = \pi/4$.

When x_0 is perfectly determined (left column in Fig. 2.24), the argument of $F(k)$ presents three plateaus at the values $-\phi, 0$ and ϕ for the ranges of k corresponding to the three peaks of the modulus. When $\delta x \neq 0$, the argument presents a linear dependence with k with a slope δx as illustrated in Fig. 2.24 for $\delta x = 6, 9, 150$ pixels.

To determine the central pixel x_0 and minimize δx , we minimize the spread of the argument $\arg(F(k))$ for the range of k corresponding to the central peak of $|F(k)|$. We determined the width of the peaks from the three-Gaussian fit. This defines the interval $[-\Delta k, \Delta k]$ (gray area in Fig. 2.24) on which we minimize the variation of $\arg(F(k))$ by changing x_0 . The spread of $\arg(F(k))$ between $\pm \Delta k$ is displayed in the left panel of Fig. 2.25. As expected, the spread of $\arg[F(k)]$ is approximately equal to zero for $\delta x = 0$

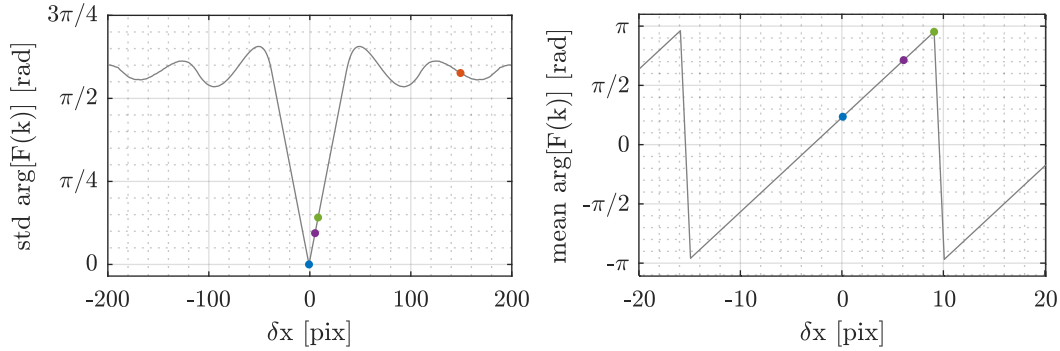


Figure 2.25: Effect of an error δx on the determination of x_0 . **Left:** For $\delta x = 0$, the central pixel is correctly evaluated and the standard deviation of the argument $\text{std}(\arg[F(k)])$ for $k \in [-\Delta k, \Delta k]$ is minimal. The color dots are the values obtained for an error $\delta x = \{0, 6, 9, 150\}$ pix. The linear change of $\arg[F(k)]$ due to δx results in an increase of $\text{std}(\arg[F(k)])$ until the 2π periodicity of the argument leads to a saturation. **Right:** The argument of $F(k)$ averaged over $k \in [k_0 - \Delta k, k_0 + \Delta k]$ coincides with ϕ for $\delta x = 0$ (in this example $\phi = \pi/4$). Any error δx adds a phase contribution linearly dependent on δx and saturating for large δx due to the 2π periodicity.

and increases linearly and in a symmetric way when $|\delta x|$ increases until the argument varies so much between $-\pi$ and π than its standard deviation saturates around $\pi/2$. The right panel of Fig. 2.25 illustrates the change of argument due to δx . If δx is assumed equal to 0 when it is not, it results in a mistake on the phase estimation.

After minimization of δx , the modulus and argument of the integrated fringes resemble Fig. 2.26 and we evaluate the phase by averaging the argument between $k = k_0 \pm \Delta k$:

$$\phi_{\text{exp}} = \arg \left[\frac{1}{2\Delta k} \int_{k_0 - \Delta k}^{k_0 + \Delta k} F(k) dk \right]. \quad (2.70)$$

Alternative method A more visual method consists in fitting the data assuming a Gaussian envelope and using as fit parameters the fringe contrast C , the wave vector k , the phase ϕ , the Gaussian height A and width σ and the central pixel x_0 . As the harmonic approximation is valid for a large range of our experimental parameters, this method gives results compatible the Fourier method.

However, the error on the fit parameters is significant, in particular due to the high correlation between x_0 and ϕ . This method is therefore both less precise and less general than the Fourier transform. It is nonetheless relevant for simulations of the fringes as they require a hypothesis on the shape of the envelope. It is for example the case in sec 2.4.2.4 where simulations are used to correct the experimental fringes from technical noise. For a small number of atoms, it is sometimes interesting to merge the signal corresponding to different m_F states. This is possible when the interference patterns have a similar width, after determination of the central pixel of each cloud. The merging introduces new errors, for example on the central pixels of each clouds and on the width of the clouds, but the merging of the signals leads to a significant improvement of the signal to noise ratio (Fig. 2.26).

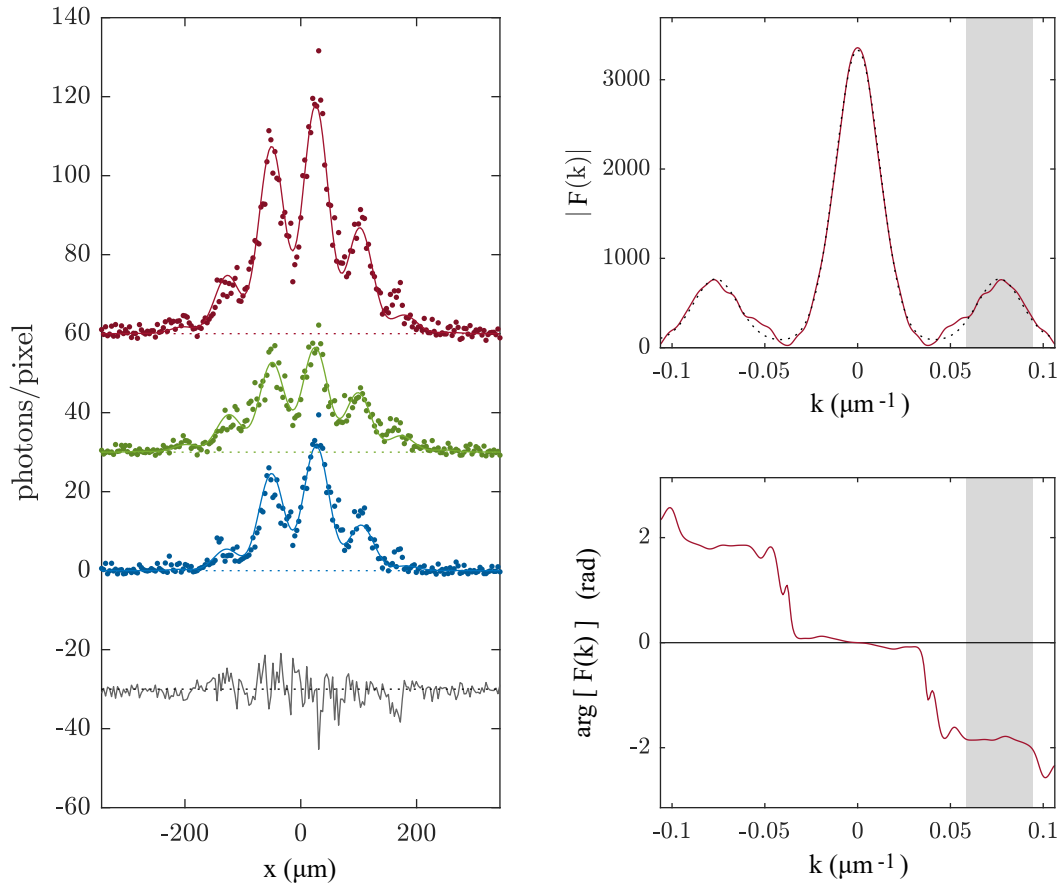


Figure 2.26: Analysis of single-shot interference patterns. **Left:** Transverse profiles integrated over the longitudinal direction of the region of interest and centered on their respective reference pixel. They are shifted along the vertical axis for clarity and their respective baseline is indicated by the dashed lines. The blue and green curves corresponds to the two m_F states containing the highest atom number and the red curve corresponds to the total signal. The dots are the data points and the plain lines are the fit assuming a Gaussian envelope. The gray line is the fit residual for the summed signal. **Right:** Modulus (top) and argument (bottom) of the Fourier transform of the total signal. The gray area corresponds to the area of integration used to determine the phase. The phase extracted from both methods is $\phi \approx -2$ rad.

Limitations The phase analysis from the interference patterns is limited to the case $k_0 \gg \Delta k$, i.e. when the peaks of the Fourier transform can be well resolved. On the interference fringes, this corresponds to a fringe spacing small compared to the envelope width such that many fringes can be resolved. When this is not the case, the phase becomes difficult to extract.

2.4.2.3 Global phase statistics: averaging and fluctuations

The repetition of a measurement in identical conditions tends to increase its reliability. The phase presented on most plots results from the averaging of the global phase obtained from the individual treatment of at least 5 single realizations.

However, the repetition of the phase measurement gives access to more information than simply a reliable phase. From the statistical phase fluctuations, one can compute the statistical phase coherence and distinguish between phase locking and dephasing.

The treatment of phase statistics requires the use of circular statistical tools to account for the 2π periodicity. The probability distribution of a sample of phase values $\{\phi_n\}$ with $n = 1 \dots N$, is represented as a histogram in polar coordinates on the unit circle. The angle of a bin corresponds to its phase and its length indicates the percentage of values ϕ_n it contains.

The circular statistics also define the mean resultant vector $\bar{\rho}$ from which the mean phase and phase coherence are deduced. The mean resultant vector of a sample of N phases values ϕ_n is defined by:

$$\bar{\rho} = \frac{1}{N} \sum_{n=1}^N e^{i\phi_n}. \quad (2.71)$$

The argument of the mean resultant vector is equivalent to the mean value of the phase.

$$\bar{\phi} = \arg(\bar{\rho}). \quad (2.72)$$

The modulus of ρ , named resultant length, is defined by:

$$\bar{R} = |\bar{\rho}|. \quad (2.73)$$

Its value is 0 in the case of a random phase distribution and 1 for a Dirac peak. Therefore, it is equivalent to the statistical phase coherence, more commonly defined as $\langle \cos(\phi_n) \rangle$. The circular standard deviation ϕ_s is defined by:

$$\phi_s = \sqrt{2 \ln(\bar{R})}. \quad (2.74)$$

2.4.2.4 Post selection and noise correction

Phase statistics for post selection The statistical distribution allows the post selection of the data to exclude the experimental shots where the setup behaved irregularly from the analysis. A fast pre-analysis of the data is done to determine on every single realization the atom number, the wave vector and the center of the envelope from a Gaussian fit presented in Sec. 2.4.2.2. These three parameters are expected to follow normal distributions and allow to detect irregular shots. Quantities such as the phase or the fringe contrast are never used to post-select the data.

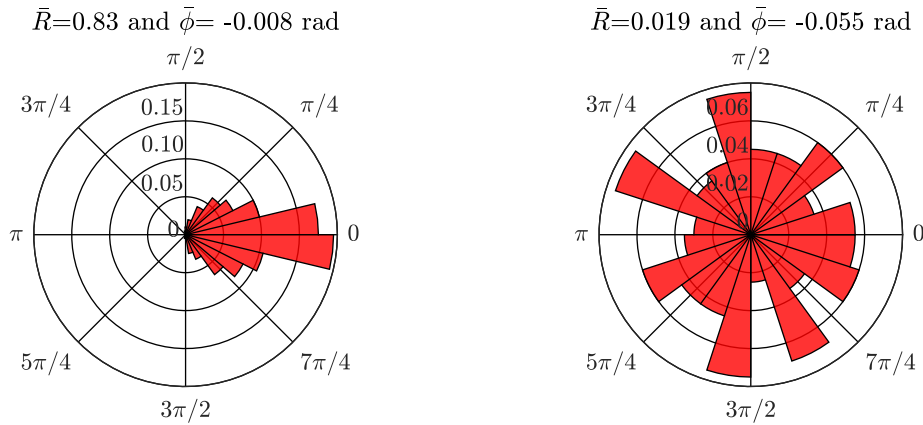


Figure 2.27: Phase distributions in circular statistics for two situations resulting in a zero averaged phase. **Left:** The individual phase values are statistically close to zero, resulting in a narrow distribution of $\bar{R} \approx 1$. This is a signature of a state statistically phase-locked on $\phi = 0$. **Right:** The phase is not statistically reproducible, such that the phase coherence \bar{R} is reduced to 0.02. The averaged phase is $\phi = 0$ as a result of the averaging of values randomly distributed over $[-\pi, \pi]$. This indicates a statistical decoherence.

Noise correction by comparison to simulated patterns The measurement of the interference fringes unavoidable involves detection noises which broaden the measured phase distribution. To estimate the broadening, we simulate a large number of interference patterns in the Gaussian approximation for which we decide the mean values and fluctuations of the phase, contrast and wave vector. A typical noise-free profile is displayed on the left panel of Fig. 2.28. On each simulated patterns, we add the following contributions:

- The statistical noise on the atom number is introduced by choosing N in a Gaussian distribution of width given by the experimental observations.
- The diffusion in the light sheet is taken into account using a simplified model introduced in Sec. 2.4.1.2. From the diffusion in the light sheet, the position of each atom is displaced by a distance corresponding to the centroid deviation, characterized by the normal distribution of mean value $R = 10 \mu\text{m}$ and standard deviation $\sigma_R = 3 \mu\text{m}$. The direction in which the atom is displaced is picked up randomly in the xz -plane using polar coordinates.
- For each one of the N atoms, the number of detected photons is picked up from a normal distribution centered on \bar{p} , the averaged number of photons detected per atom experimentally determined from the calibration presented in Sec. 2.4.1.1, and of width $2\sqrt{\bar{p}}$ reflecting the photon shot noise and the amplification noise of the camera.
- The photons imaged from each atom are not detected exactly at the position of the atom but as a spot, due to the point spread function. They are forming a Gaussian distribution of width $7 \mu\text{m}$.
- The photon positions are finally binned on a grid of $4 \mu\text{m}$ corresponding to the size of the camera pixel in object space.

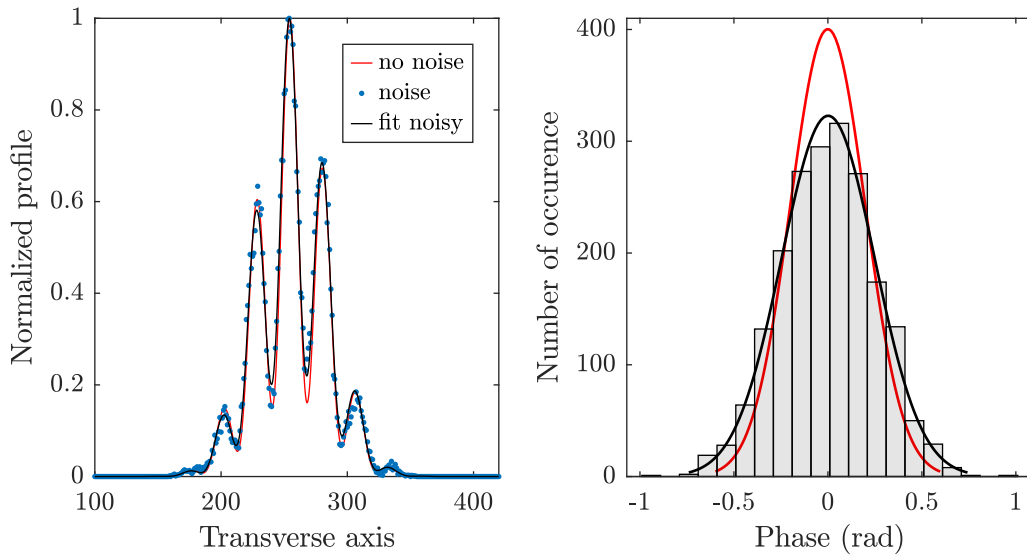


Figure 2.28: Noise impact on single fringe profile and phase distribution. Left: Typical fringe profile. The noise-free profile is generated using the Gaussian approximation and the parameters $k = 0.23$, $\phi_0 = 0$, $\delta\phi_0 = 0.2$, $C = 0.7$ (red line). The noise is implemented, considering the atom number $N = 3500$, the photon per atom $PPA = 10$, the typical imaging parameters and pixel size, and results in the blues dots. The noisy profile is then fitted (black line) to extract the phase. **Right:** The noise-free phase distribution is obtained by generating 2000 patterns with a phase spread of $\Delta\phi = 0.2$ (red line). The noise leads to a broadening of the distribution, in this case $\Delta\phi = 0.23$ (black line).

A typical noisy profile integrated along z is presented in the left panel of Fig. 2.28. A Gaussian fit of this profile allows to extract the phase. Doing this on a large number of simulated profiles with a phase sampled in a Gaussian distribution, we can compare the phase distributions with and without detection noise and estimate the broadening coefficient. This is displayed on the right panel of Fig. 2.28 for 2000 simulated profiles.

Pixel size We learn from the simulations the main source of error on the phase determination is the imaging resolution. The phase corresponds to a fringe displacement and the evaluation of this displacement is limited by the pixel size. By convention, we consider that the Gaussian modulation reads $\cos(kx + \phi)$ such that a phase of π corresponds to a fringe displacement of half a fringe spacing, i.e. π/k in pixel units. The smallest displacement measurable is one pixel therefore the phase can be determined by steps of $\phi = k$ with k the value of the wave vector in inverse pixel unit. The larger the wave vector, the less precision on the phase determination. This sets the minimal value of the noisy distribution, even for a perfectly narrow noise-free phase distribution.

The effect of the pixel size appears clearly when simulating the broadening for a set of noise-free distributions. Fig. 2.29 compares the broadening of the noise-free phase distribution width between $\Delta\phi_{\text{nf}} = [0, 0.7]$ rad for two values of the wave vector. Experimentally, these parameters correspond to a strong and weak tunnel coupling respectively. The atom number is $N = 3500$ atoms and the fringe contrast is $C = 0.7$.

For $\Delta\phi_{\text{nf}} = 0$, the noise due to the pixel size introduces a large broadening, comparable to $k/2$, the half-pixel resolution. For $\Delta\phi_{\text{nf}} < k$, the broadening does not strongly depend

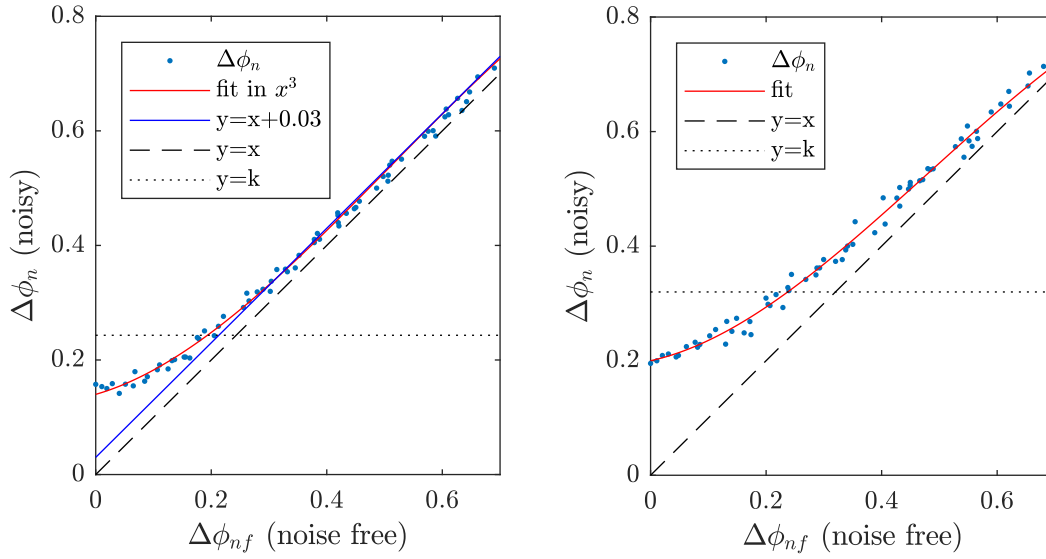


Figure 2.29: Broadening of the phase distributions. The noise-free distribution width is varied between $\Delta\phi_{\text{nf}} = 0$ rad and $\Delta\phi_{\text{nf}} = 0.7$ rad for $k = 0.23$ (left) and $k = 0.32$ (right) in units of inverted pixels, $C = 0.7$, $\phi = 0$. The statistics are computed from 200 simulated patterns in each case. For small $\Delta\phi_{\text{nf}}$, the broadening is very large, dominated by the error introduced by the pixel size. In this regime, knowing $\Delta\phi_{\text{n}}$ does not allow a precise determination of the corresponding noise-free distribution. For larger $\Delta\phi_{\text{nf}}$, the broadening resembles an offset. For $k = 0.23$ (left), a polynomial fit yields $\Delta\phi_{\text{n}} = -.94\Delta\phi_{\text{nf}}^3 + 1.44\Delta\phi_{\text{nf}}^2 + 0.29\Delta\phi_{\text{nf}} + 0.14$ (red line) and is similar to $\Delta\phi_{\text{n}} = \Delta\phi_{\text{nf}} + 0.03$ (blue line) for $\Delta\phi_{\text{nf}} > k$. For $k = 0.32$ (right), $\Delta\phi_{\text{n}} = -\Delta\phi_{\text{nf}}^3 + 1.44\Delta\phi_{\text{nf}}^2 + 0.22\Delta\phi_{\text{nf}} + 0.2$ the error introduced by the pixel size is larger.

on the noise-free distribution. In this regime, the correction can be done by a polynomial fitting of the $\Delta\phi_{\text{n}}$ as a function of $\Delta\phi_{\text{nf}}$ but the correction is not very precise. For $\Delta\phi_{\text{nf}} > k$, the broadening is close to an offset on the noise-free distribution and the noise correction is unambiguous.

Aside from the wave vector and noise-free phase distribution width, many parameters are susceptible to affect the broadening: mean phase, mean contrast and contrast distribution, wave-vector distribution, atom number... Therefore, to estimate the broadening on every data set, we developed a routine which determines, for the noisy experimental distribution and for fixed imaging parameters, the corresponding noise-free phase distribution. This is expected to correspond to the phase fluctuations of the system discussed in Sec. 1.3.4.

2.4.3 Estimation of the atom number difference

2.4.3.1 Experimental implementation

The atom number difference is measured after 46 ms TOF. However, in order to measure the atom number on each site, the overlap of the wave functions must be prevented. Experimentally, this is achieved by a fast modification of the trap geometry following two possible protocols.

Separation without crossing Figure 2.30(a). In this approach, the barrier separating the clouds is quickly ramped to a high value to displace the trap minima further away from each other and increase the slope of the confining potential. In this context, the change of trapping geometry is non-adiabatic compared to the time-scale of the dipolar motion in the trap. Consequently, the transverse position of the atoms right after the change of geometry does not match the trap minima any longer and the atoms experience a transversal kick toward the new trap minima. By switching off the trap after the momentum transfer, we can make the clouds fly in opposite direction and prevent the wave functions overlap.

The separation between the clouds after TOF depends on the displacement of the trap minima and on the duration before switch-off. The maximal kick is obtained by maximizing the trap minima displacement (therefore we increase the dressing amplitude to its maximal value) and by holding the atoms in the trap until the atoms reach the new trap minima. Assuming that the change of trap geometry is instantaneous, the atomic clouds are still at the same transverse position right after separation such that they are at an extrema of amplitude of the dipolar motion triggered by the change of geometry. The frequency of the dipolar mode is identical to the frequency of the separation trap $f_x = 2.4$ kHz. The holding time corresponding to the maximal acceleration of the clouds is the quarter of a dipolar oscillation period: $t_h \approx 0.1$ ms.

This method limits the deformation of the clouds but it fails to give a kick to the tail of the wave functions located in the barrier.

Separation with crossing Figure 2.30(b). The principle of the second protocol consists on the contrary in decreasing the dressing amplitude to reach a single-well geometry. The atomic clouds evolve toward the new position of the single minimum and get accelerated toward each other. The maximal acceleration is acquired when the clouds reaches the trap minimum. The trap is switched off and the clouds propagate in opposite direction after crossing. To maximize the effect, we first separate the clouds to a trap of large well spacing in a time longer than the dipolar motion time-scale of the clouds. The change toward a static trap is performed in $360 \mu\text{s}$.

2.4.3.2 Noise correction and number squeezing factor

The measurement of the atomic imbalance is affected by the detection noise which broadens the imbalance distribution. This correction is more straightforward than for the phase, as it simply consists in evaluating the contribution of the detection noise to the measured signal.

The atom number in the left and right site of the double-well is determined by integrating the photon signal in two regions of interest (ROI) around the left and right clouds. On each of the A pixels of the ROI, a background signal contributes to the measured signal such that the total signal in the left and right ROI reads:

$$S_{L,R} = \sum_{i=1}^{N_{L,R}} p_i + \sum_{j=1}^A b_j. \quad (2.75)$$

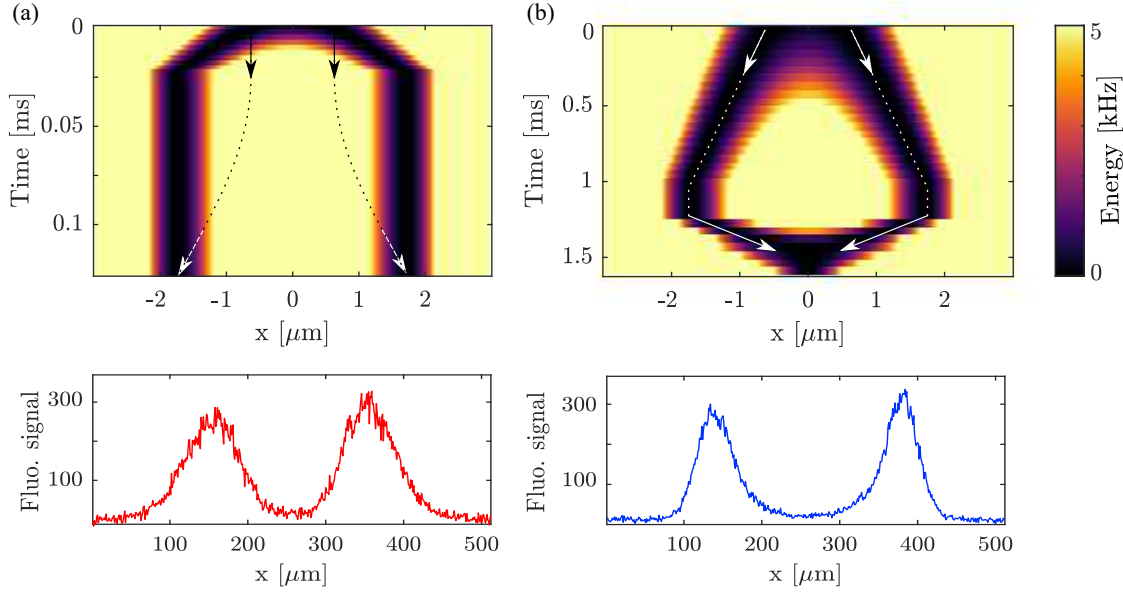


Figure 2.30: Protocols to measure the atomic imbalance. The upper plots display the simulated transverse trap potential over time. The trap minima are the darker regions. The color scale is saturated at 5 kHz for clarity. The dashed lines sketch the center of motion of the two clouds, and the arrow at final time indicates the direction of the momentum transferred to the clouds. **(a) Separation without crossing.** The distance between the trap minima is increased quasi-instantaneously to displace the atoms from the trap minima. The two atomic clouds evolve toward the new trap minima and reach it after a quarter of a dipolar oscillation. At this time, their momentum is maximal and switching off the trap results in the propagation of the clouds in opposite direction. The lower panel is an experimental profile integrated along z . This separation protocol limits the deformation of the clouds and the distance between them. **(b) Separation with crossing.** The distance between the trap minima is slowly increased (1 ms). After a short waiting time, the dressing is turned off in 0.4 ms such that the atomic clouds experience a single trap and evolve toward the new minimum. They acquire a velocity and evolve toward each other. After switch-off, the clouds cross and evolve afterward in opposite directions. The separation with crossing leads to a significant deformation of the clouds and limit their overlap.

The noise is indistinguishable from the signal and is therefore evaluated in a region without atoms having the same size as the ROI (left panel in Fig. 2.31). We note B the noise signal integrated over the A pixels. By repeating the measurement numerous time, we build the distribution of the fluorescence signal imbalance $s = S_L - S_R$. It follows a Gaussian distribution, the variance of which reads:

$$V(s) = \bar{p}V(N_L - N_R) + 2\bar{p}N + V(B), \quad (2.76)$$

with \bar{p} the average number of photon per atom and N the averaged number of atoms. In Eq. (2.76), the first term originates from the atomic number squeezing while the two other terms correspond to the detection noise (photon detection noise and background noise respectively). The term $V(s)$ is measured from the individual measurements of $S_{L,R}$, $\bar{p}N$ corresponds to $\langle S_L + S_R \rangle - \langle B \rangle$ the averaged signal difference to which we subtract the averaged value of the integrated noise. Therefore, we can deduce the width of the normalized imbalance corrected from detection noise:

$$\Delta n = \frac{\sqrt{V(N_L - N_R)}}{N} = \frac{\sqrt{V(s) - 2\bar{p}N - V(B)}}{\bar{p}N} \quad (2.77)$$

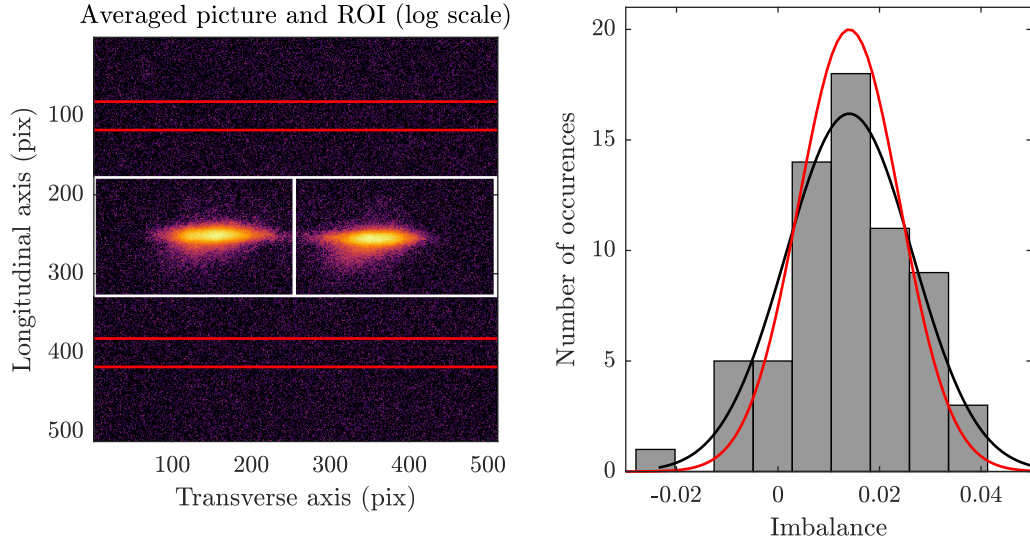


Figure 2.31: Imbalance treatment and noise correction. **Left:** Averaged fluorescence picture in log scale displaying the two regions of interest in the area delimited by the white squares, as well as the regions where the background noise is estimated (between the red rectangles above and below the clouds). **Right:** Imbalance distribution for 53 repetitions and fit (black line). It results in an averaged imbalance $\bar{n} = 0.014$ and a width of $\Delta n = 0.013$. Taking onto account the detection noise allows a correction of the distribution width to $\Delta n = 0.01$. The red line corresponds to the corrected Gaussian distribution. The number-squeezing factor is $\xi_N = 0.56$.

which is narrower than the one without correction:

$$\Delta n_{\text{un}} = \frac{\sqrt{V(s)}}{\langle S_L + S_R \rangle} \quad (2.78)$$

and the number squeezing factor reads:

$$\xi_N = \sqrt{N} \Delta n = \sqrt{\frac{V(s) - 2N\bar{p} - V(B)}{\bar{p}^2 N}}. \quad (2.79)$$

In Fig. 2.31, the width of the uncorrected imbalance distribution is $\Delta n_{\text{un}} = 0.013$, corresponding to a number squeezing factor of $\xi_{N,\text{un}} = 0.69$. After detection noise correction, the width of the imbalance distribution is reduced to $\Delta n = 0.01$ and the number squeezing factor is $\xi_N = 0.56$. In this case, the detection noise degrades the number-squeezing factor by 25%.

3 Relaxation of the Josephson oscillations in a 1D-BJJ

The 1D-BJJ presents a rich many-body dynamics partly due to its elongated character. For example, [135] uses MCTDHB [136] to compute numerically the exact quantum dynamics of a small number of atoms. It shows that the Josephson oscillations predicted in the 0D case are susceptible to exhibit additional collapses and revivals, as well as a fragmentation of the exact wave function. A compatible result is obtained for larger atom number in [38] using the truncated Wigner approximation and the truncated conformal space approach.

Cold atoms are known for their tunability and high controlability. Therefore, the initial state of the 1D-BJJ can be precisely prepared to explore situations with various degrees of complexity. In this chapter, we focus on the situations the closest to the 0D predictions, for which the initial state is characterized by a homogeneous phase difference and no atomic imbalance. In this case, the 1D dynamics predicted by the sine-Gordon model is qualitatively identical to the case described by the TMBH model. It predicts oscillations at a frequency [38] slightly smaller than the plasma frequency of the TMBH model.

Despite being the simplest non-equilibrium dynamics that we can experimentally investigate, it already contradicts both the 1D and 0D predictions.

3.1 Preparation of the initial state

3.1.1 Experimental requirements

The experimental observation of Josephson oscillations requires the preparation of an initial state obeying several constraints that we can classify in two categories.

Limiting longitudinal fluctuations and inhomogeneities The first category covers the requirements allowing us to treat the system in the TMBH framework. As the TMBH model describes 0D system, it approximately applies to the experimental system only if its 1D characteristics are strongly suppressed or take place on a different timescale [137].

For a system elongated along z , it imposes that the local imbalance $n(z, t)$ and local relative phase $\phi(z, t)$ present limited variations along z . In this case, the imbalance and relative phase integrated along z define a global imbalance $n(t)$ and a global relative phase $\phi(t)$ that we identify with the observables of the Bose-Hubbard model.

On the one hand, it implies that the phase and density fluctuations, due to longitudinal phononic modes, must be negligible and ideally identical for both components. On the other hand, the inhomogeneities originating for the harmonic confinement must be limited.

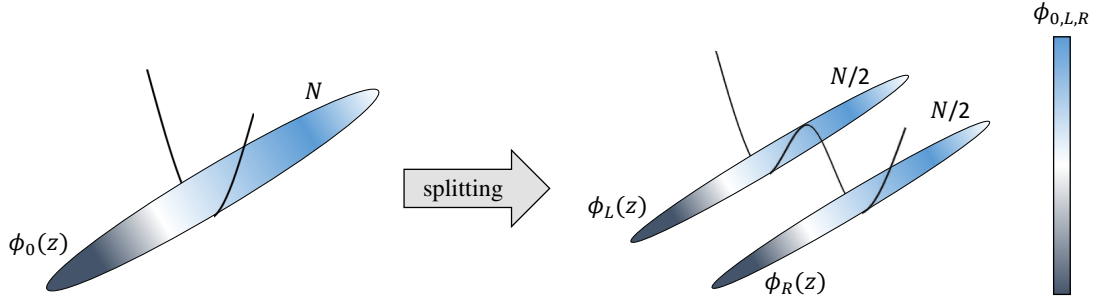


Figure 3.1: Schematic of the symmetric splitting of a 1D-BEC The initial wave function is separated into two components by continuously raising a potential barrier. The phase fluctuations $\phi_0(z)$ of the initial cloud are copied to the two components $\phi_0(z) = \phi_L(z) = \phi_R(z)$. Therefore, the phase difference is homogeneous $\phi = \phi_L(z) - \phi_R(z)$. After splitting the clouds have an identical atom number $N_L = N_R = N/2$ and present identical atomic density $N_L(z) = N_R(z)$. The imbalance $n \propto N_L(z) - N_R(z) = 0$ is insensitive to the longitudinal inhomogeneities.

We presented in Sec. 1.2.4 that the density and extension of the cloud in a harmonic trap depend on its atom number. Therefore, the imbalance is strictly homogeneous only when it is equal to zero.

A protocol limiting both the fluctuations and the inhomogeneities consists in splitting coherently a single wave function into two identical components as illustrated in Fig. 3.1. This is realized by raising a potential barrier while maintaining the detuning ϵ to zero to perform a symmetric splitting of the wave function. In this case, it has been shown in [138–140] that the longitudinal phase fluctuations of the initial cloud $\phi_0(z)$ are transferred to the two wave functions after splitting so that $\phi_0(z) = \phi_L(z) = \phi_R(z)$. Therefore, the phase fluctuations of the two condensates can be limited by reducing those of the single condensate before splitting, for example by working at low temperature (in our case $T \approx 20$ nK). The identical phase fluctuations leads to a homogeneous phase difference $\phi(z) = \phi_L(z) - \phi_R(z) = 0$ in all point of the condensates after symmetric splitting.

In term of atomic densities, the symmetric splitting results in two condensates containing half of the total atom number such that the imbalance is also homogeneous. The consequence of the harmonic trap geometry is investigated in more details in Sec. 4.2.3.2 for a situations where it plays a significant role.

Preparing a coherent non-equilibrium dynamics The second category of constrains refers to the preparation of an initial state that shows an oscillating dynamics. In the TMBH model, the Josephson oscillations are observed for any (ϕ, n) obeying:

$$\frac{\Lambda}{2} n^2 - \sqrt{1 - n^2} \cos(\phi) < 1. \quad (3.1)$$

As a symmetric splitting leads to $n = 0$, any value of the phase $\phi \neq \{0, \pi\}$ results in an oscillating dynamics. According to the equations of motions Eqs. (1.120,1.121), tuning the phase relies on introducing a detuning ϵ to use the phase accumulation term:

$$\dot{\phi}(t) = \frac{\epsilon(t)}{\hbar}. \quad (3.2)$$

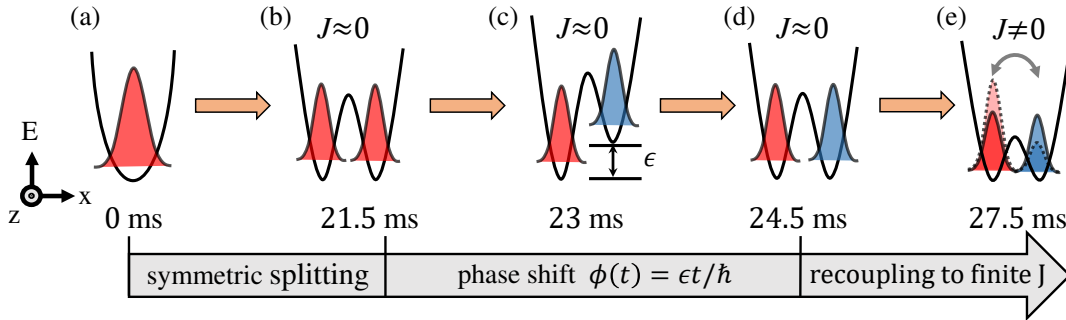


Figure 3.2: Schematic of the preparation of an oscillating dynamics. (a,b) A single wave function is symmetrically split in two components to ensure $n = 0$. (c,d) In a trap of negligible coupling, a detuning is introduced to accumulate a phase according to $\dot{\phi}(t) = \epsilon(t)/\hbar$. The detuning is linearly increased over 1.5 ms and decreased to 0 over the next 1.5 ms to bring back the system in a symmetric trap. (e) The barrier is lowered to increase the tunneling and the dynamics is studied in this final trap.

This implies $J = 0$ and therefore requires that the symmetric splitting is performed up to a barrier height realizing experimentally $J \approx 0$ as represented in the schematic of Fig. 3.2 (a→b). In this case, the detuning can be used to prepare any required phase while maintaining $n = 0$. The detuning $\epsilon(z)$ must be an homogeneous detuning along z to be identified to the parameter ϵ of the TMBH model. After the ramp of ϵ , the initial state is prepared (Fig. 3.2 (b→c→d)). The last step is a symmetric recoupling between the two clouds, to allow a tunneling dynamics, initiated by the phase difference (Fig. 3.2 (d→e)).

The duration of the various steps has a strong impact on the phase coherence of the initial state. Indeed, the preparation of the initial state requires to work in a decoupled trap, where phase diffusion decreases the phase coherence over time. In Sec. 1.3.4.5, we showed that the phase diffusion rate can be decreased by working with a number-squeezed state provided by an adiabatic splitting. Therefore, the duration of the symmetric splitting is defined to maintain the adiabaticity long enough to decrease the imbalance fluctuations after decoupling and limit the phase diffusion during the rest of the preparation sequence. The duration of the remaining steps of the sequence are determined to be as short as possible without exciting dipolar oscillations through either a vertical sloshing when detuning the trap (which involves a vertical displacement) or a transverse sloshing when recoupling the clouds.

In the following, we detail how we experimentally implement these requirements.

3.1.2 Coherent splitting of the wave function by linear ramp

A major asset of the atom chip is the tunability of the trapping potential. We detailed in Sec. 2.3.2.4 that the trap geometry can be modified using the rf fields generated by the chip wires. The intensity in each wires allows a modification of the barrier height corresponding to J in the TMBH model. A modification of the ratio θ between these currents results in an energy shift between the minima of the two sites and control the parameter ϵ of the TMBH model.

The splitting is performed by a linear increase of the dressing amplitudes. The ramp

involves four experimental parameters: the dressing amplitudes of the initial and final trap I_{rf}^i and I_{rf}^f , the ramp duration T and the tilt angle θ .

Determination of the initial single-well potential All traps obeying $I_{\text{rf}} < 0.42$ present a single minimum and the most appropriate initial trap is not obvious. Indeed, while the ramp aims at an adiabatic splitting for the transverse dynamics, the change of trapping geometry is not adiabatic for the longitudinal dynamics. In particular, after defining the double-well potential, the atom number is brutally divided by two without compensation from the longitudinal trap geometry. This leads to a breathing motion at the frequency $\omega = \sqrt{3}\omega_z^f$ [141]. The lower panels in Fig. 3.3 display interference fringes obtained by overlap of two condensates after splitting of a single condensate. After splitting, the two condensates evolve in the final trap for difference durations before being imaged in TOF. The breathing motion appears clearly on the longitudinal extension of the fringes.

The choice of the initial trap aims to limit the amplitude of the breathing motion. We compare two ramps of $T = 10$ ms to the final trap $I_{\text{rf}}^f = 0.65$ of frequency $\omega_z = 2\pi \times 13$ Hz.

The first ramp starts from the harmonic single-well trap characterized by $I_{\text{rf}}^i = 0$. In this case, the initial longitudinal frequency is $\omega_z = 2\pi \times 22$ Hz, i.e. almost twice larger than the one of the final trap. The dependence of ω_z with I_{rf} is displayed in Fig. 2.16. It shows that during the splitting ramp, the trap is first decompressed in the longitudinal direction, before being compressed again once a double-well is defined. The longitudinal extension after TOF is displayed in Fig. 3.3 (orange curve) for various holding times. The longitudinal extension of the fringes shows oscillations at the frequency compatible with the one of a breathing motion. The second ramp limits the change of longitudinal frequency during the splitting, similarly as [107]. To this aim, the initial trap is dressed with $I_{\text{rf}}^i = 0.3$, corresponding to a quartic trap obtained for a dressing amplitude slightly below the double-well threshold. This avoids the decompression of the single-well trap. The resulting breathing motion is displayed in Fig. 3.3 (purple curve).

From this comparison, we deduce that it is preferable to start from the harmonic single-well even though this maximizes the change of longitudinal geometry. Optimized ramps have been discussed in [142] in the context of our experiment.

Determination of the final double-well potential To prevent an evolution of the imbalance during the phase preparation, the splitting is performed toward a decoupled final trap. Experimentally, decoupled refers to any trap configuration in which the tunneling timescale is slow compared to the timescale of the preparation sequence. This corresponds to a rather large range of intensities I_{rf} . However, there is no advantage in splitting to a strongly decoupled trap. The description provided in Sec. 1.3.4.6 shows that after breaking the adiabaticity, the phase diffuses and its coherence decreases. By splitting to a double-well potential with high barrier, the system is likely to spend a large duration of the ramp in decoupled traps, resulting in a lower phase coherence after splitting.

We check that the final trap is decoupled and symmetric by measuring the phase and imbalance after different waiting times. The trap is decoupled if n remains constant and $\Delta\phi$ increases and it is symmetric if ϕ remains constant. The symmetry of the trap is determined by varying the detuning through θ and we call θ_s^f the angle for which the trap is symmetric.

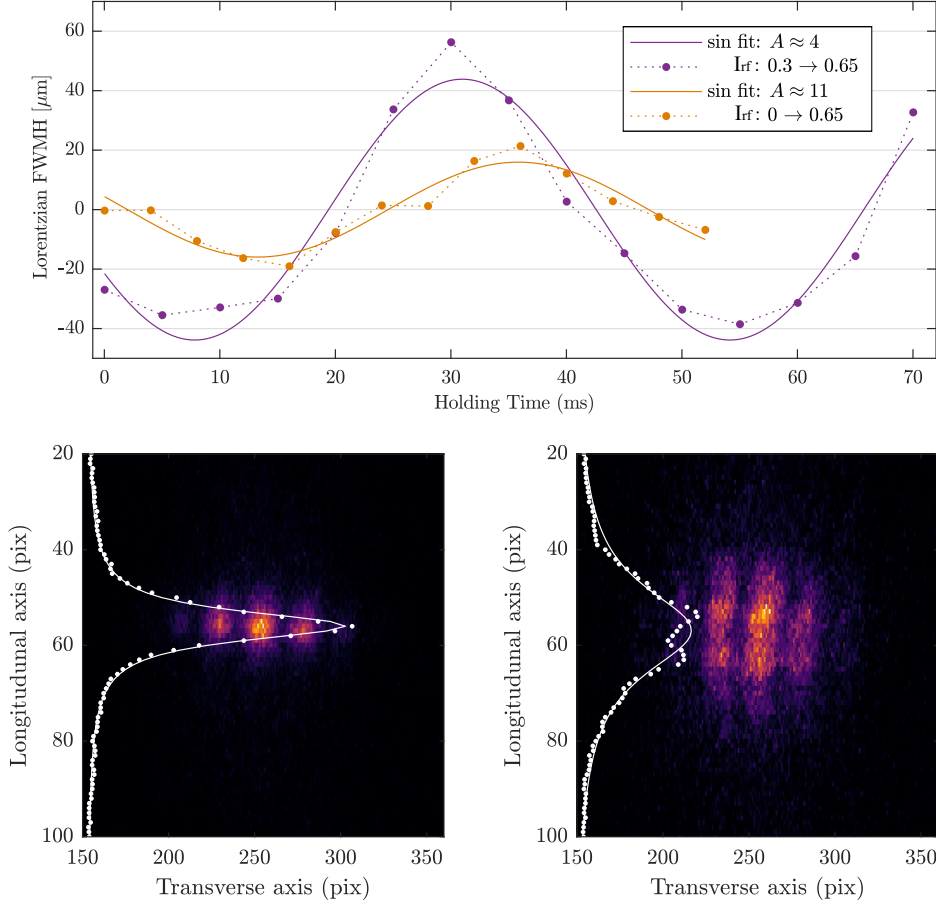


Figure 3.3: Comparison of the breathing amplitude for two initial traps. **Top panel:** Splitting in $T = 10$ ms toward $I_{\text{rf}}^f = 0.65$ starting from $I_{\text{rf}}^i = 0$ (orange) and from $I_{\text{rf}}^i = 0.3$ (purple). The change of atom number and trap frequency excites a breathing mode, the amplitude of which depends on the initial trap. After splitting, the longitudinal extension of the interference fringes is measured in TOF. This relates to the longitudinal extension of the clouds. In both cases, the condensates length oscillates at the frequency $\omega = 2\pi\sqrt{3} \times 13$ Hz, compatible with the frequency of a breathing motion. For both curves, the length at equilibrium is subtracted for clarity. For the ramp starting from the harmonic trap $I_{\text{rf}}^i = 0$ the breathing amplitude is 35% compared to 70% when starting from $I_{\text{rf}}^i = 0.3$. **Lower panels:** Interference fringes after splitting of a condensate initially in $I_{\text{rf}}^i = 0.3$. In the final trap $I_{\text{rf}}^f = 0.65$, the clouds are held for 0 ms (left) and for 30 ms (right). The breathing appears clearly on the longitudinal extension of the fringes.

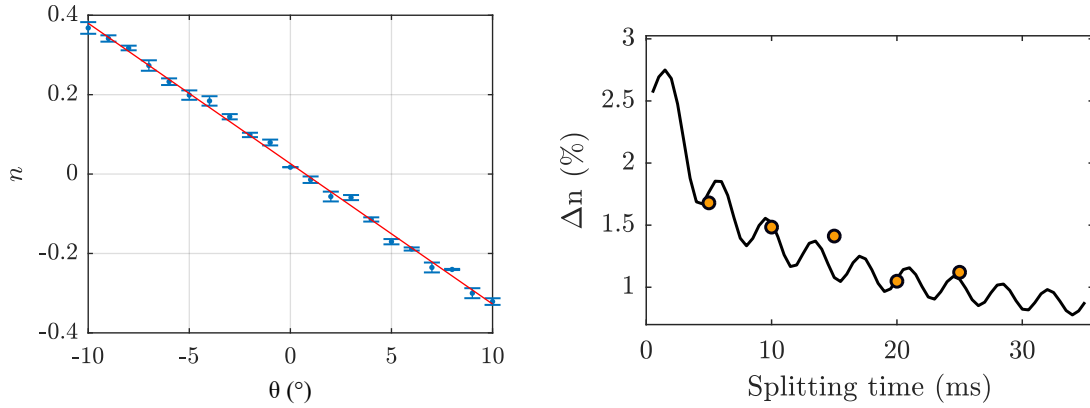


Figure 3.4: Determination of the splitting symmetry and duration. **Left:** Splitting in $T = 10$ ms toward $I_{\text{rf}}^f = 0.65$ with various θ to determine the symmetric splitting. **Right:** Imbalance fluctuations after various splitting durations. The splitting duration is varied between 0 ms and 25 ms. The experimental points (orange) are compared to a simulation using the MC-like model using 100 points and the initial state $\Delta n = 0.024$ and $\Delta\phi = 0.12$.

Splitting symmetry and duration While θ_s^f is the angle corresponding to a symmetric final trap, it is generally not the value of θ used during the ramp. Indeed, experimental imperfections tend to slightly tilt the trap during the ramp, resulting in an evolution of the imbalance and a decoupling for $n \neq 0$. Therefore, we introduce a tilt angle compensating the technical imperfections such that the adiabaticity is broken for $n = 0$. This generally results in a finite value of ϕ . The value θ_s for which $n = 0$ after splitting is determined by performing a splitting with various angle as illustrated in the left panel of Fig. 3.4.

The duration of the splitting ramp is chosen to decrease significantly the imbalance fluctuations. For this, we ramp the intensity from $I_{\text{rf}}^i = 0$ to $I_{\text{rf}}^f = 0.65$ with $\theta = \theta_s$ and vary the splitting duration between 5 ms and 25 ms after which we measure the imbalance fluctuations. The results are displayed in the right panel of Fig. 3.4. This shows a minimum of imbalance fluctuations around 20 ms.

A more rigorous approach would require to vary both θ and the ramp duration T to determine $\theta_s(T)$ but would also be more time consuming. As our purpose is not to optimize the number-squeezing but simply to reduce Δn enough to limit phase diffusion, this measurement is satisfying enough to proceed with a splitting duration of $T = 21.5$ ms.

3.1.3 Phase accumulation

Trap characterization In the decoupled trap with $n = 0$, the equation of motion governing the phase evolution simply reads:

$$\dot{\phi}(t) = \frac{\epsilon}{\hbar}, \quad (3.3)$$

such that the phase ϕ can be modified by a change of ϵ . The detuning ϵ is not directly accessible experimentally, but is linked to the experimental angle θ by:

$$\frac{\epsilon}{\hbar} = a\theta + b, \quad (3.4)$$

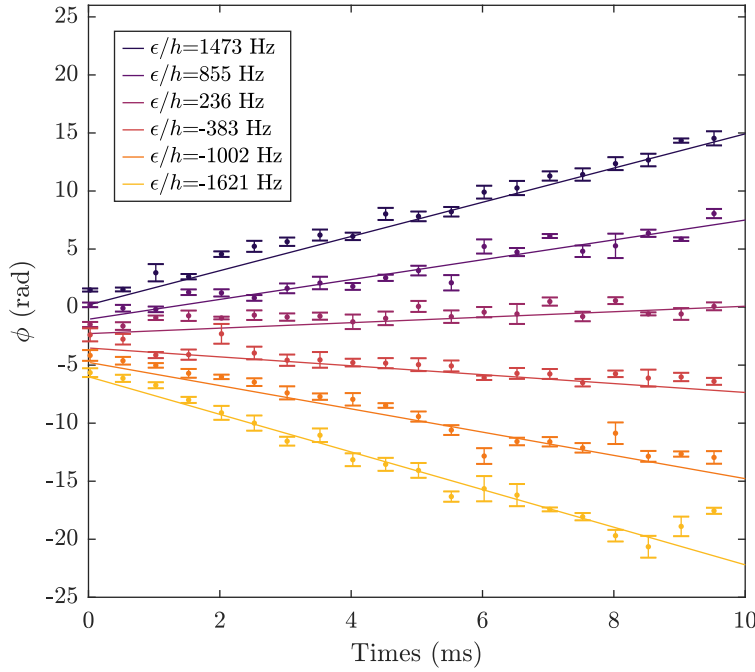


Figure 3.5: Phase shifter. The phase difference between two condensates in a detuned trap increases linearly at a rate proportional to the detuning ϵ . ϵ is experimentally controlled through the angle θ varied in this case between $[-5 : 2 : 5]^\circ$. For each experimental angle θ , the measurement of the phase for various accumulation times allows to deduce ϵ/h from the slope and to retrieve the link between θ and ϵ/h , in this case $\epsilon/h = -309\theta - 74$ Hz. The initial phase value originates from two contributions: a fixed offset corresponding to the phase after splitting $\phi_s = -2.58$ rad as well as a contribution of the phase evolution during the ramp of detuning up to θ such that the curves of various θ present different offset values.

with a, b two constants. To determine a and b , we tilt the trap up to a fixed value of θ and measure the phase after various accumulation times. As θ and the corresponding ϵ are fixed, the phase evolution obtained by integration of Eq. (3.3) reads:

$$\phi(t) = \frac{\epsilon}{\hbar}t + \phi_0, \quad (3.5)$$

where ϕ_0 is a phase offset. The measurement is displayed in Fig. 3.5 for $\theta = [-5 : 2 : 5]^\circ$ and the linear evolution of the phase is compatible with the predictions of the TMBH model. Therefore, the slopes read $\dot{\phi} = \epsilon/h$ and allow to deduce $\epsilon/h = -309\theta - 74$ Hz.

Figure 3.5 shows that the initial phase ϕ_0 depends on the angle considered. The reason is that, in order to avoid exciting a vertical sloshing, we ramp the angle linearly from its value after splitting (in this case $\theta_s = -0.4^\circ$) to its maximal value $\theta = [-5 : 2 : 5]^\circ$ over a time $T_r = 2$ ms, during which the phase evolves. The value phase ϕ_0 increases with $|\theta|$ and the sign of the offset is given by the sign of $309\theta + 74$ Hz. In addition, the splitting with the angle θ_s results in a finite phase value ϕ_s after splitting. This offset appears in the fit and is estimated to be $\phi_s = -2.58$ rad.

Initial phase preparation The preparation of the initial phase in the decoupled trap relies on three ramps of detunings. The first ramp of duration T_{r1} consists of a linear

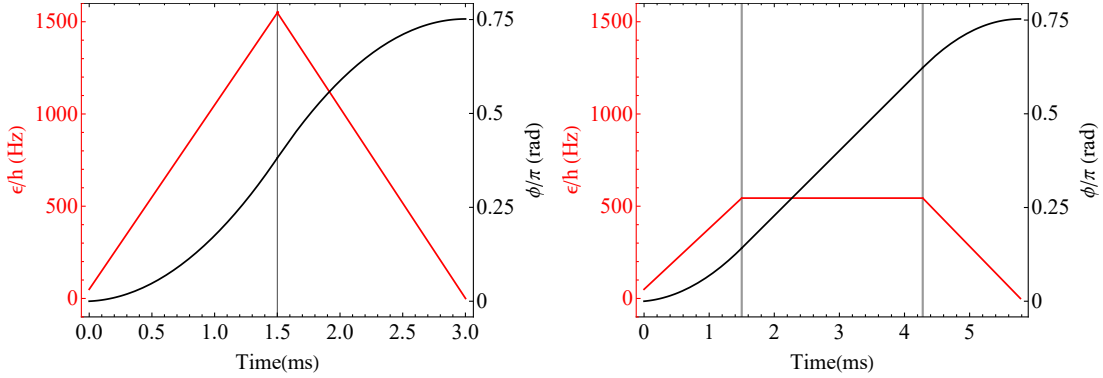


Figure 3.6: Phase preparation. Simulations resulting in $\phi = 3\pi/4$ following two sequences. Left: Linear increase of detuning in 1.5 ms from $\epsilon_s/h = 50$ Hz to $\epsilon_m/h = 1548$ Hz corresponding to an angle $\theta_m = -5.25^\circ$. Without holding time, the detuning is then decreased to $\epsilon_f/h = 0$ in 1.5 ms. Right: A similar phase is obtained by tilting to a small angle $\epsilon_m = 544$ Hz ($\theta_m = -1$) but requires a holding time of $T_h = 2.8$ ms between the two ramps. The duration of the ramps "up" and "down" are maintained to 1.5 ms.

increase of detuning between ϵ_s/h (value after splitting associated to θ_s) and ϵ_m/h . The second ramp is a holding time T_h with constant ϵ_m/h to let the phase evolve linearly according to Eq. (3.5). The last ramp of duration T_{r2} consists in decreasing linearly the detuning between ϵ_m/h and $\epsilon_f/h = 0$ (detuning value associated to θ_s^f for which the decoupled trap is symmetric). This last ramp is necessary to perform the subsequent symmetric recoupling. The typical ramp of detuning is:

$$\frac{\epsilon(t)}{h} = \begin{cases} \frac{\epsilon_m - \epsilon_s}{h} \frac{t}{T_{r1}} + \frac{\epsilon_s}{h}, & \text{for } t < T_{r1} \\ \frac{\epsilon_m}{h} & \text{for } T_{r1} < t < T_{r1} + T_h, \\ -\frac{\epsilon_m}{h} \frac{t}{T_h} + \frac{\epsilon_m}{h} \frac{T_{r1} + T_h + T_{r2}}{T_{r2}}, & \text{for } t > T_{r1} + T_h. \end{cases} \quad (3.6)$$

The phase is obtained by integration of this equation, after taking into account the experimental values of ϵ_s and ϕ_s . Many configurations of ϵ_m , T_{r1} , T_h and T_{r2} result in an identical relative phase. Figure 3.6 illustrates two configurations leading to a phase $\phi = 3\pi/4$ where we consider $\phi_s = 0$ for simplicity. In the left panel of Fig. 3.6, we consider $T_{r1} = T_{r2} = 1.5$ ms and $T_h = 0$. In this case, the ramps must reach $\epsilon_m/h = 1548$ Hz ($\theta_m = -5.25^\circ$) to prepare a phase of $3\pi/4$. The second protocol also consists in two ramps "up" and "down" in $T_{r1} = T_{r2} = 1.5$ ms but we restrict ϵ_m/h to a lower value, in this case $\epsilon_m/h = 544$ Hz ($\theta_m = -2^\circ$). In this case, the preparation of a $\phi = 3\pi/4$ requires the holding time of $T_h = 2.8$ ms and the final phase mainly results from the linear accumulation in the detuned trap.

While the two procedures are equivalent for the average phase values, we favor the first one, which is faster, in order to limit the phase diffusion. We change the initial phase by modifying ϵ_m/h rather than the timings. After this stage, we proceed to the recoupling to study the tunneling dynamics.

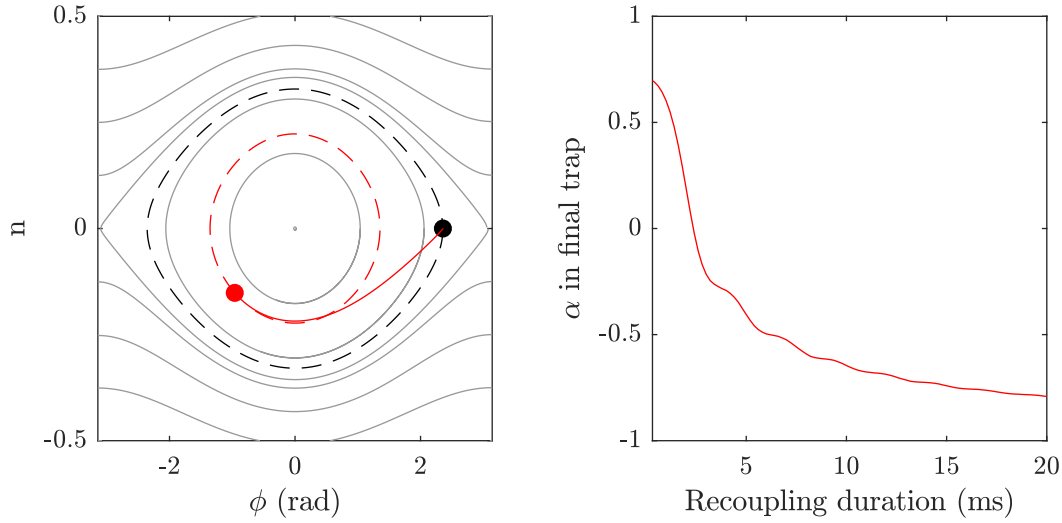


Figure 3.7: Impact of the recoupling on the oscillation amplitudes. **Left:** Evolution of $N = 3000$ atoms in the (ϕ, n) space. The gray trajectories represent the evolution in the final trap. The state before recoupling is represented by the black dot, in this case $(\phi_0 = 3\pi/4, n_0 = 0)$. For an instantaneous recoupling, the prepared state evolves along the black dashed trajectory. However, for a finite recoupling duration, the system evolves during the recoupling in a trap of increasing coupling. The red line shows the evolution in the (ϕ, n) space for a recoupling in 3 ms where the dressing amplitude is ramped down linearly from $I_{\text{rf}} = 0.65$ to $I_{\text{rf}} = 0.5$. While this evolution is displayed in the (ϕ, n) space along with the trajectories in the final trap (gray lines), this evolution occurs in a dynamical trap and does not cross trajectories. The evolution after recoupling (dashed red line) is given by the state at the end of the recoupling. **Right:** α characterizing the trajectories after recoupling for various recoupling duration 0 ms and 20 ms. This shows that the value of α is always smaller than for the instantaneous recoupling, such that a recoupling always decreases the amplitudes of the oscillations in the final trap.

3.1.4 Recoupling

Linear recoupling ramp The recoupling consists in lowering the tunnel barrier to allow an oscillating dynamics between the two wave packets. If the recoupling duration is very short, it leads to a transverse horizontal sloshing. If it is on the contrary very slow compared to the tunneling dynamics, the system undergoes a significant dynamics during the recoupling in a trap of time-dependent $J(t)$. Experimentally, we balance these constraints by linearly ramping down the dressing amplitude over 3 ms.

After recoupling, we observe that the phase and imbalance differ from the values before recoupling. In particular, both the phase after recoupling and the amplitude of the phase oscillations are significantly smaller than the prepared phase. This feature can be understood in the TMBH model.

For the initial state $(\phi_0 \neq 0, n_0 = 0)$, an instantaneous change of J would result in phase oscillations of amplitude ϕ_0 . Therefore, we deduce from Eq. (1.100) that the trajectory is characterized by $\alpha_0 = -\cos(\phi_0)$ and the amplitude of the imbalance oscillations reads $N_0 = \sqrt{2\sqrt{\alpha_0\Lambda - 1 + \sqrt{1 - 2\alpha_0\Lambda + \Lambda^2}}/\Lambda}$ with Λ corresponding to the final trap. However, due to the finite ramp duration, the system evolves during the ramp. For this prepared state and a linear ramp of dressing amplitude, such an evolution results in a decrease of α compared to α_0 as illustrated in Fig. 3.7.

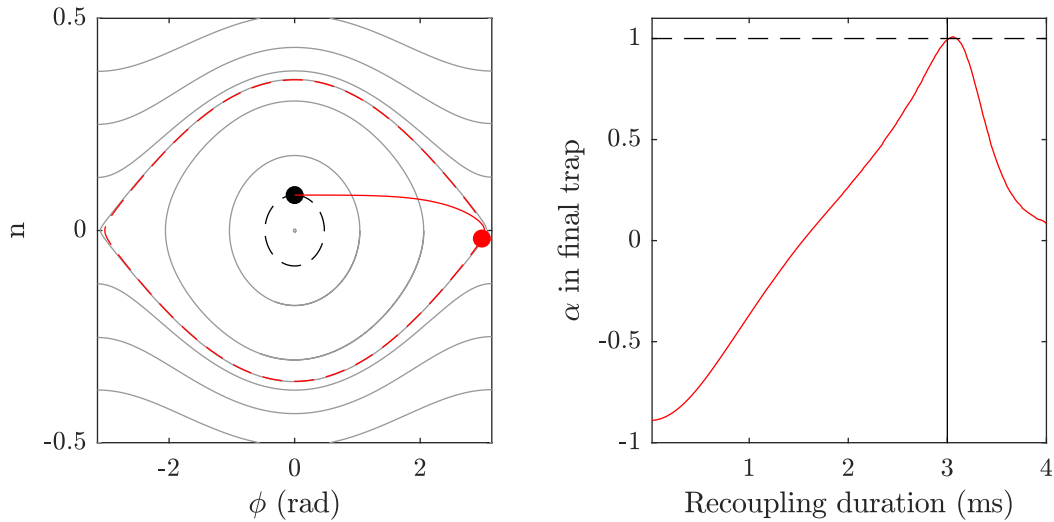


Figure 3.8: Recoupling of $N = 3000$ atoms in 3 ms from $I_{rf} = 0.65$ to $I_{rf} = 0.5$ with an initial state chosen to maximize the amplitude of the oscillations after recoupling. The initial state considered is $(\phi_0 = 0, n_0 = 0.0835)$ to reach α just below 1 (transition value to the MQST) at the end of the recoupling. This illustrates that the initial state can be chosen to maximize the amplitude after recoupling when performing a linear recoupling in a fixed duration.

Interestingly, the TMBH predicts that the decrease of α can be avoided by considering an identical dressing ramp but a different initial state. In this case, the value of α after recoupling can exceed α_0 significantly. We illustrate this in Fig. 3.8 where the ramp is identical as previously discussed but the initial imbalance is chosen to lead to the higher value of $\alpha < 1$ after recoupling. It shows that the recoupling allows to reach oscillating trajectories of large amplitude by changing slightly the initial state. The situation depicted in Fig. 3.8 is not entirely favorable experimentally, due to the fluctuations which, so close to the separatrix, could lead to a dynamics partly in the oscillating regime and partly in the MQST. However it shows that further experiments could be performed with phase amplitudes significantly larger than presented in this manuscript.

Restriction on the final trap Finally, the recoupled trap in which the tunneling dynamics is studied must allow a treatment in the TMBH framework. The initial state is expected to lead to an oscillation of both the phase and the imbalance. However, when $n \neq 0$, the harmonicity of the trap implies that the length and atomic density of the two condensates differ.

The left column in Fig. 3.9 illustrates the effect of the trap geometry for $N = 5000$ atoms and a global imbalance $n = 0.5$. The lengths of the clouds are given by the atom number and the trap frequencies, chosen in the range of the experimental parameters $\omega_z = 2\pi \times 10$ Hz and $\omega_r = 2\pi \times 1500$ Hz. In this case, we see that the local imbalance varies strongly along z . The phase and imbalance but also Λ can only be defined locally and the dynamics of the coupled condensates mixes oscillating and self-trapped dynamics. The most extreme case corresponds to the edges of the longest cloud, for which the imbalance is 1 and the phase difference is no longer defined.

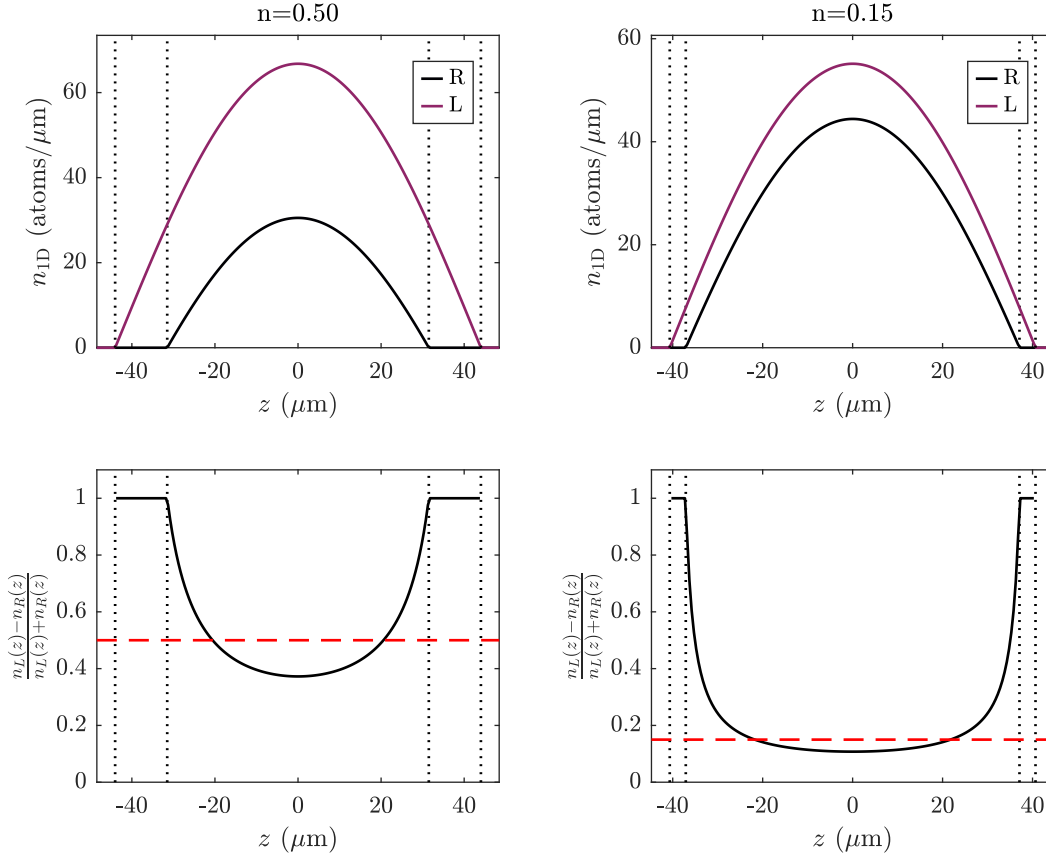


Figure 3.9: Inhomogeneous atomic densities and local atomic imbalance. **Top:** Longitudinal atomic densities for the right (black) and left (purple) condensates for a total atom number $N = 5000$ atoms with a total imbalance $n = 0.5$ (left) and $n = 0.15$ (right). The trap frequencies are $\omega_z = 2\pi \times 10$ Hz and $\omega_r = 2\pi \times 1500$ Hz. **Bottom:** The inhomogeneous densities of the two BECs lead to a local definition of the imbalance. The system presents local regimes of tunneling. In particular, the imbalance is 1 at the edges of the longest cloud. In this case, the phase is not defined and the system is totally self-trapped. For small global imbalance, the effect of the inhomogeneities is reduced and can be neglected to define global quantities.

While this effect is unavoidable, it is negligible for small imbalance as displayed in the right column of Fig. 3.9. It shows that the imbalance variations are limited and then only a small portion of the cloud is totally self-trapped.

To limit the effect of the inhomogeneities of atomic densities, we consider imbalance amplitudes $N_0 < 0.15$. This sets constraints on Λ and/or Φ_0 . As a compromise, we define $\Lambda < 63$ such that the largest oscillation amplitude is $n_c = 0.25$ and restrict the phase amplitude as $\Phi_0 < 0.75\pi$ such that $N_0 < 0.15$. For a maximal atom number of $N = 5000$ atoms and a typical on-site interaction energy of $U/h \approx 1$ Hz, the limit set on Λ leads to $J/h < 40$ Hz. This is experimentally realistic and still allows to change J/h by an order of magnitude.

3.2 Relaxation of the oscillating tunneling dynamics

In the following, we present the time evolution of the two global observables phase and imbalance associated to an initial state ($\phi \neq 0, n = 0$) before recoupling. The phase fluctuations are above the uncertainty limit as the phase distribution is broadened by effects such as temperature and interaction-induced dephasing, but remains narrow.

3.2.1 Relaxation versus dephasing and dissipation

Qualitative observations Typically, the evolution of the phase and imbalance resembles Fig. 3.10 and leads to the following qualitative observations:

1. The mean values of the global phase and global imbalance present an oscillating dynamics.
2. The oscillations are strongly suppressed over time in what appears as an exponential decay.
3. The error bars on the mean values do not show an obvious increase over time.

The first observation is expected from the mean-field TMBH model and consists in Josephson oscillations as described in Sec. 1.3.2. However, instead of everlasting oscillations, our system exhibits a damping over a short timescale (10–15 ms). Claiming that the observed damping is a relaxation requires to exclude several dephasing effects.

Exclusion of a statistical dephasing To compute the mean values of the phase and imbalance, we average the individual values extracted from a set of fluorescence pictures measured with the exact same sequence and identical experimental conditions. The averaging mitigates the effect of the fluctuations around the mean values.

Performing several measurements supposedly identical consists in reverse engineering the Monte-Carlo (MC) like simulation presented in Sec. 1.3.4. The MC state is built by sampling the initial distributions with a large number of individual classical points and propagating them deterministically over time using the mean-field equations of motion.

A measurement of the phase/imbalance consists in projecting the state on one value of the phase/imbalance distribution. Therefore, a single shot measurement is in the idea equivalent to the phase or imbalance value of one point of the MC-like model, picked up randomly. Given that the propagation equations are correct, a measurement at a time t is equivalent to a randomly chosen MC point propagated up to the time t from which we read the phase or imbalance. However, where the MC required at least 500 points to give a stable mean value, the experimental measurements require 5 realizations only.

A statistical dephasing refers to an effect where the phase and/or imbalance becomes less and less reproducible over time, even when repeating exactly the experimental sequence. This corresponds to a broadening of the distributions. The MC-like approach applied to our experimental initial state predicts a statistical dephasing presented in Sec. 1.3.4.4. It is displayed in Fig. 1.15 and exhibits an exponential damping of the mean phase and imbalance in a timescale compatible with the experimental observations of Fig. 3.10.

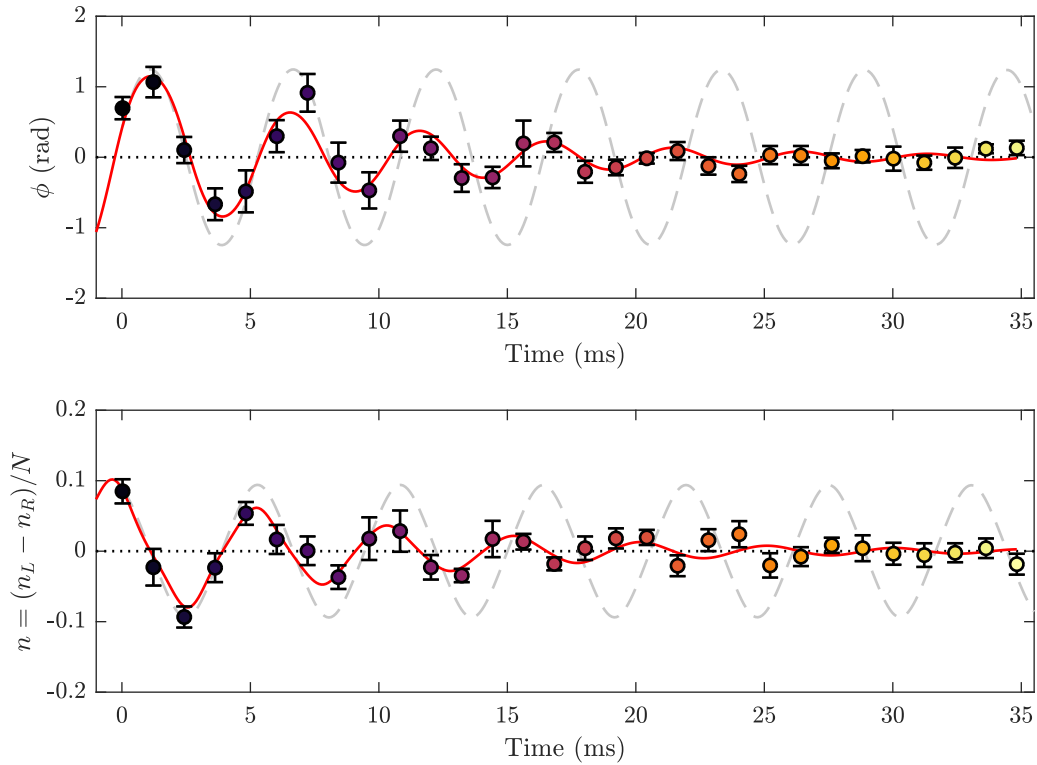


Figure 3.10: Time evolution the phase and imbalance in a trap of finite coupling. The tunneling dynamics of $N = 3500$ atoms is initialized by a global phase difference and shows damped oscillations over time. Red line: Fit using the pendulum solution of Eqs. (3.22, 3.23) and allowing to establish the TMBH parameters: $J/h = 8\text{Hz}$ and $\Lambda = 153$. Grey dashed line: Undamped evolution as predicted by the TMBH model for identical parameters.

However, a very important distinction between the two situations must be emphasized. The decay on the mean values in the MC like simulations occurs through an increase of the phase and imbalance fluctuations. On the imbalance measurement, this would translate into an increase of the error bar or equivalently into a broadening of the imbalance distribution saturating below n_c . On the phase, it would appear as an increase of the error bars up to a saturation value due to the 2π periodicity. It also appears in circular statistics as a decrease of the coherence to $R = 0$. We compare the experimental phase fluctuations of the initial state with those after decay of the mean values. The results, typically displayed in Fig. 3.11, shows that the phase coherence obtained for the initial and final states are comparable, which rejects a statistical dephasing.

The experimental absence of statistical dephasing implies that a contribution is missing in the mean-field equation of motion or equivalently that an energy contribution is missing in the associated Hamiltonian of Eq. (1.99), in order to explain the experimental observations. This is not totally unexpected as the TMBH model is a 0D model which cannot fully describe a 1D system. The elongated character of the system can lead to an effective phase-locking with small statistical fluctuations as presented in the following.

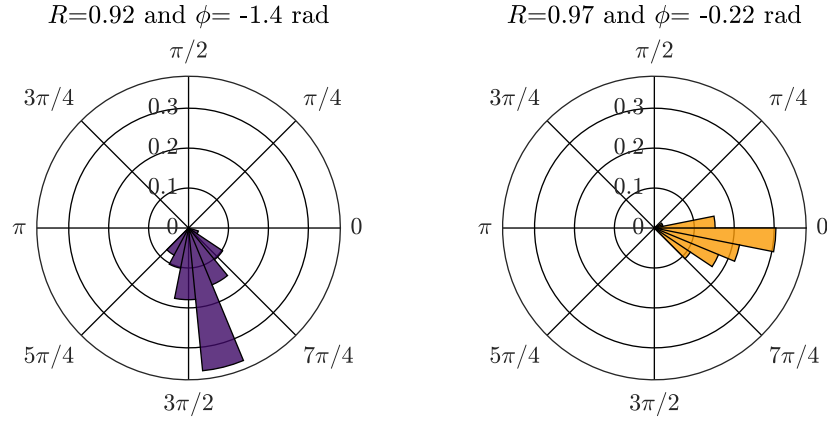


Figure 3.11: Phase distributions of the initial and final state. The global phase is extracted from 50 realizations obtained in identical experimental conditions and plotted in a circular diagram. Both states show a high statistical phase coherence $R \approx 1$. The initial phase coherence, slightly decreased by the interaction-induced phase diffusion, increases over time. The mean value of the global phase, initially prepared as $\phi = -1.4$ rad damps toward $\phi = -0.22$ rad, which is indistinguishable from $\phi = 0$ when considering the imaging resolution.

Exclusion of the inhomogeneous tunneling While we attempt to minimize longitudinal inhomogeneities, we consider in this paragraph how they could lead to a zero global phase and which experimental signatures could allow to identify local evolutions. We refer to the local atomic density as $\mathcal{N}(z)$, leading to a local definition of $\Lambda(z)$:

$$\Lambda(z) = \frac{g_{\perp} \mathcal{N}(z)}{2J}. \quad (3.7)$$

For simplicity, we consider independent slices along z such that $\mathcal{N}(z)$ is constant over time. In this case, the definition of the local tunneling frequency becomes:

$$\omega(z) = \frac{2J}{\hbar} \sqrt{1 + \Lambda(z)}. \quad (3.8)$$

The maximal atomic density is located at the center of the cloud (Fig. 3.9), resulting in a higher frequency than at the edges. The amplitude of the oscillations is also z -dependent. As a consequence, after a given number of oscillations, the local values of the phase and imbalance present so much variation along z that the global values obtained by integration of the full signal are $\phi = 0$ and $n = 0$. As this effect is reproducible, the statistical spreads of the global phase and global imbalance remain small.

Rigorously, the inhomogeneous tunneling must take onto account the interaction between slices as well as the dependence of J with $\mathcal{N}(z)$ and with z . Indeed the barrier height is by construction the highest at the center of the trap and decreases when increases the distance to the center. These effects however add limited corrections. We currently investigate the mean-field evolution in 1D and 3D taking onto account rigorously the trap geometry. This is done in collaboration with [143, 144] using 1D and 3D stochastic GPE. So far, it results in inhomogeneous tunneling but not in a phase-locking.

Experimentally, detecting inhomogeneous tunneling cannot be done on the imbalance data. Indeed, the separation protocol required to prevent the wave packets overlap deforms the clouds and prevent a local analysis. However, local dynamics should appear on

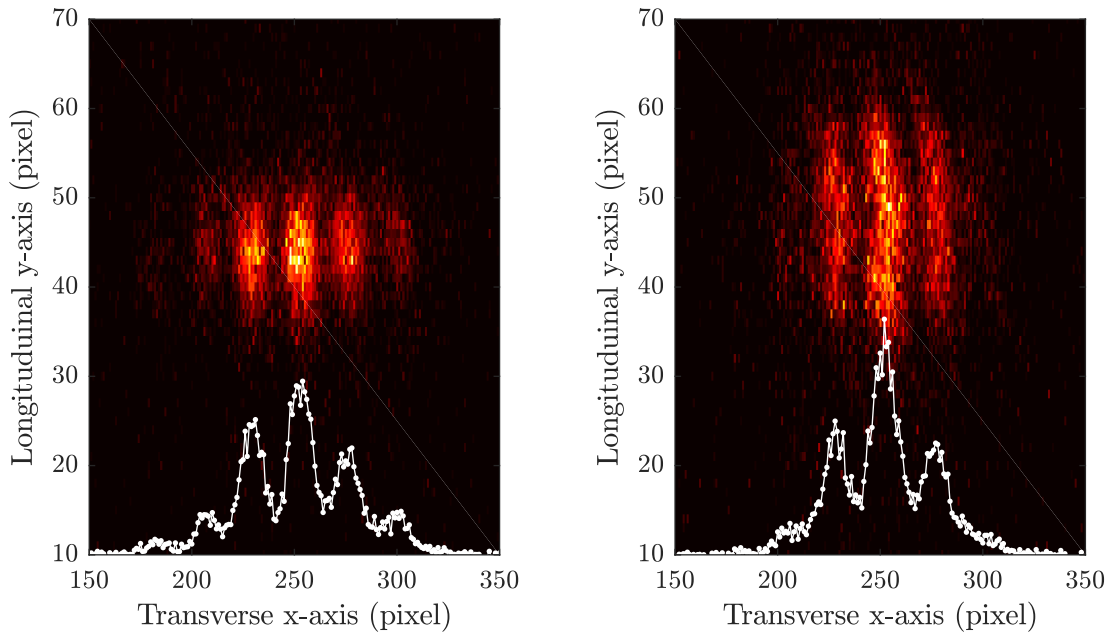


Figure 3.12: Single realization of interference fringes. **Left:** Initial state after global phase imprinting. The straight fringes show that the phase is uniformly imprinted. After integration along z (white line), the asymmetry of the pattern shows that the phase is non zero. **Right:** Typical interference pattern after the global phase stabilizes at $\phi = 0$. The fringes remain straight and the integrated contrast remains constant, such that the zero phase does not originate from the integration of local phase values. Instead, the phase-locking occurs along the entire length of the clouds. The breathing in this case gives a better effective resolution.

the interference fringes, where a local phase corresponds to a local displacement of the fringes along z . Therefore, inhomogeneous tunneling leads to a wriggling of the fringes. Figure 3.12 shows two individual fringe patterns corresponding to the prepared state (left) and to the final state where $\phi = 0$ (right) and indicates that the fringes remain straight.

Quantitatively, the local dynamics decreases the integrated contrast and can be computed on single realizations and displayed over time. Figure 3.13 displays the integrated contrast (averaged over 10 realizations) and shows that the dynamics might present local features at short time but that the final contrast after 20 ms is comparable to the one of the prepared state.

While the imaging resolution limits our access to local information and cannot allow to exclude local dynamics entirely, the constant values of the integrated contrast is a strong indication that inhomogeneous tunneling is dominated by a global phase relaxation.

Energy dissipation by heating or atomic losses A decay of the mean values can also originate from heating processes. In this case, energy losses can occur due to excitations to higher transverse modes beyond the description of the TMBH model [145, 146]. We can exclude this effect in our system as it would degrade the integrated fringes contrast. Energy can also be dissipated if the system is not well isolated, for example through atomic losses [147–150]. Our imaging system allows a very reliable estimation of the atom number such that we can exclude atomic losses as displayed in the left panel of Fig. 3.14.

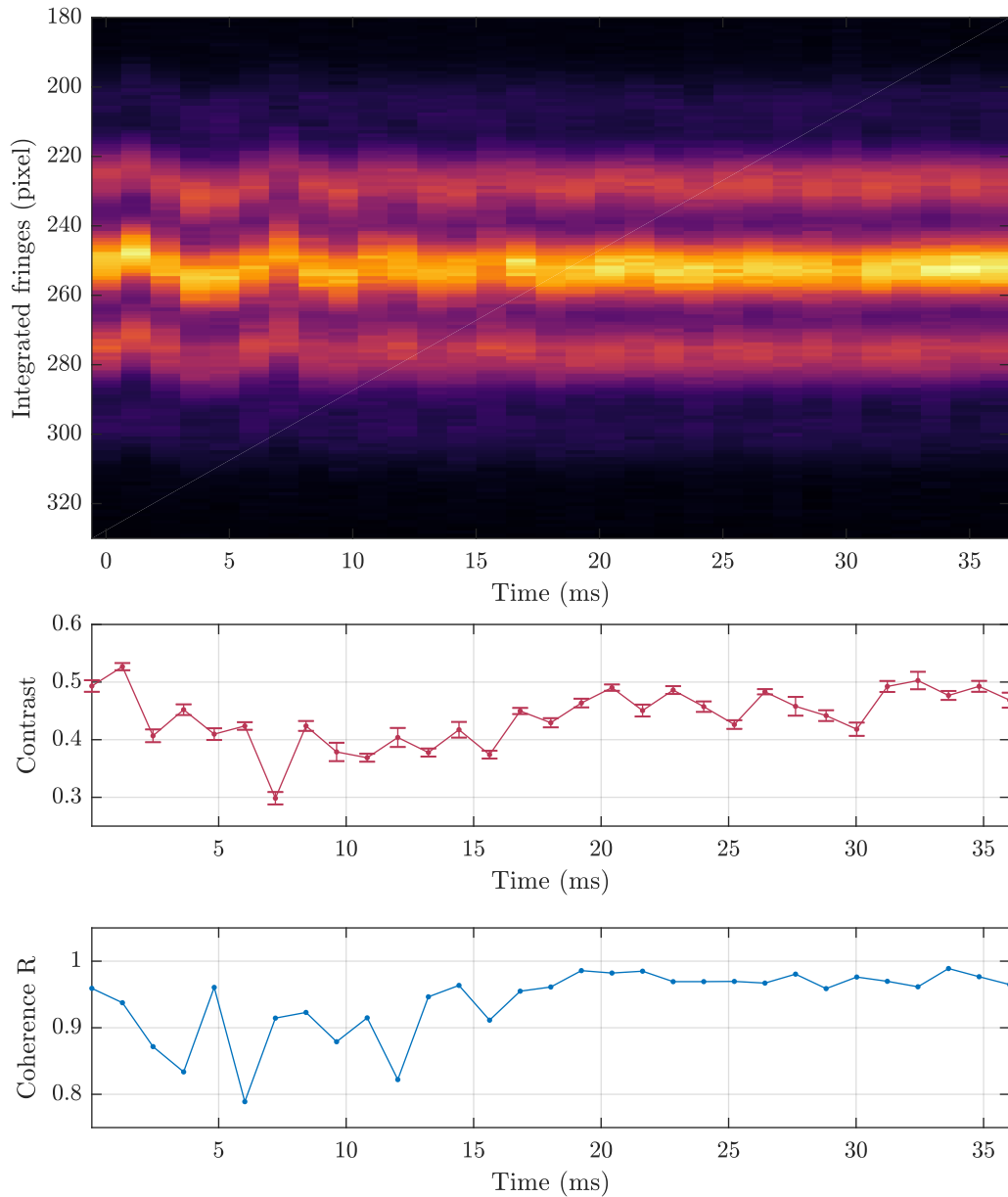


Figure 3.13: Phase evolution over time. **Top:** Averaged time evolution displayed as a carpet. The fringe patterns associated to a tunneling time are averaged and integrated to provide a slice of the carpet plot. It displays very clearly the oscillation of the fringes and the stabilization after 20 ms. The averaged carpet however does not allow to distinguish between the effect of longitudinal integration and statistical averaging. **Middle:** Evolution of the averaged contrast. The contrast of the single shots is extracted and the repeat over 10 realizations allows a better estimate. During the dynamics, the contrast slightly decreases indicating that the phase evolves at different frequencies. However, after 20 ms, the contrast reaches its initial value again, showing a global phase locking. **Bottom:** Time evolution of the coherence. The coherence is computed from the statistics of the global phase. The low statistics (10 realizations) does not allow a very reliable estimate but the coherence seems to be generally lower during the oscillating dynamics and saturate slightly below $R = 1$ after 20 ms.

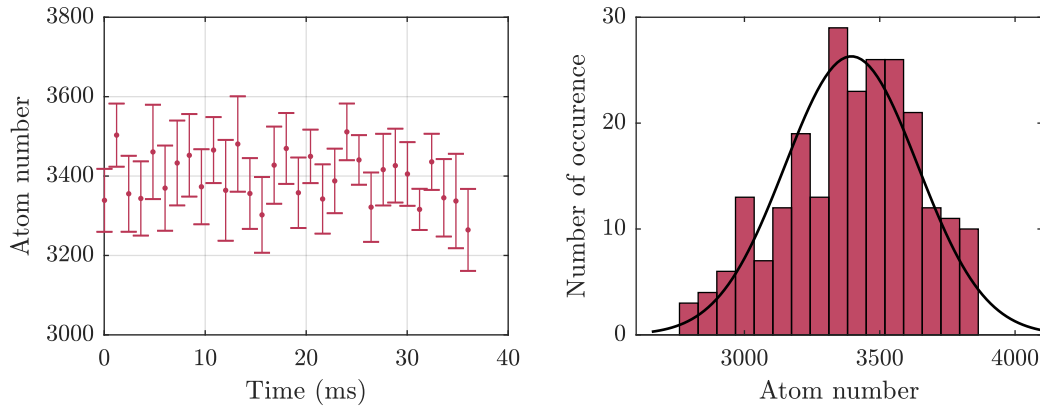


Figure 3.14: Atom number. **Left:** Time evolution of the atom number extracted from statistical averaging. The atom number is constant over the timescale of the relaxation. **Right:** Atom number distribution. The distribution is a Gaussian, the edges of which are cut off by the post selection.

Discussion The relaxation to a phase-locked equilibrium state does not occur through excitations to higher transverse modes nor through atomic losses. The energy introduced in the system by the state preparation is likely transferred to higher longitudinal modes available in the condensate. The density of excitations in the $k = 0$ mode with the associated energy could in principle be redistributed to higher longitudinal modes of energy E_k with a density n_k satisfying energy conservation. These modes are well predicted at equilibrium by the sine-Gordon model.

However, we did not find any mechanism susceptible to transfer the energy of the $k = 0$ mode to higher k modes of the sine-Gordon model in a way compatible with our observations. In collaboration with [151], we attempted various theoretical approaches, including quenches in the sine-Gordon model using exact solutions in the single-mode approximation, truncated Wigner approximation and variational Gaussian approach. This led for example to [38]. However, none of these reproduces the rapid timescale of the relaxation nor the full decay of the mean values with reduced fluctuations.

One possibility is that a transfer mechanism from $k = 0$ toward higher mode of the sine-Gordon model might be missing in the description. This can come from the approximations which do not fully describe the coupling between the transverse and longitudinal dynamics. Going beyond the currently used hypothesis done to solve the model is extremely demanding. Another possibility is that the energy of the modes predicted by the sine-Gordon model are inaccurate. This would imply that a transfer of only few excitations could lead to a larger energy transfer and take all the energy out of the $k = 0$ mode. In both cases, the relaxation questions the sine-Gordon theory, which has proven very successful in describing the equilibrium behavior of a 1D-BJJ. Therefore, the microscopic mechanism leading to the relaxation still escaped general understanding and the description of the relaxation relies on an empirical model.

3.2.2 Empirical model for the relaxation

3.2.2.1 Dissipative BJJ in the TMBH model

Dissipation term We established in Sec. 3.2.1 that the mean-field equation of motion of the TMBH model do not predict a relaxation even when including initial fluctuations. In the following, we introduce an empirical dissipative term in the equations of motion to reproduce the damping of the mean values. No assumption is made on the origin of this generic dissipative term, which can be attributed to any effect beyond the TMBH model. It however assumes a constant value of atom number N , interaction energy U and tunneling rate J during the dynamics.

As proposed by [87], we consider a dissipative contribution based on the analogy of the BJJ with a momentum-shortened pendulum. The friction of a pendulum in a media of viscosity η is described by $-\eta\dot{\phi}(t)$ with $\dot{\phi}(t)$ the angular velocity. In the analogy, we recall that the angle of the pendulum is analogous to the phase of the BJJ. In the equations of motion Eqs. (1.120, 1.121), we therefore introduce a dimensionless viscosity η normalized to the total atom number N for consistency with the definition of the normalized imbalance n . The damped equations of motion of a BJJ read:

$$\dot{\phi}(t) = \frac{\epsilon}{\hbar} + \frac{2J}{\hbar} \left[\Lambda n(t) + \frac{n(t)}{\sqrt{1-n^2(t)}} \cos \phi(t) \right], \quad (3.9)$$

$$\dot{n}(t) = -\frac{2J}{\hbar} \sqrt{1-n^2(t)} \sin \phi(t) - \frac{\eta}{N} \dot{\phi}(t). \quad (3.10)$$

Application to experimental data We first attempted to describe the data with the damped equations of motion. We detail in Sec. 3.2.2.3 that the fit converges and displays both a satisfying goodness of the fit and white noise of the residual. This indicates that the dissipation associated to the viscosity η is an appropriate description of our data. However, the values of η extracted from the fit shows strong correlations with J and Λ (i.e. U) which prevents us to extract a reliable value of the damping using this approach. This led us to define alternative fit formulas using a comparable model but a new set of fit parameters.

3.2.2.2 Analytical pendulum model of the dissipative BJJ

Approximation of the damped rigid pendulum Finding new fit formulas based on the same model consists in establishing the analytical solutions of Eqs. (3.9, 3.10). This introduces a new set of fit parameters with different correlations and different physical insights. We seek to define fit parameters directly connected to the data, like the oscillation frequency and oscillations amplitudes rather than J or Λ . The advantage is that, if a constrain on a fit parameter is required, we have a better understanding of the physical meaning of its boundaries. For example, we can constrain the amplitude of the imbalance oscillations within the error bars of its mean values rather than constraining Λ which affects at once the frequency and amplitudes of both the phase and imbalance oscillations.

The analytical solutions of a damped and momentum-dependent pendulum of arbitrary initial energy are not trivial. Instead, we resort to the approximation of a rigid pendulum, which gave satisfying results for $\Lambda > 5$ in the undamped case. Due to the harmonic longitudinal confinement, we established that the system must obey $\Lambda > 60$ to limit local dynamics. Therefore, we do not expect to be in a regime where the momentum-shortening plays a significant role.

To recover the pendulum analogy, we first consider a symmetric BJJ ($\epsilon = 0$). Following a similar approach as for Eq. (1.104), we establish the pendulum-like equation in a dissipative medium:

$$\ddot{\phi}(t) + \frac{2}{\tau}\dot{\phi}(t) + \omega_0^2 \sin(\phi(t)) = 0, \quad (3.11)$$

where ω_0 is the plasma frequency and τ is a characteristic decay time defined by:

$$\frac{2}{\tau} = \frac{2J}{\hbar} \frac{\eta}{N} (\Lambda + \lambda). \quad (3.12)$$

Figure 3.15 displays the comparison of the numerical results of the damped TMBH model with the damped pendulum in the oscillating regime. The agreement between the two approaches is remarkable, which means that the momentum-shortening is negligible and that the analytical solutions of a rigid damped pendulum are expected to describe the dissipative BJJ.

Heuristic solutions of a generic BJJ with dissipation The analytical derivation presented in Sec. 1.3.2.2 relies on energy conservation and cannot be done exactly with dissipation. As a result, the decay is heuristically determined by combining the results of the damped pendulum in the harmonic regime with the results of the ideal BJJ.

In the harmonic regime, Eq. (3.11) is exactly solvable and results in sinusoidal oscillations exponentially damped over time with the characteristic damping time τ . The damping also affects the oscillation frequency as:

$$\omega(\tau) = \sqrt{\omega_0^2 - \frac{1}{\tau^2}}, \quad (3.13)$$

with ω_0 the undamped plasma frequency.

To extend this result to an arbitrary initial amplitude, we first consider that the damping τ affects the initial energy k_0 due to the redefinition of ω :

$$k_0(\epsilon, \tau) = \frac{1}{2\omega(\tau)} \sqrt{\dot{\phi}_0(\epsilon)^2 + 4\omega(\tau)^2 \sin^2\left(\frac{\phi_0}{2}\right)}. \quad (3.14)$$

Then, we assume that the characteristic time τ established in the harmonic regime affects oscillations of arbitrary amplitude. Therefore, τ is expected to reduce the energy $k_0(\epsilon, \tau)$ of the system. We introduce an exponential damping of the energy as $k_0(\epsilon, \tau)e^{-t/\tau}$. Combining these results with the analytical solutions of an undamped pendulum of arbitrary initial energy, we obtain the heuristic formula for the evolution of the phase of a dissipative BJJ:

$$\phi(t) = 2\sigma_0 \text{am}\left((\omega k_0 t + \delta\phi)e^{-t/\tau} \left| k_0^{-2} e^{2t/\tau} \right.\right), \quad (3.15)$$

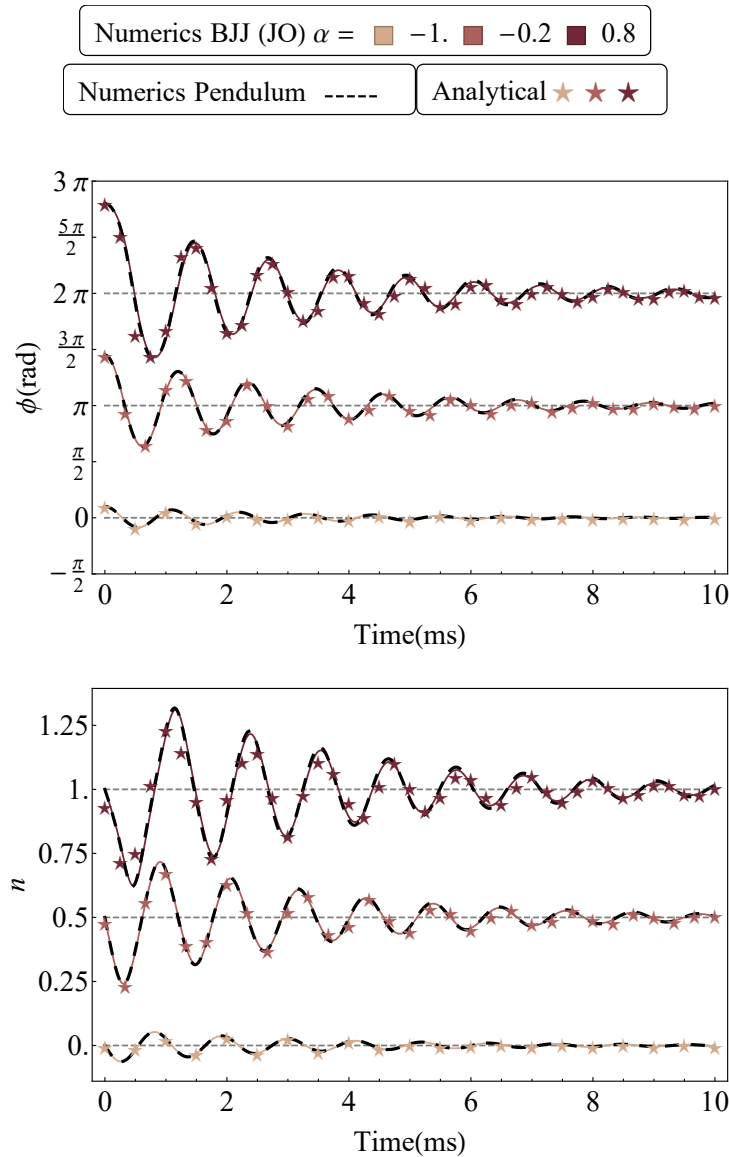


Figure 3.15: Dynamics of a dissipative BJJ in the oscillating regime for three initial phase values. Taken from [57]. Evolution of $N = 5000$ atoms in a trap characterized by $J/\hbar = 100$ Hz, $U/\hbar = 0.8$ Hz and $\eta = 120$. The initial states have an identical initial imbalance $n_0 = 0$ and differ by the value of the phase $\phi_0 = \{0.1, 0.45, 0.8\}\pi$. For the three initial states considered, the phase evolution (top) is shifted by units of π and the imbalance (bottom) is shifted by units of $n = 0.5$ for clarity. The zero of each curves is indicated by dashed gray lines around which the dynamics oscillate. Under the effect of the viscosity η , the oscillations are exponentially damped. As the oscillations damp, they become increasing harmonic, presenting a shape resembling sinusoidal oscillations and a faster frequency converging toward the plasma frequency. The plain lines are the numerical results of the dissipative BJJ, the dashed black lines are the numerical results of the corresponding rigid pendulum and the stars are the analytical pendulum solutions. The exponential envelope is very well described in all three cases. For large initial phase values, a small discrepancy is observed between the frequency of the numerical results and the one of the analytical solutions.

with $\delta\phi$ the phase shift defined by:

$$\delta\phi = \operatorname{sn}^{-1} \left(\sin \left(\frac{\phi_0}{2} \right) \middle| k_0^{-2} \right). \quad (3.16)$$

We recall that $\operatorname{am}(at|b)$ refers to the Jacobi amplitude. It defines an oscillating function of time, characterized by the harmonic frequency a and the anharmonicity $0 < b < 1$ which affects the shape of the oscillations and decreases their frequency compared to a . We also recall that σ_0 refers to the sign of ϕ_0 and is given by the sign of the initial imbalance n_0 .

The term sn^{-1} in Eq. (3.16) is the inverse SN-Jacobi elliptic function allowing to introduce a time shift of the oscillation, which would otherwise start at zero by convention. The exponential decay of $\delta\phi$ in Eq. (3.15) is imposed by the convention of the Jacobi amplitude to allow a correct definition of the plasma frequency ω .

From the analytical solution of the phase, we deduce that the evolution of the imbalance as function of $\dot{\phi}(t)$ is:

$$n(t) = \frac{N_0}{2\omega k_0} \dot{\phi}(t) + n_{\text{off}}, \quad (3.17)$$

with n_{off} the imbalance at equilibrium defined by Eq. (1.124) and N_0 the amplitude of the undamped oscillations.

Connection to the TMBH model and interpretation As for the undamped case, the parameters of the dissipative TMBH model are linked to those of the pendulum model. Equations (1.130, 1.131, 1.132) defining J , Λ and ϵ as a function of the pendulum parameters remain true in the damped case. To be more accurate, the definition of ω should be modified to take into account Eq. (3.13) but this correction is negligible for our range of parameters. It follows that the viscosity η/N can be expressed in term of measurable quantities using the definition of τ given by Eq. (3.12):

$$\frac{\eta}{N} = \frac{N_0}{k_0 \tau \omega_0}. \quad (3.18)$$

τ can be evaluated on data using the decrease of the amplitude. Indeed, we expect the initial amplitude of the oscillations to decrease by 2 at the time $t = \tau \ln(2)$. The interpretation of N_0 , ω_0 and k_0 previously given in Sec. 1.3.2.4 must be adjusted to the damped case.

N_0 is the undamped amplitude of the imbalance oscillations. It can be extracted from a maximum of the damped imbalance oscillations N_0^d reached at a time \tilde{t} . In this case the damped extrema is related to the undamped amplitude by $N_0^d = N_0 e^{-\tilde{t}/\tau}$. The frequency ω is determined accurately and ω_0 can be deduced using Eq. (3.13). k_0 is deduced from the maximum of the phase oscillation Φ_0^d reached at a time \tilde{t} through $k = \sin(\Phi_0^d/2) e^{-\tilde{t}/\tau}$.

3.2.2.3 Application to experimental data

Technical offsets: phase offset and time shift between the oscillations Before proceeding to the fit of the data, two technical contributions can be corrected on the data.

The first contribution is an offset on the phase, seen by a small shift of the averaged value around which the phase oscillates and relaxes. The offset can be attributed to a

systematic error on the phase determination. In particular, we explain in Sec. 2.4.2.2 that the phase determination is limited by the pixel size, susceptible to introduce a small systematic error on the phase.

The second technical offset appears as a time mismatch between the oscillations in phase and imbalance such that they do not appear π -out of phase as expected in the TMBH model. This delay originates from the measurement protocol which differ when measuring the phase and the imbalance.

As explained in Sec. 2.4.2.2, the phase measurement relies on an abrupt switch-off of the double-well potential and a subsequent TOF imaging. The imbalance measurement explained in Sec. 2.4.3 relies on the same principle but requires an additional separation stage to prevent the overlap of the wave-packets. Before switching off the trap, the barrier height is raised to its highest value in 1 ms to give a momentum to the atoms in the direction opposite to the barrier and excite a dipolar oscillation. After 0.2 ms, the atoms reach the maximum amplitude of the oscillation and we rapidly switch off the dressing amplitude ($\approx 360 \mu\text{s}$) to induce a crossing of the clouds in TOF.

Because it is easier to implement, the duration of the measurement sequence is identical when measuring the phase and when measuring the imbalance. However, while the imbalance measurement involves a quasi-instantaneous decoupling by raising the tunnel barrier, the phase measurement maintains the atoms in the coupled trap. It results in a systematic time shift dt between the phase oscillations and the imbalance oscillations. The evaluation of the time shift relies on the knowledge that the phase and imbalance oscillate π -out of phase. Technically, an interpolation of the imbalance data is required as the time shift is not necessarily a multiple of the experimental time step. We evaluate the time shift for each data set and obtained a value close to $dt = 1.2 \text{ ms}$.

The fit is performed on the measured phase data and on the interpolated imbalance data shifted by $-dt$. However, the temporal evolution on every experimental plot displays the measured data for both the phase and the imbalance.

Fit using the damped equations of motions We first present the fit of the data using the damped equations of motion Eqs. (3.9, 3.10) as fit formula. In this case, the fit parameters are $\epsilon, \Lambda, J, \eta$ and the initial conditions ϕ_0, n_0 . Among the various algorithms allowing to perform a least-squared fitting, we adopt the Nelder-Mead simplex algorithm *fminsearchbnd* of MatlabTM. It requires a model function, given by our coupled differential equations, a set of initial conditions and an objective function giving the quantity to minimize. In our case, we fit two sets of data (phase and imbalance over time) such that the objective function is defined as the normalized sum of the residuals squared:

$$\chi^2 = \sum_t \left[\frac{\phi_{\text{model}}(t) - \phi_{\text{data}}(t)}{\sigma_\phi(t)} \right]^2 + \sum_t \left[\frac{n_{\text{model}}(t) - n_{\text{data}}(t)}{\sigma_n(t)} \right]^2, \quad (3.19)$$

with t the array of experimental times probed in the data set, $\phi_{\text{data}}(t)$ and $n_{\text{data}}(t)$ the mean values of the phase/imbalance measured at t , $\sigma_\phi(t)$ and $\sigma_n(t)$ the standard deviations of the phase/imbalance at the time t and $\phi_{\text{model}}(t)$ and $n_{\text{model}}(t)$ the values of the phase/imbalance of the model as it adjusts to the measurements. The normalized definition of the objective function is necessary to allow an equitable treatment of the phase

	N_{at}	J/h [Hz]	η	Λ	ϵ/h [Hz]	n_0	ϕ_0 [rad]
\bar{x}	3500	19	26	128	142	-0.07	-1.2
σ	300	3	5	34	26	0.01	0.2

Table 3.1: Mean values \bar{x} and standard error σ for the measured atom number and fit parameters obtained using the damped mean-field TMBH model.

and imbalance despite the strong difference of amplitude of their respective dynamics. The value of the χ^2 and the white noise of the residuals show that the model is a suitable model to describe the data.

The error on the fit parameters and their correlations are deduced from the Hessian matrix \mathcal{H} computed at the minimum [152]. The covariance matrix (or error matrix) is deduced from the Hessian using:

$$C = 2\mathcal{H}^{-1}. \quad (3.20)$$

The diagonal elements of the covariance give the variance of the associated parameter. Therefore, the standard deviation of the i^{th} parameter is given by the square root of C . For the data presented in Fig. 3.16(a), the fit parameters and the associated errors are displayed in Table 3.1.

The correlations between parameters are given by the correlation matrix \mathcal{C} , which is obtained by:

$$\mathcal{C} = D^{-1} \times C \times D, \quad (3.21)$$

with D containing the square-root of the diagonal elements of C . For the data presented in Fig. 3.16(a), the correlations matrix reads:

$$\mathcal{C}_{\text{TMBH}} \approx \begin{pmatrix} J & \eta & \Lambda & \epsilon & n_0 & \phi_0 \\ \begin{pmatrix} 1.00 & 0.82 & -1.00 & -0.78 & -0.34 & 0.00 \\ 0.82 & 1.00 & -0.82 & -0.61 & -0.06 & -0.42 \\ -1.00 & -0.82 & 1.00 & 0.78 & 0.32 & -0.01 \\ -0.78 & -0.61 & 0.78 & 1.00 & 0.05 & 0.01 \\ -0.34 & -0.06 & 0.32 & 0.05 & 1.00 & -0.66 \\ 0.00 & -0.42 & -0.01 & 0.01 & -0.66 & 1.00 \end{pmatrix} \end{pmatrix}$$

Each element $\mathcal{C}(i, j)$ is bounded by $[-1, 1]$. The correlations between i and j increases with the absolute value of $\mathcal{C}(i, j)$. The sign of $\mathcal{C}(i, j)$ indicates correlations ($\mathcal{C}(i, j) > 0$) or anti-correlations ($\mathcal{C}(i, j) < 0$). For example, the diagonal elements are 1 as each fit parameter is totally correlated with itself. On the other side, $\mathcal{C}_{\text{TMBH}}(1, 3) = -1$ refers to the correlations between J and Λ . The perfect anti-correlation is compatible with the definition of $\Lambda = NU/2J$ such that if J increases, Λ decreases.

The correlation matrix $\mathcal{C}_{\text{TMBH}}$ indicates that η presents significant correlations with the other parameters of the TMBH model. The correlations between η and J is given by $\mathcal{C}_{\text{TMBH}}(1, 2) = 0.82$ and the correlations between J and ϵ are given by $\mathcal{C}_{\text{TMBH}}(4, 2) = -0.61$. Therefore, while the error on the fit parameters displayed in Ta-

ble 3.1 are reasonable, the correlations between the fit parameters do not allow unambiguous conclusions on the value of the damping η using this model.

Fit using the analytical solutions Using the analytical pendulum solutions, we define the fit formulas as:

$$\phi(t) = 2\sigma_0 \times \text{am}\left((\omega k_0 t + \delta\phi)e^{-t/\tau} \middle| k_0^{-2} e^{2t/\tau}\right), \quad (3.22)$$

$$n(t) = \frac{N_0}{2\omega k_0} \dot{\phi}(t) + n_{\text{off}}, \quad (3.23)$$

for which the fit parameters are ω , k_0 , $\delta\phi$, τ , ϕ_{off} , N_0 and n_{off} . With this method, the solver used to fit the data does not directly provide the covariance matrix. Instead, it returns both the non-normalized goodness-of-fit parameter R and the Jacobian matrix \mathcal{J} for the optimized fit parameters. For a number of data N_{data} and a number of fit parameters ν , we compute the mean-squared error MSE:

$$\text{MSE} = \frac{R}{N_{\text{data}} - \nu}. \quad (3.24)$$

The covariance is calculated by:

$$C = (\mathcal{J}' \times \mathcal{J})^{-1} \times \text{MSE}. \quad (3.25)$$

For the data presented in Fig. 3.16, the values of the fit parameters and the error extracted from the covariance matrix are displayed in Table 3.3. From the covariance matrix, we deduce the correlation matrix using Eq. (3.21). For the data presented in Fig. 3.16(a), it reads:

$$\mathcal{C}_{\text{heur}} \approx \begin{pmatrix} k & \omega_0 & \delta\phi & N_0 & \tau & \delta n \\ 1.00 & -0.09 & 0.02 & 0.07 & -0.65 & -0.01 \\ -0.09 & 1.00 & -0.47 & -0.06 & 0.52 & 0.01 \\ 0.02 & -0.48 & 1.00 & 0.00 & 0.03 & -0.01 \\ 0.07 & -0.06 & 0.00 & 1.00 & -0.11 & -0.02 \\ -0.65 & 0.51 & 0.03 & -0.11 & 1.00 & 0.01 \\ -0.01 & 0.01 & -0.01 & -0.02 & 0.01 & 1.00 \end{pmatrix}$$

The correlation between the characteristic damping time τ with k are rather large as $\mathcal{C}_{\text{heur}}(1, 5) = -0.65$. This large negative value is to be expected. The parameter k relates to the undamped amplitude of the phase oscillations such that a comparable fit result could be obtained when increasing the amplitude of the phase oscillations (increasing k) at the price of increasing the damping strength (decreasing τ). The correlations between τ and ω_0 are also significant, as $\mathcal{C}_{\text{heur}}(2, 5) = 0.52$, which can originate from Eq. (3.13).

However, the value of the off-diagonal terms of the correlation matrix are globally reduced compared to the damped TMBH model, including the ones of τ .

	N_{at}	J/h [Hz]	η	Λ	ϵ/h [Hz]	n_0	ϕ_0 [rad]
\bar{x}	3500	22	32	92	103	0.12	0.07
σ	300	5	7	43	46	0.04	0.04

Table 3.2: Mean values \bar{x} and standard error σ for the measured atom number and for the damped TMBH parameters deduced from the heuristic analytical solutions of the damped rigid pendulum.

Recovering the TMBH parameters We can now establish the connection between the heuristic model and the parameters of the damped TMBH model. Using the fit values of Table 3.3(a) and Eqs. (3.16, 1.111), we deduce the starting conditions $\phi_0 = 0.07(4)$ rad and $n_0 = 0.12(4)$. Due to the tunneling dynamics during the recoupling stage, these values differ from the ones of the prepared state.

The values of J , Λ , ϵ and η are deduced from Eqs. (1.130, 1.131, 1.132, 3.18). The errors on the parameters of the TMBH model are estimated by propagation of errors derived by Taylor series expansion limited to the gradient term. For a multi-variable function with correlated parameters, the error estimation must also account for the cross-terms involving products of uncertainties between the various combinations of two variables. The general formula of the error σ_f for a multi-variable $f(x_1, x_2, \dots, x_N)$ reads:

$$\sigma_f^2 = \sum_{i=1}^N \sigma_i^2 \left(\frac{\partial f}{\partial x_i} \right)^2 + 2 \sum_{i=1}^N \sum_{j \neq i}^N \left(\frac{\partial f}{\partial x_i} \right) \left(\frac{\partial f}{\partial x_j} \right) \sigma_{ij}, \quad (3.26)$$

with $\sigma_i = C(i, i)$ the variance of x_i and $\sigma_{ij} = C(i, j)$ the covariance between x_i and x_j .

For example, in the case of $J(\omega_0, N_0, k)$ defined by Eq. (1.130), the error estimated by Eq. (3.26) reads:

$$\sigma_J = \frac{\hbar \omega_0 N_0}{k} \sqrt{\left(\frac{\sigma_{\omega_0}}{\omega_0} \right)^2 + \left(\frac{\sigma_{N_0}}{N_0} \right)^2 + \left(\frac{\sigma_k}{k} \right)^2 + 2 \left(\frac{\sigma_{\omega_0 N_0}}{\omega_0 N_0} - \frac{\sigma_{k \omega_0}}{k \omega_0} - \frac{\sigma_{k N_0}}{k N_0} \right)}. \quad (3.27)$$

The mean values of the parameters of the TMBH model and their error are displayed in Table 3.2. They are compatible with the results obtained by fitting the data with the equations of motions. The errors in this case are larger as the propagation of error tends to over-estimate the error.

Robustness of the fit In Fig. 3.16, we display the dynamics obtained with three different initial conditions and show that the fit provides satisfying results in each case. Fig. 3.16(a) shows the dynamics of a large atom number $N = 3500$ atoms oscillating in an asymmetric trap of low barrier height. Fig. 3.16(b),(c) displays measurements obtained for significantly less atoms $N = 750$ oscillating in a symmetric trap with a high barrier. They differ by the value of their initial phase difference, which is twice larger in Fig. 3.16(c) than in Fig. 3.16(b). The value of the fit parameters are displayed in Table 3.3, along with the deduced TMBH parameters.

The error on the TMBH model are dominated by the uncertainty on the parameter N_0 . The amplitude of the imbalance oscillations is very small and constitutes the main source of error on the fit of the data. However, the correlations between N_0 and τ are rather limited such that the damping can still be evaluated in a reliable way.

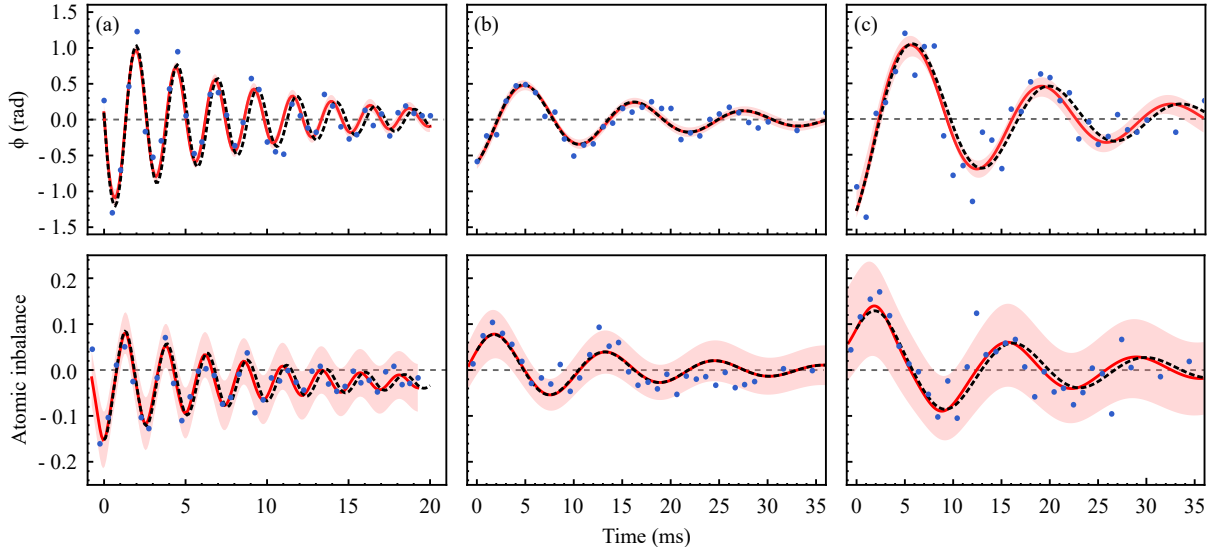


Figure 3.16: Time evolution of the phase (top) and imbalance (bottom) for various trap parameters and initial states. Taken from [57]. Blue dots: Experimental data corrected from technical offsets. Red line: Fit using the analytical formula. Red area: Error on the fit parameters of the heuristic model. Black dashed line: Fit using the damped equations of motion of the TMBH model. The fit results are summarized and compared in Table. (3.3). The three columns correspond to three different initial states and trap parameters. (a) High atom number ($N = 3500$ atoms) in an asymmetric trap ($\epsilon/h = 103$ Hz) with a large tunnel coupling ($J/h = 22$ Hz) resulting in $k_0 = 0.57(3)$. (b) Small atom number ($N = 750$ atoms) in a symmetric trap with a small initial phase difference and a weaker coupling ($J/h = 6$ Hz) leading to $k_0 = 0.31(3)$. (c) Identical atom number and trap as in (b) for a larger initial phase and therefore a larger initial energy $k_0 = 0.70(6)$.

		Fit parameters derived from pendulum							Deduced TMBH parameters			
		N_{at}	k_0	N_0	τ ms	ω_0 Hz	δn	$\delta\phi$	Λ	J/h Hz	ϵ/h Hz	η
(a)	\bar{x}	3500	0.57	0.12	8.9	2623	-0.03	-2.0	92	22	103	29
	σ	300	0.03	0.06	0.9	13	0.02	0.14	43	5	46	7
(b)	\bar{x}	750	0.31	0.08	17	554	0.01	-0.6	56	6	-0.8	21
	σ	150	0.03	0.05	3	10	0.01	0.09	65	3	8	12
(c)	\bar{x}	750	0.60	0.15	17	465	0.001	-0.7	64	5	-0.5	19
	σ	150	0.06	0.09	3	9	0.03	0.08	79	3	22	12

Table 3.3: Summary of the mean values \bar{x} and standard error σ for the measured atom number, for the fit parameters obtained with the heuristic model and for the deduced parameters of the damped mean-field TMBH model associated to the data sets of Fig. 3.16.

Comparison to the undamped evolution The determination of the TMBH parameters allows to compare the damped and undamped evolution as displayed in Fig. 3.10. One feature appearing clearly on the data after performing the fit is the change of frequency over the evolution. The oscillations have a large amplitude at short time, and therefore a frequency smaller than the plasma frequency. As the oscillations damp, the system gets closer to the harmonic regime and the frequency converges toward the plasma frequency. This shows that a simple damped sinusoidal function would give a wrong estimate of the Josephson oscillations and therefore of J and Λ .

3.2.3 Experimental dependence of the relaxation timescale

The heuristic model provides a parameter τ characterizing the relaxation timescale and presenting limited correlations with the other parameters of the model. Therefore, we use the heuristic model to extract τ in various experimental situations and draw quantitative conclusions on the relaxation timescale. We investigate the dependence of the relaxation timescale with the oscillations amplitude, the tunnel coupling strength and the atom number. This approach is limited to initial states of high statistical coherence, for which the mean trajectory is representative. In the case of low phase coherence, under the effect of interaction-induced phase diffusion or temperature, the relaxation can only be studied through the phase-locking, i.e. by studying the characteristic decay time of the fluctuations.

3.2.3.1 Initial phase and initial energy

Various initial phases with high statistical coherence In this section, we consider the oscillating dynamics of $N = 750(100)$ atoms for different values of the initial phase. The initial phase is varied by changing the detuning of the decoupled trap ($I_{rf} = 0.65$) between $\theta = [-2 : 1 : 2]^\circ$. The analysis of the fringes after phase accumulation is displayed in Fig. 3.17. The phase varies between $\phi_0 = -0.2\pi$ and -0.8π without decrease of the fringe contrast. For $\theta = \{-2, -1, 0\}^\circ$, the phase coherence is maintained. This is compatible with the TMBH predictions discussed in Sec. 1.3.4.5, according to which the phase diffusion rate does not depend on the detuning value. However, for $\theta > 0^\circ$, the phase spread increases and we can expect that the oscillating dynamics involves additional effects. The initial energy after recoupling is evaluated by k_0 :

$$k_0 = \sin(\Phi_0/2), \quad (3.28)$$

with Φ_0 the amplitude of the phase oscillations.

Effect on the relaxation timescale Figure 3.18 displays the oscillating dynamics for the initial phase values corresponding to $\theta = \{-1, 0, 1\}^\circ$. In these three cases, the fit using the analytical pendulum solutions converges. For $\theta = -2^\circ$ (smallest value of the initial phase), the amplitudes of the oscillations after recoupling are too small to be distinguished from fluctuations. For $\theta = 2^\circ$ (largest value of the initial phase), the fit does not converge. This can be attributed to the lower phase coherence and proximity of the separatrix.

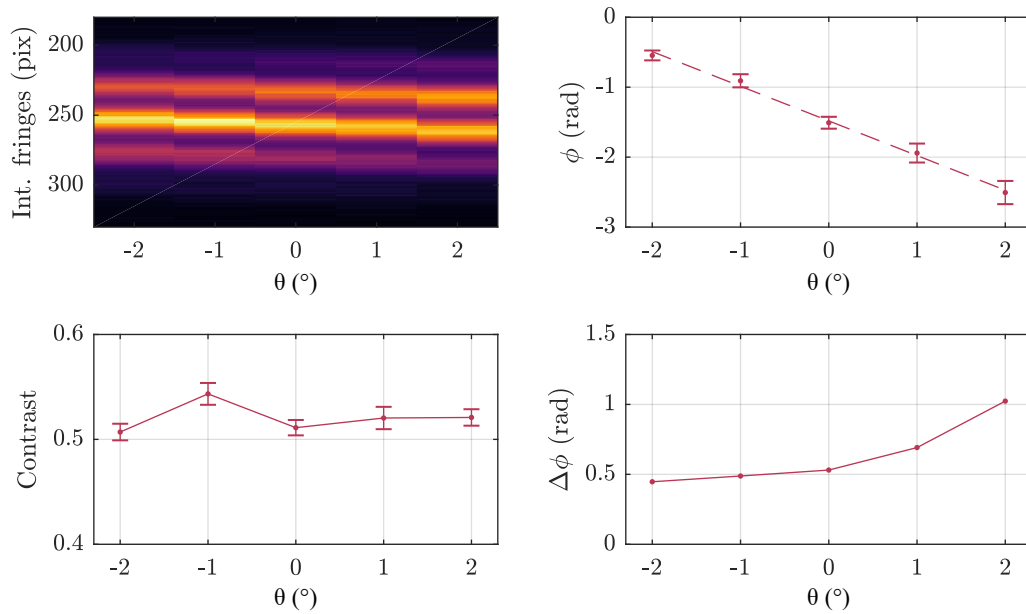


Figure 3.17: Initial states characterized by different phase values obtained by varying the trap detuning. **Top left:** Fringes integrated along the elongated direction showing a linear displacement of the fringes with the tilt angle, signature of a linear phase accumulation. **Top right:** Averaged global phase obtained by averaging the global phase extracted from the single shots. The phase presents a linear dependence with θ (dashed line is a linear fit) and the error bars increases with the tilt angle due to the finite tunnel coupling. **Bottom left:** Averaged global contrast obtained by averaging over the global contrast of the individual pictures. The contrast remains constant for the various tilt angles such that, in each case, the phase is imprinted globally. **Bottom right:** Statistical spread of the phase.

We display the amplitudes of the phase oscillations Φ_0 as a function of θ in the left panel of Fig.3.19. We observe that for each of the three cases considered, $\Phi_0 < |\phi_0|$ that we attribute to the recoupling discussed in Sec. 3.1.4. Φ_0 presents a linear dependence with α resembling the one of ϕ_0 which confirms that the fit results are reliable. Additional indications come from the plasma frequency $\omega_0 = 530(20)$ Hz, which is constant as expected from the constant atom number and identical trap geometry. The imbalance amplitude being small, it was not properly evaluated and we constrain it to increase with Φ_0 . This however, does not impact strongly the determination of the damping time τ . The deduced TMBH parameters in this case are: $J/h = 5.5(1)$ Hz, $U/h = 0.9(03)$ Hz and $\Lambda = 64(3)$.

The right panel of Fig. 3.19 displays the dependence of the characteristic damping time τ with Φ_0 extracted from the fit. The error bars corresponds to the 95% confidence interval. For the phase amplitudes considered, the initial energy in the system does not significantly affect the characteristic relaxation time.

In addition, the entire dynamics, from large oscillations amplitude to equilibrium, can be fitted with a unique value of τ without substructure appearing in the residuals. A dependence of τ with the oscillation amplitude would require that τ changes over time. Therefore, a dependence of τ with Φ_0 is at most limited. This is an important observation to fulfill by a microscopic theory, which must determine an energy transfer mechanism with

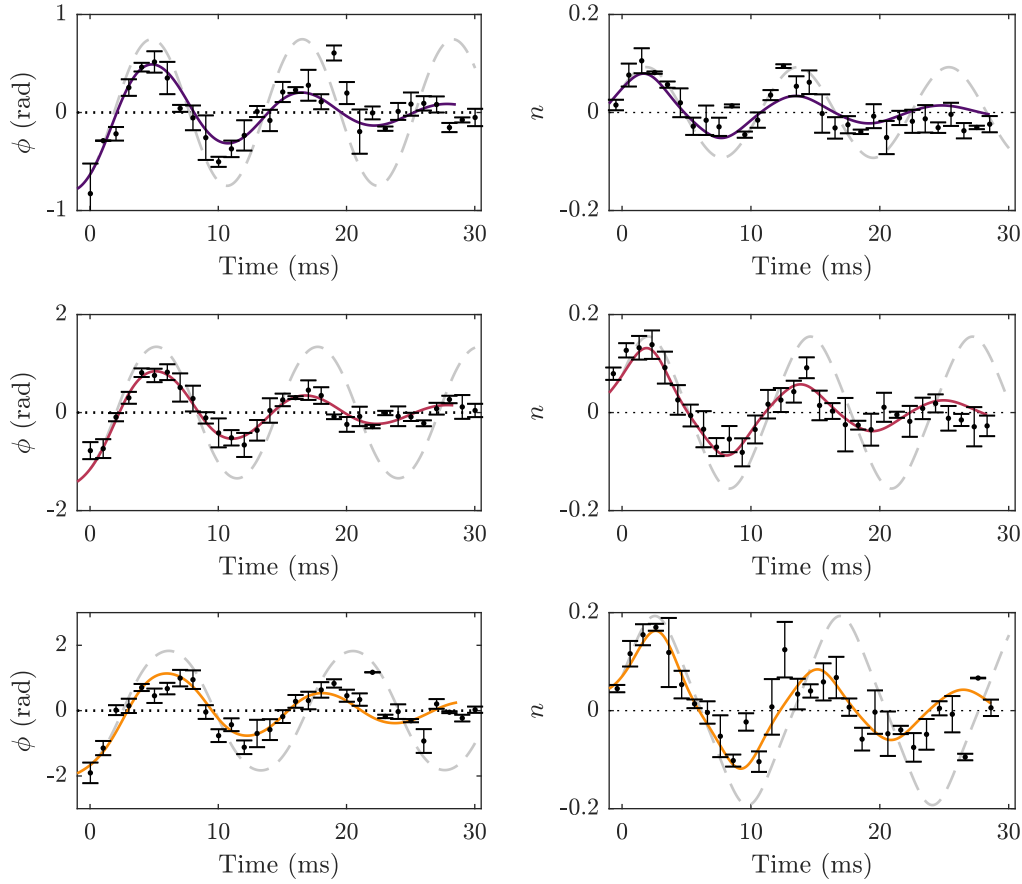


Figure 3.18: Oscillating dynamics for various initial phase. The initial phase is prepared by detuning the decoupled trap by $\theta = \{-1, 0, 1\}^\circ$ to reach $\phi_0 = -\{0.32, 0.48, 0.64\}\pi$ before recoupling. In the recoupled trap $I_{\text{rf}} = 0.575$, the dynamics of $N = 750(100)$ atoms presents oscillations in phase (left) and imbalance (right) characterized by $\Phi_0 = 0.21, 0.45, 0.56\pi$ and a constant plasma frequency $\omega_0 = 530$ Hz. The TMBH parameters deduced from the heuristic model are $J/h = 5.5(1)$ Hz, $U/h = 0.9(03)$ Hz and $\Lambda = 64(3)$ and the undamped trajectories are indicated by the dashed gray lines.

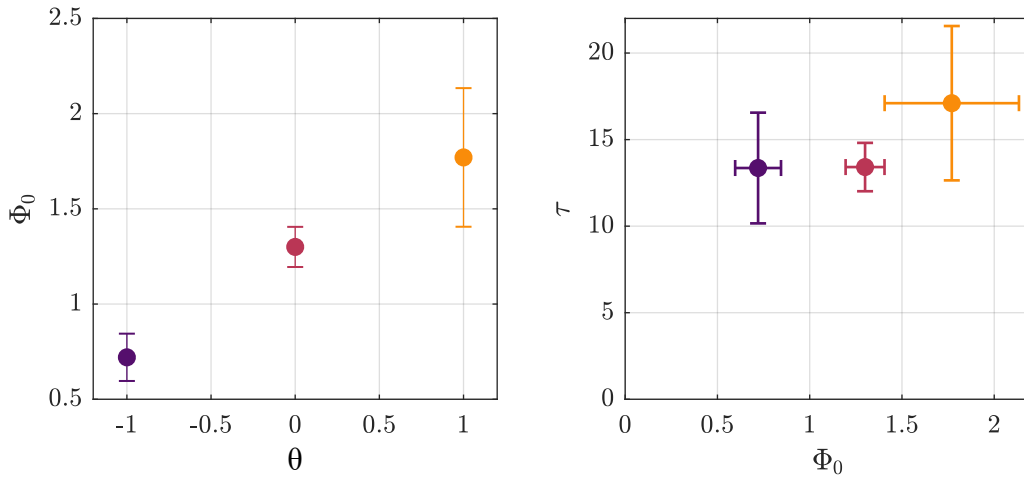


Figure 3.19: Dependence of τ with Φ_0 . **Left:** Φ_0 increases linearly with θ , which is compatible with the values of the initial prepared phase ϕ_0 . **Right:** The characteristic relaxation time does not depend on the initial phase for the range of ϕ_0 where the statistical dephasing is small.

a timescale identical regardless of the initial energy, at least up to a threshold $\Phi_0 = 0.56\pi$.

We consider in the following initial phase values where the fit gives limited error bars, which restricts the initial phase to $|\phi_0| < 1.5$ rad.

3.2.3.2 Tunnel coupling strength

Finite tunnel coupling We now investigate the impact of the barrier height, therefore of the tunnel coupling J . We change the height of the barrier by performing a recoupling of $N = 3500(500)$ atoms to $I_{\text{rf}} = \{0.5, 0.525, 0.55, 0.575, 0.6\}$. The preparation protocol is identical, resulting in comparable values of the initial imbalance $n_0 = -0.004(13)$, initial phase $\phi_0 = -1.93(35)$ rad, initial contrast $C_0 = 0.53(7)$ and initial coherence $R_0 = 0.94(3)$.

The oscillating dynamics of the phase and imbalance is displayed in Fig. 3.20 where J decreases from the top to the lower panels. It shows clearly that the oscillation frequency decreases with J (one must notice that the two lowest rows display evolution up to longer times). The phase amplitude extracted from the fit increases slightly when J decreases. As the prepared phase ϕ_0 is identical, we attribute this to the recoupling stage. The recoupling duration is fixed to 3 ms while the amplitude of the dressing ramp varies: $I_{\text{rf}} = 0.65 \rightarrow 0.5$ for the largest coupling compared to $I_{\text{rf}} = 0.65 \rightarrow 0.6$ for the smallest coupling. One can expect that the system undergoes a more significant dynamics for larger coupling values, which decreases the amplitude of the phase oscillations in the final trap. Therefore the amplitude of the phase oscillation increases in Fig. 3.20 from the top to the bottom panel. The amplitude of the imbalance oscillation involves two effects. On the one hand, as the phase amplitude increases, so does the imbalance amplitude. However, smaller tunnel coupling also decrease N_0 and this effect dominated over the recoupling effect. This explains that the amplitude of the imbalance oscillations decreases with J .

The dependence of τ and of ω_0 with I_{rf} are extracted from the fit. However, for a more meaningful comparison, we display in Fig. 3.21 the dependence of τ and ω_0 as a function of the tunnel coupling strength J deduced from Eq. 1.130. In the right panel of Fig. 3.21, we display the plasma frequency extracted from the fit as a function of the tunnel coupling strength J . The red line indicates the TMBH prediction of ω_0 for the values of J and Λ extracted from the fit. To determine Λ , we consider $N = 3500$ atoms and the averaged on-site interaction energy \bar{U} is equal to $\bar{U}/h = 0.85$ Hz. The fit results of ω_0 are compatible with the TMBH predictions.

Relaxation versus interaction-induced phase diffusion In the left panel of Fig. 3.21, we display the characteristic damping time as a function of J . For the set of data considered, the relaxation timescale does not depend on the tunnel coupling, even for very small values of J . This seems to imply that the coupling could be arbitrary low and lead to a relaxation over 15 ms. Such a conclusion would have serious consequences on the description of the interaction-induced phase diffusion presented in Sec. 1.3.4.5. However, interaction-induced phase diffusion has been observed on our experiment [107, 153], where the phase randomizes in a decoupled trap in a timescale comparable to the relaxation timescale established in Fig. 3.21. It indicates that in a trap of negligible coupling, dephasing dominates over the relaxation. The relaxation outside the oscillating regime strongly differs from the observations of this chapter. We will discuss this in Chapter 4.

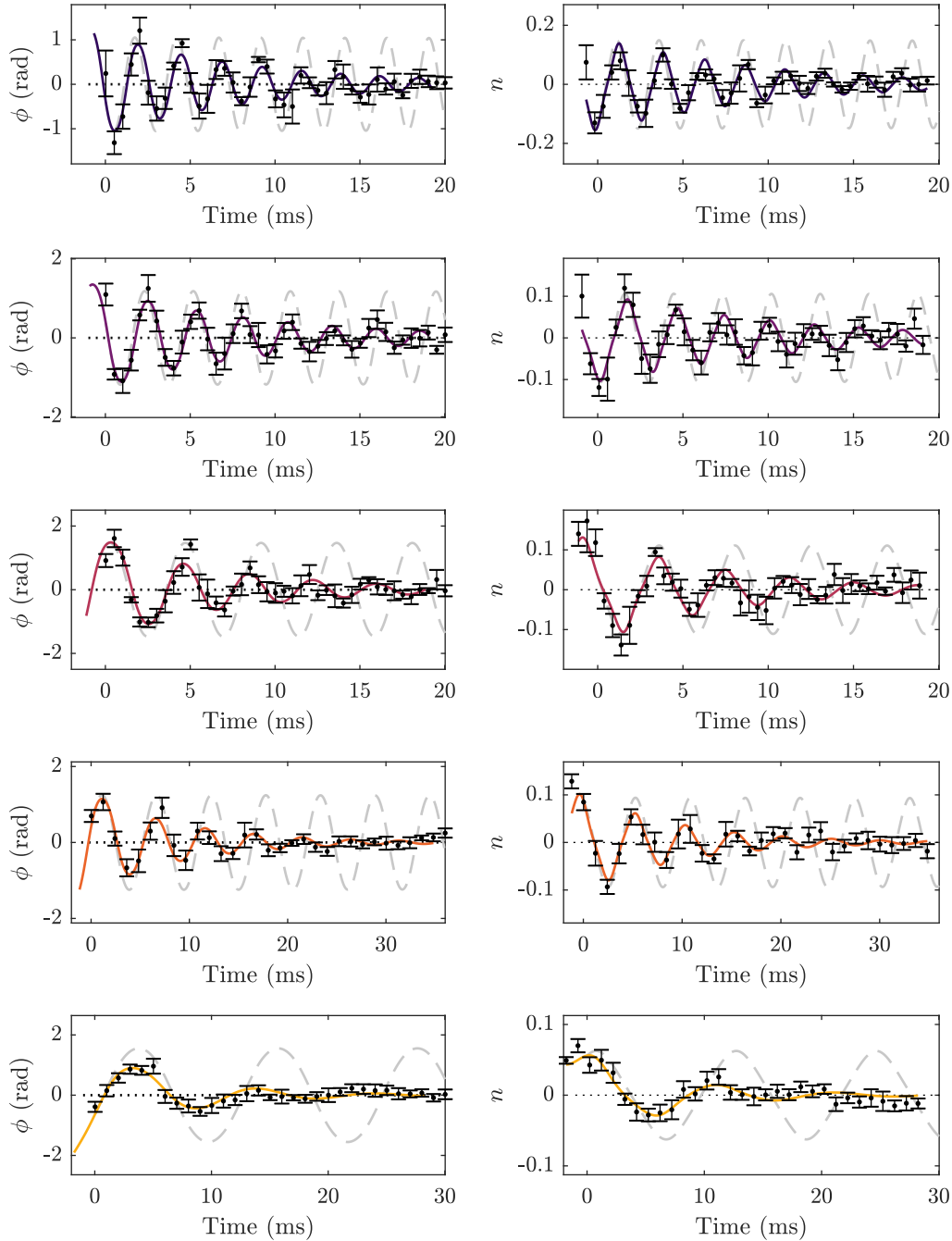


Figure 3.20: Tunneling dynamics of $N = 3500$ atoms for various tunnel coupling associated to the dressing amplitudes $I_{rf} = \{0.5, 0.525, 0.55, 0.575, 0.6\}$ (top to bottom). The fit using the heuristic model gives the TMBH parameters allowing to display the undamped trajectories (gray dashed lines).

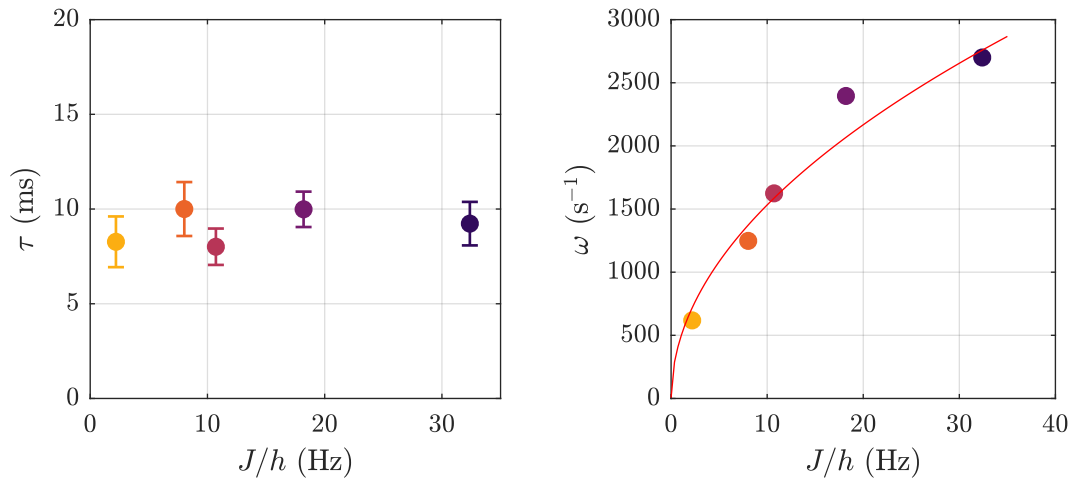


Figure 3.21: Dependence of the damping time and plasma frequency with the tunnel coupling. The tunnel coupling is modified by changing the rf dressing amplitude and J/h is extracted from the fit parameters. The values of the characteristic damping time and plasma frequency corresponds to the data presented on Fig. 3.20 with identical color coding. The atom number $N = 3500$ atoms is maintained constant, as well as the initial phase $\phi_0 = 1.93(35)$ rad. The damping time does not present as systematic variation with the tunnel coupling over an order of magnitude. The plasma frequency presents the expected dependence in $\omega \approx \sqrt{N\bar{U}} \times 2\bar{J}/h$, where $\bar{U}/h = 0.85$ Hz is the mean value of the U extracted from the fits.

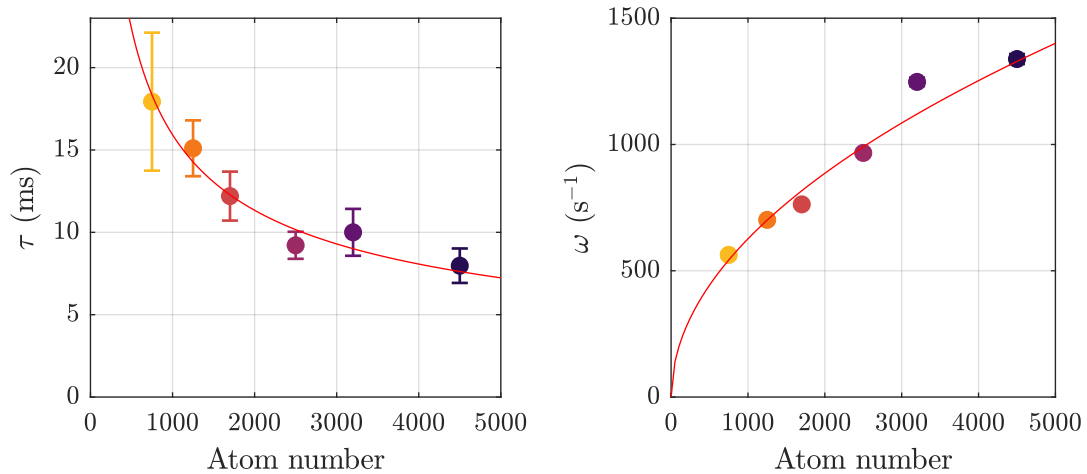


Figure 3.22: Dependence of the damping time and plasma frequency with the atom number. In the trap characterized by $J/h = 7(2)$ Hz, the atom number varies from $N = \{4500, 3200, 2500, 1700, 1250, 750\}$. The data and the fit results are displayed on Figs. (3.18, 3.20, 3.23). The damping time presents a dependence in $1/\sqrt{N}$. The plasma frequency presents the expected dependence in $\omega \approx \sqrt{N\bar{U}} \times 2\bar{J}/h$, where $\bar{U}/h = 0.71$ Hz and $\bar{J}/h = 7$ Hz are taken as the mean of the values extracted from the fits.

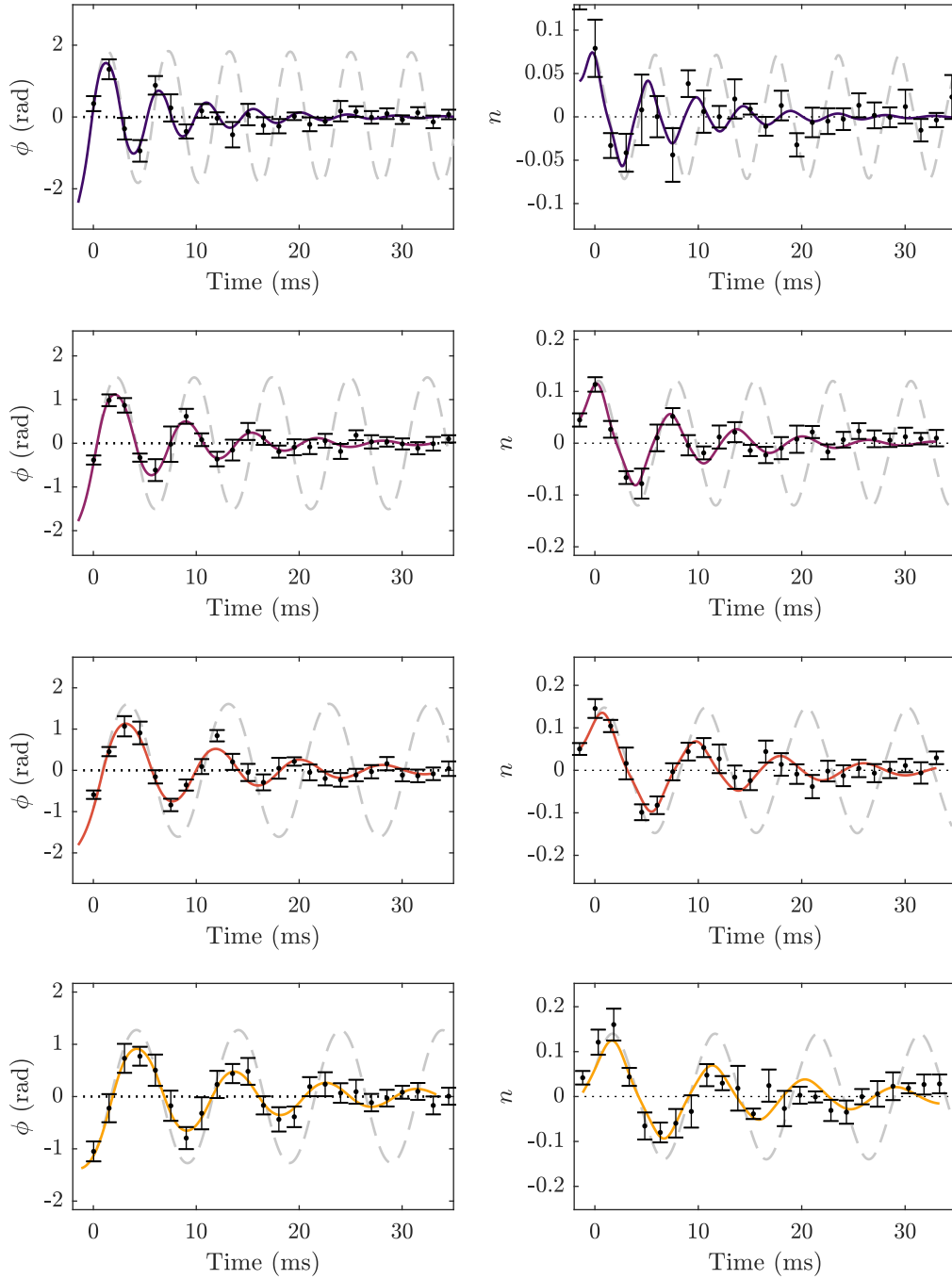


Figure 3.23: Josephson oscillations for various atom number. The atom number is decreased and takes the values (from top to bottom) $N = \{4500, 2500, 1700, 1250\}$. The TMBH parameters are $\bar{U}/h = 0.71$ Hz and $\bar{J}/h = 7$ Hz, taken as the mean of the values extracted from the fits.

3.2.3.3 Atom number

Modification of the atom number It is experimentally difficult to modify the atom number independently from the temperature. To limit the variations of temperature, we perform a rf shielding in the harmonic single-well potential by applying a rf field at a fixed frequency ω_{rf} larger than the Larmor frequency at the center of the trap. Where the evaporative cooling relies on decreasing the rf frequency to approach the trap bottom, the shielding maintains a constant frequency. As the atoms in the trap heat up over time, those reaching an energy above $\hbar\omega_{\text{rf}}$ are evaporated. It is not clear whether this protocol increases the global temperature up to the temperature corresponding ω_{rf} or if the thermalization of the remaining atoms leads to a cooling. However, the shielding allows to change the atom number by almost an order of magnitude without significant modification of the temperature.

Influence of the atom number The atom number is varied between $N = 1250(100)$ and $N = 4500(500)$ atoms. The parameters of the preparation sequence are identical in all cases and the prepared phase is $\phi_0 = -1.48(98)$ rad associated to a contrast $C_0 = 0.55(7)$ and a phase coherence $R_0 = 0.81(3)$. The typical imbalance is $n_0 = 0.006(47)$. The recoupling is performed to the trap of dressing amplitude $I_{\text{rf}} = 0.575$.

The time evolution of the phase and imbalance for the various atom numbers is displayed in Fig. 3.23 where the atom number decreases from top to bottom. The oscillation frequency decreases for smaller atom numbers, as expected in the TMBH model. The amplitude of the phase oscillations is almost identical which is expected as the recoupling ramp is identical. The amplitude of the imbalance oscillations increases as the atom number, and therefore Λ decreases. This is also compatible with the TMBH predictions.

The value of the TMBH parameters are $\bar{U}/h = 0.71$ Hz and $\bar{J}/h = 7$ Hz, obtained by averaging the values of the on-site interaction energy and tunnel coupling energy deduced from the fit parameters and Eqs. (1.130, 1.131). For the smallest atom number $N = 1250$ atoms, $\Lambda = 63$, which is close to the lowest value we allow to neglect the longitudinal inhomogeneities. To decrease the atom number further, we must consider a trap of smaller tunnel coupling. As we established that the tunnel coupling does not impact τ , we combine these results with the one of Sec. 3.2.3.1 where $N = 750(100)$ atoms and $J/h = 5.5(1)$ Hz, $U/h = 0.9(03)$ Hz and $\Lambda = 64(3)$. Here again, this is close to the lowest value of Λ we can consider.

For these data, the dependence of the plasma frequency with the atom number is represented in the right panel of Fig. 3.22. The red line indicates the predictions of ω_0 for various atom number and $\bar{U}/h = 0.71$ Hz and $\bar{J}/h = 7$ Hz. The variation of the plasma frequency is compatible with the predictions of the TMBH model.

The variation of the characteristic relaxation time τ with the atom number is displayed in the left panel of Fig. 3.22 and shows a dependence in:

$$\tau(N) = aN^b, \quad (3.29)$$

with $a = 0.47(2)$ and $b = -0.49(3)$ determined by a fit. This leads to:

$$\eta = \frac{\sqrt{N}}{U}. \quad (3.30)$$

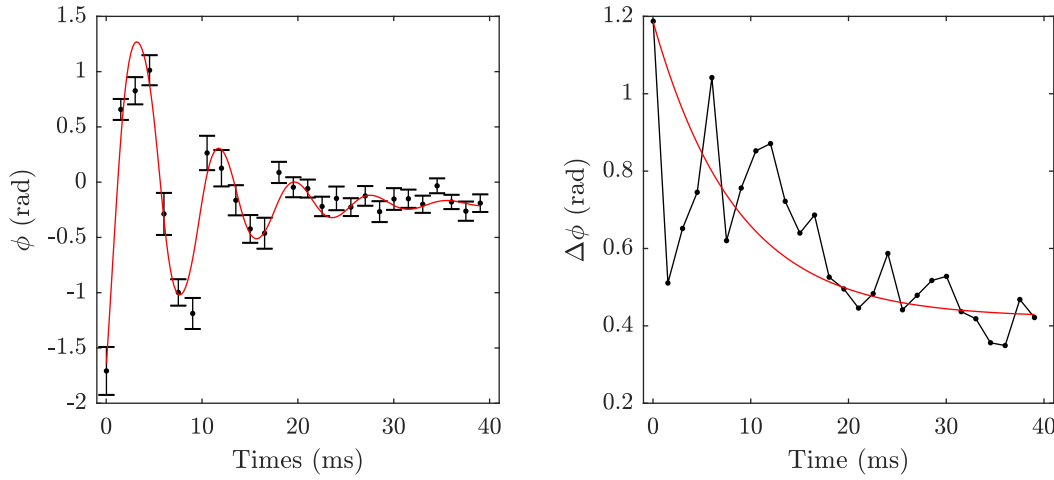


Figure 3.24: Evolution of the averaged phase and associated fluctuations. At $T = 18$ nK, the fit of the averaged phase evolution establishes the characteristic damping time $\tau = 11.6$ ms. After 25 ms, the dynamics of the mean values is indistinguishable from the statistical noise. The statistical phase fluctuations are showing an exponential decay with substructures which can be attributed to squeezing oscillations. As a guideline, we display the exponential decay matching the initial and final values of the spread and characterized by the damping time τ extracted from the mean values.

3.2.3.4 Initial temperature

For most data presented in this manuscript, the temperature of the initial condensate in the single-well potential is estimated around $T = 18$ nK using Yang-Yang thermometry [154]. This temperature is low enough to use an effective $T = 0$ description.

However, in the following, we increase the temperature by maintaining the condensate in the single-well potential before splitting. The heating rate in the initial single-well potential reads $R_T = 0.19$ nK/ms such that the temperature is varied between $T \approx 20$ nK and $T \approx 60$ nK in 200 ms. The increase of temperature before splitting strongly decreases the statistical phase coherence, as described by [155]. While this can in principle allow to evaluate the temperature, it only allows a qualitative estimation of the temperature in our experiment, as additional effects decrease the phase coherence.

Due to the decreased coherence, the mean values of the phase and imbalance are no longer representative of the dynamics and the heuristic model cannot be used to extract a relaxation timescale. Instead, we must investigate the relaxation timescale from the perspective of the statistical fluctuations, which increases the experimental complexity of the study.

Reference values We first analyze the dynamics of the phase and imbalance for the smallest initial temperature $T = 18$ nK. In this case, the mean values are representative of the dynamics and serve as a reference. The evolution of the phase and phase spread are displayed in Fig. 3.24. The fit of the mean values using the heuristic model yields $\tau = 11.6$ ms. The fluctuations decrease exponentially with a timescale comparable to the one of the mean values. At short time, the fluctuations exhibit an additional oscillating feature that we attribute to the squeezing oscillations presented in Sec. 1.3.4.3. Therefore,

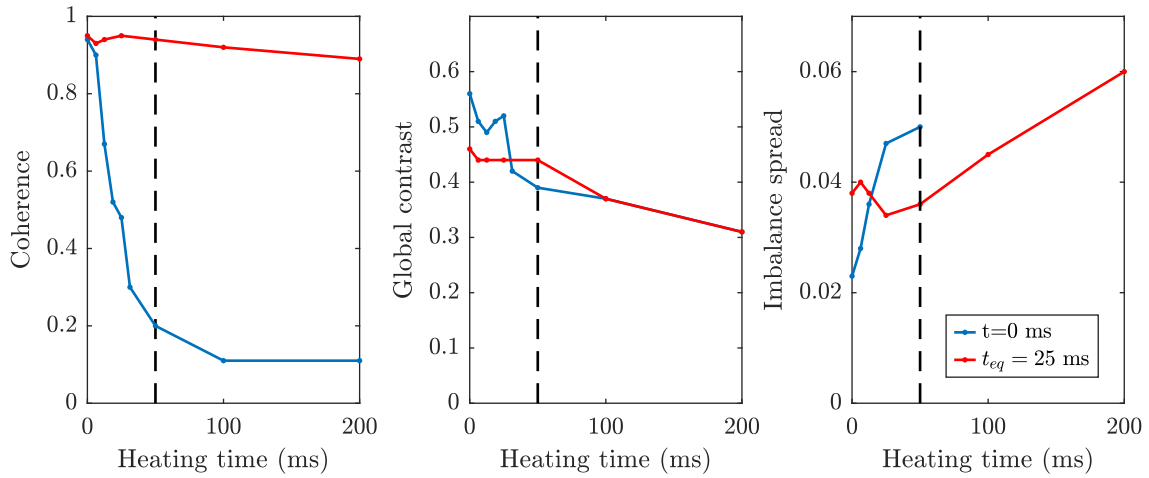


Figure 3.25: Comparison of the initial state and state after 25 ms for various temperatures.

The temperature of the system is modified by introducing a heating time. It ranges from $T = 20$ nK (no heating time) to 60 nK after $t = 200$ ms. The decrease of phase coherence of the initial state indicates an increase of temperature. We compare it the initial state to the state after 25 ms of dynamics. For low temperatures associated to a heating time $t < 50$ ms, the phase coherence is recovered and the imbalance spread stabilized, indicating a phase locking. For heating times $t > 50$ ms, the initial contrast decreases and is not recovered during the dynamics, which could indicate excitations to higher transverse states and an absence of relaxation.

an exponential fit is a crude description of the dynamics. However, the dynamics of the phase spread stabilizes after 25 ms where we consider that the relaxed state is reached.

Effect of the temperature on the relaxed state Extracting a decay time from the evolution of the fluctuations over 25 ms requires too much time for the stability of the experiment. Instead, we perform measurements with a high statistics at 25 ms where the relaxation is reached at low temperature. Figure 3.25 displays the values of the statistical coherence, global contrast and imbalance spreads and compare these quantities to their initial values.

For heating times $t < 50$ ms, corresponding to temperatures $T < 30$ nK, the increase of temperature is observed as a fast decay of the statistical phase coherence. The global contrast of the individual fringes measurement remains constant. The imbalance increases by a factor 2 between $T = 20$ nK and $T = 30$ nK. After 25 ms of tunneling dynamics, the coherence is recovered, regardless of the value of the initial state. The imbalance also reaches a constant value. These observations indicate a relaxation toward an identical final state.

However, for higher temperature values, the behavior of the system changes. The drop of contrast of the initial state can be attributed to a non-negligible thermal fraction or to longitudinal excitations. After 25 ms of dynamics, the final contrast is clearly identical to the initial one. The phase coherence is recovered but the increase of the imbalance fluctuations shows a relaxation is still possible but with a timescale is longer than at lower temperatures.

3.2.3.5 Transverse and longitudinal cloud extensions

Two important parameters remain to be studied. The first one is the transverse extension of the cloud, corresponding to the on-site interaction U . Changing the atom number within our range of parameter is not enough to induce a significant change of U . This requires to change the transverse confinement of the potential. One could imagine displacing the trap bottom of the static trap. The consequence is that the rf-dressing would lead to a different dependence of the barrier height and well-spacing and results in a different transverse confinement.

The other parameter is the longitudinal confinement which consists in investigating the 0D/1D transition. Experimentally, the "dimple" wire of the chip, which creates a local deformation of the longitudinal trap, could compress or decompress the atoms longitudinally.

However, studying these two parameters present many challenges and would require a complete characterization of the traps as well as of the heating rates and collective excitations. We recently implemented in our research group a much more efficient method to create arbitrary optical dipole potentials using a laser light shaped by a digital micromirror device [156].

3.2.3.6 Effective relaxation-free dynamics

In this section, we propose a method which could in theory result in an undamped dynamics of the mean evolution. This method is based on the established dependence of τ with the experimental parameters.

Sustained oscillations in phase Considering the phase only, the envelope of the damped oscillations is deduced from the properties of the Jacobi amplitude function with an exponential decay and reads:

$$\Phi(t) = \frac{1}{2} \arcsin(k_0 e^{-t/\tau}), \quad (3.31)$$

with $k_0 = \sin(\Phi_0/2)$ and Φ_0 the initial phase amplitude. Therefore, we can maintain Φ constant by defining a linear ramp of τ over time, such as:

$$\tau = At. \quad (3.32)$$

The value of the parameter A determines the sustained amplitude of the oscillations $\Phi = \frac{1}{2} \arcsin(k_0 e^{-1/A})$. The increase of τ relies on a modification of the atom number as we established the dependence in $\tau \propto N^{-2}$. Therefore, τ follows Eq. 3.32 when the atom number decreases as:

$$N(t) = \frac{1}{(2At)^2}. \quad (3.33)$$

As a consequence of the change of atom, the tunneling frequency, defined by Eq. (1.105) is modified such that the oscillations do not resemble undamped oscillations. To address this issue, we modify J over time to compensate the change of frequency due to N . As

we established that J does not affect τ in the oscillating regime, we expect to maintain ω constant without modifying τ . The time dependence of J follows:

$$J(A, t) = \frac{NU}{4} \left[\sqrt{1 + \left(\frac{2\hbar\omega}{NU} \right)^2} - 1 \right]. \quad (3.34)$$

We neglect in this the change of U due to the change of atom number and tunnel coupling.

Experimental regime In this model, A can be arbitrarily large, such that an amplitude $\Phi \approx \Phi_0$ can in principle be maintained. However, for large values of A , the corresponding change of atom number is too fast to be experimentally realistic. Similarly, the brutal change of J is expected to excite collective excitations and to affect both the evaporative removal of atoms and their dynamics. In addition, observing a dynamics with less than 500 atoms is experimentally challenging.

Therefore, we must define a range of Φ defining a realistic ramp of N , which sets limits to Φ_0 and A . The value of A is determined by the shape of the ramp of atom number. This implies that the sustained amplitude will be smaller than Φ_0 . The duration over which we can sustain the oscillation is determined by the boundaries of the atom number. We consider that N can vary between 6000 atoms and 500 atoms. The frequency which can be sustained depends on the boundaries of J/h that we fix as $0 \text{ Hz} < J/h < 45 \text{ Hz}$. The compensation of the damping stops when either $N < 500$ atoms or $J/h > 45 \text{ Hz}$.

A realistic sequence is displayed in Fig. 3.26. It consists in preparing $N = 6000$ atoms and an initially large phase difference $\Phi_0 = 0.8\pi$ in a trap of on-site interaction energy $U/h = 0.8 \text{ Hz}$ and of tunnel coupling J given by Eq. (3.34). The frequency is $\omega = 2\pi \times 190 \text{ Hz}$ and fulfills $\omega = \sqrt{UN_{\min}} \times 2J_{\max}/\hbar$. Therefore it is the value of frequency for which J/h reaches its upper boundary exactly when the atom number reaches its lower boundary. For any higher value of the frequency, the tunneling reaches its boundary before the atom number and reduce the time over which the damping can be compensated.

In Fig. 3.26, $A = 0.7$. During a first part of the dynamics, N and J remain constant until $\Phi(t) = \Phi_0 e^{-1/A}$, which occurs after $t = 9 \text{ ms}$. Afterward, the atom number is decreased to increase τ and maintain the amplitude $\Phi(t)$ constant. The coupling J is increased accordingly to maintain the oscillation frequency constant. The ramps stops after 32 ms, when N and J reach their experimental boundaries. At longer times, the damping can no longer be compensated.

This method could be useful to study the oscillations of the phase fluctuations which are strongly suppressed by the damping. The damping decreases quickly the amplitude of the oscillations of the phase fluctuations, making them smaller than the imaging resolution. As the fluctuations oscillate twice faster than the main value, sustaining oscillations at the frequency ω allows to sustain the fluctuations oscillations at 2ω and observe more oscillations before they become inaccessible experimentally.

Imbalance oscillations This method will not suffice to preserve the amplitude of the imbalance oscillations. Indeed, the amplitude N_0 is given by:

$$N_0 \approx \frac{2k}{\sqrt{\Lambda}}. \quad (3.35)$$

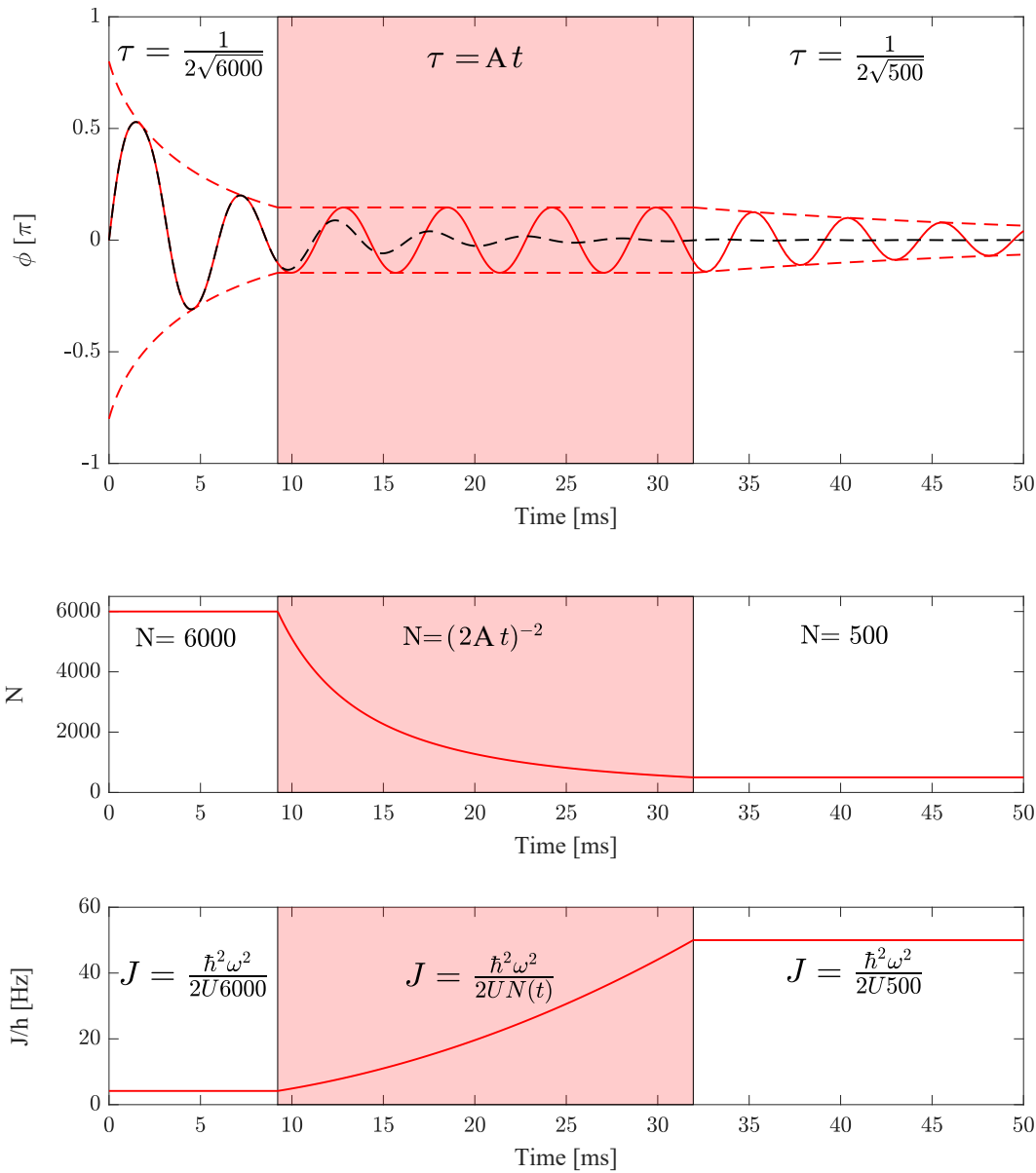


Figure 3.26: Damping compensation by change of the atom number and tunnel coupling.

The system initially consists in $N = 6000$ atoms, for which an initial phase amplitude of $\Phi_0 = 0.8\pi$ is prepared. The initial phase is however $\phi(0) = 0$ by convention of the Jacobi elliptic functions. We seek to sustain a phase oscillation of amplitude $\Phi = \frac{1}{2} \arcsin(\sin(\Phi_0/2)e^{-1/0.7})$. The damping is unavoidable in the first part of the dynamics as long as the amplitude is larger than Φ . This condition is realized after 9 ms, after which the atom number is decreased to maintain the t/τ constant. The frequency is maintained constant by increasing J . This compensation stops when N or J reach their boundary. The choice of frequency is $\omega = 2\pi \times 190$ Hz and $U/h = 0.8$ Hz such that the two parameters N and J reach their boundary at the same instant, after 32 ms of dynamics. After this, the dynamics is damped again. The dashed black line on the upper panel shows the dynamics for constant values of N and J and is fully damped after 30 ms.

With the previous ramp, the modification of N and J do not maintain Λ constant. More complicated ramps involving J, N but also the detuning ϵ might give better results to maintain both oscillations.

Limitations A first limitation is that, as we do not know the microscopic origin of the damping, we cannot exclude that the effect of the atom number on the relaxation reported in Sec. 3.2.3.3 originates from the preparation sequence. Indeed, the atom number is changed before the splitting of the wave packet and might change the relaxation timescale. If the relaxation occurs due to the change of atoms before splitting, removing atoms during the tunneling dynamics will not affect τ as required in this proposal.

In addition, this approach neglects the effect of removing atoms on the temperature T and on-site interaction U . As the dependence of the damping with U has not been investigated, it might affect the previous picture.

3.3 Conclusion

The preparation of two condensates characterized by a global phase difference has allowed us to explore the oscillating regime of a 1D-BJJ. The oscillating feature, that can be described by an effective 0D model provided by the TMBH framework, is exponentially damped over time. Due to the shape of the damping, we describe it by a dissipative term using the analogy of the BJJ with a momentum-shortened pendulum. In the regime where the momentum-shortening is negligible, we describe the data with analytical formulas to extract a characteristic relaxation time.

We established that the relaxation in the oscillating regime does not depend on the tunnel coupling strength and that $\tau \propto N^{-2}$. Therefore, the relaxation is faster for a large number of atoms. In addition, the relaxation is not sensitive to the temperature of the system under a certain threshold. Above this threshold, excitations to higher transverse modes are possible and modify the physics of the system.

An interesting question is related to the relaxed state and concerns in particular its comparison with the ground state. It would be relevant to know whether the system reaches the ground state after relaxation or if its energy remains higher. A comparison is in principle possible using the statistics of the phase and imbalance after relaxation. However, the experimental distributions of the imbalance are very narrow. The width of the phase distributions are dominated by the imaging resolution and in particular by the pixel size. The imbalance seems a more reliable quantity to focus on.

The preliminary study of the imbalance statistics indicates that the relaxed state has larger fluctuations than the ground state. However, the imbalance fluctuations Δn decreases when J increases, which is the behavior expected for the TMBH ground state. Future studies aiming at a quantitative comparison of the relaxed and ground state will require the measurement of the imbalance with a high statistics and a special care taken in maintaining the experimental parameters identical (in particular the detuning ϵ and the atom number).

4 Transition to a relaxation-free regime

The results of the previous chapter are restricted to the oscillating regime, where the spatial position of the atoms varies over time. In this case, we have established that a relaxation occurs with a timescale independent of the coupling strength. However, the observation of interaction-induced phase diffusion in traps of very small tunnel coupling indicates that the physics of the system differs when the two condensates are coupled through their relative phase evolution with constant $\dot{n}(t)$. In the following, we investigate a situation where the displacement of atoms between the two sites is suppressed while the tunnel coupling J is finite.

The TMBH model predicts that this situation is realized in the MQST regime, reached by preparing an initial imbalance above a threshold given by the separatrix. In Sec. 1.3.2.2, we established the explicit formula of the separatrix as a function of the relative phase, atomic imbalance and trap parameters. Experimentally, Λ is so large that preparing even a small imbalance realizes the transition into the MQST regime.

However, two elongated BECs differing by their atomic population are expected to present a longitudinal dynamics beyond the $k = 0$ description. Exact calculations predicts that the dynamics of an imbalanced 1D-BJJ differ substantially from the TMBH and mean-field predictions even at a very short time [135]. This deviation is associated to the development of fragmentation and a loss of the spacial coherence. Therefore, the MQST is not expected to occur for an imbalanced 1D-BJJ. Experimentally, we verified the TMBH prediction of phase diffusion, which is an effect associated to the MQST. We therefore already observed a signature of a MQST for a 1D-BJJ of negligible tunnel coupling and $n = 0$.

This chapter is a preliminary study of the dynamics of two 1D-BEC differing by their initial atom number. We do not seek to establish a 1D description but rather to draw qualitative conclusions on the role of a local dynamics, using a model based on an array of independent BJJ.

4.1 Initial state preparation by asymmetric splitting

The experimental preparation of an atomic imbalance is illustrated in Fig. 4.1.

Adiabatic asymmetric splitting The first step consists in splitting a condensate from a harmonic single-well potential to a decoupled double-well potential. The splitting is done slowly enough to be considered adiabatic over most of the ramp duration. In addition to decreasing the tunnel coupling, we introduce an increasing detuning $\epsilon(t)$ over the splitting. This is realized by a constant tilt angle θ such that, for a constant value of θ , a larger inter-well spacing translates into a larger value of ϵ .

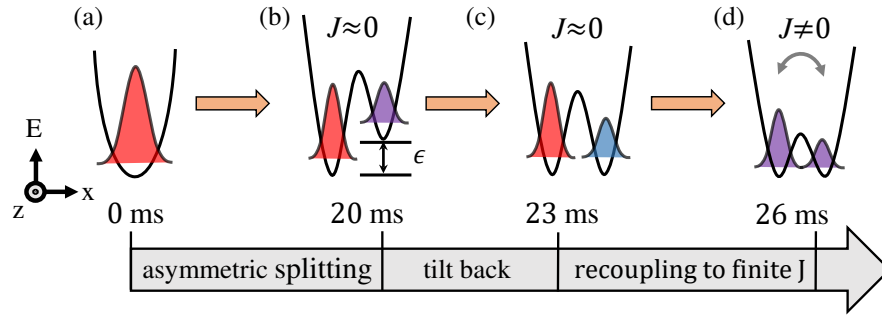


Figure 4.1: Schematic of the transverse dynamics during the imbalance preparation (a→b)

A single condensate in a harmonic single-well potential is split into two decoupled condensates differing by their atomic population. The splitting is performed over 20 ms with an increasing detuning ϵ to favor energetically one site and prepare an imbalance. (b→c) Over 3 ms, the detuning is lowered to reach a symmetric trap. (c→d) A symmetric recoupling is performed to study the dynamics of an imbalanced state in a trap of finite coupling.

The TMBH model provides a qualitative description of the phase and imbalance evolution during an asymmetric splitting. In this model, a detuning displaces the equilibrium imbalance by δn , which reads:

$$\delta n \approx -\frac{\epsilon}{NU} \text{ for } \Lambda \gg 1. \quad (4.1)$$

For an adiabatic splitting of duration T , the system follows the equilibrium state defined by $(\phi(t) = 0, n(t) = -\epsilon(t)/NU)$. Therefore, the adiabatic preparation of a final imbalance n_f can be achieved by a linear ramp of detuning:

$$\epsilon(t) = -\frac{NU n_f}{T} t. \quad (4.2)$$

As we expect the adiabaticity to be broken during the ramp, the numerical solutions of the equations of motion Eqs. (1.120, 1.121) give a more realistic picture. The simulated ramp duration T_s is reduced to account for the linear increase of dressing amplitude $I_{\text{rf}} = 0 \rightarrow 0.42$:

$$T_s = \left(1 - \frac{I_{\text{rf}}^i}{I_{\text{rf}}^f}\right) T, \quad (4.3)$$

with $I_{\text{rf}}^i = 0.42$ and I_f the final dressing amplitude. Using the experimental parameters $I_f = 0.65$ and $T = 20$ ms, the duration of the simulated splitting is $T_s = 7$ ms. It follows that the definition of the ramp of detuning reads:

$$\epsilon(t) = -NU n_f \left(\frac{t}{T} + \frac{I_{\text{rf}}^i}{I_{\text{rf}}^f} \right), \text{ with } t \in [0, T_s]. \quad (4.4)$$

Therefore, the initial state for the simulation is $(\phi_0 = 0, n_0 = -n_f I_{\text{rf}}^i / I_{\text{rf}}^f)$. The splitting also decreases the coupling J as:

$$J(t) = h \times 87 \exp \left[- \left(\frac{t \times T}{0.10 \times I_{\text{rf}}^f} \right)^{5/2} \right]. \quad (4.5)$$

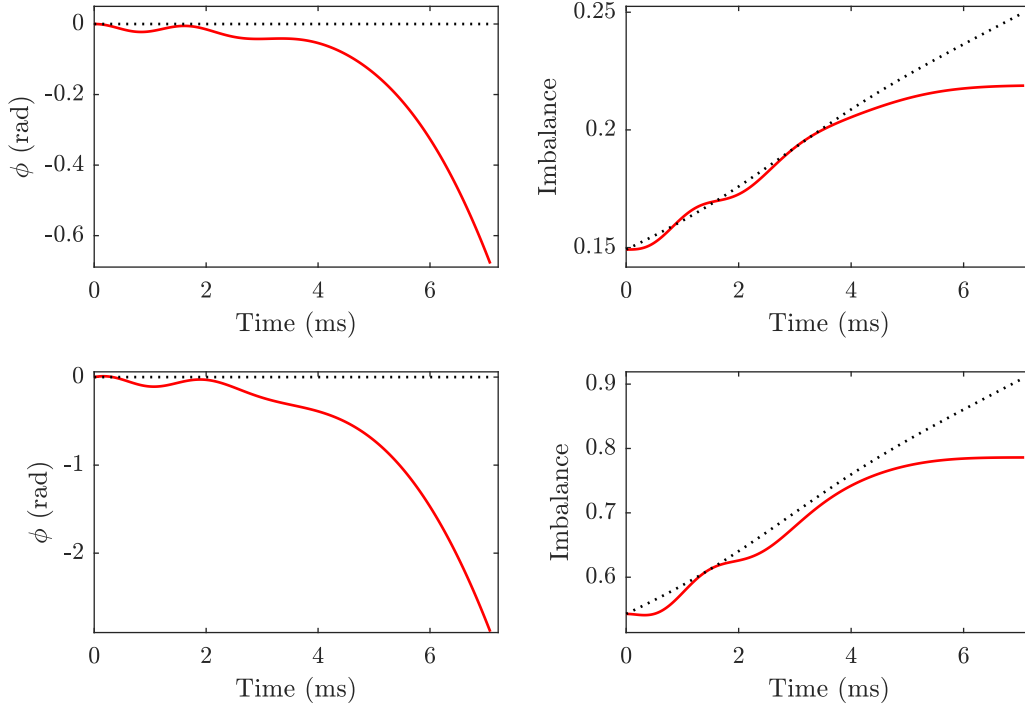


Figure 4.2: Simulation of an asymmetric splitting for small or large imbalance preparation. The atom number is $N = 2100$ atoms and $U/h = 1$ Hz. During the splitting, the detuning ϵ is linearly increased and the tunnel coupling J is decreased by a linear ramp of dressing intensity. The simulation starts with the dressing amplitude $I_{\text{rf}}^i = 0.42$ for which the detuning is $\epsilon = -NU n_f 0.42 / I_{\text{rf}}^f$ with $I_{\text{rf}}^f = 0.65$. **Top:** Splitting with small detuning aiming at $n_f = 0.25$. **Bottom:** Splitting with large detuning aiming at $n_f = 0.9$. The dashed lines indicate the equilibrium state, characterized by $\phi = 0$ and $n = -\epsilon(t)/(NU)$. The numerical solutions using the equations of motion first follow the equilibrium state, then slowly deviate from the equilibrium state. After the adiabaticity is broken, the imbalance is fixed and the phase evolves linearly.

In this case, we consider the atom number $N = 2100$ atoms and $U/h = 1$ Hz. Figure 4.2 presents the results of the simulations using $n_f = 0.25$ (top row) and $n_f = 0.9$ (bottom row). It shows that the adiabaticity is broken during the splitting such that the imbalance does not reach n_f . Therefore, to reproduce the imbalance measured after splitting, the value of n_f must be adjusted to a higher value. In Fig. 4.3, we display the values of the imbalance measured after a splitting with various angles θ (blue dots). We simulate the ramp of detuning lasting $T_s = 7$ ms and adjust n_f such that the final imbalance obtained numerically matches the measurement. In Fig. 4.3, the values of n_f are indicated by the red dots and a fit is represented by the red line.

For small imbalances, n_f and final imbalance have comparable values as the adiabaticity is maintained over most of the splitting duration. However, as the tilt angle increases, the adiabaticity is broken for smaller imbalance values and a constant ramp duration in this case does not allow to exceed an imbalance of 0.9 after splitting.

Limitations The choice of a linear ramp of detuning is a simplified description. Experimentally, the ramp consists in a linear increase of I_{rf} , which does not result in a linear

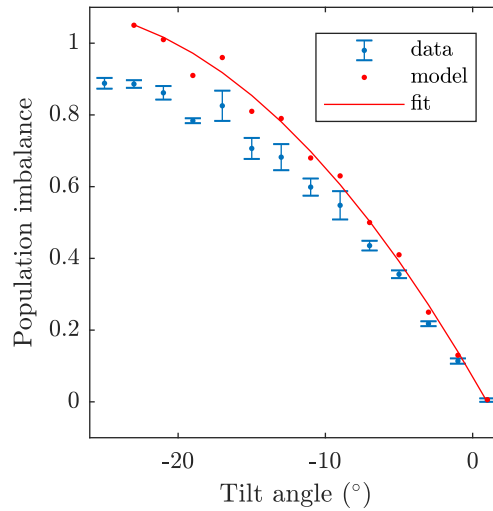


Figure 4.3: Atomic imbalance obtained after an asymmetric tilt The asymmetric splitting results in an privileged accumulation of atoms in one site of the double-well. For small tilt angles, the imbalance increases linearly with the angle $|\theta|$. However, for larger tilt angles, the imbalance saturates as the adiabaticity is broken at an early time of the ramp and preparing imbalance above 0.9 cannot be achieved using the tilt only.

increase of the inter-well spacing, as displayed in Fig. 2.16. Therefore, for a constant tilt angle θ , the increase of the detuning ϵ is not strictly linear. The linear ramp however describes qualitatively how an atomic imbalance can be prepared using an asymmetric splitting.

The second limitation is that, even though the detuning can be arbitrarily large in the model, the description only hold true in the two-mode approximation. Therefore, the final value of the detuning cannot exceed the limitations discussed in Sec. 1.3.1.

Symmetric recoupling In order to study the dynamics of an imbalanced state in a coupled trap, we want to perform a recoupling to a symmetric trap of finite coupling J . We decided to proceed in two steps, first re-establishing $\epsilon = 0$ in the decoupled trap over 3 ms and then increasing J to a finite value in 3 ms. The two-step recoupling limits the imbalance evolution during the recoupling.

However, the ramp of ϵ toward $\epsilon = 0$ displaced to equilibrium position to $(\phi = 0, n = 0)$ too quickly for the system to follow. In this case, the mean phase evolves at the rate $\propto NU n(t) - \epsilon(t)$. Therefore, as ϵ decreases to 0 for a constant $n(t)$, the phase accumulation rate increases.

Phase contrast and coherence As the initial imbalance increases, the measured phase shows increasing effect of the longitudinal extension. The left panel of Fig. 4.4 displays the integrated fringes contrast for various imbalance values and shows a clear decay of the contrast as the imbalance increases. This can be partly explained by the imbalance itself, which decreases the fringes visibility as for an optical interferometer. However, this effect is not enough to explain the decay of the integrated fringes contrast and shows that the

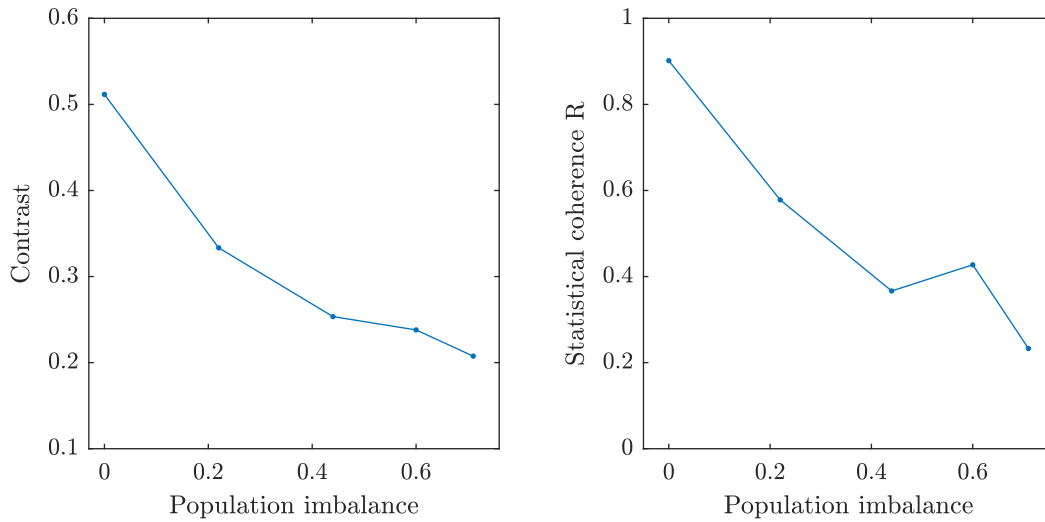


Figure 4.4: The increasing imbalance affects the phase along the condensates and its statistical reproducibility. The experimental values of the integrated contrast fringes (left) decreases for higher imbalance. This is in part due to local phase fluctuations which reduced the global contrast after integration. The statistical coherence (right), obtained by averaging the global phase over many realizations, decreases as the imbalance increases.

phase evolves locally. The statistical phase coherence is also strongly decreased by the asymmetric splitting. This can be in part due to the very low contrast which does not allow a reliable determination of the phase.

4.2 Decay and relaxation

4.2.1 Experimental evolution of the mean values

We perform a measurement of $N = 2100$ atoms in the recoupled trap $I_{\text{rf}} = 0.55$. The preparation is done with the splitting angle $\theta = 11^\circ$ such that the initial imbalance is $n = 0.48$ and the phase is $\phi = -3.7$ rad after recoupling. The evolution of the phase and imbalance up to 70 ms of dynamics is displayed in Fig. 4.5. The mean values of the imbalance present a decay over time in a time comparable to the timescale of the relaxation observed in the oscillating regime. Due to the similarity with the behavior observed in the oscillating regime, we attempt to describe the decay in the MQST by extending the dissipative BJJ to the MQST regime.

4.2.2 Dissipative BJJ in the MQST

4.2.2.1 Numerical models

The experimental observations indicate a decay of the mean values presenting similarities with the exponential decay in the Josephson oscillations regime. In the following, we present the extension of the dissipative BJJ to the MQST [57]. The equations of motion

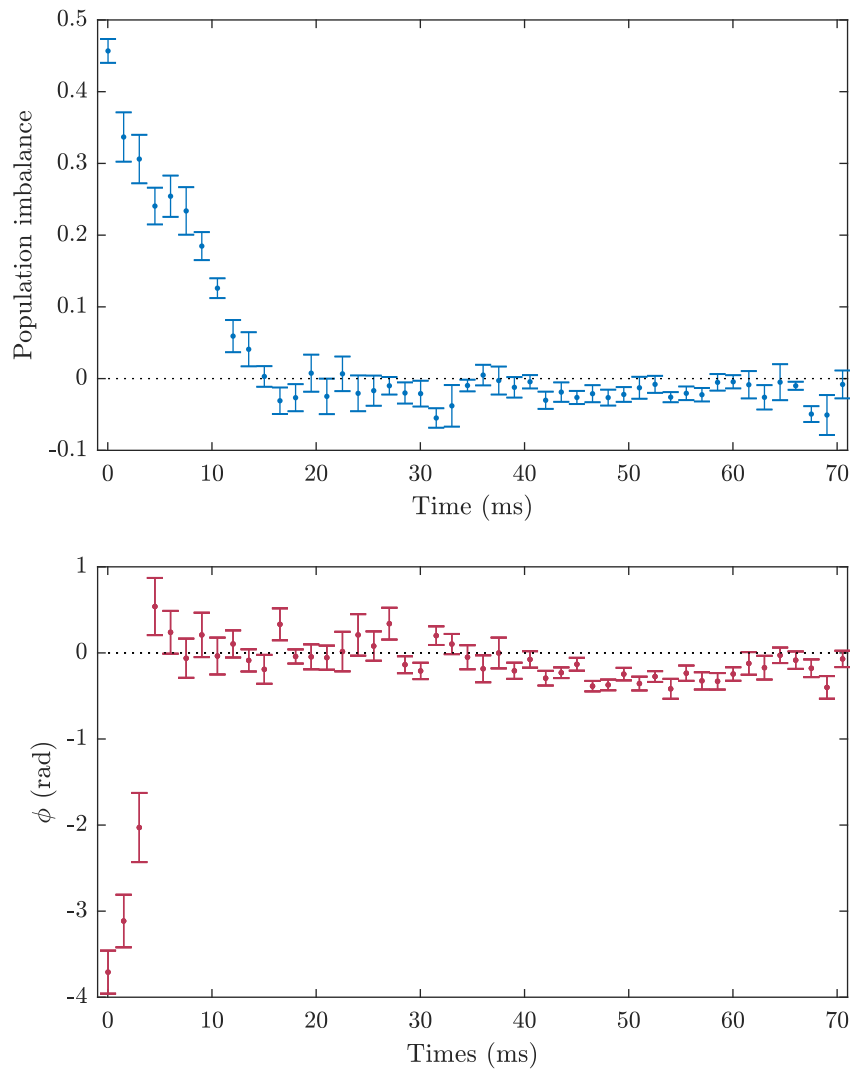


Figure 4.5: Evolution of the phase and imbalance in the MQST The initial imbalance $n_0 = 0.48$ for $N = 2100$ atoms leads to a self-trapped evolution in the recoupled trap $I_{\text{rf}} = 0.55$. The mean values of the atomic imbalance and of the phase decay to $n = 0$ and $\phi = 0$ with two different timescales.

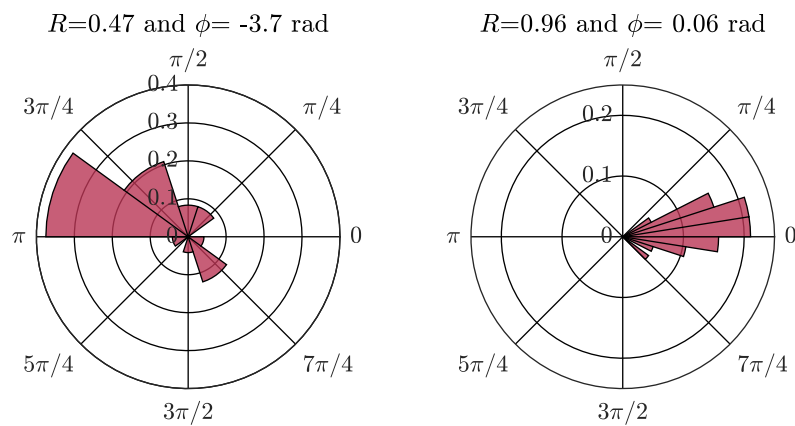


Figure 4.6: Initial and final phase distributions. The initial coherence is degraded by statistical and local fluctuations. After 70 ms the phase statistics show a phase-locking.

are given by Eqs. (3.9, 3.10) where η is the dimensionless empirical viscosity independent on the initial conditions. In Fig. 4.7, we display the numerical solution in a trap characterized by $J/h = 100$ Hz, $U/h = 0.8$ Hz and $N = 5000$ atoms. The initial phase is $\phi_0 = -\pi$ such that any imbalance $n_0 \neq \{0, \pm 1\}$ leads to a self-trapped dynamics. We consider $n_0 = \{0.15, 0.45, 0.6\}$ and shift the imbalance evolution by units of 1 for clarity. The chosen value of the viscosity is $\eta = 120$.

The numerical solutions show that the system, initially in the MQST, damps until it reaches the separatrix. Larger imbalance values result in longer durations before the system reaches the separatrix. Afterwards, the system enters the oscillating regime, where the oscillations are damped exponentially as presented in chapter 3.

This situation is analogous to a pendulum in a viscous media characterized by enough initial energy to swing over. Due to the viscosity, its energy and velocity decrease, until it can no longer swing over and undergoes damped oscillations. Larger imbalance corresponds to a higher initial energy such that it takes more rotations to reach the oscillating regime. The numerical solutions of a rigid pendulum in a dissipative media are compatible with the dissipative BJJ equations. The range of validity of the pendulum analogy is identical as in the oscillating regime. In this case, we can also establish the analytical formula describing the damping.

4.2.2.2 Analytical pendulum solution in the MQST

The analytical pendulum solutions are obtained as in the oscillating regime by damping $k_0(\omega, \tau)$ exponentially using the characteristic damping time τ . The equation of the phase established Eq. (3.15) is in principle valid both in the self-trapping and in the oscillating regime. It describes accurately the oscillating regime up to $\alpha \approx 1$, decreasing the oscillations envelope exponentially and increasing the frequency of the oscillations towards ω as displayed in Fig.4.7.

The decay in the MQST is also very well described by Eq. (3.15). It reproduces the decrease of the imbalance (and therefore of the phase accumulation slope) until the time \tilde{t} at which $\alpha(\tilde{t}) = 1$ where the system reaches the separatrix. At this time, the Jacobi amplitude presents a divergence which must be excluded to avoid a non-physical behavior of the dynamics. Right after crossing the separatrix, the system undergoes large amplitude oscillations where the behavior is no longer described by Eq. (3.15). The exponential decay of the amplitudes is still well evaluated, but not the change frequency. As the numerical solutions of the rigid remain very close to the TMBH predictions, we conclude that the pendulum analogy remains true, but that the assumption of exponential decay derived from the harmonic regime must be adjusted.

Therefore, we define two timescales for the oscillations of extremely large amplitude. A first one τ applies to the envelope and a second one τ_2 accounts for the increase of the frequency. To make these two timescales appears in Eq. (3.15), we decompose the Jacobi amplitude in the two functions it involves [91]. The envelope is defined by a $2 \arcsin(k_0 e^{-t/\tau})$. The oscillating component results from the Jacobi SN function $\text{sn}(\omega k_0 e^{-t/\tau_2} t | (k_0 e^{-t/\tau_2})^{-2})$. We normalize the Jacobi SN by its argument to maintain the oscillation between -1 and 1 .

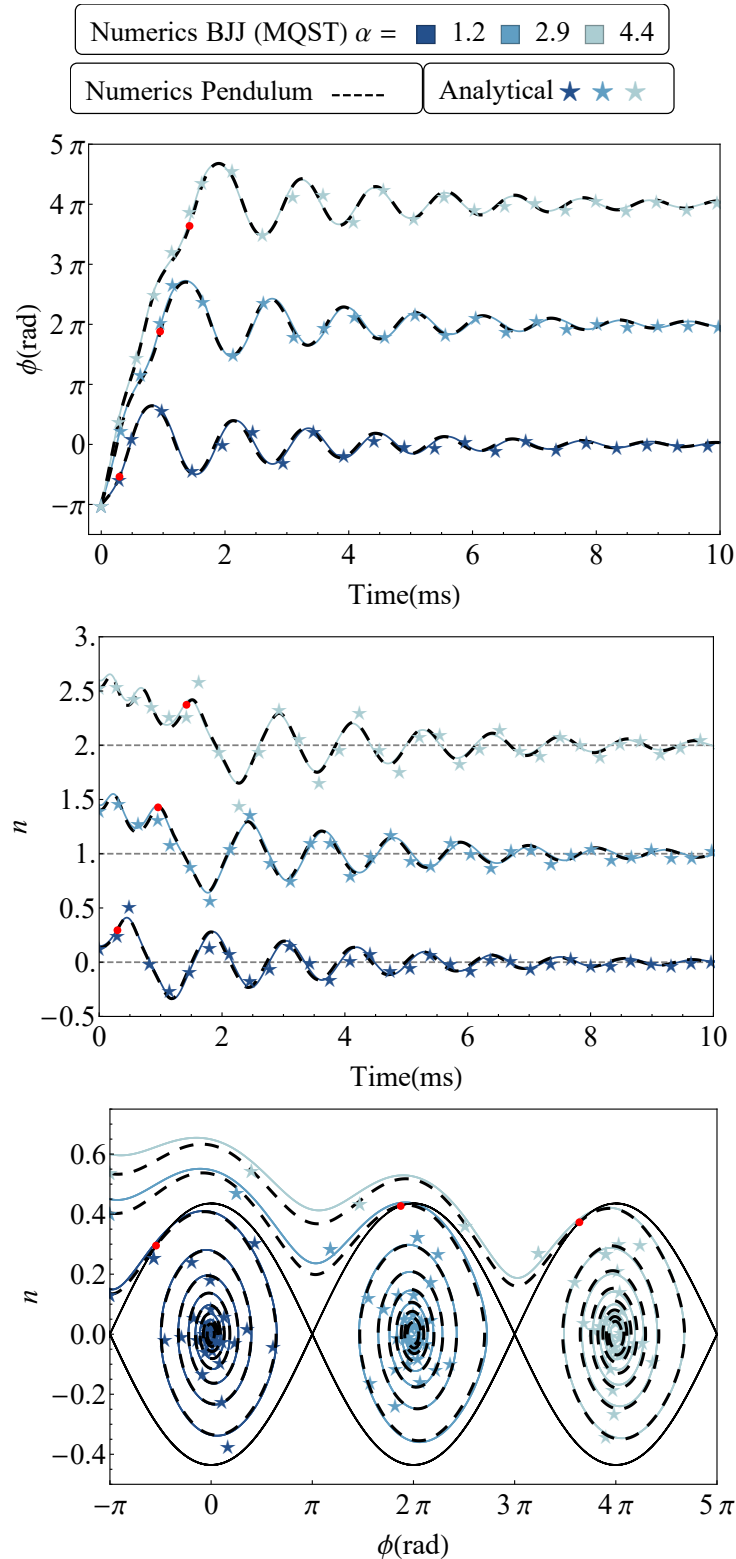


Figure 4.7: Time evolution of the phase (a) and atomic imbalance (b) and phase portrait representation (c) for $N = 5000$ atoms, $J/h = 100$ Hz, $U/h = 0.8$ Hz and the dimensionless viscosity $\eta = 120$. The three initial states differ by $n_0 = \{0.15, 0.45, 0.6\}$ and $\phi = -\pi$ corresponding $\alpha_0 = \{1.2, 2.9, 4.4\}$. The imbalance evolution is shifted by one unit for each initial state for clarity and their respective zero is indicated by a gray dashed line. We represent the numerical solutions of the equations of motion of the BJJ in the mean-field TMBH model (color plain lines), the numerical solutions of the equivalent rigid pendulum (black dashed line) and the corresponding analytical solutions (color stars). Taken from [57].

For large amplitude oscillations, we define the phase by:

$$\phi(t) = \frac{2\sigma_0}{k_0 e^{-t/\tau_2}} \arcsin(k_0 e^{-t/\tau}) \times \operatorname{sn}\left((\omega k_0 t + \delta\phi) e^{-t/\tau_2} \middle| k_0^{-2} e^{2t/\tau_2}\right). \quad (4.6)$$

The evolution of the imbalance has a general expression as function of $\dot{\phi}(t)$:

$$n(t) = \frac{N_0}{2\omega k_0} \dot{\phi}(t) + \delta n, \quad (4.7)$$

with δn the imbalance at equilibrium and N_0 the amplitude of the undamped oscillations.

4.2.3 Relaxation through local dynamics

4.2.3.1 Experimental evidences of a local relaxation channel

Several observations indicate that the relaxation in the MQST differs from the one in the oscillating regime.

Mean values Figure 4.5 shows that the initial state ($\phi_0 \approx -\pi[2\pi]$, $n_0 \approx 0.5$) exhibits a decay of the imbalance in 20 ms, which corresponds to a small value of the viscosity. In this case, the dissipative BJJ predicts that the system undergoes several damped oscillations after crossing the separatrix, before it reaches equilibrium. Such a behavior is not observed and indicates an intrinsic difference from the Josephson oscillations regime.

In addition, the phase shows a decay to $\phi = 0$ faster than the 20 ms required to damp the imbalance to $n = 0$. The measured damping could be an artifact coming from the 2π periodicity of the phase. However, on top of being an especially unlucky choice of sampling time, the phase accumulation rate is expected to decrease as the imbalance decreases. Therefore, 2π jumps would not occur over 20 ms of the relaxation.

Collapse of the contrast The contrast is obtained by integration of the fringes along the elongated axis. This is realized on every single realization and the individual values are averaged. We display the averaged integrated fringes contrast associated to Fig. 4.5 in the left panel of Fig. 4.8. The initial value is $C_0 = 0.3$. Such a low contrast can be attributed to the large imbalance and to phase fluctuations along z . Rapidly after the recoupling, the contrast of the individual fringes drops significantly, indicating local dynamics.

Over the following 40 ms, the contrast increases again until exceeding the initial value. After 20 ms, the contrast reaches its initial value and $n = 0$. However, it keeps increasing until saturating after 40 ms which is much longer than the relaxation time. After this, the contrast remains high and constant up to 70 ms.

Fast increase of the statistical phase spread We display the global phase coherence in the right panel of Fig. 4.8. At short time after recoupling, we observe a significant increase of the statistical phase fluctuations, which might be due to the low contrast making the phase difficult to evaluate. The phase spread decreases with the same timescale as the mean imbalance, supporting the idea of a relaxation.

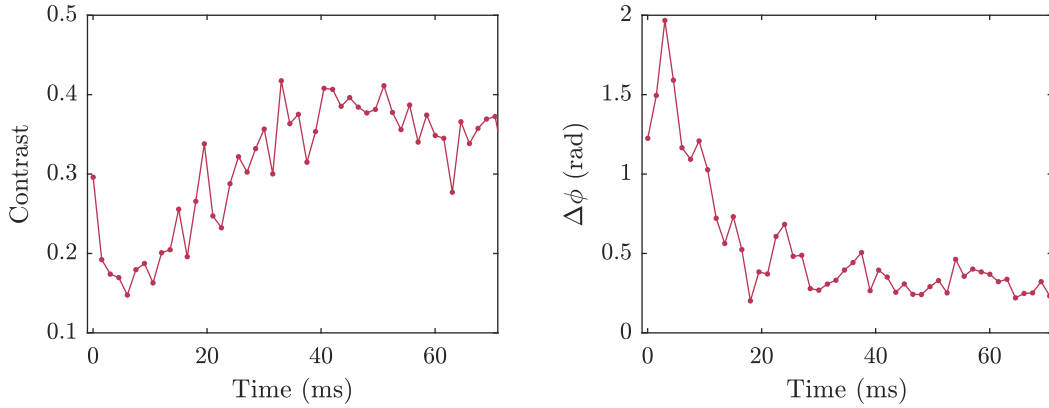


Figure 4.8: Integrated contrast and statistical phase coherence. For the MQST dynamics displayed in Fig. 4.5, the integrated contrast drops very quickly after recoupling, indicating local evolution of the phase, and therefore imbalance. The contrast is recovered after 20 ms and increases for 40 ms before saturating at a value exceeding the initial one. The statistical phase coherence increases at short time, possibly due to the low contrast which makes the phase estimation less reliable. The phase coherence is recovered after 20 ms.

4.2.3.2 Model using an array of independent BJJ

The brutal collapse of the contrast indicates that the phase evolves locally very quickly after the recoupling. We deduce that the imbalance must present a similar local dynamics. This observation can be in part explained by the fact that an imbalance as large as $n_0 = 0.48$ does not allow to neglect the local inhomogeneities of the atomic density. In the following, we present a toy-model which takes into account the local atomic densities. For this we consider the harmonicity of the longitudinal confinement and define the imbalance locally.

Contrary to the previous case where $n_0(z) = 0$, the finite global imbalance results in different cloud extensions and atomic densities such that the imbalance presents strong variations along the direction of elongation z . For simplicity, we neglect the fluctuations of the atomic density and consider that the atomic density of the clouds presents a parabolic profile described in Sec. 1.2.4. We also assume that the phase is homogeneous and neglect both the longitudinal and statistical phase fluctuations. For a global imbalance of $n = 0.5$ and a total atom number $N = 2100$ atoms, we represent in the upper panel of Fig. 4.9 the atomic density profiles of the clouds in the trap $I_{\text{rf}} = 0.55$. The local imbalance (middle panel in Fig. 4.9) varies strongly along the condensates. The center of the cloud presents a smaller imbalance than the global value. However, at the edge of the clouds, the difference of extension results in an imbalance of $n(z) = \pm 1$.

For simplicity, we also consider that the single-particle tunnel coupling energy J is identical along z . Therefore, Λ is defined locally as:

$$\Lambda(z) = \frac{g_{1D}N(z)}{2J} \quad (4.8)$$

with $g_{1D} = 2\hbar\omega_{\perp}a_s$ and $N(z)$ the local atom number. The local definition of the imbalance

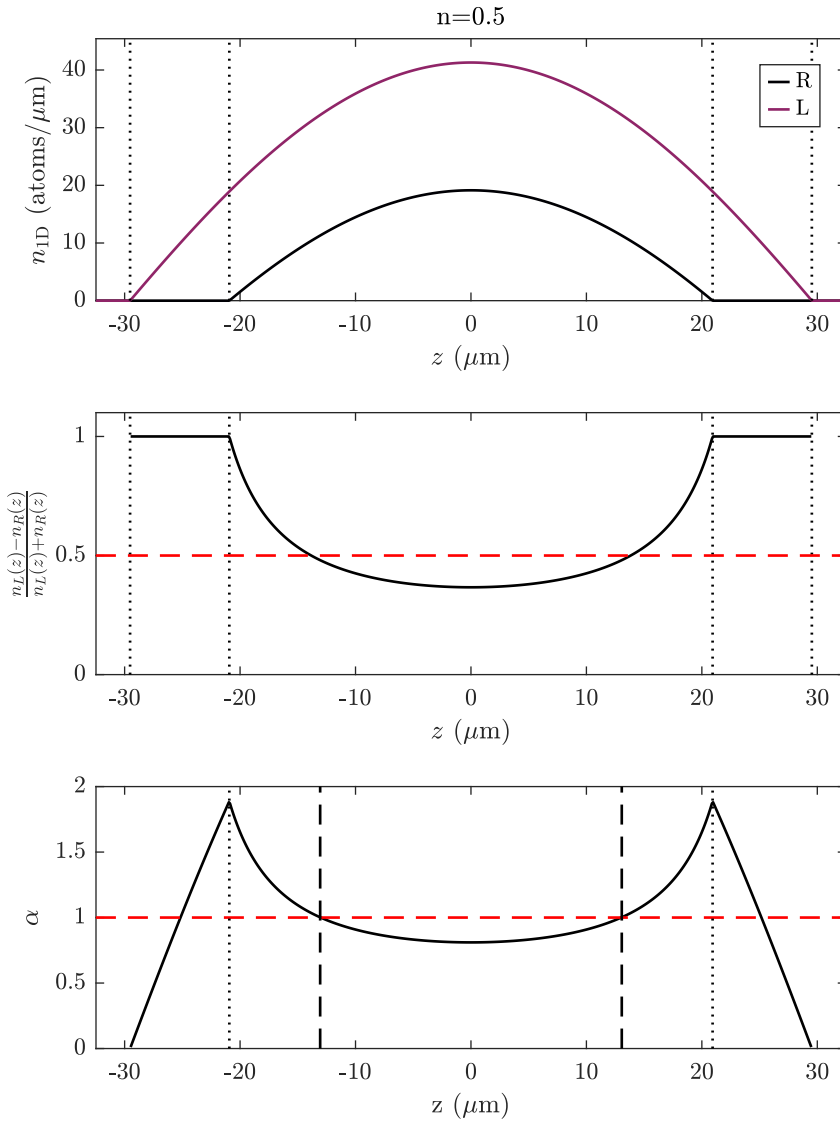


Figure 4.9: Density profiles in $I_{\text{rf}} = 0.55$ for a global imbalance $n = 0.5$. The atom number is $N = 2100$ atoms and the trap frequencies are $\omega_{\perp} = 2\pi\sqrt{1630 \times 1380}$ Hz and $\omega_z = 12.8$ Hz according to experimental measurements. The profiles computed with Eq. 1.64 clearly show that the two clouds have a different extension such that the imbalance differs strongly from the global value $n = 0.5$ (red dashed line). Bottom: Considering $J/h=40$ Hz, α varies along z . The dashed lines defines the area where $\alpha < 1$ i.e. where the system presents Josephson oscillations. The dotted lines define the smallest cloud extension beyond which the imbalance is ± 1 and the phase difference is not defined. Between the black dashed lines and the black dotted lines, the system is in the MQST regime.

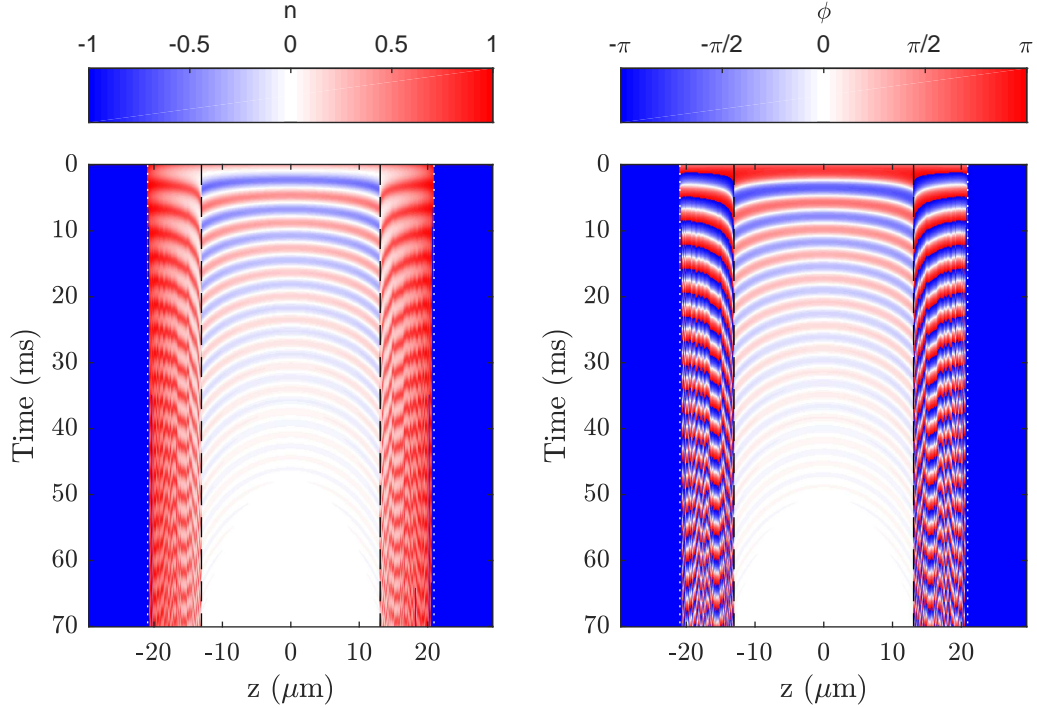


Figure 4.10: Evolution of the phase and imbalance along z for the parameters of Fig. 4.9 and for the TMBH parameters $J/h=40$ Hz and $\eta = 70$. The black dashed lines defines the area where $\alpha < 1$ i.e. where the dynamics consists of Josephson oscillations. The oscillation frequency is larger at the center of the cloud where the atomic density is higher. The white dotted line corresponds to $n = \pm 1$ and define the length of the smallest cloud. The area between the dashed black lines and white dotted lines is in the MQST where we do not include a relaxation.

and Λ implies a local definition of $\alpha(z)$:

$$\alpha(z) = \frac{\Lambda(z)}{2} n(z)^2 - \sqrt{1 - n(z)^2} \cos(\phi(z)). \quad (4.9)$$

The threshold between the JO and the MQST correspond to $\alpha = 1$. In the lowest panel of Fig. 4.9, $\alpha = 1$ is indicated by the red dashed line. It clearly shows that the central part of the cloud is in the JO regime (delimited by the black dashed lines) while the edges are in the MQST regime (between black dashed and black dotted lines).

We introduce a damping in the central part of the clouds, where we expect an oscillating dynamics for which we have evidence of a relaxation. However, we consider that the part of the cloud in the MQST regime cannot relax. The restriction of the relaxation to the oscillating regime is one possibility to obtain a relaxation process with different features and to explain the discrepancy between the data and Sec. 4.2.2. We also consider a value of η identical for the entire part of the clouds in the JO regime. This is not fully compatible with the observations as we know that η depends on the atom number and could therefore be considered dependent on the local atomic density.

For the simulation, we consider that the slices defined along z evolve independently. Figure 4.10 displays the local imbalance and local phase evolving over 70 ms. The central area is in the oscillating regime as displayed by the oscillation around 0 (white). Over

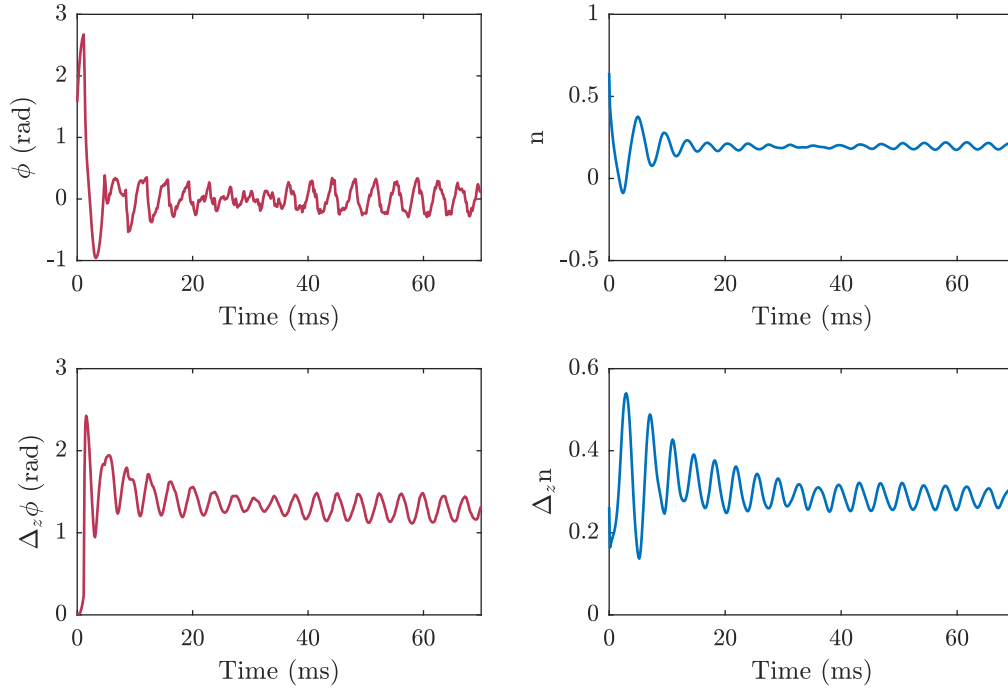


Figure 4.11: Global phase and imbalance evolution obtained by integration of the signal of Fig. 4.10 along z . A difference with the experimental determination of the global quantities is that the integration here gives equal weight to the all values $\phi(z)$ and $n(z)$ in the integration while the experimental measurement weight the signal according to its intensity, i.e. atomic density. The main feature is however that the dynamics is dominated by the evolution of the oscillating part of the cloud. The decay of the imbalance in 20 ms is slower than the one of the phase in about 5 ms. The discrepancy with the experimental results might be attributed to the many assumptions of the model, which assumes in particular the independent evolutions of the slices of the clouds.

the first 40 ms of dynamics, the dynamics presents oscillations at a frequency depending on z , where the dynamics oscillates faster at the center of the clouds. On the interference fringes, this feature appears as wiggles which decreases the integrated fringe contrast. At longer time, the oscillations are all damped due to the empirical viscosity η . It is interesting to note that the constant viscosity does not mean that the local phase and imbalance value reach 0 at the same time. The areas of the cloud in the MQST regime are identified by the small oscillation of the imbalance which remains of constant sign and a phase accumulation characterized by the 2π jumps (jumps from red to blue). The blue area on each side, where $n = -1$, corresponds to the area where the phase is not defined.

The integrated values, similar to the global phase and imbalance, are displayed in Fig. 4.11. The phase value decays to $\phi = 0$ in approximately 5 ms while the imbalance decays in about 20 ms. The local model therefore describes the difference of decay times between the global phase and imbalance. The phase spread immediately increases before decreasing and stabilizing. This spread is computed as the standard deviation of the local phase, and is not to be mistaken for the statistical phase spread. It is linked to the fringes contrast such that a large spreads testify of a small contrast. This is also compatible with the experimental observations.

Two differences are however relevant. The first one is that the imbalance presents oscillations differing from the experimental observations. In addition, it stabilizes around a positive value while we observe a decay to 0. Both discrepancies can be attributed to the main assumption of the model, namely that the slices evolve independently.

Indeed, the local dynamics create excitations, such as a local depletion of atom in the center, which propagate along the condensate. In addition, the tunneling of the atoms from one well to the other change the size of both clouds and re-define the local density. A similar process occurs with the phase, for which the initial fluctuations should also be included in a more complex model. The interaction between the slices is expected to modify the dynamics significantly. Through the relaxation at the center of the cloud, we can expect a decrease of the local inhomogeneities and eventually a relaxation of the entire system. In this sense, the center of the cloud defines a local relaxation channel, through which the dynamics could relax all along the clouds.

According to this model, as we increase the imbalance, we expect to decrease the size of the oscillating relaxing channel and to make the relaxation slower and slower. Eventually, we could expect that the imbalance is so high that the entire system in the MQST regime where no relaxation would occur.

4.3 Transition to a relaxation-free regime

We test the previous hypothesis by measuring the dynamics of states initialized by increasing values of the global atomic imbalance. The total atom number is $N = 3500$ atoms and the initial imbalance is varied between $n_0 = 0$ and $n_0 = 0.65$. The initial phase is not tuned in this data set as it tends to increase with the initial imbalance. As preparing a larger imbalance requires detuning to larger values, the phase evolution during the preparation increases with ϵ and therefore with n_0 . The contrast of the fringes decreases strongly such that, even though we display the phase evolution for completeness, more reliable information are extracted from the imbalance evolution.

The dynamics of the imbalance is reported in Fig. 4.12. The corresponding spreads of the imbalance are presented in the two panels of Fig. 4.13. The time evolution of the global phase, its statistical spread and integrated fringe contrast are displayed in Fig. 4.14, separated in two columns for clarity.

The initial state ($\phi \approx 0, n_0 \approx 0$) is obtained by a symmetric splitting and serves as reference. The evolution displayed by the yellow curves in Figs. 4.12, 4.13, 4.14 indicates that this situation is close to equilibrium: the spreads of the phase and imbalance are small and constant over time while the contrast of the integrated fringes is high and constant.

When increasing the imbalance (orange curves in Figs. 4.12, 4.13, 4.14), the imbalance presents a decay to $n = 0$ after a first oscillation down to $n = 0$. The spread of the imbalance increases slightly at short time before reaching the reference value. The phase on the other side shows an oscillating feature around $\phi = 0$ damped to $\phi = 0$ in a timescale comparable with the imbalance decay. While this resembles the dynamics of the dissipative BJJ presented in the previous chapter, this behavior is incompatible with the TMBH prediction, even with a dissipative contribution. Indeed, a phase oscillation

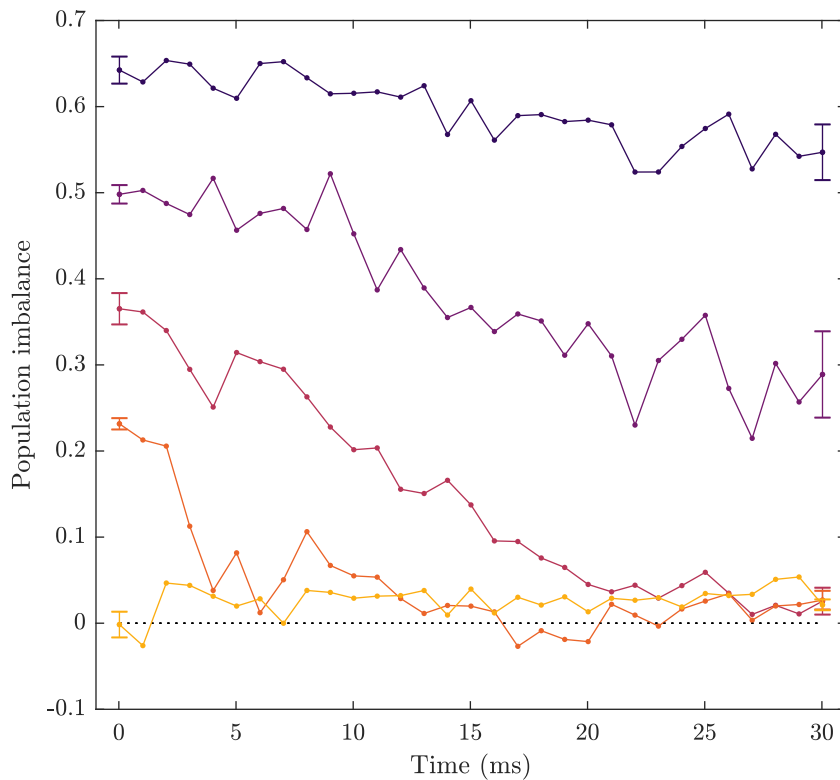


Figure 4.12: Evolution of the atomic imbalance for different initial imbalance values. The total atom number is $N = 3500$ atoms and the imbalance varies between $n_0 = [0, 0.65]$. The lowest imbalance serves as reference to indicate the equilibrium value. In this case, the trap presents a negligible asymmetry. For initial imbalance values $n_0 < 0.4$, the imbalance decreases to $n = 0$ at long time. The time requires to reach equilibrium increases with the initial imbalance. Above a threshold, the imbalance decreases very slowly and the dynamics is dominated by a dephasing. For very large values, the decrease of the imbalance is negligible.

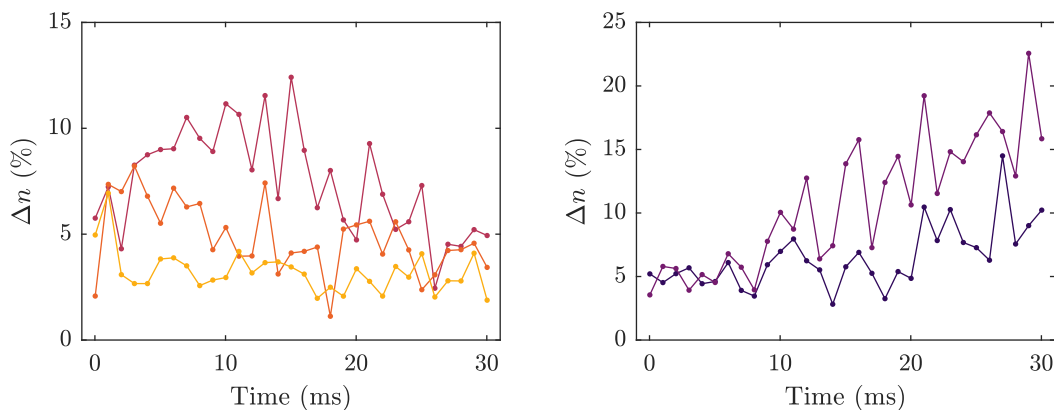


Figure 4.13: Evolution of the imbalance fluctuations for various initial imbalance values. The left panel corresponds to $n_0 < 0.4$ where the dynamics decreases to $n = 0$ at long time. The imbalance fluctuations decrease at the timescale of the relaxation. The right panel corresponds to $n_0 > 0.4$. The imbalance fluctuations increase over time and no relaxation is observed.

around 0 is a clear signature of the Josephson oscillation regime and can only occur with an imbalance oscillation around 0. Therefore, the relaxation at small imbalance shows that the global dynamics results from an inhomogeneous dynamics. The contrast, initially degraded by the imbalance and longitudinal excitations, increases slowly to the reference value. The relaxation is therefore observed, even though the mean values and the contrast present two timescales. This observation is compatible with the idea of a relaxation channel in the central part of the clouds.

For a larger initial imbalance (red curves in Figs. 4.12, 4.13, 4.14), the imbalance decays to 0 in a significantly longer time. The phase does not show an oscillation but damps to 0 with a comparable timescale. The longer timescale can be understood by a reduction of the size of the relaxation channel such that the relaxation takes longer to affect the entire cloud. The contrast, which has a significantly lower value, increases with a slower timescale. It might reach the reference value in a timescale longer than the largest time measured.

For higher initial imbalance ($n_0 > 0.4$), the behavior differs significantly. The imbalance evolution decays very slowly but the statistical spreads increase, showing that a dephasing mechanism competes with the relaxation. The contrast does not increase significantly. For even large initial imbalance values, the relaxation of the mean values is inhibited. The mean values of the phase and imbalance present close to no evolution. The contrast remains at a very low value. The spread of the imbalance increases over time while the phase is random. This indicates that the relaxation does not occur above a threshold which can correspond to a suppression of the oscillating area in the center of the cloud.

4.4 Conclusion

The study of two elongated condensates differing by their atom number shows many differences compared to the Josephson oscillating regime. In this case, the trap geometry plays a significant role as it leads to a local definition of the phase, imbalance and tunneling parameters. The experimental observations have established that the relaxation is observed below a threshold of imbalance, above which the dynamics is dominated by a dephasing mechanism. Our current understanding is that, due to the local atomic density, the tunneling dynamics along the condensate mixes several dynamical regimes, resembling Josephson oscillations in some areas and resembling self-trapped dynamics in others. A relaxation might occur through the oscillating channels where we established clearly the presence of a relaxation. Through inter-atom interaction, the relaxation could occur along the entire extension of the clouds.

As the imbalance is increased further, this oscillating channel is reduced to a smaller and smaller area of the cloud, explaining that the relaxation takes longer. Above a threshold, the clouds are above the oscillation threshold and no relaxation could occur.

This mechanism needs to be supported by a model beyond the TMBH array presented in this section, to include the interaction between the atoms on a same site. While other models would be suitable for this, including Gross-Pitaevskii simulations, they do not contain an intrinsic relaxation mechanism and do not easily allow to include an empirical dissipation in the oscillating channel.

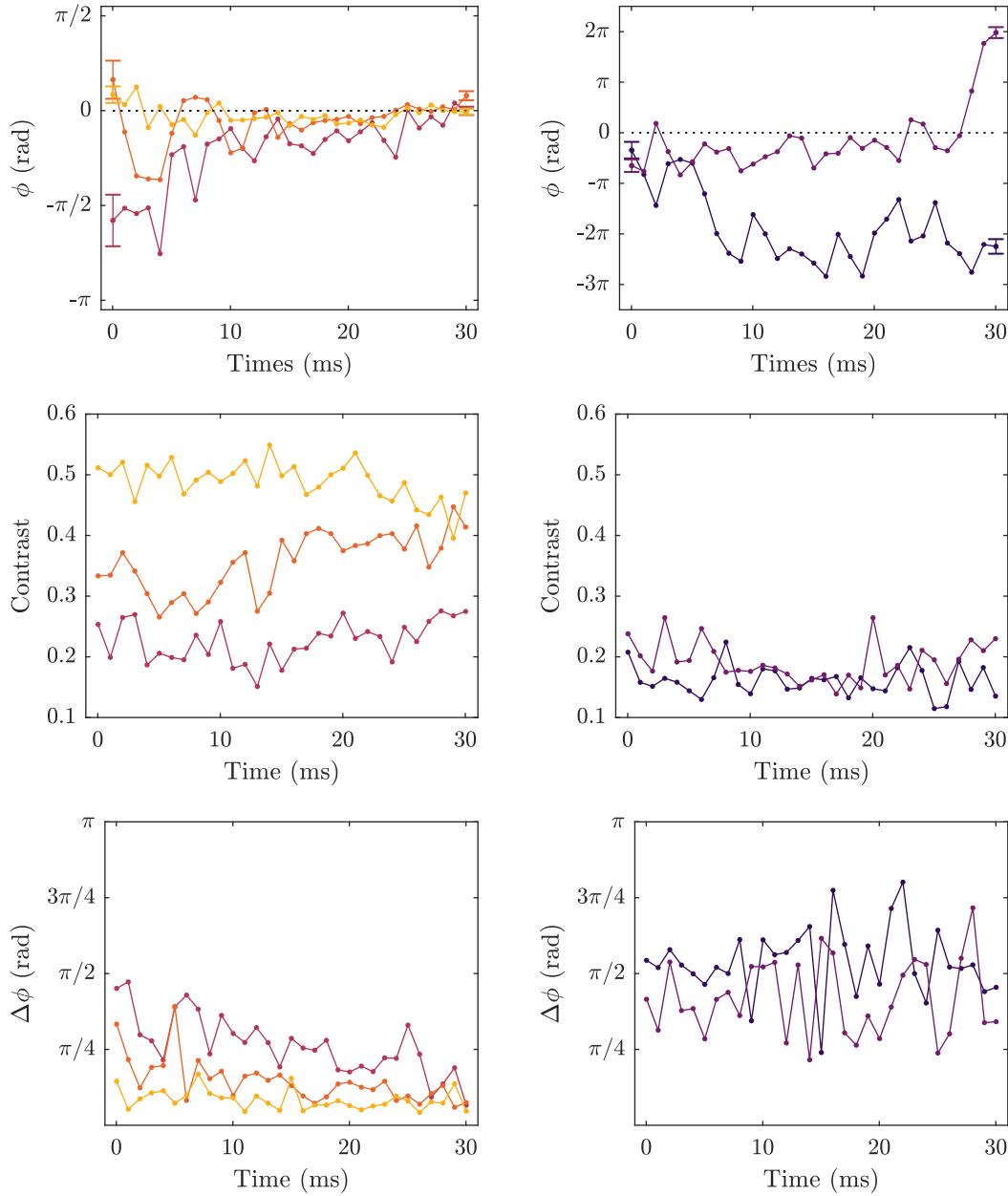


Figure 4.14: Evolution of the global phase, integrated fringes contrast and statistical phase spread for various initial imbalance values. The two columns distinguished between $n_0 < 0.4$ (left) and $n_0 > 0.4$ (right). For $n_0 < 0.4$, a relaxation occurs as indicated by the global phase $\phi = 0$ and the reduction of the phase spread toward the reference value. The contrast requires a longer time to reach the equilibrium value as the imbalance increases. We deduce that it takes a longer time for the entire cloud to reach equilibrium. For $n_0 > 0.4$, the relaxation is dominated by a dephasing such that, for large enough imbalance values, the relaxation is not observed.

Experimentally, a protocol allowing to investigate this regime in a controlled and detailed way relies on a change of design of the trapping potential [156]. A particularly promising geometry consists in a box trap in which the imbalance could be studied with limited inhomogeneities of densities.

5 Outlook: Consequence of a relaxation on the splitting of a 1D Bose gas

The work presented in this thesis has demonstrated that the dynamics of two elongated Bose gases characterized by a phase difference and a high phase coherence exhibits a relaxation toward a phase-locked equilibrium state. The underlying microscopic mechanism is currently under investigation [143, 151, 157, 158]. So far, theoretical efforts have only partly reproduced the relaxation and its dependence with the experimental parameters.

One challenge in determining the theoretical origin of relaxation comes from the complexity of the experimental setting: the exact trap geometry, the temperature-induced fluctuations, the preparation sequence and in particular the splitting, the statistical fluctuations of the atom number, the time-of-flight... These aspects present different degrees of relevance and difficulty to model.

In this section, we not review the various models under investigation as each one of them requires a different and significant theoretical background. Instead, we present a project we intend to pursue related to the number-squeezing generation by splitting of a one-dimensional Bose gas in two halves. We evaluate the contribution of the relaxation phenomenon on this experiment and present preliminary data in this direction.

The microscopic origin of the relaxation being unknown, including it in situations beyond the ones experimentally observed relies on hypotheses. However, we can expect that the relaxation modifies our understanding of the adiabatic splitting provided in Sec. 1.3.4.6. We investigate this possible effect in the first part of this chapter, relying on the Monte-Carlo-like model introduced in Sec. 1.3.4.

To reduce the impact of the relaxation, we consider in the second part of this chapter the two-step splitting protocol, for which the splitting duration is significantly reduced. In this case, we present preliminary results which set experimental limits on how short the ramp duration can be in our setup and we explain why the parametric amplification protocol might be a more promising option.

5.1 Adiabatic splitting

5.1.1 Estimation of the effective duration of the relaxation

In the case of an adiabatic splitting, the trap geometry is modified over a duration which exceeds the characteristic relaxation time. During the splitting, the system evolves in a trap with decreasing tunnel coupling under the effect of repulsive inter-atom interaction

and tunneling. However, we have established in Sec. 3.2 that the relaxation timescale remains constant under a change of the tunnel coupling value, as long as it is not negligible. Therefore, we can expect the relaxation to play a role in the description of the splitting. In particular, we could expect that such a slow splitting leads to the preparation of the relaxed state. However, it is likely that the relaxation does not occur over the entire ramp duration. The latter can be divided in three stages.

- The first part of the ramp is required to raise the dressing amplitude from $I_{\text{rf}} = 0$ to $I_{\text{rf}} = 0.42$ where a double-well potential can be defined. For a linear ramp of I_{rf} from $I_{\text{rf}} = 0$ to $I_{\text{rf}} = 0.65$ in 21.5 ms as considered in this manuscript, this first stage lasts 13.9 ms. During this time, the trap is a single-well potential and we cannot predict the impact of the relaxation from the experimental observations.
- After this, the tunnel coupling is decreased and the relaxation can occur independently of J according to Sec. 3.2 as long as the tunneling is not negligible i.e. as long as the adiabaticity criterion is fulfilled. The estimation of the breakdown of adiabaticity depends strongly on the details of the ramp. For a perfectly symmetric splitting, we have seen in Sec. 1.3.4.6 that the adiabaticity is not broken suddenly but smoothly until the loose adiabaticity criterion is no longer fulfilled. This time can be estimated by simulating specific ramps and initial states as presented in Sec. 1.3.4.6. A simpler approach has been developed by [153] assuming that the system follows the ground state until the adiabaticity is suddenly broken. It establishes a criterion benefiting from an analytical expression that gives an estimate of the time where the adiabaticity is broken. In this model, the degree of adiabaticity is defined by:

$$A(t) = \frac{5}{16\sqrt{2}} \left(\frac{R}{\sigma}\right)^{5/2} \frac{t^{3/2}}{\omega_0} \exp\left[\frac{1}{2} \left(\frac{Rt}{\sigma}\right)^{5/2}\right], \quad (5.1)$$

with R the splitting rate defined for this criterion as $R = (0.65 - 0.42)/21.5$ ms, ω_0 the plasma frequency in the trap of $I_{\text{rf}} = 0.42$, $\sigma = 0.1$ deduced from the dependence of J with I_{rf} established in Sec. 2.3.2.6. In this model, the adiabaticity is broken when $A(t) = 1$. For this specific ramp, it predicts the breakdown of the adiabaticity after 20.4 ms for $N = 3500$ atoms and $U/h = 1$ Hz.

- After the adiabaticity breaks down, we do not expect a relaxation resembling the one in the oscillating regime. Instead the dynamics is dominated by the interaction-induced phase diffusion.

This estimation concludes that the relaxation is effective over 6.5 ms of the entire splitting duration, which is not negligible compared to the relaxation timescale. However, more subtle effects are likely to alter this simple picture. For example, a slight asymmetry of the trap results in an earlier decoupling as explained in Sec. 1.3.4.5 and leads to a shorter effective relaxation duration, while the relaxation might allow the system to remain closer to the ground predictions and increase the duration over which the splitting is adiabatic.

5.1.2 Simulation of a linear splitting with relaxation

What can relax? While the previous section estimates the time over which the relaxation could occur, it does not state which quantities could relax. The splitting presents one important difference compared to the situation investigated in Sec. 3.2. In Sec. 3.2, the dynamics originates from a global phase difference, which results from energy added to the system during the preparation. The relaxation can be seen as a transfer of this energy toward other observables that we do not measure.

During a symmetric splitting, the mean values of ϕ and n remain equal to zero, such that this energy contribution is absent and only the fluctuations of the phase and imbalance present a dynamics. Therefore, one can wonder which quantities could be affected by the relaxation. To answer this question, one must bear in mind that the relaxation leads to a phase-locking. Therefore, one could imagine that the relaxation could counter-balance a statistical dephasing occurring during the splitting. In this scenario, the relaxation is susceptible to affect the evolution of the fluctuations of the phase and imbalance, especially if they tend to increase.

The following natural question is: would the relaxation resemble the one described in Sec. 3.2? In particular, would the viscosity η take comparable values? That seems very likely. Indeed, the timescale of the relaxation reported in Sec. 3.2 does not depend on the phase and imbalance in the oscillating regime. This is clearly shown by extracting the damping time for various initial phases, as well as by the fact that the full dynamics, from far away from equilibrium to equilibrium, can be fitted by a single value of the damping time. Therefore, the description of the dynamics in term of the viscosity η might be unchanged when the mean values of the phase and imbalance remain $\phi = 0$ and $n = 0$.

In the following, we include the relaxation in the description of the splitting by combining the empirical viscosity in the equations of motion presented in Sec. 3.2.2.1 and the Monte-Carlo-like approach of Sec. 1.3.4.6. We expect different behaviors depending on whether the initial state is in the ground state or presents larger initial fluctuations.

Initial ground state For a system initially in the ground state, including a constant viscosity η as long as the tunneling is non-negligible clearly violates the Heisenberg uncertainty principle. Indeed the initial ground state is characterized by $\Delta n_{\text{GS}} \Delta \phi_{\text{GS}} = 1/N$ and the fluctuations of one quadrature can only be decreased at the price of increasing the other. However, the empirical viscosity originates from a semi-classical model which ignores the limitation set by the Heisenberg uncertainty product and damps every individual classical point to the equilibrium state, therefore leading to $\Delta n = 0$ and $\Delta \phi = 0$. As a consequence, the viscosity cannot be included in the simulation as long as the adiabaticity is maintained. As the adiabaticity breaks down and the fluctuations differ from the ground state prediction, we can expect different scenarios.

It might be that the relaxation acts as soon as the fluctuations differ from the ones of the ground state, such that the system follows the ground state predictions better than in the undamped case. To avoid violating the Heisenberg uncertainty product, the corresponding η must be significantly smaller than the one discussed in Sec. 3.2.

The second scenario is that, as the relaxed state presents fluctuations larger than the ground state, the system does not exhibit any relaxation as long as the fluctuations are

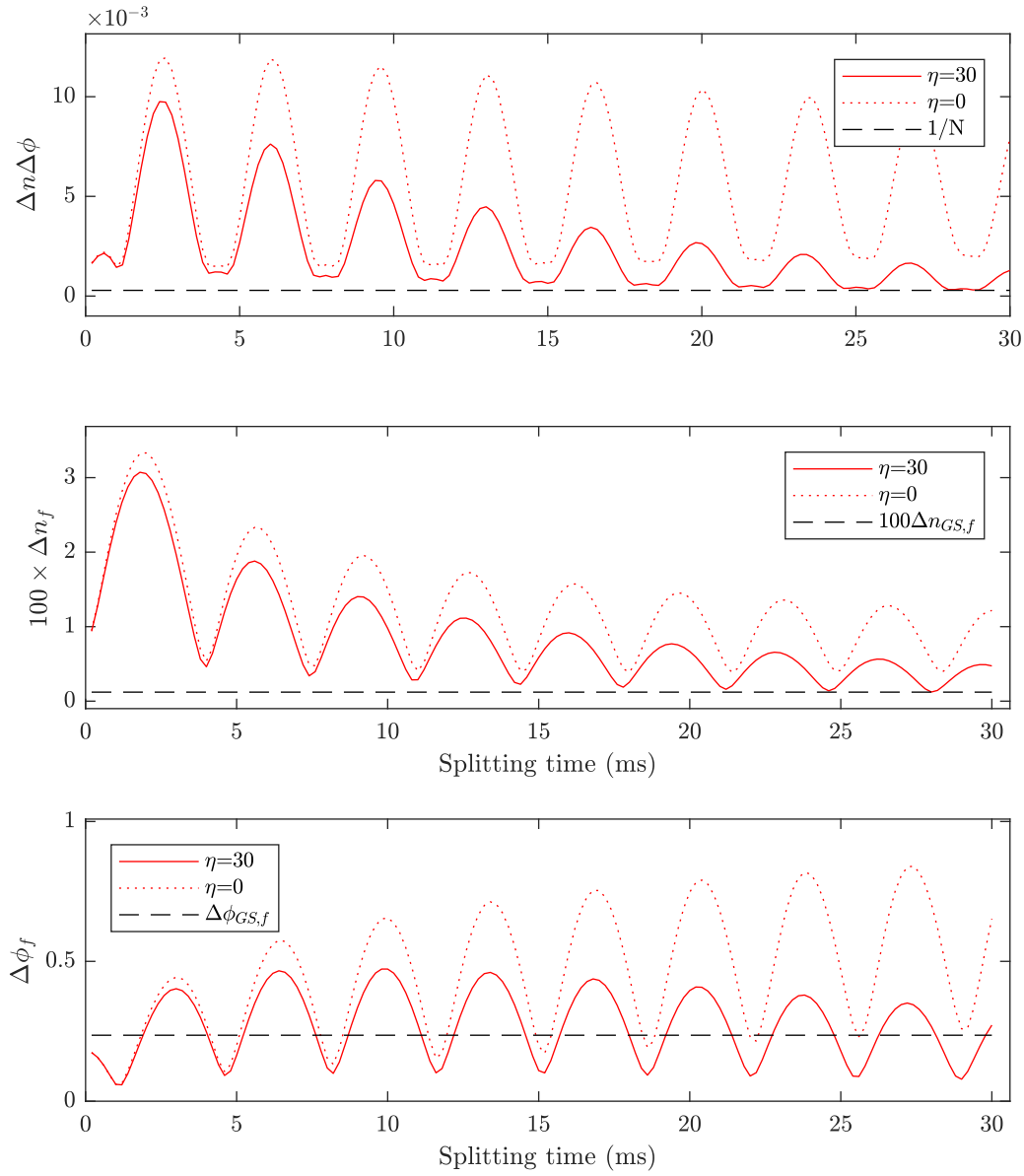


Figure 5.1: Final fluctuations of the phase and imbalance after a splitting in various duration with and without damping. The initial state is $\Delta n_0 = \Delta n_{\text{GS}}$ and $\Delta \phi_0 = 5\Delta \phi_{\text{GS}}$ where Δn_{GS} and $\Delta \phi_{\text{GS}}$ refer to the ground state of $N = 3500$ atoms in $I_{\text{rf}} = 0.42$ and $U/h = 1$ Hz. The splitting is performed in a time varying between 0.2 ms and 30 ms considering no relaxation (dashed red line) and a damping of constant value $\eta = 30$ (solid red line). Top: Comparison of the product $\Delta n_f \Delta \phi_f$ of the final fluctuations values with the Heisenberg limit. For a splitting duration up to 30 ms, the product of the final fluctuations with damping remains larger than the Heisenberg limit such that the semi-classical model does not contradict the quantum limitations. The evolution of the Δn_f (middle) and of $\Delta \phi_f$ (bottom) as a function of the total splitting time shows that the dissipation term tends to improve the number-squeezing by decreasing the minima of the oscillations of Δn_f . Over time, the relaxation also displaces the splitting duration at which the minima are reached. The black dashed line refers to the ground state fluctuations of the final trap, by opposition to Δn_{GS} and $\Delta \phi_{\text{GS}}$. This explains that for a very fast splitting, $\Delta n_f \approx \Delta n_{\text{GS}}$ is above the dashed line while $\Delta \phi_f \approx 5\Delta \phi_{\text{GS}}$ is below the dashed line.

below those of the relaxed state. If the splitting duration is such that the fluctuations can exceed the one of the relaxed state, one could imagine that this excess energy is relaxed such that the fluctuations do not increase but saturate at the relaxed values.

In these hypotheses, the relaxation always improves the final number-squeezing, either helping the system to follow the ground state or dissipating any energy exceeding the one of the relaxed state. However, these hypotheses are difficult to check experimentally as the initial state is likely to differ from the ground state.

Initial state with increased phase fluctuations As presented in Sec. 1.3.4.6, it is likely that the experimental initial state has increased phase fluctuations compared to the ground state. In this case, we assume as in Sec. 1.3.4.6 that $\Delta n_0 \Delta \phi_0$ significantly exceeds $1/N$. We assume that the viscosity term η takes a constant and finite value compatible with the experimental observations as long as the tunneling is non-negligible, after which we fix $\eta = 0$.

We have seen in Sec. 1.3.4.6 that in this case, the fluctuations oscillate π -out-of-phase and that their value at the end of the splitting strongly depends on the splitting duration. The final value of the fluctuations present oscillations as a function of the splitting duration, reproducing the time at which the loose adiabaticity criterion breaks down. The relaxation tends to change the frequency and amplitude of these oscillations and is likely to modify the optimal splitting duration as well as the final number-squeezing.

We illustrate the splitting with relaxation by simulating $N = 3500$ atoms for which the value of the dimensionless viscosity is chosen as $\eta = 30$ for J/h between 87 Hz (highest value) and 0.5 Hz. This lower value of J/h is chosen arbitrarily in this case as its precise value does not significantly impact the final fluctuations. We consider an initial state such that $\Delta n \Delta \phi$ always remains above $1/N$ to avoid reaching the limitations of the semi-classical approach. For this, we consider $\Delta n_0 = \Delta n_{\text{GS}}$ and $\Delta \phi_0 = 5 \Delta \phi_{\text{GS}}$. We display in Fig. 5.1 the final values of the fluctuations for a splitting duration varying between 0.2 ms and 30 ms. We compare the results to the undamped predictions ($\eta = 0$). The relaxation in this simulation improves the number-squeezing factor by decreasing the fluctuations of the atomic imbalance. The optimal splitting duration is slightly shorter than in the undamped case. Mainly, the relaxation limits the amplitude of the oscillations of Δn and makes the choice of the splitting time less critical.

The relaxation also affects the phase fluctuations. In this example, we observe that the relaxation counter-acts the dephasing occurring in the undamped case. If this prediction is experimentally confirmed, this effect is very relevant, as it means that the relaxation during the splitting contributes to the high statistical phase coherence between the two halves.

5.2 Two-step splitting

5.2.1 Two-step splitting with relaxation

A way to reduce the impact of the relaxation is to implement faster splitting protocols. As presented in Sec. 1.3.4.7, the two-step splitting is a promising protocol to generate

high number-squeezed state in a shorter duration than the adiabatic splitting. It relies on two ramps designed to use the fluctuations dynamics to reduce the number fluctuations.

We consider the scheme parameters defined in Sec. 1.3.4.7, in which a first ramp, between $I_{\text{rf}} = 0.42$ and $I_{\text{rf}} = 0.6$ is performed in 1 ms after which the system evolves during an additional 2.6 ms. The following ramp, toward $I_{\text{rf}} = 0.65$ takes an additional 14.4 ms but does not improve the number squeezing significantly. One could imagine replacing it by a quasi-instantaneous splitting to a decoupled trap (such as $I_{\text{rf}} = 0.8$).

Therefore, the two-step splitting can in principle be performed in less than 4 ms (from $I_{\text{rf}} = 0.42$). From the results displayed in Fig. 5.1, the relaxation does not seem to play an important role for such a short timescale. Therefore, we do not expect the relaxation to affect strongly the predictions of the two-step splitting protocol.

5.2.2 Preliminary results on the implementation of the first ramp

In order to implement a two-step splitting scheme, one must first verify that the dynamics of Δn and $\Delta\phi$ after the first ramp exhibits oscillations. The preliminary experiments performed in this direction present number-squeezing oscillations to be carefully interpreted.

Experimental results The splitting is performed in 4 ms to the trap $I_{\text{rf}} = 0.55$. From the study of the damped oscillations presented in Sec. 3.2, this trap corresponds to $J/h \approx 32$ Hz and $U/h \approx 0.85$ Hz. For $N = 2500$ atoms, the corresponding Josephson frequency of $\omega = 2\pi \times 375$ Hz such that the fluctuations are expected to oscillate at $\omega = 2\pi \times 750$ Hz.

Experimentally, we measure the atomic imbalance at various times following the splitting by introducing a holding time between 0 ms and 2.8 ms in the final trap. The fluctuations of the atomic imbalance are deduced from a large statistics (70-80 repetitions) and the distributions are corrected as in Sec. 2.4.3.2. The number-squeezing factor ξ_n displayed in the left panel of Fig. 5.2 exhibits a clear oscillating feature. The frequency can be estimated by a fit with a sine function. Without constraints on the fit parameters, the frequency extracted from the fit reads $\omega = 2\pi \times 750$ Hz, which is compatible with the predictions of the TMBH model.

However, while the oscillation of ξ_n seems to indicate that the system evolves as expected for the two-step protocol, the measurements show that the inter-cloud spacing oscillates over time at a comparable frequency. This is displayed in the right panel of Fig. 5.2. Therefore, the fast splitting induces a sloshing motion which affects the description of the TMBH model.

Degradation of the measurement accuracy due to the clouds overlap The sloshing of the wave functions brings the clouds periodically closer to each other, which increases the wave functions overlap and increases the error on the imbalance estimation. This is compatible with the fact that the minimal distance between the cloud corresponds to the largest error. We can simulate this error with a simplified model. We assume a symmetric trap and a perfectly number-squeezed system where each clouds contains exactly $N/2$ atoms.

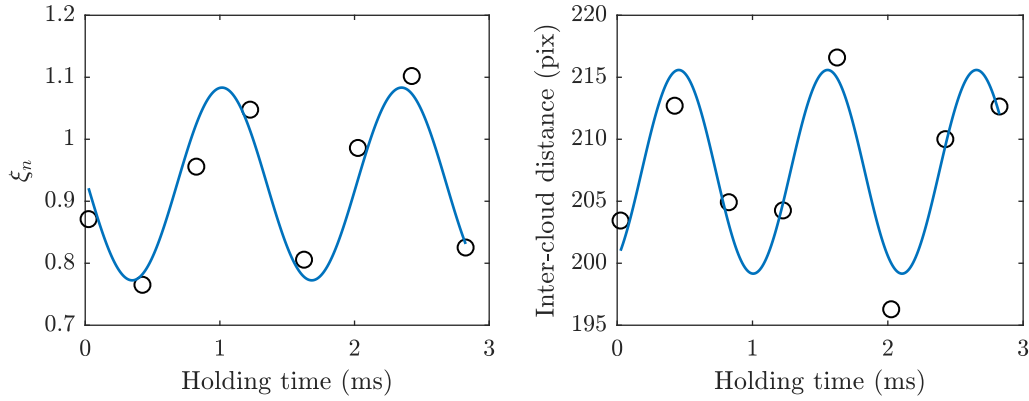


Figure 5.2: Dynamics of the number-squeezing factor and inter-cloud spacing after a fast splitting to a strongly coupled trap. Left: Evolution of the number-squeezing factor over the 3 ms following a splitting in 4 ms from $I_{\text{rf}} = 0$ to $I_{\text{rf}} = 0.55$. In the final trap, the expected plasma frequency for $N = 2500$ atoms is $\omega_0 = 2\pi \times 375$ Hz and the sine fit of the number-squeezing factor evolution yields $\omega = 2\pi \times 750$ Hz $= 2\omega_0$. This oscillation seems to indicate that the first ramp of the two-step protocol can be realized on the experiment. However, this measurement must be compared to the oscillation of the inter-well spacing (right panel). The distance between the two clouds oscillates at $\omega = 2\pi \times 910$ Hz. This indicates that the fast splitting excites a sloshing of the clouds in the final trap, which can be at the origin of the oscillation of the number-squeezing factor.

However, due to the finite overlap, we can miscount the atoms in the left or right cloud and attribute an atom to the improper cloud. We assume a Gaussian shape of the transverse wave functions:

$$f_{L,R}(x) = \frac{N_{L,R}}{\sigma_{L,R}\sqrt{2\pi}} \exp\left[-\frac{(x - x_{L,R})^2}{2\sigma_{L,R}^2}\right]. \quad (5.2)$$

Here, $x_{L,R}$ is the center of the clouds, $N_{L,R}$ the total atom number in each cloud and $\sigma_{L,R}$ the rms. The limit between the integration areas is the value x_0 verifying:

$$f_L(x_0) = f_R(x_0). \quad (5.3)$$

For two identical clouds, x_0 is simply $(x_L + x_R)/2$ but its more general expression reads:

$$x_0 = \frac{x_R\sigma_L^2 - x_L\sigma_R^2 - \sigma_L\sigma_R\sqrt{(x_L - x_R)^2 - 2(\sigma_L^2 - \sigma_R^2)\log\left(\frac{N_L\sigma_R}{N_R\sigma_L}\right)}}{\sigma_L^2 - \sigma_R^2}. \quad (5.4)$$

The overlap between the two wave functions is given by:

$$\epsilon = \int_{x_0}^{\infty} f_L(x)dx + \int_{-\infty}^{x_0} f_R(x)dx, \quad (5.5)$$

that we can compute explicitly as

$$\epsilon = \frac{1}{2} \left(1 - \frac{N_L}{N_L + N_R} \text{Erf}\left[\frac{x_0 - x_L}{\sqrt{2}\sigma_L}\right] + \frac{N_R}{N_L + N_R} \text{Erf}\left[\frac{x_0 - x_R}{\sqrt{2}\sigma_R}\right] \right). \quad (5.6)$$

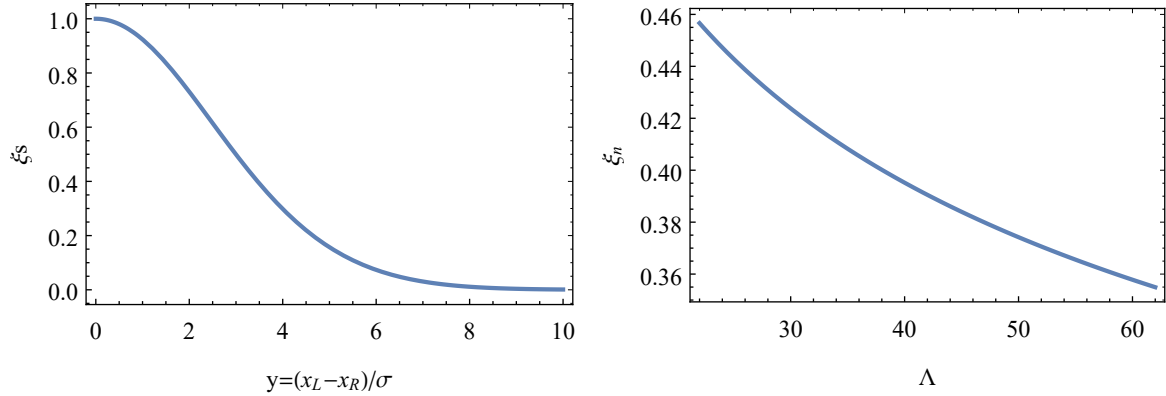


Figure 5.3: Variations of the number-squeezing factor due to a sloshing of the wave functions. Left: The sloshing modifies the overlap of the wave functions and introduces an error on the determination of the number-squeezing factor. A larger overlap increases the number-squeezing as a result of a miscount of atoms on the right and left clouds. Right: The sloshing of the clouds modifies the tunnel coupling and the corresponding Λ . The ground state fluctuations depend on the value of Λ such that an oscillation of J and Λ results in an oscillation of the number-squeezing factor.

In the case of symmetric wave functions, $x_0 = (x_L + x_R)/2$, the overlap normalized to the total atom number reads:

$$\epsilon_s = \frac{1}{2} \left(1 - \text{Erf} \left[\frac{y}{2\sqrt{2}} \right] \right), \quad (5.7)$$

with $y = (x_L - x_R)/\sigma$. For a perfect overlap of the wave functions, atoms have an identical probability to be counted on the left or right cloud such that $\epsilon = 1/2$ and we recover the binomial fluctuations. The squeezing factor then reads:

$$\xi_{n,s} = \frac{\Delta N}{N} = 2\sqrt{\epsilon_s(1 - \epsilon_s)}. \quad (5.8)$$

This shows that the error on the squeezing increases with the wave functions overlap. The variations of $\xi_{n,s}$ with y are displayed in the left panel of Fig. 5.3. It shows that as the sloshing brings the two clouds closer, the number-squeezing factor is increased due to the larger overlap of the wave functions. This is in qualitative agreement with the experimental observations displayed in Fig. 5.2.

Oscillations of the coupling strength The sloshing of the clouds can add another contribution to the squeezing oscillations. As the inter-cloud distance oscillates, one could expect that the tunnel coupling J , and therefore Λ , oscillates accordingly. As an estimate, we consider the impact of a change between $\Lambda = 20$ and $\Lambda = 60$ on the number-squeezing factor of the corresponding ground state. This is displayed in the right panel of Fig. 5.3. This shows that, as the sloshing leads to an oscillation of Λ , the corresponding number-squeezing factor oscillates. When the clouds are the closest, Λ is the smallest and the number-squeezing factor is maximal. This is also compatible with the experimental observations.

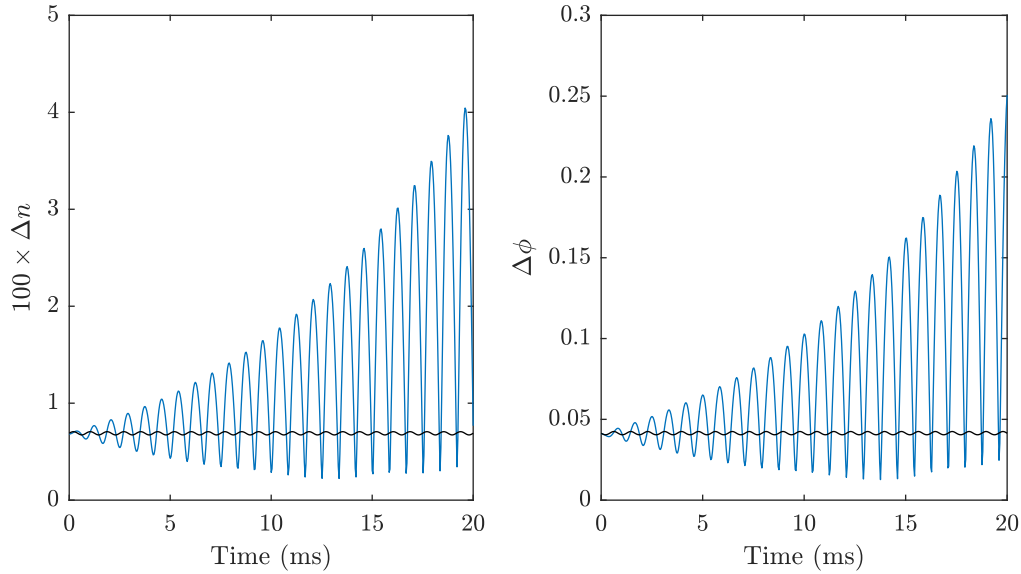


Figure 5.4: Parametric amplification of the fluctuations values. The initial fluctuations are the ground state fluctuations of the trap characterized by $\bar{J}/h = 50$ Hz, $\bar{\Lambda} = 35$. The tunnel coupling is then modulated at twice the average plasma frequency, in this case $\bar{\omega} = 2\pi \times 600$ Hz. The amplitude of the modulation is arbitrarily chosen to 10 Hz. The relaxation mechanism is not included as the initial fluctuations fulfill the minimal uncertainty product. The amplitude of the oscillations of Δn (left) and $\Delta\phi$ (right) increase during the modulation. The values of the minima reach lower values in a first part of the modulation and the imbalance fluctuations reach lower values than the ones of the ground state. During this stage, the modulation is such that the coupling decreases each time Δn is maximal. At longer time, the phase spread is significantly increased such that a dephasing occurs and the minima do not decrease further but increase at each oscillations. In this case, the lowest number-squeezing factor is obtained after 13 ms of modulation.

Conclusion The two step-splitting is a promising shortcut to the adiabatic splitting. Its shorter ramp durations are likely to limit the relaxation and are susceptible to generate high number-squeezed states. However, the first experimental implementation shows that a fast splitting introduces a sloshing motion of the condensates leading to an oscillation of the measurement error and to an oscillation of the tunnel coupling. Both these effects contribute to an oscillation of the number-squeezing factor. When the frequency of the sloshing is comparable to twice the Josephson frequency, these contributions are difficult to distinguish. By construction of our double-well, these timescales cannot differ significantly.

The sloshing sets a lower limit to the duration of the splitting ramps. However, the sloshing at $\omega = 2\pi \times 750$ Hz, i.e at twice the expected Josephson frequency in this trap results in an oscillation of the tunnel coupling at the same frequency. This situation is precisely the one defined by the parametric amplification of squeezing. This scheme can be seen as a generalization of the two-step splitting. It relies on the modulation of the tunnel coupling around an averaged value \bar{J} at the frequency equal to twice the plasma frequency $\bar{\omega}$ defined by \bar{J} . This approach relies on the dynamics of the fluctuations in the changing trap such that the tunnel coupling is periodically decreased each time Δn reaches a maximum of oscillations.

We illustrate this protocol in Fig. 5.4, where we display the evolution of $\Delta n(t)$ and $\Delta\phi(t)$ over the duration of the modulation. The averaged \bar{J} reads $\bar{J}/h = 50$ Hz such that $\bar{\Lambda} = 35$ and $\bar{\omega} = 2\pi \times 600$ Hz. The sinusoidal modulation of $J(t)$ is performed with the arbitrary amplitude 10 Hz. The initial fluctuations corresponds to the ground state fluctuations of the averaged trap. The evolution of the fluctuations shows an increase of the amplitude of the fluctuations which can lead to a number-squeezing factor lower than the one of the ground state. This value cannot be compared to the one of the two-step splitting as in this case, the splitting was performed to a value of J lower than \bar{J} which explains the smaller number-squeezing factor.

This simulation shows that the parametric amplification can be predicted by the MC-like simulation but it is too preliminary to conclude whether this scheme can be implemented. For example, the larger initial phase fluctuations are susceptible to affect the modulation ramp. In the MC-like model, we can understand it as follow: the classical points at the edge of the phase distribution are further away from equilibrium and oscillate at a frequency lower than the plasma frequency. Therefore, the modulation at twice the Josephson frequency does not allow to modify their trajectory as expected. For large $\Delta\phi_0$, the modulation instead lead to a faster dephasing. Therefore, the modulation generally does not lead to a parametric amplification.

The relaxation, which is likely to play a role for long modulation durations, makes the picture even more complex. It leads to a phase locking which limits the dephasing and might allow the parametric amplification even for large initial phase distributions. However, with the MC-like simulation, the fluctuations decrease to zero and the most favorable scheme is to let the distributions evolve in a fixed trap rather than to modulate the tunnel coupling. As we know that this picture breaks down due to the Heisenberg limit, the proper description of the parametric amplification goes beyond the MC-like model developed here and requires to include the Heisenberg limit in the model.

Bibliography

- [1] D. Podolsky, G. N. Felder, L. Kofman, and M. Peloso. Equation of state and beginning of thermalization after preheating. *Phys. Rev. D*, 73(2):023501, 2006.
- [2] L. Kofman, A. Linde, and A. A. Starobinsky. Towards the theory of reheating after inflation. *Phys. Rev. D*, 56(6):3258–3295, 1997.
- [3] A. Arrizabalaga, J. Smit, and A. Tranberg. Equilibration in φ^4 theory in $3 + 1$ dimensions. *Phys. Rev. D*, 72(2):025014, 2005.
- [4] J. Berges, Sz. Borsányi, and C. Wetterich. Prethermalization. *Phys. Rev. Lett.*, 93(14):142002, 2004.
- [5] P. Braun-Munzinger, D. Magestro, K. Redlich, and J. Stachel. Hadron production in Au–Au collisions at RHIC. *Phys. Lett. B*, 518:41–46, 2001.
- [6] U. Heinz and P. Kolb. Early thermalization at RHIC. *Nucl. Phys. A*, 702(1):269–280, 2002.
- [7] C. Kollath, A. M. Läuchli, and E. Altman. Quench Dynamics and Nonequilibrium Phase Diagram of the Bose-Hubbard Model. *Phys. Rev. Lett.*, 98(18):180601, 2007.
- [8] M. Eckstein, M. Kollar, and P. Werner. Thermalization after an Interaction Quench in the Hubbard Model. *Phys. Rev. Lett.*, 103(5):056403, 2009.
- [9] M. Moeckel and S. Kehrein. Crossover from adiabatic to sudden interaction quenches in the Hubbard model: prethermalization and non-equilibrium dynamics. *New J. Phys.*, 12(5):055016, 2010.
- [10] R. Barnett, A. Polkovnikov, and M. Vengalattore. Prethermalization in quenched spinor condensates. *Phys. Rev. A*, 84(2):023606, 2011.
- [11] A. Polkovnikov, K. Sengupta, A. Silva, and M. Vengalattore. Colloquium: Nonequilibrium dynamics of closed interacting quantum systems. *Reviews of Modern Physics*, 83(3):863–883, 2011.
- [12] M. Srednicki. Chaos and quantum thermalization. *Phys. Rev. E*, 50(2):888–901, 1994.
- [13] J. M. Deutsch. Quantum statistical mechanics in a closed system. *Phys. Rev. A*, 43(4):2046–2049, 1991.
- [14] P. Reimann. Foundation of Statistical Mechanics under Experimentally Realistic Conditions. *Phys. Rev. Lett.*, 101(19):190403, 2008.

- [15] C. Gogolin, M. P. Müller, and J. Eisert. Absence of Thermalization in Nonintegrable Systems. *Phys. Rev. Lett.*, 106(4):040401, 2011.
- [16] M. Rigol and M. Fitzpatrick. Initial-state dependence of the quench dynamics in integrable quantum systems. *Phys. Rev. A*, 84(3):033640, 2011.
- [17] A. Riera, C. Gogolin, and J. Eisert. Thermalization in Nature and on a Quantum Computer. *Phys. Rev. Lett.*, 108(8):080402, 2012.
- [18] M. Rigol, V. Dunjko, and M. Olshanii. Thermalization and its mechanism for generic isolated quantum systems. *Nature*, 452(7189):854–858, 2008.
- [19] M. A. Rigol, V. Dunjko, and M. Olshanii. Erratum: Thermalization and its mechanism for generic isolated quantum systems. *Nature*, 481(7380), 2012.
- [20] M. Rigol and M. Srednicki. Alternatives to Eigenstate Thermalization. *Phys. Rev. Lett.*, 108(11):110601, 2012.
- [21] M. Gring, M. Kuhnert, T. Langen, T. Kitagawa, B. Rauer, M. Schreitl, I. Mazets, D. Adu Smith, E. Demler, and J. Schmiedmayer. Relaxation and Prethermalization in an Isolated Quantum System. *Science*, 337(6100):1318–1322, 2012.
- [22] I. Bloch, J. Dalibard, and W. Zwerger. Many-body physics with ultracold gases. *Rev. Mod. Phys.*, 80:885–964, 2008.
- [23] W. Ketterle, D. S. Durfee, and D. M. Stamper-Kurn. Making, probing and understanding Bose-Einstein condensates. *arXiv:cond-mat/9904034*, 1999. arXiv: cond-mat/9904034.
- [24] C. Chin, R. Grimm, P. Julienne, and E. Tiesinga. Feshbach resonances in ultracold gases. *Rev. Mod. Phys.*, 82(2):1225–1286, 2010.
- [25] B. S. Rem, A. T. Grier, I. Ferrier-Barbut, U. Eismann, T. Langen, N. Navon, L. Khaykovich, F. Werner, D. S. Petrov, F. Chevy, and C. Salomon. Lifetime of the Bose Gas with Resonant Interactions. *Phys. Rev. Lett.*, 110(16):163202, 2013.
- [26] S. Trotzky, Y-A. Chen, A. Flesch, I. P. McCulloch, U. Schollwöck, J. Eisert, and I. Bloch. Probing the relaxation towards equilibrium in an isolated strongly correlated one-dimensional Bose gas. *Nat. Phys.*, 8(4):325–330, 2012.
- [27] R. Bücker, A. Perrin, S. Manz, T. Betz, Ch Koller, T. Plisson, J. Rottmann, T. Schumm, and J. Schmiedmayer. Single-particle-sensitive imaging of freely propagating ultracold atoms. *New J. Phys.*, 11(10):103039, 2009.
- [28] J. F. Sherson, C. Weitenberg, M. Endres, M. Cheneau, I. Bloch, and S. Kuhr. Single-atom-resolved fluorescence imaging of an atomic Mott insulator. *Nature*, 467(7311):68–72, 2010.

- [29] W. S. Bakr, A. Peng, M. E. Tai, R. Ma, J. Simon, J. I. Gillen, S. Fölling, L. Pollet, and M. Greiner. Probing the Superfluid–to–Mott Insulator Transition at the Single-Atom Level. *Science*, 329(5991):547–550, 2010.
- [30] T. Giamarchi. *Quantum Physics in One Dimension*. International Series of Monographs on Physics. Oxford, Clarendon Press, 2003.
- [31] M. A. Cazalilla, R. Citro, T. Giamarchi, E. Orignac, and M. Rigol. One dimensional bosons: From condensed matter systems to ultracold gases. *Rev. Mod. Phys.*, 83(4):1405–1466, 2011.
- [32] F. D. M. Haldane. "Luttinger liquid theory" of one-dimensional quantum fluids. I. Properties of the Luttinger model and their extension to the general 1d interacting spinless Fermi gas. *J. Phys. C: Solid State Phys.*, 14(19):2585–2609, 1981.
- [33] F. D. M. Haldane. Effective Harmonic-Fluid Approach to Low-Energy Properties of One-Dimensional Quantum Fluids. *Phys. Rev. Lett.*, 47(25):1840–1843, 1981.
- [34] J. Cuevas-Maraver, P. G. Kevrekidis, and F. editors Williams. The sine-Gordon Model and its Applications. In *Nonlinear Systems and Complexity*. Springer International Publishing, Cham, 2014.
- [35] V. Gritsev, A. Polkovnikov, and E. Demler. Linear response theory for a pair of coupled one-dimensional condensates of interacting atoms. *Phys. Rev. B*, 75(17):174511, 2007.
- [36] B. Bertini, D. Schuricht, and F. H. L. Essler. Quantum quench in the sine-Gordon model. *JSTAT*, 2014(10):P10035, 2014.
- [37] M. Kormos and G. Zaránd. Quantum quenches in the sine-Gordon model: A semi-classical approach. *Phys. Rev. E*, 93(6):062101, 2016.
- [38] D. X. Horváth, I. Lovas, M. Kormos, G. Takács, and G. Zaránd. Nonequilibrium time evolution and rephasing in the quantum sine-Gordon model. *Phys. Rev. A*, 100(1):013613, 2019.
- [39] J.-S. Caux and J. Mossel. Remarks on the notion of quantum integrability. *JSTAT*, 2011(2):P02023, 2011.
- [40] T. Langen, R. Geiger, and J. Schmiedmayer. Ultracold Atoms Out of Equilibrium. *Annu. Rev. Condens. Matter Phys.*, 6(1):201, 2015.
- [41] T. Schweigler, V. Kasper, S. Erne, I. Mazets, B. Rauer, F. Cataldini, T. Langen, T. Gasenzer, J. Berges, and J. Schmiedmayer. Experimental characterization of a quantum many-body system via higher-order correlations. *Nature*, 545(7654):323–326, 2017.
- [42] R. Gati and M. K. Oberthaler. A bosonic Josephson junction. *J. Phys. B*, 40(10):R61–R89, 2007.

- [43] W. Hänsel, P. Hommelhoff, T. W. Hänsch, and J. Reichel. Bose–Einstein condensation on a microelectronic chip. *Nature*, 413(6855):498–501, 2001.
- [44] H. Ott, J. Fortagh, G. Schlotterbeck, A. Grossmann, and C. Zimmermann. Bose–Einstein Condensation in a Surface Microtrap. *Phys. Rev. Lett.*, 87(23):230401, 2001.
- [45] J. Reichel and V. Vuletic. *Atom Chips*. Wiley, VCH, 2011.
- [46] R. Folman, P. Kruger, J. Schmiedmayer, J. Denschlag, and C. Henkel. Microscopic atom optics: from wires to an atom chip. *arXiv:0805.2613 [quant-ph]*, 2008.
- [47] S. Hofferberth, I. Lesanovsky, B. Fischer, J. Verdu, and J. Schmiedmayer. Radiofrequency-dressed-state potentials for neutral atoms. *Nat. Phys.*, 2(10):710–716, 2006.
- [48] I. Lesanovsky, S. Hofferberth, J. Schmiedmayer, and P. Schmelcher. Manipulation of ultracold atoms in dressed adiabatic radio-frequency potentials. *Phys. Rev. A*, 74(3):033619, 2006.
- [49] S. Hofferberth, B. Fischer, T. Schumm, J. Schmiedmayer, and I. Lesanovsky. Ultracold atoms in radio-frequency dressed potentials beyond the rotating-wave approximation. *Phys. Rev. A*, 76(1):013401, 2007.
- [50] T. Schumm, S. Hofferberth, L. M. Andersson, S. Wildermuth, S. Groth, I. Bar-Joseph, J. Schmiedmayer, and P. Krüger. Matter-wave interferometry in a double well on an atom chip. *Nat. Phys.*, 1(1):57–62, 2005.
- [51] A. D. Cronin, J. Schmiedmayer, and D. E. Pritchard. Optics and interferometry with atoms and molecules. *Rev. Mod. Phys.*, 81(3):1051–1129, 2009.
- [52] G. M. Tino and M. A. editors Kasevich. Interferometry with Atoms. In *Course 188: Atom Interferometry*. IOS Press, Proceedings of the International School of Physics ”Enrico Fermi”, 2014.
- [53] E. G. Dalla Torre, E. Demler, and A. Polkovnikov. Universal Rephasing Dynamics after a Quantum Quench via Sudden Coupling of Two Initially Independent Condensates. *Phys. Rev. Lett.*, 110(9):090404, 2013.
- [54] L. Foini and T. Giamarchi. Nonequilibrium dynamics of coupled Luttinger liquids. *Phys. Rev. A*, 91:023627, 2015.
- [55] L. Foini and T. Giamarchi. Relaxation dynamics of two coherently coupled one-dimensional bosonic gases. *EPJ - st*, 226:2763–2774, 2017.
- [56] M. Pigneur, T. Berrada, M. Bonneau, T. Schumm, E. Demler, and J.g Schmiedmayer. Relaxation to a Phase-Locked Equilibrium State in a One-Dimensional Bosonic Josephson Junction. *Phys. Rev. Lett.*, 120(17):173601, 2018.

- [57] M. Pigneur and J. Schmiedmayer. Analytical pendulum model for a bosonic Josephson junction. *Phys. Rev. A*, 98(6):063632, 2018.
- [58] S. N. Bose. Plancks Gesetz und Lichtquantenhypothese. *Z. Phys.*, 26:178, 1924.
- [59] A. Einstein. Zur Quantentheorie des idealen Gases. *Sitzungsberichte der Preussischen Akademie des Wissenschaften*, 3:18, 1925.
- [60] J.C. Pethick and H. Smith. *Bose-Einstein condensation in dilute gases*. Cambridge Univ. Press, 2008.
- [61] L. Pitaevski and S. Stringari. *Bose-Einstein Condensation*. International series of monographs on physics 116. Oxford Univ. Press, 2003.
- [62] J. F. Annett. *Superconductivity, superfluids, and condensates*. Oxford master series in physics Condensed matter physics. Oxford Univ. Press, 2010.
- [63] W. Ketterle and N. J. van Druten. Bose-Einstein condensation of a finite number of particles trapped in one or three dimensions. *Phys. Rev. A*, 54(1):656, 1996.
- [64] N. D. Mermin and H. Wagner. Absence of Ferromagnetism or Antiferromagnetism in One- or Two-Dimensional Isotropic Heisenberg Models. *Phys. Rev. Lett.*, 17(22):1133–1136, 1966.
- [65] P. C. Hohenberg. Existence of Long-Range Order in One and Two Dimensions. *Phys. Rev.*, 158(2):383–386, 1967.
- [66] D. S. Petrov, G. V. Shlyapnikov, and J. T. M. Walraven. Regimes of Quantum Degeneracy in Trapped 1d Gases. *Phys. Rev. Lett.*, 85(18):3745–3749, 2000.
- [67] J. T. M. Walraven. Thermodynamic and Collisional Properties of Trapped Atomic Gases. *Les Houches, lecture notes*, 2008.
- [68] D. A. Steck. Rubidium 87 D Line Data. 2015.
- [69] N. N. Bogoliubov. On the theory of superfluidity. *J. Phys.(USSR)*, 11:4–2, 1947.
- [70] E. P. Gross. Structure of a quantized vortex in boson systems. *Il Nuovo Cimento*, 20(3):454–477, 1961.
- [71] L.P. Pitaevskii. Vortex Lines in an Imperfect Bose Gas. *Zh. Eksp. Teor. Fiz.*, 40:646, 1961.
- [72] L. Salasnich, A. Parola, and L. Reatto. Effective wave equations for the dynamics of cigar-shaped and disk-shaped Bose condensates. *Phys. Rev. A*, 65(4), 2002.
- [73] C. Menotti and S. Stringari. Collective oscillations of a one-dimensional trapped Bose-Einstein gas. *Phys. Rev. A*, 66(4), 2002.
- [74] F. Gerbier. Quasi-1d Bose-Einstein condensates in the dimensional crossover regime. *Europhys. Lett.*, 66(6):771–777, 2004.

- [75] K. K. Das, M. D. Girardeau, and E. M. Wright. Crossover from One to Three Dimensions for a Gas of Hard-Core Bosons. *Phys. Rev. Lett.*, 89(11), 2002.
- [76] A. Muñoz Mateo and V. Delgado. Effective mean-field equations for cigar-shaped and disk-shaped Bose-Einstein condensates. *Phys. Rev. A*, 77(1):013617, 2008.
- [77] A. Smerzi, S. Fantoni, S. Giovanazzi, and S. R. Shenoy. Quantum Coherent Atomic Tunneling between Two Trapped Bose-Einstein Condensates. *Phys. Rev. Lett.*, 79(25):4950–4953, 1997.
- [78] S. Raghavan, A. Smerzi, S. Fantoni, and S. R. Shenoy. Coherent oscillations between two weakly coupled Bose-Einstein condensates: Josephson effects, oscillations, and macroscopic quantum self-trapping. *Phys. Rev. A*, 59:620, 1999.
- [79] E. A. Ostrovskaya, Y. S. Kivshar, M. Lisak, B. Hall, F. Cattani, and D. Anderson. Coupled-mode theory for Bose-Einstein condensates. *Phys. Rev. A*, 61(3):031601, 2000.
- [80] D. Ananikian and T. Bergeman. Gross-Pitaevskii equation for Bose particles in a double-well potential: Two-mode models and beyond. *Phys. Rev. A*, 73(1):013604, 2006.
- [81] M. Albiez, R. Gati, J. Fölling, S. Hunsmann, M. Cristiani, and M. K. Oberthaler. Direct Observation of Tunneling and Nonlinear Self-Trapping in a Single Bosonic Josephson Junction. *Phys. Rev. Lett.*, 95(1):010402, 2005.
- [82] Roberto Franzosi, Vittorio Penna, and Riccardo Zecchina. Quantum Dynamics of Coupled Bosonic Wells Within The Bose-Hubbard Picture. *Int. J. Mod. Phys. B*, 14:943–961, 2000.
- [83] W. P. Schleich. Quantum Optics in Phase Space. Wiley, VCH, 2001.
- [84] J. Javanainen. Oscillatory exchange of atoms between traps containing Bose condensates. *Phys. Rev. Lett.*, 57(25):3164–3166, 1986.
- [85] M. W. Jack, M. J. Collett, and D. F. Walls. Coherent quantum tunneling between two Bose-Einstein condensates. *Phys. Rev. A*, 54(6):R4625–R4628, 1996.
- [86] I. Zapata, F. Sols, and A. J. Leggett. Josephson effect between trapped Bose-Einstein condensates. *Phys. Rev. A*, 57(1):R28–R31, 1998.
- [87] I. Marino, S. Raghavan, S. Fantoni, S. R. Shenoy, and A. Smerzi. Bose-condensate tunneling dynamics: Momentum-shortened pendulum with damping. *Phys. Rev. A*, 60(1):487–493, July 1999.
- [88] A. J. Leggett. Bose-Einstein condensation in the alkali gases: Some fundamental concepts. *Rev. Mod. Phys.*, 73(2):307–356, 2001.

- [89] C. Liang, K. Wei, B. J. Ye, H. M. Wen, X. Y. Zhou, and R. D. Han. Dynamics and Ground State Properties of Two-component Bose-Einstein Condensate in Different Hyperfine States. *J. Low Temp. Phys.*, 161(3):334–347, 2010.
- [90] J. Marion and S. T. Thornton. *Classical Dynamics of Particles and Systems*. Brooks-Cole, 5 edition, 2004.
- [91] M. Abramowitz and I. A. Stegun. *Handbook of Mathematical Functions*. Dover Publications, Inc., Nova Iorque, 10 edition, 1972.
- [92] P. Buonsante, R. Franzosi, and V. Penna. Single-particle-sensitive imaging of freely propagating ultracold atoms. *Laser Phys.*, 14(10):554, 2004.
- [93] G. J. Milburn, J. Corney, E. M. Wright, and D. F. Walls. Quantum dynamics of an atomic Bose-Einstein condensate in a double-well potential. *Phys. Rev. A*, 55(6):4318, June 1997.
- [94] E.J. Mueller, T.-L. Ho, M. Ueda, and G. Baym. Fragmentation of Bose-Einstein condensates. *Phys. Rev. A*, 74(3):033612, 2006.
- [95] K. W. Mahmud, H. Perry, and W. P. Reinhardt. Quantum phase-space picture of Bose-Einstein condensates in a double well. *Phys. Rev. A*, 71(2), 2005.
- [96] M. Jääskeläinen and P. Meystre. Dynamics of Bose-Einstein condensates in double-well potentials. *Phys. Rev. A*, 71(4):043603, 2005.
- [97] M. Jääskeläinen and P. Meystre. Coherence dynamics of two-mode condensates in asymmetric potentials. *Phys. Rev. A*, 73(1):013602, 2006.
- [98] F. Sols. Randomization of the phase after suppression of the Josephson coupling. *Physica B: Condensed Matter*, 194-196:1389–1390, 1994.
- [99] M Lewenstein and L You. Quantum Phase Diffusion of a Bose-Einstein Condensate. *Phy. Rev. Lett.*, 77(17):3489–3493, 1996.
- [100] Y. Castin and J. Dalibard. Relative phase of two Bose-Einstein condensates. *Phys. Rev. A*, 55(6):4330–4337, 1997.
- [101] J. Javanainen and M. Wilkens. Phase and Phase Diffusion in a Split Bose-Einstein Condensate. *Phy. Rev. Lett.*, 78:4675, 1997.
- [102] A. J. Leggett and F Sols. Comment on Phase and Phase Diffusion in a Split Bose-Einstein Condensate. *Phy. Rev. Lett.*, 81(6):1344, 1998.
- [103] J. Javanainen and M. Y. Ivanov. Splitting a trap containing a Bose-Einstein condensate: Atom number fluctuations. *Phys. Rev. A*, 60(3):2351–2359, 1999.
- [104] G.-B. Jo, Y. Shin, S. Will, T. A. Pasquini, M. Saba, W. Ketterle, D. E. Pritchard, M. Vengalattore, and M. Prentiss. Long Phase Coherence Time and Number Squeezing of Two Bose-Einstein Condensates on an Atom Chip. *Phys. Rev. Lett.*, 98(3):030407, 2007.

- [105] J. Estève, C. Gross, A. Weller, S. Giovanazzi, and M. K. Oberthaler. Squeezing and entanglement in a Bose–Einstein condensate. *Nature*, 455(7217):1216–1219, 2008.
- [106] K. Maussang, G. E. Marti, T. Schneider, P. Treutlein, Y. Li, A. Sinatra, R. Long, J. Estève, and J. Reichel. Enhanced and Reduced Atom Number Fluctuations in a BEC Splitter. *Phys. Rev. Lett.*, 105(8):080403, 2010.
- [107] T. Berrada, S. van Frank, R. Bücke, T. Schumm, J.-F. Schaff, and J. Schmiedmayer. Integrated Mach–Zehnder interferometer for Bose–Einstein condensates. *Nat. Commun.*, 4:2077, 2013.
- [108] G. Jäger, T. Berrada, J. Schmiedmayer, T. Schumm, and U. Hohenester. Parametric-squeezing amplification of Bose-Einstein condensates. *Phys. Rev. A*, 92(5):053632, 2015.
- [109] J. Grond, J. Schmiedmayer, and U. Hohenester. Optimizing number squeezing when splitting a mesoscopic condensate. *Phys. Rev. A*, 79(2):021603, 2009.
- [110] B. Juliá-Díaz, T. Zibold, M. K. Oberthaler, M. Melé-Messeguer, J. Martorell, and A. Polls. Dynamic generation of spin-squeezed states in bosonic Josephson junctions. *Phys. Rev. A*, 86(2):023615, 2012.
- [111] W. Muessel, H. Strobel, D. Linnemann, T. Zibold, B. Juliá-Díaz, and M. K. Oberthaler. Twist-and-turn spin squeezing in Bose-Einstein condensates. *Phys. Rev. A*, 92(2):023603, 2015.
- [112] H. Gimpel. *Magnetische Oberflächen für Atome-Interferometer*. Diploma thesis, Universität Heidelberg, 2002.
- [113] C. Becker. *Eine neuartige magneto-optische Falle für Atomchip-Experimente*. Diploma thesis, Universität Heidelberg, 2002.
- [114] S. Haupt. *Setup a new Experiment with ultracold ^{87}Rb Atoms: Toward Quantum Information Processing on a Atom Chip*. PhD thesis, Universität Heidelberg, 2003.
- [115] P. Krüger. *Coherent matter waves near surfaces*. PhD thesis, Universität Heidelberg, 2004.
- [116] S. Hofferberth. *Experiments with ultracold atoms and Bose-Einstein condensated in microtraps near surfaces*. Diploma thesis, Universität Heidelberg, 2004.
- [117] S. Wildermuth. *One-dimensional Bose-Einstein condensates in micro-traps*. PhD thesis, Universität Heidelberg, 2005.
- [118] S. Manz. *Density correlations of expanding one-dimensional Bose gases*. PhD thesis, TU Wien, 2011.
- [119] T. Betz. *Phase correlations of coupled one-dimensional Bose gases*. PhD thesis, TU Wien, 2011.

- [120] M. Trinker, S. Groth, S. Haslinger, S. Manz, T. Betz, S. Schneider, I. Bar-Joseph, T. Schumm, and J. Schmiedmayer. Multilayer atom chips for versatile atom micro-manipulation. *Appl. Phys. Lett.*, 92(25):254102, 2008.
- [121] T. Schumm. *Bose-Einstein condensates in magnetic double-well potentials*. PhD thesis, Université Paris XI, 2005.
- [122] S. Hofferberth. *Coherent manipulation of Bose-Einstein condensates with rf adiabatic potentials*. PhD thesis, Universität Heidelberg, 2007.
- [123] R. Bücker. *Fluorescence imaging of ultracold atoms*. Diplomas thesis, Universität Heidelberg, 2007.
- [124] R. Bücker. *Twin-atom beam generation in a one-dimensional Bose gas*. PhD thesis, TU Wien, 2013.
- [125] W. Rohringer. *Stochastic Optimization in an Ultracold Atom Experiment*. Diploma thesis, TU Wien, 2008.
- [126] W. Rohringer, R. Bücker, S. Manz, T. Betz, Ch. Koller, M. Göbel, A. Perrin, J. Schmiedmayer, and T. Schumm. Stochastic optimization of a cold atom experiment using a genetic algorithm. *Appl. Phys. Lett.*, 93(26):264101, 2008.
- [127] V. S. Bagnato, G. P. Lafyatis, A. G. Martin, E. L. Raab, R. N. Ahmad-Bitar, and D. E. Pritchard. Continuous Stopping and Trapping of Neutral Atoms. *Phys. Rev. Lett.*, 58(21):2194–2197, 1987.
- [128] D. E. Pritchard. Cooling Neutral Atoms in a Magnetic Trap for Precision Spectroscopy. *Phys. Rev. Lett.*, 51(15):1336–1339, 1983.
- [129] J. Estève, C. Aussibal, T. Schumm, C. Figl, D. Maily, I. Bouchoule, C. I. Westbrook, and A. Aspect. Role of wire imperfections in micromagnetic traps for atoms. *Phys. Rev. A*, 70(4):043629, 2004.
- [130] T. Schumm, J. Estève, C. Figl, J.-B. Trebbia, C. Aussibal, H. Nguyen, D. Maily, I. Bouchoule, C. I. Westbrook, and A. Aspect. Atom chips in the real world: the effects of wire corrugation. *EPJD*, 32(2):171–180, 2005.
- [131] P. Krüger, L. M. Andersson, S. Wildermuth, S. Hofferberth, E. Haller, S. Aigner, S. Groth, I. Bar-Joseph, and J. Schmiedmayer. Potential roughness near lithographically fabricated atom chips. *Phys. Rev. A*, 76(6):063621, 2007.
- [132] H. Perrin and B. M. Garraway. Chapter4: Trapping Atoms With Radio Frequency Adiabatic Potentials. In *Advances In Atomic, Molecular, and Optical Physics*, volume 66, pages 181–262. Academic Press, 2017.
- [133] G. Reinaudi, T. Lahaye, Z. Wang, and G. Guéry-Odelin. Strong saturation absorption imaging of dense clouds of ultracold atoms. *Opt. Lett.*, 32(21):3143–3145, 2007.

- [134] Y. D. van Nieuwkerk, J. Schmiedmayer, and F. Essler. Projective phase measurements in one-dimensional Bose gases. *SciPost Phys.*, 5(5):046, 2018.
- [135] K. Sakmann, A. I. Streltsov, O. E. Alon, and L. S. Cederbaum. Exact Quantum Dynamics of a Bosonic Josephson Junction. *Phys. Rev. Lett.*, 103(22):220601, 2009.
- [136] O. E. Alon, A. I. Streltsov, and L. S. Cederbaum. Multiconfigurational time-dependent Hartree method for bosons: Many-body dynamics of bosonic systems. *Phys. Rev. A*, 77(3):033613, 2008.
- [137] I. Bouchoule. Modulational instabilities in Josephson oscillations of elongated coupled condensates. *Eur. Phys. J. D*, 35(1):147–154, 2005.
- [138] R. Bistritzer and E. Altman. Intrinsic dephasing in one-dimensional ultracold atom interferometers. *Proc. Natl. Acad. Sci. USA*, 104:9955–9959, 2007.
- [139] T. Kitagawa, S. Pielawa, A. Imambekov, J. Schmiedmayer, V. Gritsev, and E. Demler. Ramsey Interference in One-Dimensional Systems: The Full Distribution Function of Fringe Contrast as a Probe of Many-Body Dynamics. *Phys. Rev. Lett.*, 104:255302, 2010.
- [140] T. Kitagawa, A. Imambekov, J. Schmiedmayer, and E. Demler. The dynamics and prethermalization of one-dimensional quantum systems probed through the full distributions of quantum noise. *New J. Phys.*, 13:073018, 2011.
- [141] W. Rohringer. *Dynamics of One-Dimensional Bose Gases in Time-Dependent Traps*. Phd thesis, TU Wien, 2014.
- [142] J.-F. Mennemann, D. Matthes, R.-M. Weishäupl, and T. Langen. Optimal control of Bose–Einstein condensates in three dimensions. *New J. Phys.*, 17(11):113027, 2015.
- [143] J.-F. Mennemann, H.-P. Stimming, and N. J. Mauser. *Wolfgang Pauli Institute, Vienna*. Private Communication.
- [144] S. Erne. *School of Mathematical Sciences, Nottingham*. Private Communication.
- [145] T. Lappe, A. Posazhennikova, and J. Kroha. Fluctuation damping of isolated, oscillating Bose-Einstein condensates. *Phys. Rev. A*, 98(2):023626, 2018.
- [146] J. Polo, V. Ahufinger, F. W. J. Hekking, and A. Minguzzi. Damping of Josephson Oscillations in Strongly Correlated One-Dimensional Atomic Gases. *Phys. Rev. Lett.*, 121(9):090404, 2018.
- [147] F. Trimborn, D. Witthaut, and S. Wimberger. Mean-field dynamics of a two-mode Bose–Einstein condensate subject to noise and dissipation. *J. Phys. B*, 41(17):171001, 2008.
- [148] G. Ferrini, D. Spohner, A. Minguzzi, and F. W. J. Hekking. Noise in Bose Josephson junctions: Decoherence and phase relaxation. *Phys. Rev. A*, 82(3):033621, 2010.

- [149] Y. Japha, S. Zhou, M. Keil, R. Folman, C. Henkel, and A. Vardi. Suppression and enhancement of decoherence in an atomic Josephson junction. *New J. Phys.*, 18(5):055008, 2016.
- [150] Y. Li and W.-. Li. Phase Dissipation of an Open Two-Mode Bose–Einstein Condensate. *Chin. Phys. Lett.*, 34(7):070303, 2017.
- [151] G. Zaránd, G. Takács, and I. Lovas. *Budapest University of Technology and Economics, Budapest*. Private Communication.
- [152] I. Hugues and T. Hase. *Measurements and their Uncertainties: A practical guide to modern error analysis*. Oxford, 2010.
- [153] T. Berrada. *Interferometry with Interacting Bose-Einstein Condensates in a double-Well Potential*. Springer Thesis, 2016.
- [154] M. J. Davis, P. B. Blakie, A. H. van Amerongen, N. J. van Druten, and K. V. Kheruntsyan. Yang-Yang thermometry and momentum distribution of a trapped one-dimensional Bose gas. *Phys. Rev. A*, 85(3):031604, 2012.
- [155] R. Gati, B. Hemmerling, J. Fölling, M. Albiez, and M. K. Oberthaler. Noise Thermometry with Two Weakly Coupled Bose-Einstein Condensates. *Physical Review Letters*, 96(13):130404, 2006.
- [156] M. Tajik, B. Rauer, T. Schweigler, F. Cataldini, J. Sabino, F. S. Møller, S.-C. Ji, I. E. Mazets, and J. Schmiedmayer. Designing Arbitrary One-dimensional Potentials on an Atom Chip. *arXiv:1908.01563*, 2019.
- [157] I. Mazet. *TU Wien, Atominstitut, Vienna*. Private Communication.
- [158] F. Essler and Y. Van Nieuwkerk. *Rudolf Peierls Centre for Theoretical Physics, Oxford*. Private Communication.



Die approbierte gedruckte Originalversion dieser Dissertation ist an der TU Wien Bibliothek verfügbar.
The approved original version of this doctoral thesis is available in print at TU Wien Bibliothek.

Acknowledgements

Over the six years of my PhD, I had the chance to be surrounded by exceptionally friendly and stimulating people, whose unfailing support allowed this thesis to be completed. I have so many reasons to thank them all that I am likely to forget some, for which I ask them to forgive me.

First of all, I am immensely grateful to my supervisor Jörg Schmiedmayer. He gave me the opportunity to carry on this project, along with his trust to make the most out of it. Jörg, thank you for leading me out of the tracks, both in science and on the skiing slopes of Obergurgl. Maybe as important to my eyes, he shared with me his love for the Viennese lifestyle up to the point where I made it my own.

Thank you also to Thorsten Schumm, for so many reasons that I cannot list them all. Most of all, I am grateful for his friendship, that I value above everything he did for me over my thesis. He taught me all I needed to know about the experiment, including the subtle and indescribable intuition that is required for the daily care of such a complex set up. I am grateful for the many times he came back in the lab, despite all he had to do for his own group, and for his generous involvement toward me. His support along these many years have been decisive to complete this work.

The entire team of Rb2 is obviously also having a special share in this section. I thank Robert Bucker, Sandrine Van Frank and Tarik Berrada, with whom I so easily discussed during my first visit to Vienna that joining the team became obvious to us all. Most of the data presented in this manuscript were taken with Tarik and I loved our time in the lab and our complete inability to be angry at each other beyond the end of a day. I thank Jean-Francois Schaff, who set the first stone of this project. I will forever regret that he left the team too early for us to do this project together. The team later welcomed Marie Bonneau, Mira Maiwöger, Filippo Borselli and Tiantian Zhang to whom I wish a lot of success with this experiment.

A particular thank you to Andreas Angerer, who supported me both professionally and personally. His endless curiosity and stubbornness in understanding helped me push the project forward in a way I could not have managed otherwise. I am also grateful for his patience and his aptitude to follow me in my crazy projects. Without you this manuscript would never have existed.

Then come a big thank you to my beloved friends and colleagues of the Atominstitut. To Camille Leveque, my French buddy who patiently suffers me making endless fun of his hair and ridiculously strong French accent. To Andrew Kanagin, who quickly learned after his arrival that his loud enthusiasm and good mood was not welcome on a Monday morning and who is the best companion one could dream of for a grilled sausage and an evening beer. To Thomas Astner, I would be so bored without your continuous and melodious flow of complains. No one can understand better my love for cooking channels and I value very much our culinary exchanges which fill my phone with juicy pictures.

To Filippo Borselli, for his phenomenal and sparkling temper. To Joao Sabino, I rarely laughed so much as when you entered my office the first time and said you would stay only three months. I think it was two years ago... To Federica Cataldini, so constantly absent-minded that we fear to lose her during holidays. Her bad luck in traveling became legendary and an endless source of entertainment worthy of a novel. For all these high quality evenings of grilling in the courtyard, drinking and watching movies at the coffee corner and taking holidays together in the shabby streets of Krakow and Budapest, I am grateful!

A general thank you to the other members of the group, past and present, that I did not mention before: Wolfgang Rohringer, Kathrin Butzak, Florian Steiner, Fritz Diorico, Matthias Schreitl, Georg Winkler, Bernhard Rauer, Thomas Schweigler, the previous generation that I missed deeply each time one of them was leaving; Ferhat Loubar and Ricarda Schönbichler, two project students that I am particularly happy to have met; Amin Tajik, Wenzel Kersten, Marion Mallweger, Frederik Moller and all the other members who will ensure the perpetuity of our group.

I also got deeply inspired by many theoretical discussions, in particular with Igor Mazet, from whom I got key elements to make progress on this project. I also thank Eugene Demler for the high density of inputs over our discussions. It was always a pleasure discussing with you. I am grateful to Gergely Zaránd, Izabella Lovas and Gabor Takacs from the Budapest University of Technology and Economics, for their persistent motivation in searching the underlying theory supporting our observations. I thank the team of the Wolfgang Pauli institute for their continuous effort in investigating another possible model. A special thank to Sebastian Erne, back then in Heidelberg, for his involvement and soothing temper. I am glad you are to join our group in a near future. I am grateful to Fabian Essler for challenging me so stubbornly on our observations and for his eternal skepticism, which forced me to be utterly convincing about our observations until I convinced both him and myself. These few hours of discussions in Granada forced me to take full responsibility of my project and made me grow as a physicist. I will never forget that.

A special thank to Fabian's student Yuri van Nieuwkerk, with whom I have so much in common. While I enjoy tremendously our scientific exchanges, they will never equal my pleasure in simply talking with you about art and music. Receiving your long emails always make my day brighter. I wish you to always keep your scientific sharpness and your heartwarming enthusiasm about all things.

I am grateful to Augusto Smerzi and Markus Oberthaler for agreeing so promptly on being respectively my thesis referee and examiner. Augusto, I hope you will find in this thesis a good use of the model you developed 20 years ago. I would have been at a loss analyzing our data without it, because, empirical as it is, no model proved better! Markus, thank you for coming to Vienna on this meaningful day. I might regret my decision during the questions sessions, but I am very glad you are in the examination committee. I would have wanted no one else more than you!

I was very fortunate to be a student of the CoQuS doctoral program, which supported my various travels and my secondment, and allowed me to connect with a significant network of young scientists. I met through this program exceptional people, in particular Marissa Guistina, who I learned afterward was actually almost my neighbor and who

became among the best friends I ever got.

I had the privilege to spend three months of my thesis in the group of Dana Anderson in Jila (Boulder, Colorado). I am full heartily grateful to Dana for this opportunity which changed my thesis. Seeing another group brought such a fresh wind on my own way to work as to change altogether my perception of my own project. I met wonderful people during this time, Carrie Weidner, Seth Caliga and Cameron Straatsma, with whom I had the most obvious understanding. I still miss them daily. During my stay, I lived with wonderful people: Debbie and James Fungafat, with whom I felt part of the family and something even bigger. Their kindness and generosity bring many people around them that I feel highly privileged to have met.

Of course I want to thank my family, who supported me in my decision to move my entire life to Vienna and who never failed to comfort me in the time it took me to adjust to this new environment. I am also grateful to Reingard Angerer for making me feel so welcome in the Angerer family. I would not feel half as much at home in Austria without her and the member of the Angerer family: Sophie, Peter, Anna and Maria.



Die approbierte gedruckte Originalversion dieser Dissertation ist an der TU Wien Bibliothek verfügbar.
The approved original version of this doctoral thesis is available in print at TU Wien Bibliothek.

List of publications

The results presented in this thesis have been published in:

- **Relaxation to a Phase-locked Equilibrium State in a One-dimensional Bosonic Josephson Junction**
M. Pigneur, T. Berrada, M. Bonneau, T. Schumm, E. Demler, J. Schmiedmayer,
Physical Review Letters 120, 173601, published April 27, 2018
- **Analytical Pendulum Model for a Bosonic Josephson Junction**
M. Pigneur and J. Schmiedmayer,
Physical Review A 98, 063632, published December 26, 2018

These results were reported in the following newspaper and scientific popularization journal:

- **Ultrakalte Atomwolken verblüffen Physiker**
Der Standard, 12 May 2018
- **Quantenzigarren in rätselhaftem gleichtakt.**
M. Pigneur,
Spektrum der Wissenschaft 9.18, Rubrik Forschung aktuell, September, 2018

Resulting from a previous project:

- **Epitaxial Graphene on 4H-SiC(0001) Grown under Nitrogen Flux: Evidence of Low Nitrogen Doping and High Charge Transfer.**
E. Velez-Fort, C. Mathieu, E. Pallecchi, M. Pigneur, M. Silly, R. Belkhou, M. Marangolo, A. Shukla, F. Sirotti and A. Ouerghi,
ACS Nano, accepted on November 13, 2012

MARINE PIGNEUR, MSc

Neustiftgasse 96/2/5
1070 Vienna, Austria
Phone: +43 6.60.12.62.302
Mail: marine.pigneur@tuwien.ac.at

French nationality
Born on 26.09.1989 in Briançon (05)



Curriculum Vitae

Education and qualifications

- Since 2013 **Vienna University of Technology, Institute for Atomic and Subatomic Physics**, Vienna, Austria
Experimental thesis under the supervision of Prof. Jörg Schmiedmayer, group of “Atomic physics and quantum optics”
Subject: Dynamics of a driven bosonic Josephson junction (one-dimensional Bose-Einstein condensates on an atom chip)
- 2012-2013 **ENS (Ecole Normale Supérieure) and Magistère in Fundamental Physics, University of Paris-Sud XI**, Paris, France
Master’s degree ICFP (International Concepts in Fundamental Physics), Speciality: Condensed Matter Physics (with distinction)
- 2010-2012 **Magistère in Fundamental Physics, University of Paris-Sud XI**, Orsay, France
Licence’s degree and 1st year of Master’s study in Fundamental Physics (with distinction).
- 2008-2010 **University of Paris-Sud XI**, Orsay, France
Licence STS PMCP (with distinction)
Intensive university-level preparation for French competitive national entrance examinations to Magistères and Grandes Ecoles.
- 2007-2008 **Lycée du Parc**, Lyon, France
Preparation for French competitive national entrance examinations to the Grandes Ecoles.
- 2004-2007 **Lycée d'Altitude**, Briançon, France
French scientific leaving-certificate (with highest distinction)

Work Experience and Internships

- 2015, April-June:** Visiting PhD student in JILA, NIST-University of Colorado (Boulder, CO, US), group of Dana Anderson
- 2013, January-April:** Scientific internship at SPEC CEA, Saclay (Service de Physique de l’Etat Condensé, Commissariat à l’Energie Atomique) supervised by Marcello GOFFMAN (Quantronic Group), France
Subject: Majorana and Andreev States in Hybrid Circuits combining Spin-active and Superconducting Materials (MASH project)
Keywords & techniques: superconductivity, 2D electron gas physics, hybrid system, electronic lithography, cryogenic environment, transport measurement at low temperature and high magnetic field
- 2012, April-July:** Scientific internship at LPN Marcoussis (Laboratoire de Photonique et Nanostructures), France supervised by Abdelkarim OUERGI. Characterization in collaboration with TEMPO beamline, Synchrotron SOLEIL, France
Subject: Study of graphene nanoribbons epitaxially grown on SiC substrate and functionalization by nitrogen and oxygen
Keywords & techniques: 1D-structure of graphene, nanofabrication, LEED, AFM, Raman spectroscopy, highly resolved XPS, ARPES.
- 2011, May-July:** Scientific internship at Synchrotron SOLEIL, TEMPO beamline supervised by Fausto SIROTTI, France
Subject: Spectroscopy of photoelectrons of ultrathin films of gadolinium and of gadolinium/cobalt alloys using synchrotron radiation.
Keywords & techniques: magnetism, epitaxial growth, spectroscopy using synchrotron radiation (XPS, XMCD)

Scholarships

- 2013** Admission to the highly selective CoQuS doctoral program www.coqus.at